Yi Ding · Zhonghua Zhang

Nanoporous Metals for Advanced Energy Technologies

Springer

Nanoporous Metals for Advanced Energy Technologies

Yi Ding · Zhonghua Zhang

Nanoporous Metals for Advanced Energy Technologies

Springer

Yi Ding
Institute for New Energy Materials and Low-Carbon Technologies
Tianjin University of Technology
Tianjin
China

Zhonghua Zhang
School of Materials Science and Engineering
Shandong University
Jinan
China

ISBN 978-3-319-29747-7 ISBN 978-3-319-29749-1 (eBook)
DOI 10.1007/978-3-319-29749-1

Library of Congress Control Number: 2016931599

Printed on acid-free paper

This Springer imprint is published by Springer Nature
The registered company is Springer International Publishing AG Switzerland

Preface

Advanced energy technologies have been and will continue to be one of the most explored fields across the multidisciplines of: materials science, chemistry, applied physics and engineering. The rapid progress of portable electronic devices and electric vehicles in recent years has aroused tremendous research interests and technological challenges for the development of higher energy and/or power density electrochemical power management devices such as fuel cells, supercapacitors, and Li batteries.

Nanostructured carbon materials have traditionally been deemed as the most suitable electrode materials in almost all above-mentioned energy technologies due to their low price, high specific surface area, and chemical stability. However, recent researches have revealed that dealloyed nanoporous metals can also function as an alternative type of electrode materials that exhibit some very unique structural properties not commonly expected from carbon-based electrodes. Amongst various unique features of dealloyed nanoporous metals, the most appreciable ones are (i) bicontinuous open framework structures tunable across the wide dimension scale; (ii) clean surfaces with well-defined and tailorable interfacial structures; (iii) superior electric conductivity; (iv) simple processing scalable for mass production.

This book aims to provide a comprehensive discussion of research in this new field to date. Chapters 1 and 2 provide a general introduction of nanoporous metals, in particular on how a historically unwanted process of alloy corrosion can be tailored to generate functional nanoporous metals and composites with tunable structural properties. Chapters 3–5 discuss the respective research advances of dealloyed nanoporous metals for applications in fuel cells, supercapacitors, and Li batteries. And finally Chap. 6 summarizes the current research activities and also proposes future prospects of employing this new class of electrode materials for other energy-related technologies.

Tianjin
Jinan
2016

Yi Ding
Zhonghua Zhang

Acknowledgments

We would like to thank our group members who have been devoting their energy and interests into this fascinating research field during the past decade. Many of them are also involved during the preparation and editing of this book, and our particular acknowledgment should extend to Dr. Xizheng Liu, Dr. Cuihua An, Dr. Huiming Yin, and Mr. Jian Li.

We also would like to acknowledge collaborations with many of our colleagues over the years. They have been generously sharing with us their expertise, ideas, research data and facilities. They are Mingwei Chen (Tohoku University), Jianguo Liu (Nanjing University), Wenbin Cai (Fudan University), Jingdong Zhang and Jens Ulstrup (Technical University of Denmark), Yan Wang (University of Jinan), Xiaohong Xu, Houyi Ma and Pengchao Si (Shandong University).

We received substantial financial support in the past decade from various funding agencies, without which our research and thus the contents of this book would not have been possible. In particular, we wish to acknowledge the Ministry of Science and the Technology of the People's Republic of China (MOST), National Natural Science Foundation of China (NSFC), Ministry of Education of the People's Republic of China (MOE), Tianjin University of Technology (TUT), Shandong University (SDU), and the local government programs from Shandong Province and Tianjin City. YD also thanks the Otto Mønsted Fond for providing a 3-month visiting professorship at the Technical University of Denmark in 2014, where part of this book was drafted.

Publishers and authors are thanked for their permission to reproduce or adapt the illustrations, tables, and figure legends. We would also like to thank the Springer publishing team, particularly to Editors Marta Moldvai, Merry Stuber, Lesley Poliner, Brian Halm, and Zoe Kennedy, for their invaluable suggestions and support to the completion of this book.

Finally, we would like to thank our family members for their love and patience whilst the book was composed.

Contents

About the Authors

Dr. Yi Ding is currently a Distinguished Professor at the Institute for New Energy and Low-Carbon Technologies, Tianjin University of Technology (TUT). He received his Bachelor and Master Degrees from University of Science and Technology of China in 1998 and 2001 (with Profs. Yadong Li and Yitai Qian), and his Ph.D. degree from Johns Hopkins University in 2005 (with Prof. Jonah Erlebacher). He joined the faculty of Shandong University at the end of 2005 as a Tai-Shan Scholar Distinguished Professor. In January 2015, he moved to TUT to establish the new energy institute focusing on nanoporous energy materials. Dr. Ding has published 98 journal articles, with a total citation over 6000 times and an H-index of 41 (Researcher ID: F-6990-2013). He has been granted 23 patents and 20 funding projects with total ca. 5 million euro.

Dr. Ding's research covers broad areas of nanoscale science and technology, particularly on creating functional nanoporous metal materials for use in advanced energy and environmental technologies. Nanoporous metals can be mass-produced by a simple alloy corrosion method, often known as *dealloying*. And these three-dimensional (3D) metallic nanostructures possess a series of unique structural properties, such as excellent mechanical rigidity and electric conductivity, and tunable porosity and surface chemistry. These intriguing properties and their combinations have resulted in a rush of research interest in materials science community in the investigation of their potentials in various modern applications such as clean energy technologies (polymer electrolyte membrane fuel cells, supercapacitors, etc.), green chemistry associated heterogeneous catalysis, and biochemical sensing technologies. These topics are now the main research themes in Dr. Ding's group.

Prof. Dr. Zhonghua Zhang was born in 1976 in Zaozhuang, China. He received his Ph.D. degree in 2003 from School of Materials Science and Engineering, Shandong University, Jinan, China. In 2004–2005, he worked as an Alexander von Humboldt postdoctoral research fellow at Institute of Materials, Ruhr University Bochum, Germany, cooperating with Prof. Dr. Gunther Eggeler. At the end of 2005, he got a full professor position in Shandong University. He has extensive experience in casting, rapid solidification, amorphous alloys, shape memory alloys, and so forth. At present, his research interests mainly focus upon dealloying mechanisms, dealloying-driven nanoporous metals, metal/metal oxide nanocomposites, transition metal chalcogenides, and their applications in energy and environment-related fields.

Chapter 1
Introduction to Nanoporous Metals

Abstract In this chapter, we briefly give an introduction to nanoporous metals (NPMs). First, we show "what are NPMs." The definition of NPMs is given, considering the characteristic length scale and porous structure. NPMs are such a kind of metallic materials with interconnected backbones (ligaments) and pores (channels) on the nanoscale. Here, the term "nanoporous" is different from "mesoporous," which is defined by the International Union of Pure and Applied Chemistry (IUPAC). Moreover, the length scale of nanopores (several to hundreds of nanometers) in NPMs is several orders of magnitude smaller than that (above tens of microns) of pores in normal metal foams. The pore distribution in NPMs could be ordered, or random, or the combination of the former two. Many methods could be used to fabricate NPMs, and dealloying is the most important one. Second, the microstructural characteristics of NPMs are outlined. Besides the prototype nanoporous gold (NPG), many pure elements (transition metals, elements from IIIA-VA groups, and even semiconductor elements) and alloys could be fabricated into a nanoporous structure. Both bulk (up to centimeters) and nanosized (zero-dimensional (0D), 1D, and 2D) NPMs have been reported. Metallic ligaments and nanopore channels in dealloying-driven NPMs are topologically and morphologically equivalent, i.e., they are inverses of each other in three-dimensional space. The microstructure of NPMs may be homogeneous, and NPMs with multiscale or multilevel porous structures can also be prepared. In addition, the crystalline orientation and lattice defects of NPMs depend upon the microstructure of the precursor alloys and the dealloying process. Third, the properties of NPMs are summarized. Due to their unique microstructures, nanoporous metallic materials combine the properties of both metals and nanostructured materials. Thus NPMs show the structure-related electrical, magnetic, mechanical, optical, catalytic, and electrocatalytic properties. Moreover, the microstructures and the related properties of NPMs could be facilely designed and modulated. Last, we discuss the potential applications of NPMs. Owing to their unique microstructures and related properties, NPMs show promising applications in sensors, actuators, fuel cells, lithium-ion batteries (LIBs), supercapacitors, metal–air batteries, water splitting, synthesis of chemicals, hydrogen storage, automobile exhaust treatment, drug loading and release, bonding materials, and so forth.

Y. Ding and Z. Zhang, *Nanoporous Metals for Advanced Energy Technologies*, DOI 10.1007/978-3-319-29749-1_1

Keywords Nanoporous metals · Microstructure · Properties · Applications · Dealloying

1.1 What Are Nanoporous Metals

Nanoporous metals (NPMs) are such a kind of metallic materials with interconnected backbones (ligaments) and pores on the nanoscale, Fig. 1.1 [1]. Tappan et al. [2] call them as "foam" and have defined a nanoporous metal foam as a three-dimensional structure comprised of interconnected metallic particles or

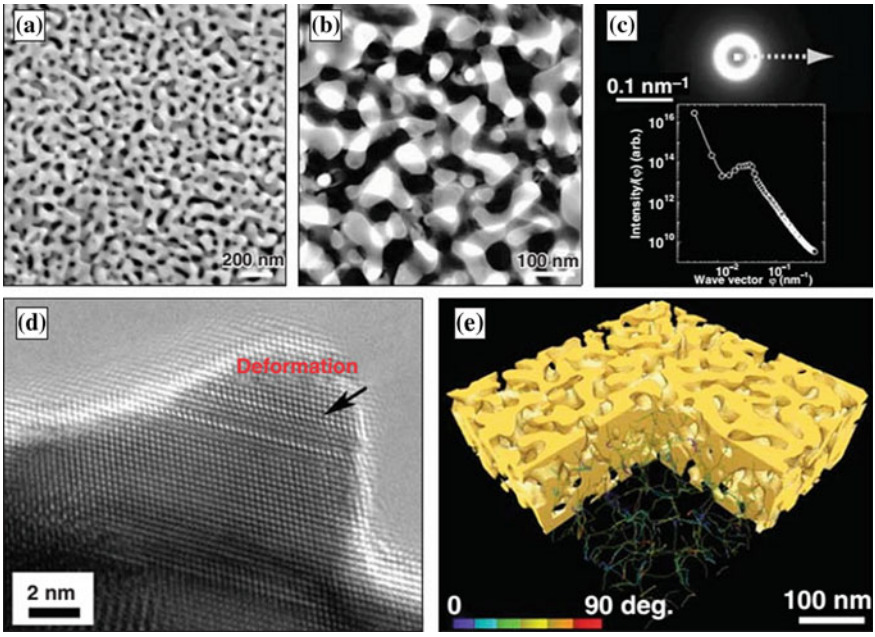

Fig. 1.1 (**a**) Scanning electron microscopy, (**b**) transmission electron microscopy, and (**d**) high-resolution transmission electron microscopy micrographs of nanoporous gold (NPG). (**c**) Representative rotational-averaged fast Fourier transform (FFT) power spectrum and intensity profile of NPG with a strong signal-to-noise ratio. The *dotted arrow* in the FFT spectrum represents the integration direction of the intensity profile. The detectable peak in the profile proves that the microstructure of NPG is quasiperiodic. (**e**) Three-dimensional structure of NPG imaged by electron tomography. A part of the 3D image is shown as the skeletal network of gold ligaments. The various colors of the skeletal network represent the deviation angles of the skeletonized ligaments from the z-axis (the surface normal of the film) as indicated by the color bar from 0° (*purple*) to 90° (*red*). (Reproduced from Ref [1]. Copyright 2004, Materials Research Society)

filaments, which exhibits a porosity of no less than 50 % and in which submicron pores (including micropores, mesopores, and macropores 50–1000 nm in diameter) measurably contribute to the specific surface area of the foam. Different from their bulk counterparts, NPMs possess unique mechanical, physical, chemical, and biological properties associated with their porous nanoarchitectures.

To the best of our knowledge, the term "nanoporous" first appeared in the published paper entitled "Brittle fracture of a Au/Ag alloy induced by a surface film" by Kelly, Frost, Shahrabi, and Newman [3]. They reported that brittle cracks, both intergranular (IG) and transgranular (TG) in nature, were formed by high-speed loading of a thin foil covered with a dealloyed (nanoporous gold) layer. In the earlier literature, for example, Forty [4] have observed in TEM that the originally structureless AuAg film become a maze-like structure of gold-rich islands separated by more transparent channels after dealloying in 50 % aqueous nitric acid solution. Subsequently, "the dealloyed residue" was used in Keir and Pryor's paper, when studying the dealloying of Cu–Mn alloys [5]. They have found that the surface of the Cu-50 %Mn alloy polarized for 20 h at 0.00 V was highly porous and the dealloyed residue completely penetrated through the original alloy sheet [5]. In addition, "sponge" was also used for the dealloyed structure. Cassagne et al. [6] found that a 30-day etched Cu_3Au sample was completely converted into a brittle, virtually pure gold "sponge" while retaining the external shape and orientation of the original alloy single crystal. Moreover, the surface is porous with a mean pore size of $\sim$0.1 micrometer [6].

The definition of "nanoporous" is also different from that of "mesoporous." According to the International Union of Pure and Applied Chemistry (IUPAC) nomenclature, porous materials can be classified into three categories: micropore (the pore size is smaller than 2 nm), mesopore (the pore size is in the range of 2–50 nm), and macropore (the pore size is larger than 50 nm, normally 50–1000 nm). Therefore, it often has been pointed out that the term "nanoporous" is meaningless from the standpoint of IUPAC nomenclature [7]. Eventually, the length scale of nanopores in nanoporous materials ranges from several nanometers to hundreds of nanometers. Thus, NPMs could be "mesoporous" or "macroporous," depending upon the characteristic size of nanopores in them. And at present, the term "nanoporous" is widely accepted, and is extensively used in the published papers. Here, the prefix "nano" refers to the size scale of nanoporous materials.

Although sometimes NPMs are called as "nanoporous metallic foams" [2], it should be noted that the characteristic length scale of NPMs significantly differs from that of traditional metal foams (up to six orders of magnitude, as highlighted in Fig. 1.2 [7]). Traditional metal foams are commercially available, such as copper foam, nickel foam, iron foam, alloy foam, and so forth (Fig. 1.3). Their pore sizes range from tens of microns even to centimeters, and the pores could be easily discerned by naked eyes of human beings.

Based upon the nanoporosity distribution, NPMs can be classified into three categories: the first has a three-dimensional bicontinuous interpenetrating ligament (metal backbone)-channel (nanopore or void) structure (Fig. 1.1), the second has a regular ordered nanopore distribution (Fig. 1.4, [8]), and the third combines the

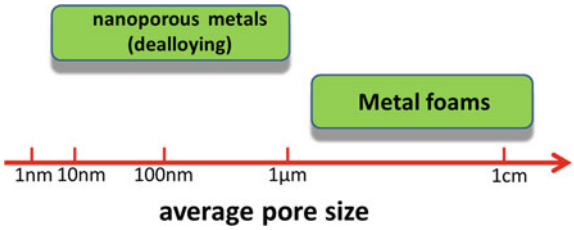

Fig. 1.2 The length scales of nanoporous metals and metal foams. Adapted from Ref. [7]

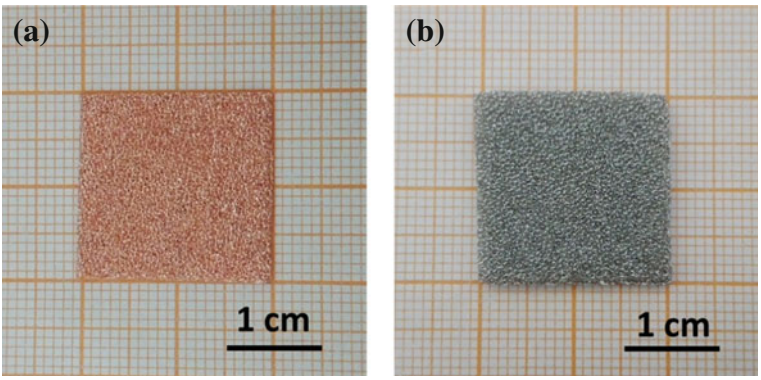

Fig. 1.3 Photographs of traditional metal foams (*left* copper foam; *right* nickel foam)

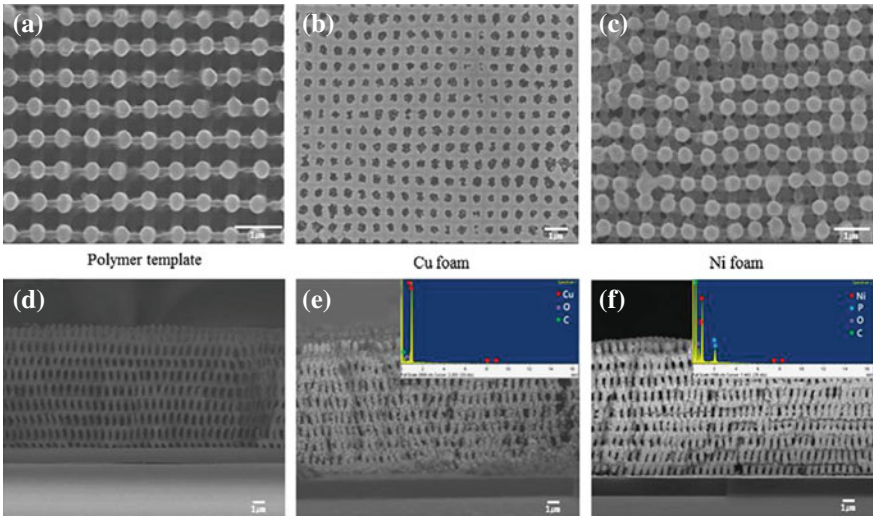

Fig. 1.4 Top and cross-sectional SEM images of electroless-plated Cu and Ni nanofoams: (**a**, **d**) PnP polymer template, (**b**, **e**) submicron Cu foams, and (**c**, **f**) submicron Ni foams. (Reproduced from Ref. [8]. Copyright 2014, Elsevier)

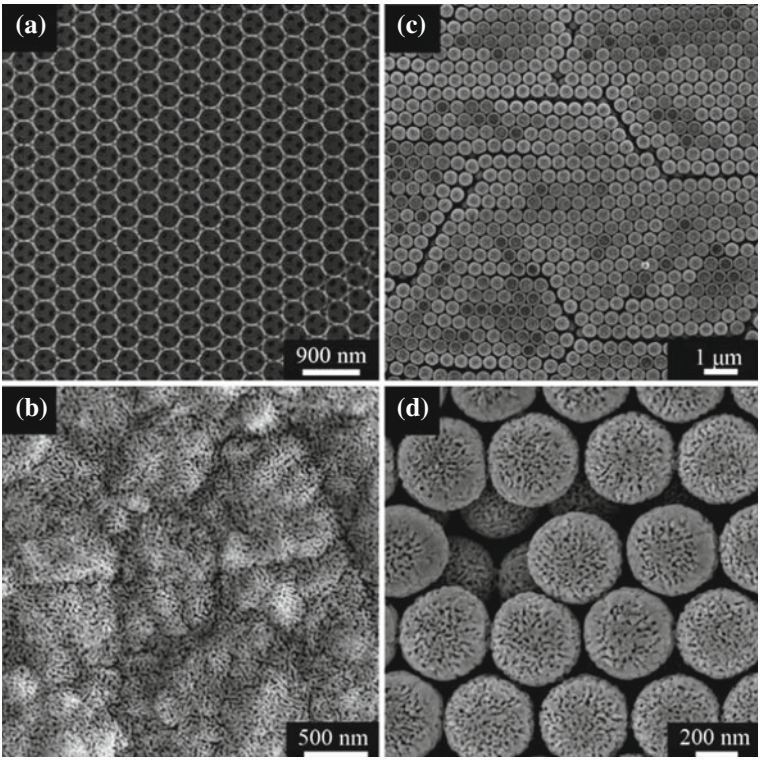

Fig. 1.5 Scanning electron microscope images showing: (**a**) a silica inverse opal template; (**b**) a porous gold film obtained by electrodeposition without the use of an opal template; (**c**, **d**) low- and high-magnification SEM images, respectively, of a porous gold opal template. (Reproduced from Ref. [9]. Copyright 2012, American Chemical Society)

characteristics of the former two kinds of NPMs (Fig. 1.5, [9]). Normally, NPMs with a bicontinuous interpenetrating ligament–channel structure can be fabricated by the dealloying strategy, and template methods are frequently used to prepare NPMs with more regular pore distribution. And the combination of dealloying with template methods could produce NPMs with two kinds of nanopore features (Fig. 1.5).

Many methods have been developed to fabricate nanoporous metallic materials, such as dealloying, [4, 10] templating, [8] anodization, [11] laser etching, [12] combustion synthesis, [2] sol–gel, [2] nanosmelting of hybrid polymer–metal oxide aerogels, [2, 13] chemical reduction based upon a mathematical fractal model, [14] thermal decomposition, [15] and so on. Tappan et al. [2] have believed that combustion synthesis of MBTA complexes is a flexible, general approach for the formation of a wide range of nanoporous metallic foams of a large number of metals (including Fe, Co, Ni, Cu, Zn, Pd, Ag, Pt, Au), and has potentials for scalability. Most recently, Avisar-Levy et al. [14] have shown that chemical reduction of metal

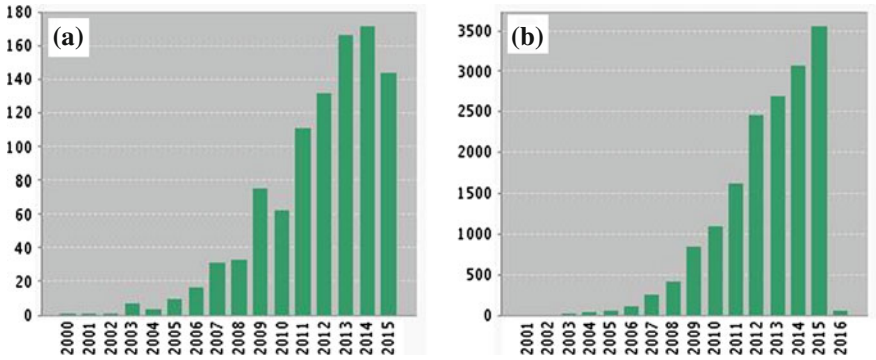

Fig. 1.6 Statistics on (**a**) published papers and (**b**) citations per year since 2000 (until Dec. 07, 2015), based upon Web of Science (subject words: "dealloying" and "*porous")

complexes at a low but constant temperature preserves alloy composition and produces a highly porous metallic material (>90 % porosity) with open interconnected fractal porosity extended down to a nanoscale. These porous metallic materials that consist of nanocrystallites can be obtained for a wide range of binary systems and pure metals (pure metals: Co, Ru, Rh, Pd, Ag, Ir, Pt; binary systems: Pt_3Ru_2, Co_2Pt_3, CoPt, Co_2Pt, IrPt, Rh_2Ru, Rh_3Ru_2, RhRu, Ir_2Ru, IrRu). And they have argued that geometrical analysis of several NPMs and alloys suggests that the three-dimensional structure of these materials may be represented by a mathematical fractal model.

Among all the above strategies, dealloying is no doubt the top star. Since the pioneer work of Erlebacher et al. [10] the dealloying strategy has become the most important method to produce NPMs in the past 15 years. More and more attention has been paid to dealloying-driven nanoporous metallic materials. Figure 1.6 outlines the development trend (published papers and citations per year, based upon Web of Science) of dealloying-driven NPMs. It can be clearly seen that this dealloying-related field grows exponentially since 2000. In the following chapters of this book, we mainly focus upon nanoporous metallic materials fabricated by dealloying or the combination of dealoying with other method(s).

1.2 Microstructural Characteristics of Nanoporous Metals

Nanoporous gold (NPG) is the prototype of NPMs. Hitherto, many nanoporous pure metals have been reported, including NP–Au, NP–Pt, NP–Pd, NP–Ag, NP–Cu, NP–Ni, NP–Co, NP–Fe, NP–Cr, NP–Mn, NP–Ru, NP–Ir, NP–Os, NP–Rh, NP–Ti, NP–W, NP–Mo, NP–Nb, NP–Cd [2, 4, 10, 14, 16–26]. Besides transition metals (TMs), NPMs from IIIA-VA groups have also been reported, such as Ga, Sn, Bi, Pb [26–28]. Figure 1.7 shows the SEM image of nanoporous Sn fabricated by dealloying $Al_{75}Sn_{25}$ alloy in the HCl solution. The bicontinuous ligament–channel

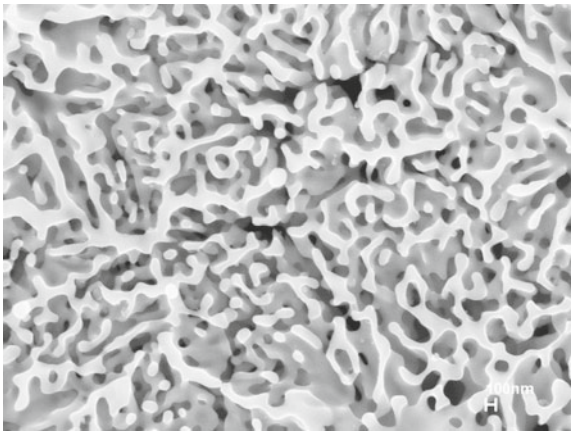

Fig. 1.7 SEM image of nanoporous tin (Sn) by dealloying of rapidly solidified $Al_{75}Sn_{25}$ alloy in a 5 wt% HCl solution at room temperature

structure can be clearly observed. It is interesting that even semiconductor elements (Si and Ge) could also be produced into nanoporous structures [29–31]. Wada et al. [29] have synthesized freestanding bulk three-dimensional nanoporous Si using dealloying of Mg_2Si in a metallic Bi melt. The nanoporous Si as negative electrode shows high lithium capacity nearing their theoretical limits, and greatly extended cycle lifetimes, considerably improving the battery performance compared with those using electrodes made from silicon nanoparticles [29]. Most recently, Yin et al. [31] presented a controllable and affordable preparation of porous nanostructured germanium with interesting photoresponsive properties from GeO_2 powders through an electrochemical reduction (Ge nanoparticles)–alloying (Ca_xGe) process in molten salt and post-zero energy-consumption water etching (dealloying). All the elements to form a nanoporous structure are highlighted in the periodic table, Fig. 1.8.

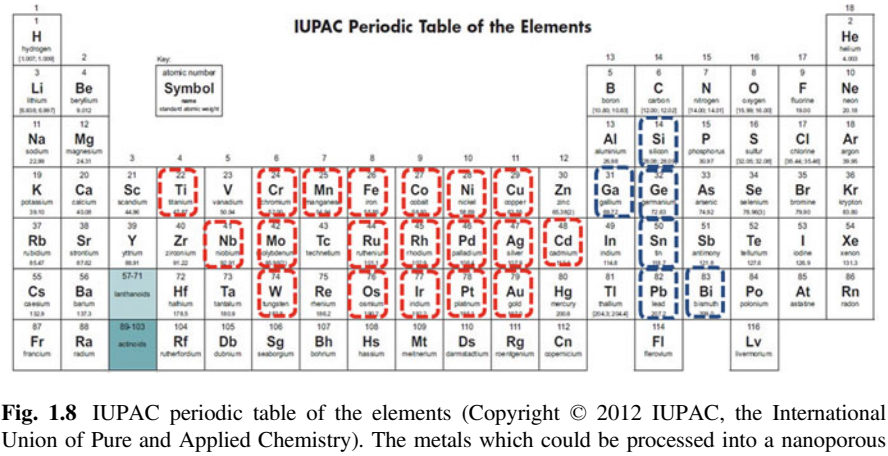

Fig. 1.8 IUPAC periodic table of the elements (Copyright © 2012 IUPAC, the International Union of Pure and Applied Chemistry). The metals which could be processed into a nanoporous form have been highlighted by *red* or *blue dashed* rectangles

Besides pure elements, numerous nanoporous binary, ternary, and even multi-component alloys have also been reported, such as Au-based alloys, [32, 33] Pt-based alloys, [34–41] Pd-based alloys, [42–46] Ru-based alloys, [14] and so forth. For example, ultrafine nanoporous Au-based alloys (AuPt, AuPd, AuPdPt) could be fabricated by dealloying Al_2Au-type precursors doped with a proper amount of Pt, Pd or Pt/Pd in HCl or NaOH solutions [32]. Further, the same group has found that the addition of Ni and/or Co has no influence on phase constitution of rapidly solidified Al–Au–M (M = Ni, Co, or Ni/Co) alloys and a single-phase $Al_2(Au,M)$ intermetallic compound can be identified in these ternary and quaternary precursor alloys. The Al–Au-based precursors can be fully dealloyed in an alkaline solution under free corrosion conditions, and the dealloying results in the formation of novel ultrafine nanoporous Au-based alloys (AuNi, AuCo and AuNiCo) with ligaments/channels of $\sim$5 nm and extraordinarily high structural stability against thermal annealing [33].

NPMs could be prepared into bulk forms with the shape size of up to centimeters. Figure 1.9 shows the macrograph of nanoporous Cu ribbon, rod, and sheet which were fabricated by a two-step dealloying of an Al-40 at.% Cu alloy [47]. Millimeter-sized nanoporous AuPt alloys were fabricated by potential-controlled electrochemical dealloying of $(Au_{1-x}Pt_x)_{25}Ag_{75}$ precursors in 1 M $HClO_4$ solution [48]. These bulk samples are good candidates for investigation of mechanical properties of NPMs, as well as applications in electrochemical or chemical actuators.

Nanosized NPMs with diverse morphologies were also reported in the literature, including zero-dimensional (0D), 1D, and 2D nanostructures. The $Ag_{50}Au_{50}$ (wt%, white gold) alloy leaves are commercially available (Fig. 1.10a). After dealloying in nitric acid, NPG films with thickness of $\sim$100 nm were obtained and the color became dark red, Fig. 1.10b [49]. NPG films with thickness of several microns can

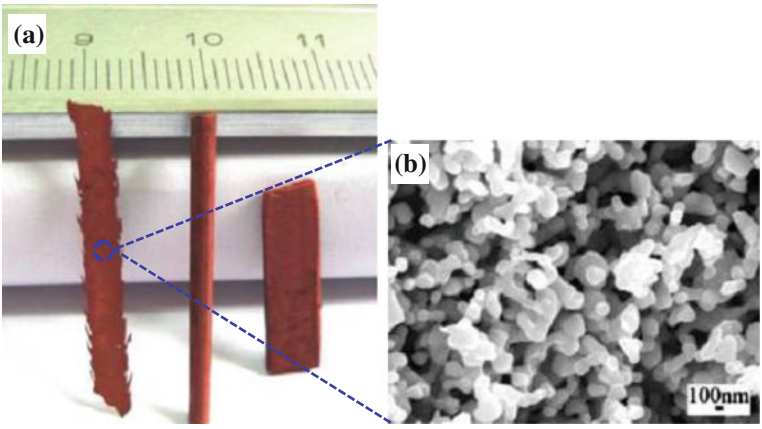

Fig. 1.9 **a** Macrograph showing the nanoporous Cu ribbon, rod, and sheet by the two-step dealloying of Al-40 at.% Cu (from *left* to *right*). **b** SEM image showing the ligament–channel structure of nanoporous Cu ribbon. (Reproduced from Ref. [47]. Copyright 2009, American Chemical Society)

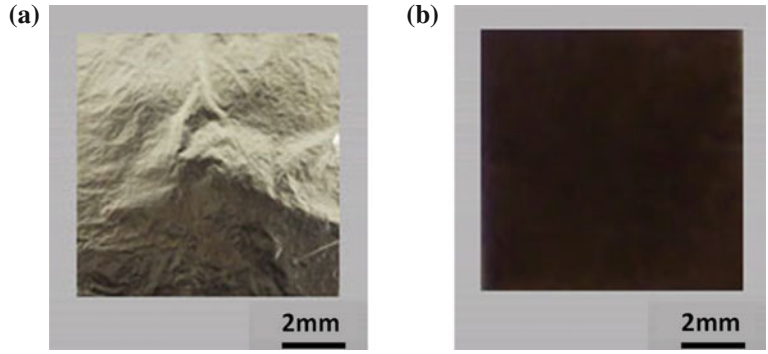

Fig. 1.10 Optical images of white gold leaf (**a**) before and (**b**) after dealloying in nitric acid for 30 min. Adapted from Ref. [49]

be obtained by electrochemical alloying/dealloying of Au–Zn alloys in an ionic liquid [50]. The fabrication process involves the electrodeposition of a binary Au–Zn alloy at gold wires, followed by subsequent electrochemical dealloying of the less noble component zinc from the alloy surface. Liu et al. [51] have reported that nanoporous Pt–Co alloy nanowires could be synthesized by electrodeposition of Co-rich Pt_1Co_{99} alloy into anodic aluminum oxide (AAO) membranes, followed by a dealloying treatment in a mild acidic medium. The nanoporous Pt–Co nanowires consist of porous skeletons with tiny pores of 1–5 nm and crystalline ligaments of 2–8 nm. Gu et al. [52] reported the fabrication of a new type of metallic nanoporous nanotube structure based on a facile and effective combination of nanocrystal growth and surface modification. By controlling the individual steps involved in this process, such as nanowire growth, surface modification, thermal diffusion, and dealloying, Au–Ag alloy nanoporous nanotubes (NPNTs) can be prepared with tailored structural features and predesigned functionalities, Fig. 1.11. Wang et al. [53] achieved successful synthesis of a variety of monodisperse nanoporous alloy nanoparticles via a facile chemical dealloying process using nanocrystalline alloys as precursors. Figure 1.12 shows the TEM and HRTEM images of nanoporous Pt–Ni alloy nanoparticles before and after dealloying [53].

Regardless of bulk samples or 2D films, it should be noted that nanoporous metallic materials generally have good mechanical integrity, monolithic shapes, and robust flexibility (Figs. 1.9, 1.10, and 1.11). These structural features ensure that nanoporous metallic samples can be well separated, treated, and operated in the fabrication, functionalization, and subsequent application stages. For example, NPG films are good electrode materials or electrode substrates. We can directly put NPG films onto the surface of glassy carbon electrodes without any binder and/or conductive agents.

Through transmission electron tomography, Fujita et al. [54] have found that gold ligaments and nanopore channels in NPG are topologically and morphologically equivalent, i.e., they are inverses of each other in three-dimensional space (Fig. 1.1). Further statistical analysis reveals that this bicontinuous nanostructured

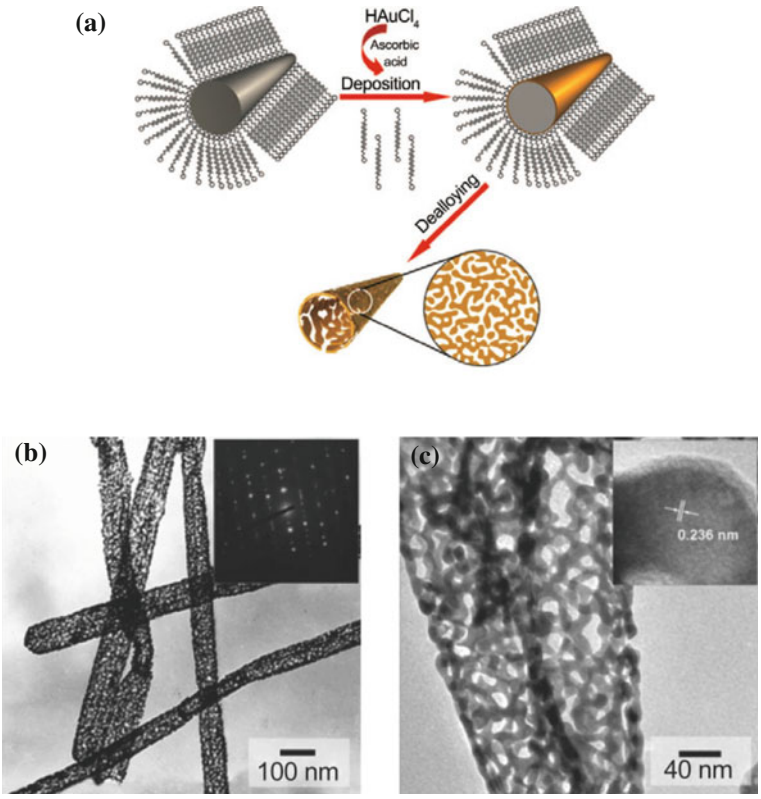

Fig. 1.11 (**a**) Schematic illustration of the synthesis process of Au–Ag alloy NPNTs. (**b**, **c**) TEM images of Au–Ag alloy NPNTs [52]

material is actually quasiperiodic and has, on average, a near-zero surface curvature. Using spherical-aberration-corrected transmission electron microscopy, they further reported that a high density of atomic steps and kinks is observed on the curved surfaces of NPG, comparable to 3–5 nm nanoparticles, which are stabilized by hyperboloid-like gold ligaments [55]. Moreover, the atomic steps/kinks are associated with the convex and concave curvatures of the gold ligaments.

In general, gold ligaments separated by pore channels in each domain that is inherited from the original grains of precursor alloys have the same crystal orientation, exhibiting a single crystal feature in the length scale of the precursor grains. As shown in Fig. 1.13a, b, we can clearly observe the grain-like characteristic of NPG ribbons, which is inherited from the rapidly solidified $Al_{66.6}Au_{33.4}$ precursor alloy [16]. TEM and HRTEM images verify the nanoporous structure of the NPG ribbons (Fig. 1.13c, d). The SAED pattern of f.c.c. Au[112] zone axis and FFT pattern of f.c.c. Au[110] zone axis confirm the single crystal nature of all of the frame of observation (insets of Fig. 1.13c, d). Moreover, lattice fringes can be seen extending throughout all of the ligaments shown in the HRTEM image (Fig. 1.13d).

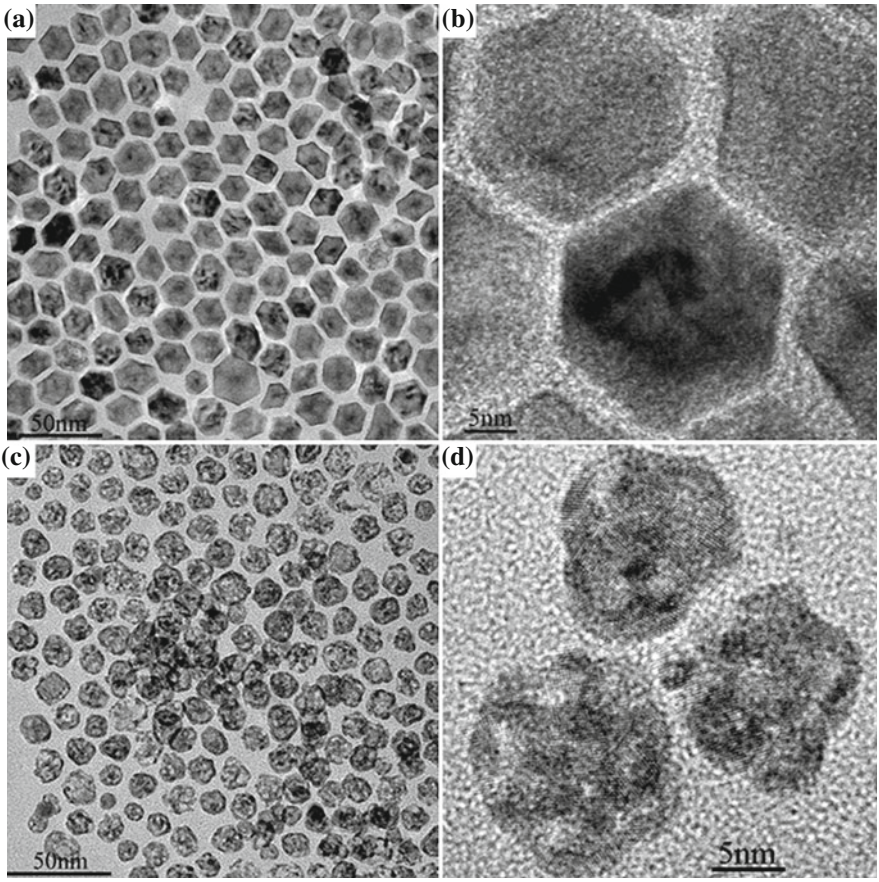

Fig. 1.12 Nanoalloys observed by TEM and HRTEM. **a** TEM image of Pt-Ni nanoparticles. **b** HRTEM image of Pt-Ni nanoparticles. **c** TEM image of nanoporous Pt-Ni alloys. **d** HRTEM image of nanoporous Pt-Ni alloys. (Reproduced from Ref. [53]. Copyright 2011, Nature Publishing Group)

The ligaments/channels sizes are 10–20 nm in these NPG ribbons, but the grain size may range from several microns to tens of microns. For other NPMs (like NP–Pd, NP–Pt, etc.), however, the grain sizes are comparable or even smaller than the length scale of ligaments [16]. For metallic glass precursors, there actually exist no "grains" in their microstructures (composed of short-range and medium-range order clusters). The ligaments were found to be comprised of nanocrystals with a grain size of about 5 nm in nanoporous Pd dealloyed from $Pd_{30}Ni_{50}P_{20}$ metallic glass [56].

Various crystal defects, such as dislocations, twins, and stacking faults, have been observed in dealloyed NPG samples. Figure 1.14 shows twins, dislocations, and stacking faults in NPG obtained by chemical dealloying of rapidly solidified $Al_{80}Au_{20}$ alloy in the 20 wt% NaOH aqueous solution [57]. Generally, the

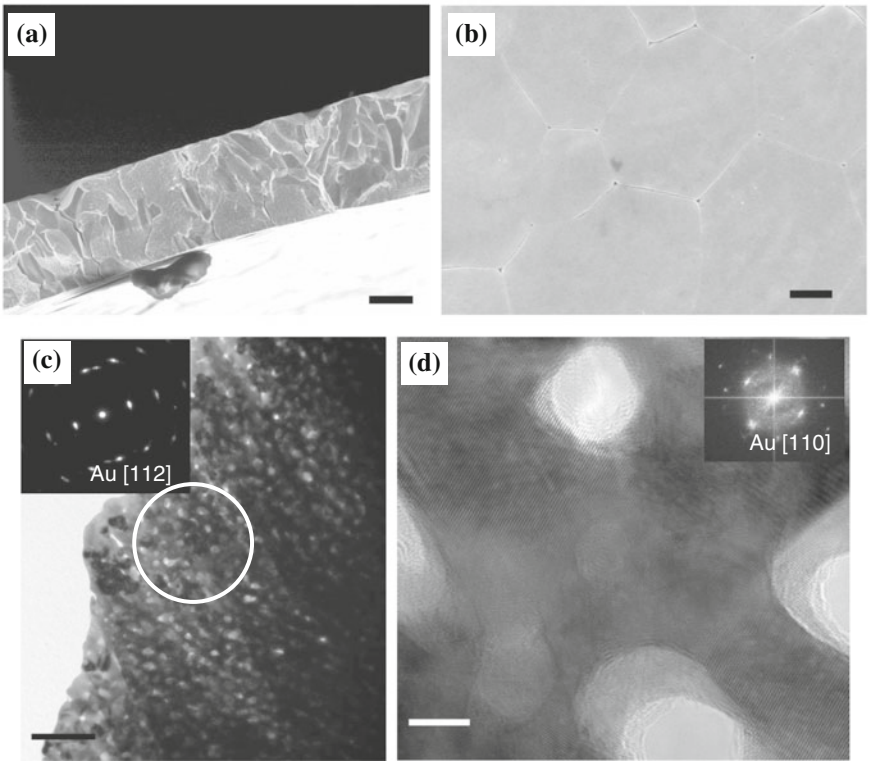

Fig. 1.13 **a** Section-view SEM image of the NPG ribbons by dealloying of the rapidly solidified $Al_{66.6}Au_{33.4}$ alloy in the 20 wt% NaOH solution. Scale bar, 10 μm. **b** Plan-view SEM image of the surface of the NPG ribbons, Scale bar, 1 μm. **c** TEM image showing the nanoporous structure of the NPG ribbons. The selected area is highlighted by a *white circle*. (*Insert*) SAED pattern of the f.c.c. Au [112] zone axis from the selected area in (**c**). Scale bar, 100 nm. **d** HRTEM image of the NPG ribbons. (*Insert*) Corresponding FFT pattern of the f.c.c. Au [110] zone axis. Scale bar, 5 nm. (Reproduced from Ref. [16]. Copyright 2009, American Chemical Society)

chemically dealloyed samples (free corrosion) have a low density of crystal defects in comparison with the NPG samples prepared by electrochemical dealloying. This is probably because the fast formation of nanoporosity with the assistance of applied potentials produces large residual stresses and resultant plastic deformation during dealloying [1].

In some cases, we need nanoporous metallic materials with homogeneous nanopore/ligament distributions, as shown in Fig. 1.1. At the same time, we can also tune the structures/compositions of the precursor alloys and the dealloying parameters, and obtain NPMs with diverse nanopore/ligament distributions. We will briefly summarize NPMs with multiscale or multilevel porous structures.

Multimodal pore size distribution (*hierarchically porous nanostructures*). Ding and Erlebacher [58] have developed a two-step dealloying strategy (dealloying/annealing/plating/annealing/redealloying) to create multimodal pore

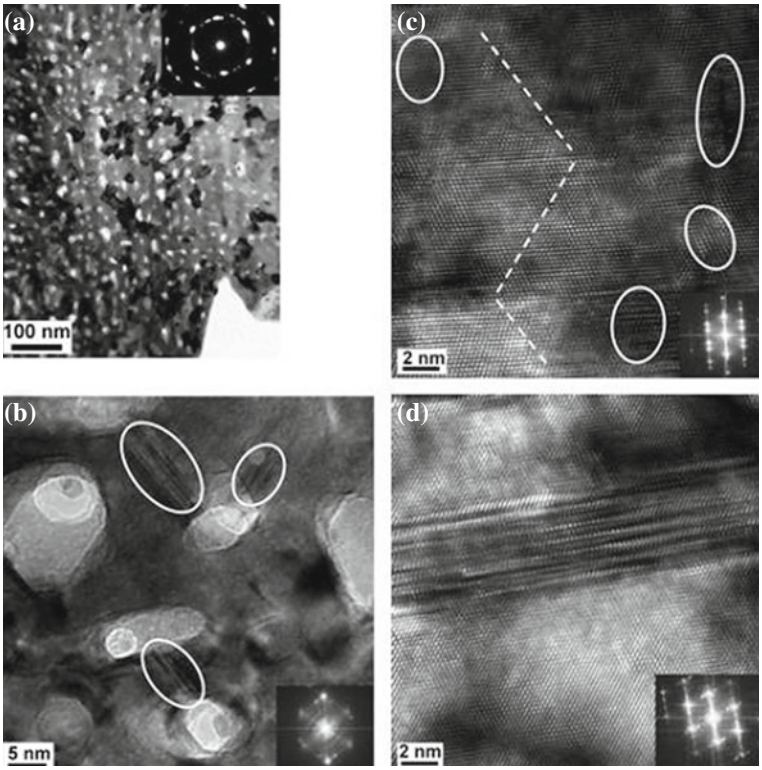

Fig. 1.14 **a** TEM and **b–d** HRTEM images showing the nanoporous structure and lattice defects (stacking faults, twins, and dislocations) of NPG by dealloying the rapidly solidified $Al_{80}Au_{20}$ alloy in the 20 wt% NaOH aqueous solution. The inserts show the corresponding **a** SAED and **b–d** FFT patterns. (Reproduced from Ref. [57]. Copyright 2009, American Chemical Society)

size in NPG, Fig. 1.15a, b. And they have argued that some of the general characteristics of the proposed method that are worthy of immediate exploration include (1) applicability to any system that exhibits porosity evolution upon dealloying (not just Au/Ag alloys), (2) fabrication of trimodal and higher order porous architectures by additional annealing/plating/redealloying cycles, and (3) independent tunability of pore sizes, and even pore topology. Zhang et al. [57] presented a simple one-step dealloying strategy to synthesize NPG ribbons with bimodal channel size distributions through design of the Al–Au precursor alloys. The $Al_{80}Au_{20}$ precursor is composed of two phases (Al and Al_2Au), and the complete etching of the Al phase leaves the large-sized channels (hundreds of nanometers) while the dealloying of the Al_2Au phase leads to the formation of highly porous channel walls (tens of nanometers), Fig. 1.15c, d. Recently, Qi and Weissmüller developed a dealloying–annealing–dealloying strategy to fabricate a hierarchical nested network nanostructure in NPG, starting from a dilute solid solution of AgAu [59]. They controlled electrochemical corrosion of the dilute AgAu precursor yielding nanoporous Ag–Au

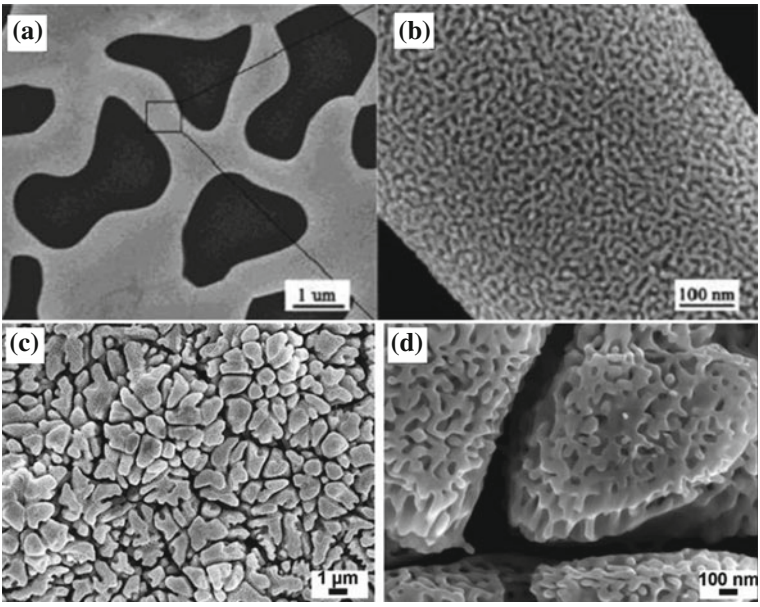

Fig. 1.15 (**a**, **b**) A 2D/3D hybrid NPG structure, where the dimension of unit structure in 2D (1–2 μm) is 2 orders of magnitude larger than that in 3D substructure (~8 nm). Here, 100 nm thick gold leaf was used, and the second stage annealing was carried out at 500 °C for 8 h. (Reproduced from Ref. [58]. Copyright 2003, American Chemical Society) (**c**, **d**) SEM images of NPG by dealloying the rapidly solidified $Al_{80}Au_{20}$ alloy in the 5 wt% HCl aqueous solution. (Reproduced from Ref. [57]. Copyright 2009, American Chemical Society)

alloy as an intermediate product, and coarsening of the porous alloy created the large ligaments of the upper hierarchy level. Most recently, a modified dealloying–annealing–dealloying strategy was developed by the same group for monolithic samples of NPG with a hierarchical structure comprising two nested networks of solid "ligaments" on distinctly different structural length scales, starting from a ternary AgAuPt precursor [60]. The beneficial impact of adding Pt to the Ag–Au master alloys is to reduce the lower hierarchy level ligament size (~6 nm). Furthermore, Pt favors the retention of Ag during the first dealloying step even when the master alloy has a high Au content. Lee et al. [61] developed a straightforward and flexible materials synthesis platform for hierarchically porous gold materials using bijels as templates. They have believed that a synergistic combination of nanocasting and chemical dealloying allows for the benchtop fabrication of monolithic gold with hierarchical bicontinuity on widely separated length scales. Besides monolithic samples (films, ribbons, bulk sheets), hierarchically nanoporous nanostructures have also been reported. For example, Sattayasamitsathit et al. [62] reported tailor-made highly ordered macro/mesoporous hierarchical metal architectures by combining sphere lithography, membrane template electrodeposition, and alloy-etching processes. The new double-template preparation route involves the electrodeposition of Au/Ag alloy within the interstitial (void) spaces of

polystyrene (PS) microspheres which are closely packed within the micropores of a polycarbonate membrane (PC), followed by dealloying of the Ag component and dissolution of the microsphere and membrane templates.

Ordered random nanoporous architectures. Chae et al. [9] have demonstrated a templating–dealloying method to introduce two length scales of porosity in a capacitive porous Au electrode (Fig. 1.5). One length scale is defined by the naturally formed porosity in a silver–gold alloy when the silver is oxidatively stripped (dealloyed). An inverse opal template forms porosity on the other length scale that is relatively well ordered. Sattayasamitsathit et al. [63] reported a highly developed 3D interconnected network of micropores with a nanoporous metal coating. The formation of these nano/microporous structures involves the electrodeposition or sputtering of metal alloys onto the lithographically patterned multilayered microporous carbon, followed by preferential chemical dealloying of the less noble component.

Nanoporous periodic arrays. Wang et al. [64] have demonstrated that a combination of a "top-down" approach (substrate-conformal imprint lithography) and two "bottom-up" approaches (dewetting and dealloying) enables fabrication of perfectly ordered two-dimensional arrays of NPG nanoparticles (Fig. 1.16). The dewetting of Au/Ag bilayers on the periodically prepatterned substrates leads to the interdiffusion of Au and Ag and the formation of an array of Au–Ag alloy nanoparticles. The array of alloy nanoparticles is transformed into an array of NPG

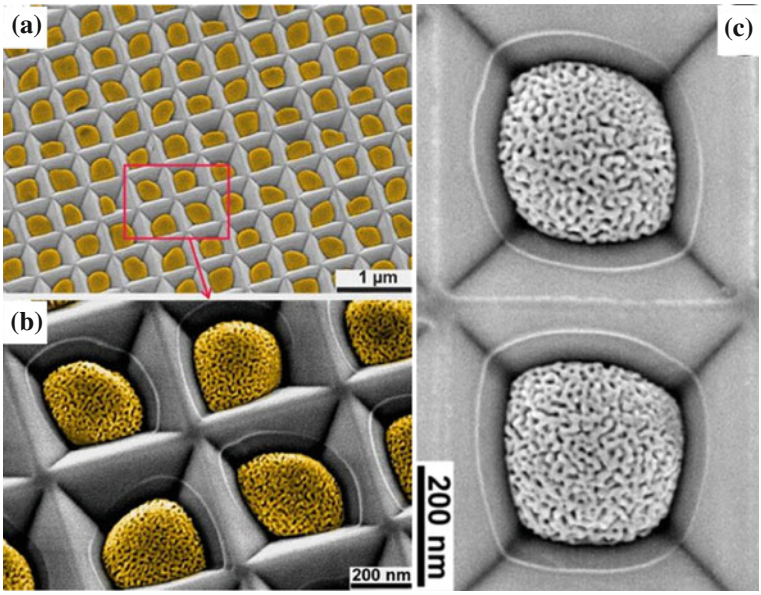

Fig. 1.16 (**a**, **b**) SEM images (*false color*) at 25° tilt of the perfectly ordered array of the nanoporous gold nanoparticles formed from the 15 nm Au/30 nm Ag bilayers, (**c**) SEM micrographs of ordered array of nanoporous gold nanoparticles formed after dealloying. (Reproduced from Ref. [64].)

nanoparticles by a following dealloying step. The same group further fabricated gold films with periodic stripes of nanoporous structure using pulsed laser annealing in a mask projection arrangement in combination with a dealloying process [65]. An Ag–Au alloy is first formed in the exposed areas of Ag/Au bilayers by annealing, and then the Ag is removed from Ag–Au alloy by submerging in HNO_3 solution and NPG is formed. In addition, Isasa et al. [66] fabricated NPG periodical linear patterns by laser interference thermal treatment and subsequent chemical dealloying.

Nanoporous metallic composites. Zhang et al. [67] presented a facile route to fabricate NPG composites (NPGCs) through chemical dealloying of two phase Al–Au alloys comprising Al_2Au and AlAu intermetallic compounds under free corrosion conditions. The microstructures of the NPGCs are composed of intracellular and intercellular areas which exhibit two kinds of nanoporous structures with different length scales of ligaments/channels. The nanoporous structure of the intracellular areas forms due to the dealloying of Al_2Au and that of the intercellular area forms owing to the dealloying of AlAu. Later, Zhang et al. [68] have found that the dealloying of a single-phase $Al_{75}Pt_{15}Au_{10}$ precursor (Al_2(Au,Pt)) leads to the formation of the nanoporous $Pt_{60}Au_{40}$ nanocomposites which consist of two zones with distinct ligament/channel sizes and compositions (Fig. 1.17a, b). The formation mechanism of the nanoporous $Pt_{60}Au_{40}$ nanocomposites can be rationalized based upon surface diffusion of more noble elements and spinodal decomposition during dealloying. Qi et al. [69] fabricated magnetic nanoporous Cu(NPC)/$(Fe,Cu)_3O_4$ composites by one-step chemical dealloying of ternary Al–Cu–Fe alloys with different compositions in an NaOH solution. The NPC/$(Fe,Cu)_3O_4$ composites are composed of an NPC matrix with ligament/channel sizes of 20–40 nm and octahedral $(Fe,Cu)_3O_4$ embedded particles of 600–800 nm (Fig. 1.17c). Similarly, nanoporous silver (NPS)/Fe_3O_4 nanocomposites can be prepared by chemical dealloying of rapidly solidified Al–Ag–Fe precursors in a 20 wt% NaOH solution (Fig. 1.17d) [70]. Besides these monolithic ribbons with thickness of tens of microns, one-dimensional nanoporous composites have also been reported. For example, Guo et al. [71] fabricated gold nanorods in a porous shell of an AuAg alloy via a dealloying process of the core–shell Au@AuAg nanorods at room temperature.

Hollow metallic nanostructures. It should be noted that these hollow nanostructures do not belong to typical NPMs. However, here we still give a brief introduction to this type of metallic nanostructures. Lee et al. [72] studied the dealloying process of AgPdPt nanoframes using electrochemical quartz crystal microbalance. Chen et al. [73] synthesized Pt_3Ni nanoframes with surfaces that offer three-dimensional molecular accessibility through interior erosion of the starting crystalline $PtNi_3$ polyhedra. The edges of the Pt-rich $PtNi_3$ polyhedra are maintained in the final Pt_3Ni nanoframes. Both the interior and exterior catalytic surfaces of this open-framework structure are composed of the nanosegregated Pt-skin structure, which exhibits enhanced oxygen reduction reaction (ORR) activity. Zhang et al. [74] fabricated nanocages by depositing a few atomic layers of platinum (Pt) as conformal shells on palladium (Pd) nanocrystals with well-defined facets and then etching away the Pd templates. With the use of Pd

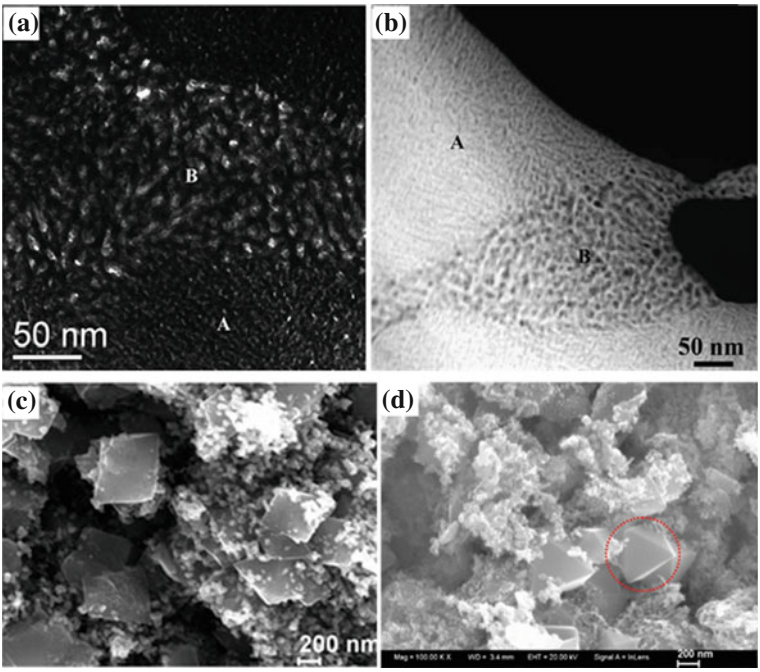

Fig. 1.17 (**a**) TEM and (**b**) STEM images showing the microstructure of the np-$Pt_{60}Au_{40}$ nanocomposites fabricated by dealloying the rapidly solidified $Al_{75}Pt_{15}Au_{10}$ precursor in the 20 wt % NaOH solution. (Reproduced from Ref. [68]. Copyright 2011, The Royal Society of Chemistry) (**c**) SEM image of the nanoporous Cu(NPC)/$(Fe,Cu)_3O_4$ composites fabricated by dealloying the $Al_{62.5}Cu_{20}Fe_{17.5}$ precursor in a 20 wt% NaOH solution. (Reproduced from Ref. [69]. Copyright 2011, The Royal Society of Chemistry) (**d**) SEM image of the nanoporous silver (NPS)/Fe_3O_4 nanocomposites fabricated by dealloying the $Al_{95}Ag_{2.5}Fe_{2.5}$ precursor in a 20 wt% NaOH solution. (Reproduced from Ref. [70]. Copyright 2013, The Royal Society of Chemistry) An octahedral Fe_3O_4 nanoparticle is highlighted by a *dotted circle* in (**d**)

nanoscale cubes and octahedra as templates, they obtained Pt cubic and octahedral nanocages enclosed by (100) and (111) facets, respectively, which exhibited distinctive catalytic activities toward oxygen reduction. In addition, Schaefer et al. [75] prepared double-walled Ag–Pt nanotubes by galvanic replacement and dealloying, using Ag nanotubes as the template.

1.3 Properties of Nanoporous Metals

Due to their unique microstructures, nanoporous metallic materials combine the properties of both metals and nanostructured materials, exhibiting structure-related electrical, magnetic, mechanical, optical, catalytic, and electrocatalytic properties. In the following, we will outline the physical and chemical properties of nanoporous metallic materials.

Electrical and thermal properties. For monolithic samples, NPMs have good electrical and thermal conductivity because of their three-dimensional interconnected ligaments. Preliminary experiments have shown that the electrical resistivity of nanoporous Au, Ag, Cu ribbons is only one to two orders of magnitude higher than that of bulk Au, Ag, and Cu, indicating the unique electron transfer mechanism of NPMs compared with their bulk counterparts [16]. Fujita et al. [76] reported the electric conductivity of three-dimensional (3D) NPG at low temperatures and in strong magnetic fields. They have found that topologically disordered 3D nanoporosity leads to extremely low magnetoresistance and anomalous temperature dependence as the characteristic length of NPG is tuned to be 14 nm. Xia et al. [77] measured the thermal and electrical conductivities of nanoporous Au films in the temperature range 93–300 K. They have found that both the thermal and electrical conductivities are temperature dependent and significantly lower (1–2 orders of magnitude) than those of bulk Au. The corresponding Lorenz number of nanoporous Au is strikingly similar to that of bulk Au, however, the Debye temperature of nanoporous Au is decreased compared to the bulk value. They have concluded that nanoporous Au foils should be comprised of macroscopic, single-crystalline porous grains rather than nanocrystals. Yang et al. [78] have reported that the electrical resistivity of bulk nanoporous copper is about three orders of magnitude higher than bulk pure copper. In addition, it has been found that surface adsorption would have a significant influence on the electrical conductivity of NPMs. The conductivity of NPG was observed to vary reversibly with the induced surface charge, when being in situ measured during the charging and decharging in the electrolytes [79]. Wahl et al. [80] have reported that the electrical resistance of NPG can be tuned by charging the surfaces of the porous structure in an electrolyte. Reversible variations in the resistance up to approximately 4 and 43 % occur due to charging in the regimes of double-layer charging and specific adsorption, respectively (Fig. 1.18). They have argued that the strong resistance variation of up to 43 % in the regime of specific adsorption is due to the reversible formation of a

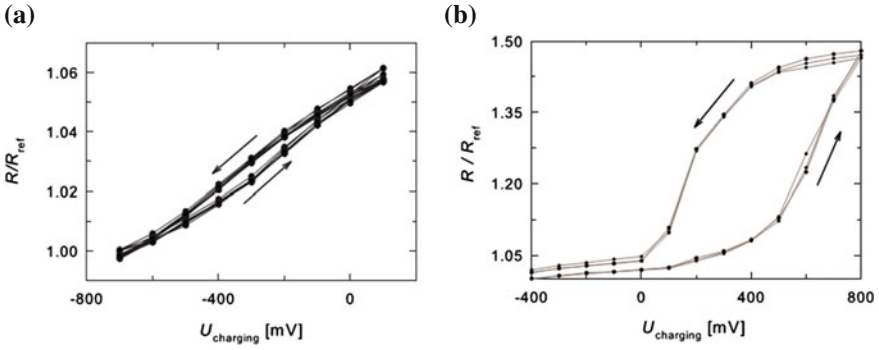

Fig. 1.18 Variation in resistance R of nanoporous Au with a voltage $U_{charging}$ used for charging during consecutive chronoamperometric cycles between (**a**) $U_{charging}$ = −700 mV/+100 mV and (**b**) −400 mV/+800 mV. (Reproduced from Ref. [80]. Copyright 2010, American Institute of Physics)

chemisorbed surface layer acting as scattering centers for the charge carriers. Later, Steyskal et al. [81] have observed that the electrical resistance (R) of nanoporous platinum reversibly changes by 4 % upon electrochemical surface charging in an oxygen adsorption/desorption regime, and have believed that the sign inversion of the resistance with charging may be related to the electronic structure of the surface oxide.

Magnetic properties. Sun et al. [82] have reported that nanoporous nickel dealloyed from Ni_xCu_{1-x} alloys exhibits enhanced coercivity and reduced magnetic anisotropy. Hakamada et al. [83] have reported that the coercivity (Hc) increased with increasing ligament length (L) up to 50 nm, and decreased with increasing L above 50 nm. At $L < 50$ nm, the size dependence of Hc for nanoporous Ni is lower than that for nanocrystalline Ni. The same group further found that saturation magnetization of nanoporous Ni decreased with decreasing ligament length, and was lower than that of the Ni nanoparticles when their specific surface areas were the same [84]. In addition, it has been found that the introduction of magnetic elements or magnetic nanoparticles could greatly enhance the saturation magnetization of NPMs and composites [33, 69, 70]. For example, the addition of Ni and/or Co into nanoporous Au leads to the formation of novel magnetic nanoporous Au-based alloys (np-AuNi, np-AuCo, and np-AuNiCo), Fig. 1.19 [33]. The presence of embedded octahedral Fe_3O_4 particles could greatly enhance the magnetic properties of NPS [70]. Moreover, the amount of Fe_3O_4 in the NPS/Fe_3O_4 nanocomposites and the magnetic properties of the nanocomposites could be facilely tuned by changing the composition (Ag/Fe atomic ratio) of the Al–Ag–Fe precursor alloys. And the embedded Fe_3O_4 makes these materials magnetically recyclable, which is important for the applications and separation of NPMs.

Optical properties. NPG film is a new class of optical material. Maaroof et al. [85] have found that mesoporous gold films exhibit unique dispersion in their optical response across all NIR wavelengths, and the effective optical constants are neither metal- nor insulator-like. By tailoring void content in NPG films, one can

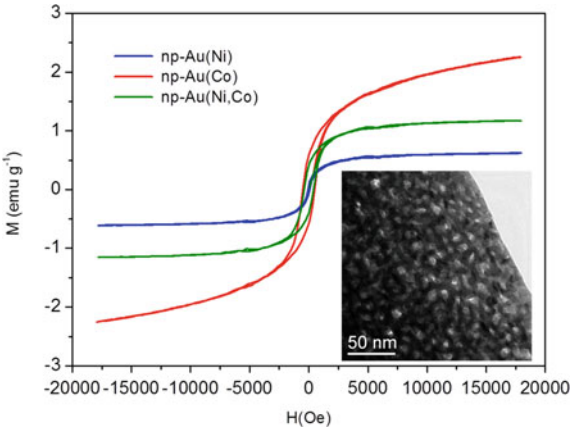

Fig. 1.19 The magnetic hysteresis (M–H) curves of the np-Au(Ni), np-Au(Co), and np-Au(Ni,Co) alloys. (*Inset*) SEM image of nanoporous Au(Co) fabricated through dealloying the rapidly solidified $Al_{66}Au_{27.2}Co_{6.8}$ alloy in the 20 wt% NaOH solution. (Reproduced from Ref. [33]. Copyright 2012, The Royal Society of Chemistry)

tailor the onset of effective plasmonic response across a wide range from 0.8 to 4 μm and emittance from around 0.9 down to low values [86]. Yu et al. [87] have demonstrated that ultrathin (100 nm) NPG membranes possess features of both planar metal films that exhibit propagating surface plasmon resonance (SPR) excitations and nanofeatured metals that exhibit localized SPR (LSPR) excitations. And the LSPR signal is directly linked to the accessibility of the interior of the NPG porosity [88]. As the structure sizes are below 50 nm, NPG films form an effective medium with a negative dielectric constant for near infrared light, and a characteristic redshift by ca. 0.85 eV compared to surface plasmons on solid gold layers is observed [89]. Tuning of the LSPR of NPMs is at the heart of manipulating light within extremely small volumes for the implementation of optical devices at the nanoscale. Qian et al. [90] have demonstrated that LSPR of gold skeleton exhibits a detectable redshift in the optical transmittance spectra, the magnitude of which depends on the thickness of the alumina layer. And optical transmission of the NPG–alumina core–shell films can be tailored through LSPR excitations of the three-dimensional gold skeleton and the alterable alumina shells as the covering dielectric [91]. Recently, Zeng et al. [92] have studied morphology-dependent plasmonic resonance in monolithic NPG nanoparticles. They have found that pore coarsening caused a blueshift in the major plasmonic extinction band of up to 200 nm, in contrast to the redshift ($\sim$50 nm) observed in semiinfinite NPG thin films. Additionally, Lang et al. [93] reported molecular fluorescence enhancement of freestanding NPG with tunable nanopore size. By the combination of dealloying and electroless gold plating, they further tailored molecular fluorescence enhancement of freestanding NPG [94].

Surface enhanced Raman scattering (*SERS*). SERS originates from the improved inelastic scattering of the molecules adsorbed on nanostructured metals and alloys. The SERS enhancements generally depend on the nanoscale characteristics of the metallic substrates, and NPG has been exploited as an attractive substrate for SERS applications. Kucheyev et al. [95] have reported that NPG with average pore widths of 250 nm exhibits the largest SERS signal for 632.8 nm excitation. Dixon et al. [96] have demonstrated that the maximum enhancement factors reach $\sim 10^4$ for 632.8 nm excitation and peak sharply in the 200 nm thickness range for films prepared at optimum etching times. The Chen's group at Tohoku University systematically investigated the SERS behaviors of NPMs. Qian et al. [97] have found that the strongest SERS enhancement of NPG takes place from the samples with an ultrafine nanopore size of 5–10 nm. The SERS intensities from the fracture surfaces of NPG are about one order of magnitude higher than those from the as-prepared samples [98]. Lang et al. [99] reported geometric effect on SERS of NPG, and found that Raman scattering can be improved by tailoring ligament and nanopore ratios. They further found that the SERS intensity dramatically increases as temperature and nanopore size decrease [100]. It was found that the residual Ag plays an important role in the SERS effect of dealloyed NPG. More residual Ag gives rise to better SERS effects when nanopore sizes are nearly identical [101]. In addition, the tunable nanoporosity leads to significant improvements in SERS of nanoporous copper [102]. Moreover, silver@nanoporous copper core–shell composites also

exhibit a dramatically improved SERS effect, and the enhancement factor strongly depends on the reaction time and Ag shell thickness [103]. Qian et al. [104] reported giant Raman enhancement on NPG film by conjugating with nanoparticles for single-molecule detection.

Mechanical properties. NPMs are a new model system for studying mechanical properties associated with three-dimensional random porous structures. Generally, nanoporous metallic samples are macroscopically brittle and exhibit almost no visible tensile or bending ductility, Fig. 1.20. As early as in 1992, Li and Sieradzki [105] first observed a microstructural length scale controlled ductile–brittle transition in NPG. Despite its macroscopic brittleness, NPG is microscopically a very ductile material as ligaments strained by as much as 200 % can be observed in the vicinity of crack tips [106]. Nanoindentation tests show that NPG is a high yield strength material, and the yield strength of the 15 nm diameter ligaments is estimated to be 1.5 GPa, close to the theoretical strength of Au [107–111]. Biener et al. [112] further demonstrated that NPMs can be envisioned as a three-dimensional network of ultrahigh-strength nanowires, thus bringing together two seemingly conflicting properties: high strength and high porosity. It has been found that the mechanical properties (modulus, yield strength, microhardness) of NPG depends upon the ligament size, [113, 114] the relative density, the residual Ag content, [115] annealing treatment [116, 117]. Jin et al. [118] have demonstrated that macroscopic, crack-free NPG samples exhibit excellent ductility in compression tests, but their yield stress is significantly lower than that expected based on scaling laws or on previous nanoindentation experiments. In 2011, Jin and Weissmüller [119] designed a material that has a hybrid nanostructure consisting of a strong metal backbone that is interpenetrated by an electrolyte as the second component. By polarizing the internal interface via an applied electric potential, they accomplished fast and repeatable tuning of yield strength, flow stress, and ductility. Liu and Antoniou [120] derived a new scaling relationship for the dependence of relative density and relative modulus on the geometric parameters such as strut

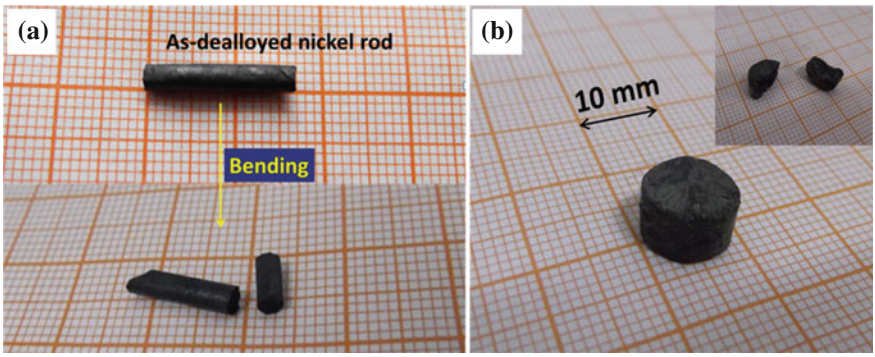

Fig. 1.20 **a** Macrographs of the nanoporous Ni rod before and after the bending process. **b** Macrograph of the nanoporous Ni rod with the diameter of 10 mm. The inset shows the two parts of the broken np-Ni rod

thickness, length, and junction size of NPMs. Recently, Wang et al. [121] have reported that NPG–polymer composite samples made from cm-sized nanoporous samples enable macroscopic tensile and four-point bending tests that show ductility, Fig. 1.21.

Catalytic properties. Due to very high specific surface area and nanosized ligaments, NPMs show excellent catalytic properties for a series of important heterogeneous reactions. Zielasek et al. [122] first pointed out that NPG is a promising material for catalytic applications (CO oxidation). Almost at the same time, Xu et al. [123] reported that unsupported NPG shows extraordinary properties toward low-temperature CO oxidation (−30 °C). Wittstock et al. [124] reported that nanoporous Au can catalyze the selective oxidative coupling of methanol to methyl formate with selectivity above 97 % and high turnover frequencies at temperatures below 80 °C. Han et al. [125] found that NPG catalysts made by dealloying could be applied in the gas-phase selective oxidation of benzyl alcohol to benzaldehyde, and deliver good catalytic activity with high selectivity under ambient reaction conditions. As to the unsupported nature of NPG, however, there is still

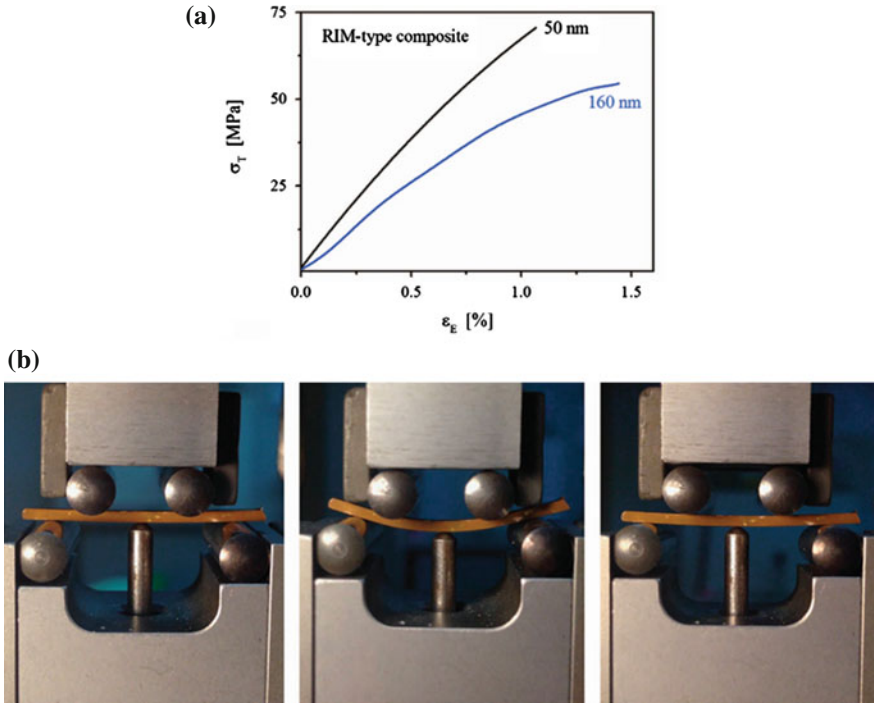

Fig. 1.21 **a** Tensile stress–strain curves of true stress (σ_T) versus engineering strain (ε_E) for RIM-type composites samples with gauge Sect. 1.2 mm^2 × 12 mm. **b** Photographs of four-point bending test with a RIM-type composite sample of ligament size 160 nm. *Left*, before loading; *center*, at maximum load; *right*, after unloading. Note the large deformability and the almost complete recovery. (Reproduced from Ref. [121]. Copyright 2015, Nature Publishing Group)

controversy. Haruta [126] argued that gold nanoporous foams can be regarded as inversely supported gold catalysts, because their surfaces might be substantially contaminated by Ag_2O fine particles or patches. The Ag residues may play a key role in the remarkable catalytic activities of NPG [127]. Liu et al. [128] also believed that the NPG synthesized by dealloying bulk Au–Ag alloy can also be considered as an inversely Ag/AgOx supported gold catalyst. In situ TEM observations provide compelling evidence that the surface defects are active sites for the catalytic oxidation of CO and residual Ag stabilizes the atomic steps by suppressing (111) faceting kinetics [55]. In addition, Asao et al. [129] discovered that NPG exhibited a remarkable catalytic activity in the oxidation of organosilane compounds with water.

Electrocatalytic properties. NPMs represent a new class of high-surface-area nanostructures, where the interconnected ligaments and channels extending in all three dimensions allow unblocked transport of medium molecules and electrons, which is particularly desirable to electrocatalysis. In 2007, Zhang et al. [130] have found that NPG dealloyed from Ag–Au shows great catalytic activity for methanol electrooxidation in alkaline solutions, but the structure quickly coarsens upon long-time potential cycling. Similar results have also been reached by Yu et al. [131] Ultrathin Pt layer-decorated NPG shows enhanced catalytic activities toward methanol electrooxidation in acidic media than the commercial Pt/C [132]. Wang et al. [133] subsequently fabricated a new type of sandwich-type nanostructured electrocatalysts, NPG–Pt–Au, that simultaneously fulfill three key requirements as a good practical formic acid electrooxidation catalyst: ultralow Pt loading, great tolerance to poisoning, and high stability. A core–shell catalyst consisting of a Pt monolayer as the shell and porous Pd–Cu nanoparticles as the core exhibits much higher ORR activity than Pt/C [134]. In addition, it is known that monometallic Pt is susceptible to deactivation or poisoning during electrocatalytic processes. Alloying with other element(s) like Cu, Co, Ni can well enhance the electrocatalytic activity and poisoning tolerance of Pt. Liu et al. [51, 135] have fabricated nanoporous Pt-based alloy nanowires through the combination of electrodeposition into AAO templates with dealloying, and these nanoporous alloy nanowires exhibit distinctly enhanced electrocatalytic activities toward methanol oxidation. Snyder et al. [136] have shown that a tailored geometric and chemical materials architecture can further improve ORR catalysis by demonstrating that a composite nanoporous Ni–Pt alloy impregnated with a hydrophobic, high-oxygen solubility and protic ionic liquid has extremely high mass activity.

1.4 Potential Applications of Nanoporous Metals

Owing to their unique microstructures and related properties, NPMs show potential applications in sensors, actuators, fuel cells, lithium-ion batteries (LIBs), supercapacitors, metal–air batteries, water splitting, synthesis of chemicals, hydrogen storage, automobile exhaust treatment, drug loading and release, bonding materials,

and so forth. In the following, we will briefly outline the main applications of nanoporous metallic materials.

Electrochemical energy storage and conversion (*fuel cells*, *LIBs*, *supercapacitors*, *metal–air batteries*). Energy consumption/production that relies on the combustion of fossil fuels is forecast to have a severe future impact on world economics and ecology. Electrochemical energy production is under serious consideration as an alternative energy/power source, as long as this energy consumption is designed to be more sustainable and more environmentally friendly. Systems for electrochemical energy storage and conversion include batteries, fuel cells, and electrochemical capacitors (ECs or supercapacitors). Although the energy storage and conversion mechanisms are different, there are "electrochemical similarities" of these three systems. Common features are that the energy-providing processes take place at the phase boundary of the electrode/electrolyte interface and that electron and ion transport are separated [137]. Due to their good electrical conductivity, high specific surface areas, and special convex/concave curvature of ligaments, NPMs could be electrode materials or backbones for construction of electrode materials, and show great potentials in applications of electrochemical energy storage and conversion, Fig. 1.22. Recent investigations well confirm this perspective. Peng et al. [138] have demonstrated that NPG could be cathode for high rate and highly reversible Li–O_2 batteries with 95 % capacity retention from cycles 1 to 100. Furthermore, the kinetics of Li_2O_2 oxidation on charge is approximately 10 times faster than on carbon electrodes. Lang et al. [139] have shown that hybrid structures made of NPG and nanocrystalline MnO_2 have enhanced conductivity, resulting in a specific capacitance of the constituent MnO_2 ($\sim$1.145 F g^{-1}) that is close to the theoretical value. In Chap. 3 of this book, we will detailedly discuss NPMs for fuel

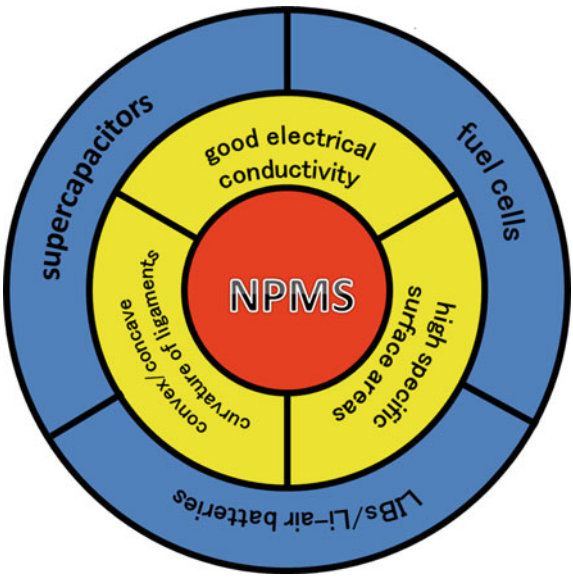

Fig. 1.22 Schematic illustration showing the potential applications of nanoporous metals (NPMs) in electrochemical energy storage and conversion owing to their good electrical conductivity, high specific surface areas, and unique convex/concave curvature of ligaments

cell applications. In Chap. 4, the applications of NPMs in supercapacitors will be addressed. And in Chap. 5, we will talk about the applications of NPMs in lithium batteries.

Sensors. NPMs (especially, NPG) have the bicontinuous ligament–channel structure and high specific areas, and will be good electrode materials or substrates for electrochemical sensors. It is known that chemisorption from the gas or liquid phase can result in a measurable resistance change in a metallic material when at least one dimension is smaller than the mean free path for electrons. Liu and Searson [140] reported single NPG nanowire sensors with the sensitivity factor of 1.0×10^{-16} cm^2, which is comparable to values reported for adsorption on ultrathin films. They found that adsorption of a monolayer of octadecanethiol onto the NPG nanowire results in a resistance change of about 3 %, because the feature size of about 10 nm in NPG nanowires is less than the mean free path for electrons in bulk gold. Liu et al. [141] have demonstrated that NPG is expected to act as a promising electrochemical sensor material for detecting trace p-NP in wastewaters because of its high sensitivity and good selectivity. In addition, nanoporous PtCo alloy was designed as an antibody carrier for preparation of a highly sensitive immunosensor for nonenzyme detection of zeranol. With zeranol concentration range (0.05–5.0 ng/mL), the immunosensor exhibited a highly sensitive response to zeranol with a detection limit of 13 pg/mL [142].

Actuators. Actuator materials can directly convert electrical or chemical energy into mechanical response through changes in material dimensions, and are often called as "artificial muscles" owing to their similarities to biological muscles. Generally speaking, the high density of conduction electrons in metals makes for highly efficient electronic screening, restricting space charge layers at interfaces to a region of essentially atomic dimensions, which is much narrower than the space charge regions in semiconductors. Thus actuation in metals is normally not measurable. Weissmüller et al. [143] have done a pioneer work for actuation of metals. They have shown that reversible strain amplitudes comparable to those of commercial piezoceramics can be induced in metals by introducing a continuous network of nanometersized pores with a high surface area and by controlling the surface electronic charge density through an applied potential relative to an electrolyte impregnating the pores. Subsequently, electrochemical actuation has been found in a series of NPMs and composites, including Au, [144] Pt, [145] Au–Pt, [48] Au–polymer composites, [146] Pd, [147], Ag, [148]. Jin et al. [48] fabricated nanoporous Au–Pt alloys with pore- and ligament size down to few nanometers by dealloying Ag–Au–Pt, and found that the linear strain reaches $\sim$1.3 % in these nanoporous alloys and strain energy density is up to 6.0 MJ/m^3. Recently, Detsi et al. [146] have presented an electrolyte-free approach to put metallic muscles to work via a metal/polymer interface in NPG/polyaniline composites, Fig. 1.23. Strain rates achieved in the single-component nanoporous metal/polymer composite actuator are three orders of magnitude higher than that of the standard three-component nanoporous metal/electrolyte hybrid actuator. In addition, Biener et al. [149] have demonstrated that surface-chemistry-driven actuation can be realized in high-surface-area materials such as NPG. They achieved reversible

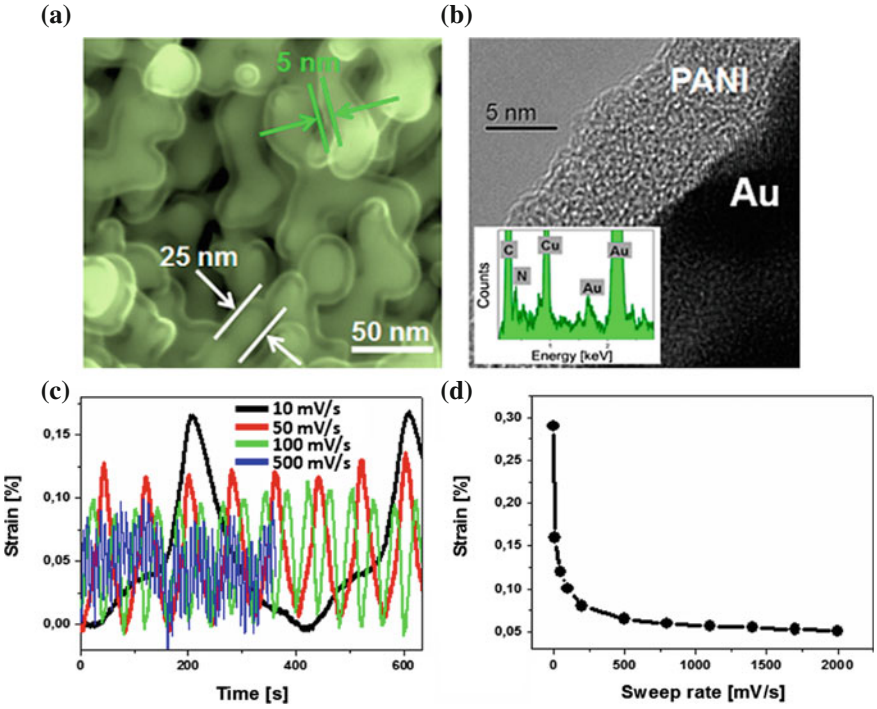

Fig. 1.23 (**a**, **b**) Microstructural characterization of NPG/PANI. Scanning and transmission electron micrographs showing a ~5 nm thick PANI skin covering the ligaments of NPG. The inset of (**b**) displays the EDX spectrum of PANI. C and N come from aniline (C6H7N); Cu and Au come, respectively, from the Cu grid used as sample holder and the NPG. (**c**, **d**) Fast actuation responses of NPG/PANI. Reversible dimensional changes are recorded at various sweep rates far beyond 1 mV/s (**c**) as a function of the time and (**d**) as a function of the sweep rate. (Reproduced from Ref. [146]. Copyright 2013, American Chemical Society)

strain amplitudes of the order of a few tenths of a per cent by alternating exposure of nanoporous Au to ozone and carbon monoxide. It should be noted that whether surface-chemistry-driven actuation will develop into an economically viable technology will strongly depend on materials cost, efficiency, and long-term stability. Most recently, we show that based upon earth's abundant and inexpensive metallic elements like Ni, Co, etc., high performance nanoporous metallic actuators (reversible stain of up to 2 % and ultrahigh work density of 11.76 MJ/m^3) could be developed [150]. Moreover, we for the first time addressed the long-term stability issue of nanoporous metallic actuators, and found the outstanding cycle life (70 % strain retention after 10,000 cycles) of nanoporous Ni actuators.

Other applications. (I) Water splitting. Cai et al. [151] have reported that the 3D nanoporous nickel films exhibited much higher electrocatalytic activity for hydrogen evolution reaction (HER) than smooth nickel foil, and their electrocatalytic

activities for HER enhanced with increase in the porosity and thickness. (II) Automobile exhaust treatment. NPG possesses excellent catalytic activities toward CO oxidation even at low temperatures, [122, 123] thus it may find potential applications in treatment of automobile exhaust treatment. (III) Organic synthesis. It has been shown that NPG could catalyze some organic reactions, such as gaseous methanol to methyl formate, [124] benzyl Alcohol to benzaldehyde, [125] and so on. Thus nanoporous metallic materials show great potentials in green synthesis of organic chemicals. (IV) Hydrogen storage. Liu et al. [152] have demonstrated that the dealloyed nanoporous Pd can absorb/desorb hydrogen or deuterium completely in a few seconds at room temperature. There is no apparent isotope effect on the sorption kinetics. Both the activation energies of hydrogen and deuterium absorption and diffusion coefficients of hydrogen and deuterium in the nanoporous Pd are similar at 423 K. However, the deuterium isotherm shows higher plateau pressure and narrower gap than the hydrogen isotherm at the same temperature. When the temperature increases to 473 K, no phase transformation can be detected for both hydrogen and deuterium. (V) Bonding materials. Flip chip assemblies are frequently used for 3D large-scale integration (LSI), and Au–Au bonding techniques have been widely studied because Au has more attractive properties, such as flexibility and oxidation resistance, than other metals. Au–Ag nanoporous sheets could be used as a joint layer for low-temperature Au–Au bonding, and show good bonding strength [153]. (VI) Biological and medical applications. Garcia-Gradilla et al. [154] have demonstrated that NPG nanowire motors offer efficient drug loading, transport and release capabilities, Fig. 1.24. Chapman et al. [155] have shown that the nanostructure of np-Au achieves close physical coupling of neurons by maintaining a high neuron-to-astrocyte surface coverage ratio. Their results show that np-Au nanotopography, not surface chemistry, reduces astrocyte surface coverage while maintaining high neuronal coverage and may enhance neuron—electrode coupling through nanostructure-mediated suppression of scar tissue formation.

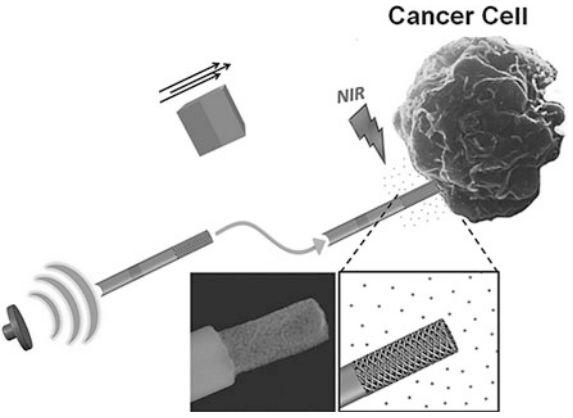

Fig. 1.24 Schematic of the ultrasound-driven movement of the drug-loaded nanoporous Au nanomotors and triggered drug release around a cancer cell. (Reproduced from Ref. [154]. Copyright 2014, Wiley-VCH)

1.5 Summary

In this chapter, we briefly give an introduction to NPMs. First, we show the definition of NPMs, the difference of NPMs from normal metal foams, the kind of NPMs and the fabrication methods of NPMs. Second, we outline the microstructural characteristics of NPMs, considering the compositions (pure elements, alloys and composites), the shapes (bulk and nanosized), and the porous microstructures (homogeneous, multimodal pore size distribution or hierarchically porous nanostructures, ordered random nanoporous architectures, nanoporous periodic arrays, nanoporous metallic composites, and hollow metallic nanostructures). Subsequently, we summarize the properties and potential applications of NPMs. NPMs combine the properties of both metals and nanostructured materials, and show the structure-related electrical, magnetic, mechanical, optical, catalytic, and electrocatalytic properties. And NPMs could find potential applications in fields, such as sensors, actuators, fuel cells, LIBs, supercapacitors, metal–air batteries, water splitting, synthesis of chemicals, hydrogen storage, automobile exhaust treatment, drug loading and release, bonding materials, and so forth.

At present, dealloying is the most important method to fabricate NPMs. Thus in the following chapters, we will review the dealloying-driven NPMs (Chap. 2) and their applications in energy-related fields including fuel cells (Chap. 3), supercapacitors (Chap. 4), and lithium batteries (Chap. 5).

References

1. Ding Y, Chen M (2009) Nanoporous metals for catalytic and optical applications. MRS Bull 34(08):569–576
2. Tappan BC, Steiner SA, Luther EP (2010) Nanoporous metal foams. Angew Chem Int Ed 49 (27):4544–4565
3. Kelly R, Frost A, Shahrabi T, Newman R (1991) Brittle fracture of an Au/Ag alloy induced by a surface film. Metall Trans A 22(2):531–541
4. Forty A (1979) Corrosion micromorphology of noble metal alloys and depletion gilding. Nature 282:597–598
5. Keir D, Pryor M (1980) The dealloying of copper-manganese alloys. J Electrochem Soc 127 (10):2138–2144
6. Cassagne T, Flanagan W, Lichter B (1986) On the failure mechanism of chemically embrittled Cu_3Au single crystals. Metall Trans A 17(4):703–710
7. Erlebacher J, Seshadri R (2009) Hard materials with tunable porosity. MRS Bull 34(08): 561–568
8. Hyeji P, Changui A, Hyungyung J, Myounggeun C, Dong Seok K, Do Kyung K et al (2014) Large-area metal foams with highly ordered sub-micrometer-scale pores for potential applications in energy areas. Mater Lett 129:174–177
9. Chae WS, Gough DV, Ham SK, Robinson DB, Braun PV (2012) Effect of ordered intermediate porosity on ion transport in hierarchically nanoporous electrodes. ACS Appl Mater Interfaces 4(8):3973–3979
10. Erlebacher J, Aziz MJ, Karma A, Dimitrov N, Sieradzki K (2001) Evolution of nanoporosity in dealloying. Nature 410(6827):450–453

11. Nishio K, Masuda H (2011) Anodization of gold in oxalate solution to form a nanoporous black film. Angew Chem Int Ed 50(7):1603–1607
12. Näth O, Stephen A, Rösler J, Vollertsen F (2009) Structuring of nanoporous nickel-based superalloy membranes via laser etching. J Mater Process Technol 209(10):4739–4743
13. Leventis N, Chandrasekaran N, Sadekar AG, Sotiriou-Leventis C, Lu H (2009) One-pot synthesis of interpenetrating inorganic/organic networks of CuO/resorcinol-formaldehyde aerogels: nanostructured energetic materials. J Am Chem Soc 131(13):4576–4577
14. Avisar-Levy M, Levy O, Ascarelli O, Popov I, Bino A (2015) Fractal structures of highly-porous metals and alloys at the nanoscale. J Alloys Compd 635:48–54
15. Zhang X, Guan P, Malic L, Trudeau M, Rosei F, Veres T (2015) Nanoporous twinned PtPd with highly catalytic activity and stability. J Mater Chem A 3(5):2050–2056
16. Zhang Z, Wang Y, Qi Z, Zhang W, Qin J, Frenzel J (2009) Generalized fabrication of nanoporous metals (Au, Pd, Pt, Ag, and Cu) through chemical dealloying. J Phys Chem C 113(29):12629–12636
17. Jia F, Yu C, Deng K, Zhang L (2007) Nanoporous metal (Cu, Ag, Au) films with high surface area: general fabrication and preliminary electrochemical performance. J Phys Chem C 111(24):8424–8431
18. Dong C-S, Gu Y, Zhong M-l, Li L, Ma M-X, Liu W-J (2011) The effect of laser remelting in the formation of tunable nanoporous Mn structures on mild steel substrates. Appl Surf Sci 257(7):2467–2473
19. Wada T, Setyawan AD, Yubuta K, Kato H (2011) Nano- to submicro-porous β-Ti alloy prepared from dealloying in a metallic melt. Scr Mater 65(6):532–535
20. Hakamada M, Motomura J, Hirashima F, Mabuchi M (2012) Preparation of nanoporous ruthenium catalyst and its CO oxidation characteristics. Mater Trans 53(3):524–530
21. Stepanovich A, Sliozberg K, Schuhmann W, Ludwig A (2012) Combinatorial development of nanoporous WO_3 thin film photoelectrodes for solar water splitting by dealloying of binary alloys. Int J Hydrogen Energy 37(16):11618–11624
22. Liu T, Zhu M, Shen H, Qin C, Cao Y (2013) The influences of dealloying temperature and time on the morphology, structure, and magnetic properties of porous Co nanoparticles. J Nanopart Res 15(3):1
23. Wada T, Kato H (2013) Three-dimensional open-cell macroporous iron, chromium and ferritic stainless steel. Scr Mater 68(9):723–726
24. Joung Wook K, Wada T, Sung Gyoo K, Kato H (2014) Sub-micron porous niobium solid electrolytic capacitor prepared by dealloying in a metallic melt. Mater Lett 116:223–226
25. Lei W, Balk TJ (2014) Using multilayer precursors to create nanoporous gold and nanoporous iridium thin films with layered architecture. Metall Mater Trans A 45(3): 1096–1100
26. Chen Q, Sieradzki K (2013) Spontaneous evolution of bicontinuous nanostructures in dealloyed Li-based systems. Nat Mater 12(12):1102–1106
27. Zhang Z, Wang Y, Wang Y (2013) A general dealloying route to synthesize nanoporous non-noble metals. J Nanosci Nanotechnol 13(2):1503–1506
28. Song T, Yan M, Qian M (2015) A dealloying approach to synthesizing micro-sized porous tin (Sn) from immiscible alloy systems for potential lithium-ion battery anode applications. J Porous Mater 22(3):713–719
29. Wada T, Ichitsubo T, Yubuta K, Segawa H, Yoshida H, Kato H (2014) Bulk-nanoporous-silicon negative electrode with extremely high cyclability for lithium-ion batteries prepared using a top-down process. Nano Lett 14(8):4505–4510
30. Liu S, Feng J, Bian X, Qian Y, Liu J, Xu H (2015) Nanoporous germanium as high-capacity lithium-ion battery anode. Nano Energy 13:651–657
31. Yin H, Xiao W, Mao X, Zhu H, Wang D (2015) Preparation of a porous nanostructured germanium from GeO_2 via a "reduction-alloying-dealloying" approach. J Mater Chem A 3 (4):1427–1430

32. Wang X, Frenzel J, Wang W, Ji H, Qi Z, Zhang Z et al (2011) Length-scale modulated and electrocatalytic activity enhanced nanoporous gold by doping. J Phys Chem C 115(11):4456–4465
33. Zhang Z, Zhang C, Gao Y, Frenzel J, Sun J, Eggeler G (2012) Dealloying strategy to fabricate ultrafine nanoporous gold-based alloys with high structural stability and tunable magnetic properties. CrystEngComm 14(23):8292
34. Xu C, Sun F, Gao H, Wang J (2013) Nanoporous platinum-cobalt alloy for electrochemical sensing for ethanol, hydrogen peroxide, and glucose. Anal Chim Acta 780:20–27
35. Xu C, Wang J, Zhou J (2013) Nanoporous PtNi alloy as an electrochemical sensor for ethanol and H_2O_2. Sens Actuators B Chem 182:408–415
36. Xu C, Zhang H, Hao Q, Duan H (2014) A hierarchical nanoporous PtCu alloy as an oxygen-reduction reaction electrocatalyst with high activity and durability. Chempluschem 79(1):107–113
37. Qiu HJ, Shen X, Wang JQ, Hirata A, Fujita T, Wang Y et al (2015) Aligned nanoporous Pt-Cu bimetallic microwires with high catalytic activity toward methanol electrooxidation. ACS Catal 5(6):3779–3785
38. Sun J, Shi J, Xu J, Chen X, Zhang Z, Peng Z (2015) Enhanced methanol electro-oxidation and oxygen reduction reaction performance of ultrafine nanoporous platinum-copper alloy: experiment and density functional theory calculation. J Power Sources 279:334–344
39. Duan H, Hao Q, Xu C (2015) Hierarchical nanoporous PtTi alloy as highly active and durable electrocatalyst toward oxygen reduction reaction. J Power Sources 280:483–490
40. Duan H, Xu C (2015) Nanoporous PtPd alloy electrocatalysts with high activity and stability toward oxygen reduction reaction. Electrochim Acta 152:417–424
41. Xu C, Hou J, Pang X, Li X, Zhu M, Tang B (2012) Nanoporous PtCo and PtNi alloy ribbons for methanol electrooxidation. Int J Hydrogen Energy 37(14):10489–10498
42. Xu C, Liu Y, Wang J, Geng H, Qiu H (2012) Nanoporous PdCu alloy for formic acid electro-oxidation. J Power Sources 199:124–131
43. Zhang Z, Zhang C, Sun J, Kou T, Zhao C (2012) Ultrafine nanoporous Cu–Pd alloys with superior catalytic activities towards electro-oxidation of methanol and ethanol in alkaline media. RSC Adv 2(31):11820
44. Xu C, Liu Y, Hao Q, Duan H (2013) Nanoporous PdNi alloys as highly active and methanol-tolerant electrocatalysts towards oxygen reduction reaction. J Mater Chem A 1(43):13542
45. Xu C, Liu Y, Zhang H, Geng H (2013) A nanoporous PdCo alloy as a highly active electrocatalyst for the oxygen-reduction reaction and formic acid electrooxidation. Chem Asian J 8(11):2721–2728
46. Zhao D, Wang Z, Wang J, Xu C (2014) The nanoporous PdCr alloy as a nonenzymatic electrochemical sensor for hydrogen peroxide and glucose. J Mater Chem B 2(32): 5195–5201
47. Qi Z, Zhao C, Wang X, Lin J, Shao W, Zhang Z et al (2009) Formation and characterization of monolithic nanoporous copper by chemical dealloying of Al–Cu alloys. J Phys Chem C 113(16):6694–6698
48. Jin H-J, Wang X-L, Parida S, Wang K, Seo M, Weissmüller J (2009) Nanoporous Au–Pt alloys as large strain electrochemical actuators. Nano Lett 10(1):187–194
49. Yan X, Xiong H, Bai Q, Frenzel J, Si C, Chen X, et al (2015) Atomic layer-by-layer construction of Pd on nanoporous gold via underpotential deposition and displacement reaction. RSC Adv 5(25):19409–19417
50. Huang JF, Sun IW (2005) Fabrication and surface functionalization of nanoporous gold by electrochemical alloying/dealloying of Au–Zn in an ionic liquid, and the self-assembly of L-Cysteine monolayers. Adv Funct Mater 15(6):989–994
51. Liu L, Pippel E, Scholz R, Gösele U (2009) Nanoporous Pt–Co alloy nanowires: fabrication, characterization, and electrocatalytic properties. Nano Lett 9(12):4352–4358
52. Gu X, Xu L, Tian F, Ding Y (2009) Au-Ag alloy nanoporous nanotubes. Nano Res 2(5): 386–393

53. Wang D, Zhao P, Li Y (2011) General preparation for Pt-based alloy nanoporous nanoparticles as potential nanocatalysts. Sci Rep 1:37
54. Fujita T, Qian L-H, Inoke K, Erlebacher J, Chen M-W (2008) Three-dimensional morphology of nanoporous gold. Appl Phys Lett 92(25):251902
55. Fujita T, Guan P, McKenna K, Lang X, Hirata A, Zhang L et al (2012) Atomic origins of the high catalytic activity of nanoporous gold. Nat Mater 11(9):775–780
56. Yu J, Ding Y, Xu C, Inoue A, Sakurai T, Chen M (2008) Nanoporous metals by dealloying multicomponent metallic glasses. Chem Mater 20(14):4548–4550
57. Zhang Z, Wang Y, Qi Z, Lin J, Bian X (2009) Nanoporous gold ribbons with bimodal channel size distributions by chemical dealloying of Al–Au alloys. J Phys Chem C 113(4):1308–1314
58. Ding Y, Erlebacher J (2003) Nanoporous metals with controlled multimodal pore size distribution. J Am Chem Soc 125(26):7772–7773
59. Qi Z, Weissmüller J (2013) Hierarchical nested-network nanostructure by dealloying. ACS Nano 7(7):5948–5954
60. Qi Z, Vainio U, Kornowski A, Ritter M, Weller H, Jin H et al (2015) Porous gold with a nested-network architecture and ultrafine structure. Adv Funct Mater 25(17):2530–2536
61. Lee MN, Santiago-Cordoba MA, Hamilton CE, Subbaiyan NK, Duque JG, Obrey KAD (2014) Developing monolithic nanoporous gold with hierarchical bicontinuity using colloidal bijels. J Phys Chem Lett 5(5):809–812
62. Sattayasamitsathit S, Gu Y, Kaufmann K, Minteer S, Polsky R, Wang J (2013) Tunable hierarchical macro/mesoporous gold microwires fabricated by dual-templating and dealloying processes. Nanoscale 5(17):7849–7854
63. Sattayasamitsathit S, O'Mahony AM, Xiao X, Brozik SM, Washburn CM, Wheeler DR et al (2012) Highly ordered tailored three-dimensional hierarchical nano/microporous gold–carbon architectures. J Mater Chem 22(24):11950
64. Wang D, Ji R, Albrecht A, Schaaf P (2012) Ordered arrays of nanoporous gold nanoparticles. Beilstein J Nanotechnol 3:651–657
65. Dong W, Ihlemann J, Schaaf P (2014) Complex patterned gold structures fabricated via laser annealing and dealloying. Appl Surf Sci 302:74–78
66. Isasa M, Pérez N, Tavera T, Trueba M, Alkorta J, Gil Sevillano J (2013) Nanoporous gold periodical linear patterns obtained by laser interference thermal treatment. Thin Solid Films 548:69–74
67. Zhang Z, Wang Y, Qi Z, Somsen C, Wang X, Zhao C (2009) Fabrication and characterization of nanoporous gold composites through chemical dealloying of two phase Al–Au alloys. J Mater Chem 19(33):6042
68. Zhang Z, Wang Y, Wang X (2011) Nanoporous bimetallic Pt-Au alloy nanocomposites with superior catalytic activity towards electro-oxidation of methanol and formic acid. Nanoscale 3(4):1663–1674
69. Qi Z, Gong Y, Zhang C, Xu J, Wang X, Zhao C et al (2011) Fabrication and characterization of magnetic nanoporous Cu/(Fe, Cu)3O4 composites with excellent electrical conductivity by one-step dealloying. J Mater Chem 21(26):9716
70. Zhang C, Wang X, Sun J, Kou T, Zhang Z (2013) Synthesis and antibacterial properties of magnetically recyclable nanoporous silver/Fe3O4 nanocomposites through one-step dealloying. CrystEngComm 15(19):3965
71. Guo X, Ye W, Sun H, Zhang Q, Yang J (2013) A dealloying process of core-shell Au@AuAg nanorods for porous nanorods with enhanced catalytic activity. Nanoscale 5 (24):12582–12588
72. Lee C-L, Huang K-L, Tsai Y-L, Chao Y-J (2013) A comparison of alloyed and dealloyed silver/palladium/platinum nanoframes as electrocatalysts in oxygen reduction reaction. Electrochem Commun 34:282–285
73. Chen C, Kang Y, Huo Z, Zhu Z, Huang W, Xin HL et al (2014) Highly crystalline multimetallic nanoframes with three-dimensional electrocatalytic surfaces. Science 343(6177):1339–1343

74. Zhang L, Roling LT, Wang X, Vara M, Chi M, Liu J et al (2015) Platinum-based nanocages with subnanometer-thick walls and well-defined, controllable facets. Science 349(6246): 412–416
75. Schaefer S (2015) Double-walled Ag-Pt nanotubes fabricated by galvanic replacement and dealloying: effect of composition on the methanol oxidation activity. NANO 10(6):66–77
76. Fujita T, Okada H, Koyama K, Watanabe K, Maekawa S, Chen M (2008) Unusually small electrical resistance of three-dimensional nanoporous gold in external magnetic fields. Phys Rev Lett 101(16):166601
77. Xia R, Wang JL, Wang R, Li X, Zhang X, Feng X-Q et al (2010) Correlation of the thermal and electrical conductivities of nanoporous gold. Nanotechnology 21(8):085703
78. Yang Q, Liang S, Han B, Wang J, Mao R (2012) Preparation and properties of enhanced bulk nanoporous coppers. Mater Lett 73:136–138
79. Mishra A, Bansal C, Hahn H (2008) Surface charge induced variation in the electrical conductivity of nanoporous gold. J Appl Phys 103(9):094308
80. Wahl P, Traußnig T, Landgraf S, Jin H-J, Weissmüller J, Würschum R (2010) Adsorption-driven tuning of the electrical resistance of nanoporous gold. J Appl Phys 108(7):073706
81. Steyskal E-M, Besenhard M, Landgraf S, Zhong Y, Weissmüller J, Pölt P et al (2012) Sign-inversion of charging-induced variation of electrical resistance of nanoporous platinum. J Appl Phys 112(7):073703
82. Sun L, Chien C-L, Searson PC (2004) Fabrication of nanoporous nickel by electrochemical dealloying. Chem Mater 16(16):3125–3129
83. Hakamada M, Takahashi M, Furukawa T, Mabuchi M (2009) Coercivity of nanoporous Ni produced by dealloying. Appl Phys Lett 94(15):153105
84. Hakamada M, Takahashi M, Furukawa T, Mabuchi M (2010) Surface effects on saturation magnetization in nanoporous Ni. Philos Mag 90(14):1915–1924
85. Maaroof A, Cortie M, Smith G (2005) Optical properties of mesoporous gold films. J Opt A: Pure Appl Opt 7(7):303
86. Maaroof A, Gentle A, Smith G, Cortie M (2007) Bulk and surface plasmons in highly nanoporous gold films. J Phys D Appl Phys 40(18):5675
87. Yu F, Ahl S, Caminade A-M, Majoral J-P, Knoll W, Erlebacher J (2006) Simultaneous excitation of propagating and localized surface plasmon resonance in nanoporous gold membranes. Anal Chem 78(20):7346–7350
88. Ahl S, Cameron PJ, Liu J, Knoll W, Erlebacher J, Yu F (2008) A comparative plasmonic study of nanoporous and evaporated gold films. Plasmonics 3(1):13–20
89. Schilling J, Sardana N, Heyroth F (2012) Propagating surface plasmons on nanoporous gold
90. Qian L, Shen W, Das B, Shen B, Qin GW (2009) Alumina coating of ultrafine nanoporous gold at room temperature and their optical properties. Chem Phys Lett 479(4):259–263
91. Qian L, Shen W, Shen B, Qin GW, Das B (2010) Nanoporous gold–alumina core–shell films with tunable optical properties. Nanotechnology 21(30):305705
92. Zeng J, Zhao F, Qi J, Li Y, Li C-H, Yao Y et al (2014) Internal and external morphology-dependent plasmonic resonance in monolithic nanoporous gold nanoparticles. RSC Adv 4(69):36682–36688
93. Lang X, Guan P, Zhang L, Fujita T, Chen M (2010) Size dependence of molecular fluorescence enhancement of nanoporous gold. Appl Phys Lett 96(7):073701
94. Lang XY, Guan PF, Fujita T, Chen MW (2011) Tailored nanoporous gold for ultrahigh fluorescence enhancement. Phys Chem Chem Phys 13(9):3795–3799
95. Kucheyev S, Hayes J, Biener J, Huser T, Talley C, Hamza A (2006) Surface-enhanced Raman scattering on nanoporous Au. Appl Phys Lett 89(5):053102
96. Dixon MC, Daniel TA, Hieda M, Smilgies DM, Chan MH, Allara DL (2007) Preparation, structure, and optical properties of nanoporous gold thin films. Langmuir 23(5):2414–2422
97. Qian L, Yan X, Fujita T, Inoue A, Chen M (2007) Surface enhanced Raman scattering of nanoporous gold: smaller pore sizes stronger enhancements. Appl Phys Lett 90(15):153120

98. Qian L, Inoue A, Chen M (2008) Large surface enhanced Raman scattering enhancements from fracture surfaces of nanoporous gold. Appl Phys Lett 92(9):093113
99. Lang XY, Chen LY, Guan PF, Fujita T, Chen MW (2009) Geometric effect on surface enhanced Raman scattering of nanoporous gold: improving Raman scattering by tailoring ligament and nanopore ratios. Appl Phys Lett 94(21):213109
100. Lang X, Guan P, Zhang L, Fujita T, Chen M (2009) Characteristic length and temperature dependence of surface enhanced Raman scattering of nanoporous gold. J Phys Chem C 113(25):10956–10961
101. Zhang L, Chen L, Liu H, Hou Y, Hirata A, Fujita T et al (2011) Effect of residual silver on surface-enhanced raman scattering of dealloyed nanoporous gold. J Phys Chem C 115(40):19583–19587
102. Chen L-Y, Yu J-S, Fujita T, Chen M-W (2009) Nanoporous copper with tunable nanoporosity for SERS applications. Adv Funct Mater 19(8):1221–1226
103. Chen L, Zhang L, Fujita T, Chen M (2009) Surface-enhanced raman scattering of silver@ nanoporous copper core-shell composites synthesized by an in situ sacrificial template approach. J Phys Chem C 113(32):14195–14199
104. Qian L, Das B, Li Y, Yang Z (2010) Giant Raman enhancement on nanoporous gold film by conjugating with nanoparticles for single-molecule detection. J Mater Chem 20(33):6891–6895
105. Li R, Sieradzki K (1992) Ductile-brittle transition in random porous Au. Phys Rev Lett 68 (8):1168
106. Biener J, Hodge AM, Hamza AV (2005) Microscopic failure behavior of nanoporous gold. Appl Phys Lett 87(12):121908
107. Biener J, Hodge AM, Hamza AV, Hsiung LM, Satcher JH Jr (2005) Nanoporous Au: a high yield strength material. J Appl Phys 97(2):024301
108. Volkert C, Lilleodden E, Kramer D, Weissmüller J (2006) Approaching the theoretical strength in nanoporous Au. Appl Phys Lett 89(6):1920
109. Hodge AM, Hayes JR, Caro JA, Biener J, Hamza AV (2006) Characterization and mechanical behavior of nanoporous gold. Adv Eng Mater 8(9):853
110. Lee D, Wei X, Chen X, Zhao M, Jun SC, Hone J et al (2007) Microfabrication and mechanical properties of nanoporous gold at the nanoscale. Scr Mater 56(5):437–440
111. Lee D, Wei X, Zhao M, Chen X, Jun SC, Hone J et al (2007) Plastic deformation in nanoscale gold single crystals and open-celled nanoporous gold. Modell Simul Mater Sci Eng 15(1):S181
112. Biener J, Hodge AM, Hayes JR, Volkert CA, Zepeda-Ruiz LA, Hamza AV et al (2006) Size effects on the mechanical behavior of nanoporous Au. Nano Lett 6(10):2379–2382
113. Mathur A, Erlebacher J (2007) Size dependence of effective Young's modulus of nanoporous gold. Appl Phys Lett 90(6):1910
114. Hodge AM, Biener J, Hayes JR, Bythrow PM, Volkert CA, Hamza AV (2007) Scaling equation for yield strength of nanoporous open-cell foams. Acta Mater 55(4):1343–1349
115. Hodge A, Doucette R, Biener M, Biener J, Cervantes O, Hamza A (2009) Ag effects on the elastic modulus values of nanoporous Au foams. J Mater Res 24(04):1600–1606
116. Seker E, Gaskins JT, Bart-Smith H, Zhu J, Reed ML, Zangari G et al (2007) The effects of post-fabrication annealing on the mechanical properties of freestanding nanoporous gold structures. Acta Mater 55(14):4593–4602
117. Seker E, Gaskins JT, Bart-Smith H, Zhu J, Reed ML, Zangari G et al (2008) The effects of annealing prior to dealloying on the mechanical properties of nanoporous gold microbeams. Acta Mater 56(3):324–332
118. Jin H-J, Kurmanaeva L, Schmauch J, Rösner H, Ivanisenko Y, Weissmüller J (2009) Deforming nanoporous metal: role of lattice coherency. Acta Mater 57(9):2665–2672
119. Jin H-J, Weissmüller J (2011) A material with electrically tunable strength and flow stress. Science 332(6034):1179–1182
120. Liu R, Antoniou A (2013) A relationship between the geometrical structure of a nanoporous metal foam and its modulus. Acta Mater 61(7):2390–2402

121. Wang K, Kobler A, Kuebel C, Jelitto H, Schneider G, Weissmueller J (2015) Nanoporous-gold-based composites: toward tensile ductility. NPG Asia Mater 7(6):e187
122. Volkmar Z, Birte J, Christian S, Juergen B, Biener MM, Hamza AV et al (2006) Gold catalysts: nanoporous gold foams. Angew Chem Int Ed 45(48):8241–8244
123. Xu C, Su J, Xu X, Liu P, Zhao H, Tian F et al (2007) Low temperature CO oxidation over unsupported nanoporous gold. J Am Chem Soc 129(1):42–43
124. Wittstock A, Zielasek V, Biener J, Friend CM, Baumer M (2010) Nanoporous gold catalysts for selective gas-phase oxidative coupling of methanol at low temperature. Science 327(5963):319–322
125. Han D, Xu T, Su J, Xu X, Ding Y (2010) Gas-phase selective oxidation of benzyl alcohol to benzaldehyde with molecular oxygen over unsupported nanoporous gold. ChemCatChem 2(4):383–386
126. Haruta M (2007) New generation of gold catalysts: nanoporous foams and tubes—is unsupported gold catalytically active? ChemPhysChem 8(13):1911–1913
127. Moskaleva LV, Röhe S, Wittstock A, Zielasek V, Klüner T, Neyman KM et al (2011) Silver residues as a possible key to a remarkable oxidative catalytic activity of nanoporous gold. Phys Chem Chem Phys 13(10):4529–4539
128. Liu XY, Wang A, Zhang T, Mou C-Y (2013) Catalysis by gold: new insights into the support effect. Nano Today 8(4):403–416
129. Asao N, Ishikawa Y, Hatakeyama N, Yamamoto Y, Chen M, Zhang W et al (2010) Nanostructured materials as catalysts: nanoporous-gold-catalyzed oxidation of organosilanes with water. Angew Chem Int Ed 49(52):10093–10095
130. Zhang J, Liu P, Ma H, Ding Y (2007) Nanostructured porous gold for methanol electro-oxidation. J Phys Chem C 111(28):10382–10388
131. Yu C, Jia F, Ai Z, Zhang L (2007) Direct oxidation of methanol on self-supported nanoporous gold film electrodes with high catalytic activity and stability. Chem Mater 19(25):6065–6067
132. Ge X, Wang R, Liu P, Ding Y (2007) Platinum-decorated nanoporous gold leaf for methanol electrooxidation. Chem Mater 19(24):5827–5829
133. Wang R, Wang C, Cai WB, Ding Y (2010) Ultralow-platinum-loading high-performance nanoporous electrocatalysts with nanoengineered surface structures. Adv Mater 22(16):1845–1848
134. Shao M, Shoemaker K, Peles A, Kaneko K, Protsailo L (2010) Pt monolayer on porous Pd–Cu alloys as oxygen reduction electrocatalysts. J Am Chem Soc 132(27):9253–9255
135. Liu L, Scholz R, Pippel E, Gösele U (2010) Microstructure, electrocatalytic and sensing properties of nanoporous Pt46Ni54 alloy nanowires fabricated by mild dealloying. J Mater Chem 20(27):5621
136. Snyder J, Fujita T, Chen M, Erlebacher J (2010) Oxygen reduction in nanoporous metal–ionic liquid composite electrocatalysts. Nat Mater 9(11):904–907
137. Winter M, Brodd RJ (2004) What are batteries, fuel cells, and supercapacitors? Chem Rev 104(10):4245–4270
138. Peng Z, Freunberger SA, Chen Y, Bruce PG (2012) A reversible and higher-rate Li-O_2 battery. Science 337(6094):563–566
139. Lang X, Hirata A, Fujita T, Chen M (2011) Nanoporous metal/oxide hybrid electrodes for electrochemical supercapacitors. Nat Nanotechnol 6(4):232–236
140. Liu Z, Searson PC (2006) Single nanoporous gold nanowire sensors. J Phys Chem B 110 (9):4318–4322
141. Liu Z, Du J, Qiu C, Huang L, Ma H, Shen D et al (2009) Electrochemical sensor for detection of p-nitrophenol based on nanoporous gold. Electrochem Commun 11(7):1365–1368
142. Feng R, Zhang Y, Yu H, Wu D, Ma H, Zhu B et al (2013) Nanoporous PtCo-based ultrasensitive enzyme-free immunosensor for zeranol detection. Biosens Bioelectron 42:367–372
143. Weissmüller J, Viswanath R, Kramer D, Zimmer P, Würschum R, Gleiter H (2003) Charge-induced reversible strain in a metal. Science 300(5617):312–315

144. Kramer D, Viswanath RN, Weissmüller J (2004) Surface-stress induced macroscopic bending of nanoporous gold cantilevers. Nano Lett 4(5):793–796
145. Viswanath R, Kramer D, Weissmüller J (2008) Adsorbate effects on the surface stress–charge response of platinum electrodes. Electrochim Acta 53(6):2757–2767
146. Detsi E, Onck P, De Hosson JTM (2013) Metallic muscles at work: high rate actuation in nanoporous gold/polyaniline composites. ACS Nano 7(5):4299–4306
147. Viswanath R, Weissmüller J (2013) Electrocapillary coupling coefficients for hydrogen electrosorption on palladium. Acta Mater 61(16):6301–6309
148. Detsi E, Sellès MS, Onck PR, De Hosson JTM (2013) Nanoporous silver as electrochemical actuator. Scr Mater 69(2):195–198
149. Biener J, Wittstock A, Zepeda-Ruiz L, Biener M, Zielasek V, Kramer D et al (2009) Surface-chemistry-driven actuation in nanoporous gold. Nat Mater 8(1):47–51
150. Bai Q, Wang Y, Zhang J, Ding Y, Peng Z, Zhang Z (2016) Hierarchically nanoporous nickel-based actuators with giant reversible strain and ultrahigh work density. J Mater Chem C 4:45–52
151. Cai J, Xu J, Wang J, Zhang L, Zhou H, Zhong Y et al (2013) Fabrication of three-dimensional nanoporous nickel films with tunable nanoporosity and their excellent electrocatalytic activities for hydrogen evolution reaction. Int J Hydrogen Energy 38(2): 934–941
152. Liu T, Xie L, Li Y, Li X, Pang S, Zhang T (2013) Hydrogen/deuterium storage properties of Pd nanoparticles. J Power Sources 237:74–79
153. Mimatsu H, Mizuno J, Kasahara T, Saito M, Nishikawa H, Shoji S (2013) Low-temperature Au–Au bonding using nanoporous Au–Ag sheets. Japan J Appl Phys 52(5R):050204
154. Garcia-Gradilla V, Sattayasamitsathit S, Soto F, Kuralay F, Yardimci C, Wiitala D et al (2014) Ultrasound-propelled nanoporous gold wire for efficient drug loading and release. Small 10(20):4154–4159
155. Chapman CAR, Chen H, Stamou M, Biener J, Biener MM, Lein PJ et al (2015) Nanoporous gold as a neural interface coating: effects of topography, surface chemistry, and feature size. ACS Appl Mater Interfaces 7(13):7093–7100

Chapter 2
Formation and Microstructural Regulation of Nanoporous Metals

Abstract In the past 15 years, dealloying has been growing into the most important method to fabricate nanoporous metals. In this chapter, we will address the dealloying-driven formation of nanoporous metals, the methods to characterize the microstructures of nanoporous metals, as well as the strategies to regulate the microstructures of nanoporous metals. Dealloying is a common corrosion process, during which the less noble element(s) is selectively etched away and the more noble element(s) is retained to form a nanoporous structure. First, we briefly discuss the history of dealloying, including "depletion gilding" at the time of pre-Columbian Central America and the early Middle Ages in European and Near Eastern, Raney® metals dealloyed from Al-based precursors in 1920s, and dealloying to form functionalized nanoporous metals at the beginning of this century. Additionally, in the most time of last century, people were concerned with dealloying mainly from the viewpoint of corrosion/protection. To understand the dealloying mechanisms is crucial to the design/fabrication of nanoporous metals. We then outline the related mechanisms being operated in the dealloying process. Since the 1960s, in situ/ex situ experiments and computer simulations have been performed to unveil the formation mechanism of nanoporous metals during dealloying, considering the selective dissolution of the less noble element(s), the surface diffusion of the more noble element(s), the critical potential, and the parting limit. The influence of anions (like halide ions) and the phase constitution should also be taken into consideration. Nanoporous metals exhibit a three-dimensional bicontinuous ligament (metal)-channel (void) structure. Many techniques can be used to characterize the microstructures of nanoporous metals, including X-ray diffraction (XRD), scanning electron microscopy (SEM), transmission electron microscopy (TEM), high-resolution TEM, scanning TEM, scanning tunneling microscopy (STM), energy dispersive X-ray analysis, small angle neutron scattering (SANS), and so forth. Three-dimensional tomographic reconstruction is also popular to reveal the interior microstructures of nanoporous metals. In addition, the methods to evaluate the characteristic length scale and the specific surface area of nanoporous metals are also reviewed. In the last section of this chapter, we discuss how to regulate the microstructures/compositions/morphologies of nanoporous metals. First, we talk about the design of precursors for dealloying, considering the composition (elements), phase constitution, crystallinity, and

Y. Ding and Z. Zhang, *Nanoporous Metals for Advanced Energy Technologies*, DOI 10.1007/978-3-319-29749-1_2

microalloying. Second, the microstructural regulation of nanoporous metals can be achieved by controlling over the dealloying parameters, including chemical/electrochemical dealloying, the dealloying solution, temperature, the applied potential, the dealloying step (two-step or multistep), the effect of atmosphere, and dealloying in nonaqueous media. The post-dealloying treatment has also been briefly outlined. Third, we discuss the strategies which are often adopted to further modify nanoporous metals, based upon their potential applications.

Keywords Dealloying · Nanoporous metals · Formation mechanisms · Microstructural characterization · Microstructural regulation

2.1 The Dealloying Method and Its History

Dealloying is the most important method to fabricate nanoporous metals. Eventually, dealloying is a common corrosion process during which an alloy is "parted" by the selective dissolution of the most electrochemically active element(s) [1]. For a binary alloy to be dealloyed, one element should be more noble (or inert) and another element should be less noble. During dealloying, the less noble element is selectively etched away (into the dealloying solution or electrolyte) and the more noble element is retained. Figure 2.1 schematically illustrates the dealloying process of a binary alloy.

In fact, dealloying is an ancient process and has a long history. Indians of pre-Columbian Central America had invented a depletion gilding technique for the coloration of castings prepared from copper–gold alloys (also referred to as tumbaga or tumbago), Fig. 2.2 [2]. Depletion gilding is such a process by which the surface of a dilute gold alloy becomes gold-enriched by the selective removal of the less noble component. At that time, the depletion gilding process involved by either the removal of Cu from the Cu–Au alloy surface in a corrosive solution, or the dissolution of Cu oxides which were formed by heating the Cu–Au alloys in air. North Peruvian

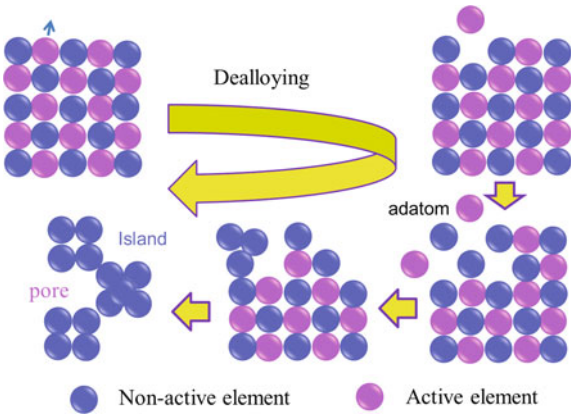

Fig. 2.1 Schematic illustration of the dealloying process of a binary alloy

Fig. 2.2 Tumbaga pectoral, Quimbaya culture, 300–1600 AD, Antiquia, Colombia. (Photo from the website: http://university.langantiques.com/index.php/Tumbaga)

craftsmen also used similar processes to decorate objects made from silver-based alloys [2]. In addition, before the early Middle Ages, European and Near Eastern goldsmiths had used a very closely related process (known as cementation) for the coloration of silver–gold alloys [2]. They removed Ag from the Ag–Au alloy objects by forming soluble chlorides, making the surface of objects gold-rich. Of course, at that time, people had not known the formation of nanoporous structures on the surface of objects during the dealloying or depletion gilding process.

Another important thing for dealloying is the invention of Raney® metals which were named after their inventor Murray Raney. In 1925, Raney got a patent on the preparation of Raney® metals [3]. Typically, Raney® metals could be fabricated by dealloying Al-based alloys (such as Al–Cu, Al–Ni, Al–Co, Al–Fe, Al–Ag, etc.) in alkaline solutions. During these processes, the more active Al is selectively removed from the Al-based alloys and the non-active element(s) is retained to form Raney® metals with high specific surface areas. Until now, Raney® metals are still important industrial catalysts for hydrogenation reactions [4]. For example, Huber et al. [5] have reported that tin-promoted Raney nickel catalyst could promote the production of hydrogen (H_2) by aqueous phase reforming of biomass-derived oxygenated hydrocarbons at temperatures near 500 K. And the performance of this non-precious metal catalyst compares favorably with that of platinum-based catalysts for production of hydrogen from ethylene glycol, glycerol, and sorbitol. However, these high surface area metal catalysts are often practiced in an engineering manner, and the correlations among structures, morphologies, and properties are less appreciated and understood.

In the most of the twentieth century, dealloying received great attention in the context of corrosion, including stress corrosion cracking (SCC) and corrosion fatigue, such as dezincification of brass [6–13]. For example, it was found that binary Cu–Zn alloys cracked intergranularly in the ammoniacal solutions, whereas cracking was transgranular in the ternary Cu–Zn–Ni alloy. Dealloying was observed to be a common feature of both modes of cracking, and occurred only during crack propagation and not during the incubation period before crack

initiation [6]. People investigated the dealloying phenomena and mechanisms of alloys in different environments, but mainly thought about how to avoid the occurrence of dealloying and to protect the alloys.

At the beginning of the new century, dealloying has been receiving renewed attention due to the fact that some alloy systems undergo nanoporosity evolution upon dealloying to form functional nanostructured porous metals. Different from the role of dealloying in corrosion/protection of alloys, this time people consider how to use the powerful top-down strategy to fabricate nanoporous metals. As early as in 1963, Pickering and Swann [14] first used transmission electron microscopy (TEM) to investigate the dealloyed microstructures of copper–gold, copper–aluminum, copper–zinc, and magnesium–aluminum alloys. They have found that the pitting or tubular type of attack may be initiated at grain boundaries and antiphase boundary junctions in ordered copper–gold alloys, gold alloys, and the superficial chemical disturbance can be as small as a six-atom cluster. In 1979, Forty [2] for the first time presented TEM micrographs for a free-standing nanoporous gold (NPG) membrane material with a pore size of approximately 20 nm, which was made by etching an Ag–Au (50–50 wt%) alloy film in 50 % HNO_3 solution. Almost at the same time (in 1980), Keir and Pryor [15] revealed the porous and brittle nature of the Cu-50 % Mn alloy polarized at 0 V for 20 h in 0.5 M NaCl solution, using scanning electron microscopy (SEM). In 1991, an in situ scanning tunneling microscope (STM) was used to observe the morphological changes accompanying the selective dissolution of Ag from low Ag content Ag–Au alloys in dilute perchloric acid [16]. In 2001, Erlebacher et al. [1] further clarified the underlying physical mechanism of dealloying of Ag–Au alloys using experiments and computer simulation. Since then, dealloying-driven nanoporous metals have been receiving more and more attention, as a novel type of nanostructured porous metallic materials.

Figure 2.3 summarizes the history of dealloying and the dealloying-driven phenomena/materials.

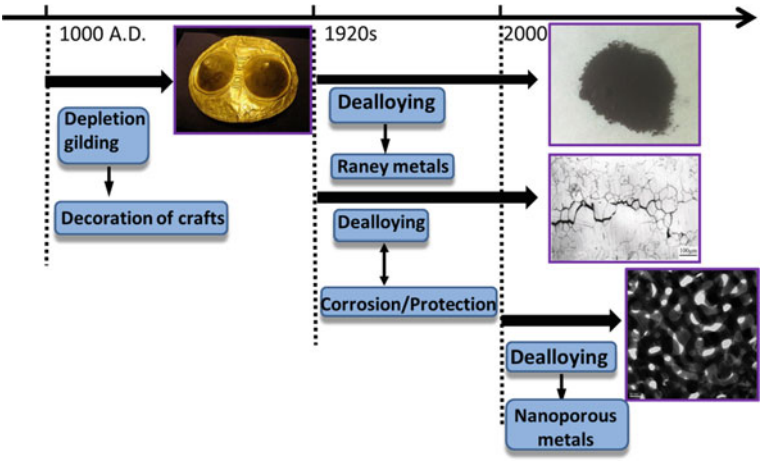

Fig. 2.3 The history of dealloying

2.2 Formation Mechanisms of Nanoporous Metals by Dealloying

Since the 1960s, efforts have been dedicated to clarify the dealloying mechanisms. Theoretically, when one metal is preferentially dissolved one or more of the following three mechanisms may operate: (i) both metals ionize followed by redeposition of the more noble metal; (ii) only the less noble metal ionizes and enters the solution while the atoms of the more noble metal aggregate by surface diffusion; (iii) only the less noble metal ionizes and enters the solution and atoms of both metals move in the solid phase by volume diffusion. However, the experimental results indicate that interdiffusion of the constituent metals in the Cu–Au alloy occurs to a significant extent and dissolution of Au does not take place, and electrochemical measurements with a Cu–Zn alloy give no indication of occurrence of the ionization–redeposition mechanism [17]. Electron microscope observations of Cu_3Au exposed to a ferric chloride solution suggested that surface diffusion or ionization and redeposition of Au occur on the walls of corrosion tunnels, and no evidence was found to support the volume diffusion theory [18]. Later, Forty et al. [2, 19, 20] proposed a corrosion disordering/diffusion reordering model, Fig. 2.4. They have argued that the formation of the island channel structure can be explained by this model in which corrosion proceeds by selective dissolution of the less noble component, thereby creating a disordered surface layer which subsequently reorders by surface diffusion of gold adatoms during dealloying of Ag–Au alloys. Pryor and Fister [21] have shown that dealloying cannot propagate into the Cu-based alloys by diffusion of solute from the bulk to the surface. Instead, dealloying is maintained by solution intrusion under conditions where continuous solute paths exist in the alloy and where solute removal results in atomic rearrangement of the depleted alloy.

Kaesche [22] has argued that dealloying requires the nucleation of terrace site vacancy clusters, since easily dissolvable kink sites of screw dislocations are blocked by noble metal atoms. Based upon the percolation theory, Sieradzki et al. [23] have

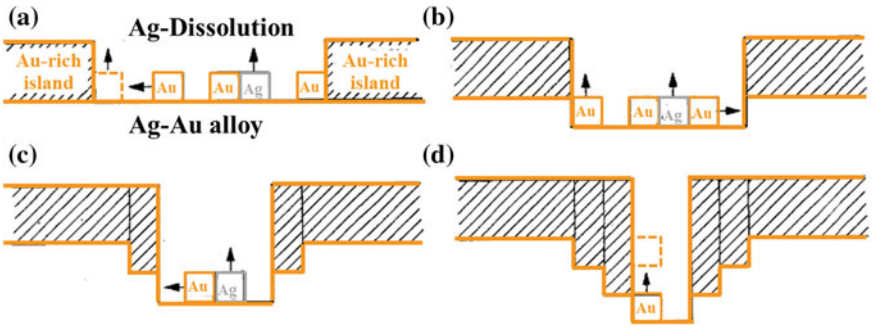

Fig. 2.4 The sequence of morphological changes occurring for an alloy undergoing corrosion disordering and reordering. Adapted from Ref. [20]

developed a new model to account for all the known features of dealloying, including a porous morphology of the dealloyed residue, coarsening of this porosity, sharp dealloying thresholds or parting limits, and the development of intermediate compositions. Their Monte Carlo simulations give a support to the mechanism involving the selective dissolution of the reactive element and surface diffusion of the more noble element during dealloying. In situ scanning tunneling microscopy (STM) results show that there exist three different regimes during dealloying of Cu_3Au [24]. At low overpotentials, two-dimensional clustering of gold atoms occurs near sites of copper dissolution due to the highly mobile nature of the surface species. At higher potentials, the electrode is largely passivated by the enrichment of gold. However, there exist small localized regions of three-dimensional roughness which may be correlated to extended dealloying catalyzed by bulk solid-state defects. When the potential is increased above the critical potential (E_c), global surface roughening occurs by nucleation and growth. At the same time, in situ STM was also used to observe the morphological changes accompanying the selective dissolution of Ag from low Ag content Ag–Au alloys in dilute perchloric acid [16]. The authors have argued that the selective dissolution can be interpreted within the framework of the kink-ledge-terrace model and percolation theory. The corrosion process leads to roughening of the surface by dissolution of Ag atoms from terrace sites at high overpotentials. Sieradzki [25] further proposed that dissolution of the less noble constituent can proceed only by injection of regions of negative curvature into the solid surface, and the critical potential for macroscopic selective dissolution is associated with a kinetic roughening transition which results from a competition between curvature-dependent dissolution and surface diffusion. Smith et al. [26] believed that the overall mechanism of formation/rearrangement of the Raney® copper structure was found to be mainly dissolution/redeposition of copper atoms, with surface or volume diffusion, or possibly both, playing a minor role.

At the very beginning of this century, a continuum model was proposed by Erlebacher et al. [1] to rationalize experiments and theoretical simulations of dealloying. They have demonstrated that nanoporosity in metals is due to an intrinsic dynamical pattern formation process involving the formation of nanopores because the more noble atoms are chemically driven to aggregate into two-dimensional clusters by a phase separation process (spinodal decomposition) at the solid/electrolyte interface. Figure 2.5 clearly shows the simulated nanoporosity evolution during dealloying of Ag–Au alloy at a fixed potential. Erlebacher [27] further described the microscopic details of porosity formation during dealloying using a kinetic Monte Carlo model incorporating site coordination-dependent dissolution of the less noble atoms and site coordination-dependent surface diffusion of all alloy components. His simulation model reproduces the entire range of phenomena associated with dealloying, including composition and geometric restrictions on dealloying (parting limit), a composition-dependent critical potential, a passivation regime, a regime of steady-state dissolution flux, and porosity formation. Moreover, the formation and undercutting of the more noble islands as well as the bifurcation of pores play an important role in the nanoporosity evolution during dealloying.

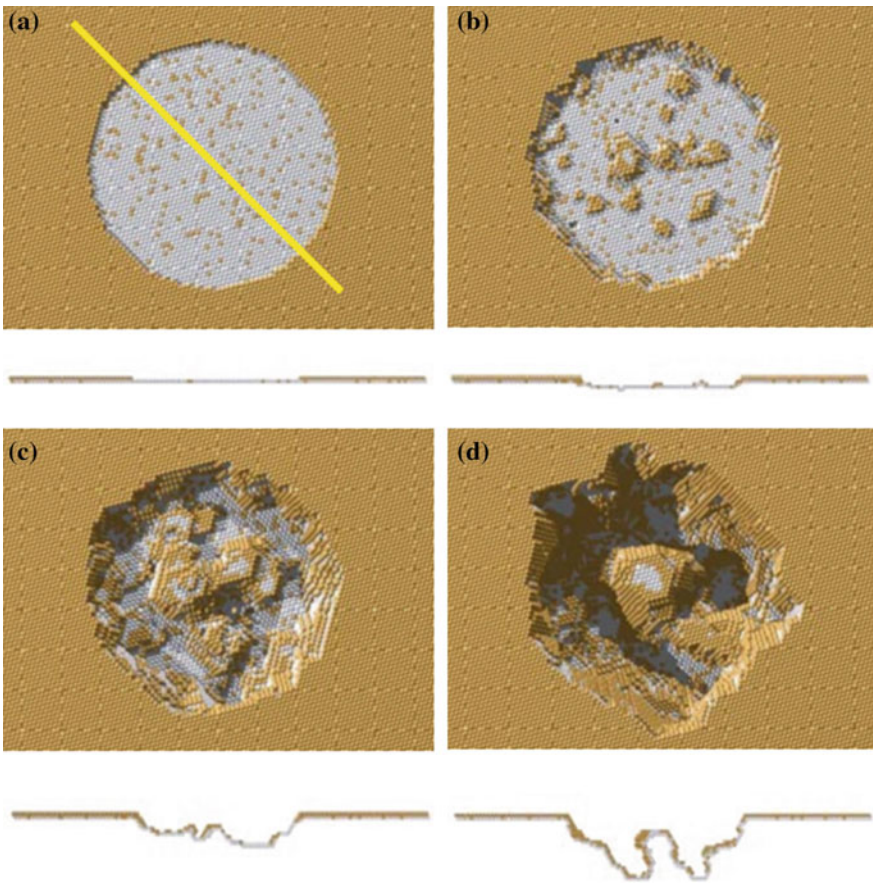

Fig. 2.5 Simulated evolution of an artificial pit in Au10–Ag90 % (at.%), ϕ = 1.8 eV. Cross sections along the (11-1) plane defined by the *yellow line* in (**a**) are shown below each plan view. **a** The initial condition is a surface fully passivated with gold except within a circular region (the "artificial pit"). **b** After 1 s, the pit has penetrated a few monolayers into the bulk. We note how there are fewer gold clusters near the side wall than at the center of the pit. **c** After 10 s, a gold cluster has nucleated in the center of the pit. **d** At 100 s, the pit has split into multiple pits; each will continue to propagate into the bulk to form a porous structure. (Reproduced from Ref. [1]. Copyright 2001, Nature Publishing Group)

Conventionally, the critical potential represents the potential marking the onset of bulk dealloying, Fig. 2.6. The current density below the critical potential is only weakly dependent on potential, and the physical processes responsible for this passive-like behavior are poorly understood. Wagner et al. [28] used in situ STM to study the nature of the surface morphology which develops at potentials less than the critical potential. They found that at fixed potential, the time-dependent evolution of the surface morphology was correlated with the observed current decay. Two general regimes of power-law behavior in the current decay exist,

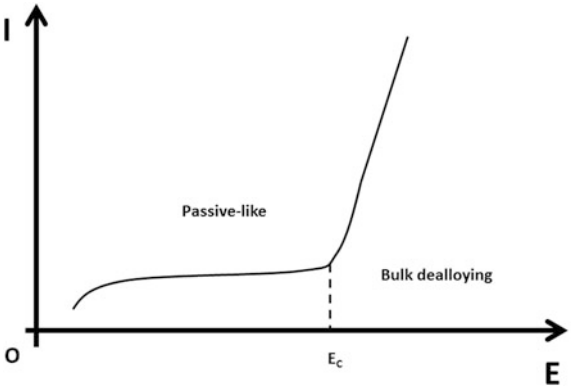

Fig. 2.6 Typical current (*I*)-potential (*E*) curve of an alloy containing one less noble element and one more noble element (for example Ag–Au alloy)

corresponding to exhaustion of an activation-controlled dissolution process (t^{-1}) and the operation of one of three mechanisms of surface mass transport control ($t^{-5/8}$, $t^{-1/2}$, and $t^{-1/4}$). Erlebacher [27] has found that an intrinsic critical potential exists as a well-defined threshold potential separating surface passivation and porosity formation behaviors, but this intrinsic critical potential typically sits at values well below the experimental measurements of the empirical critical potential. Dursun et al. [29] developed a steady-state method to accurately determine the dealloying critical potential, and found that the more traditional approach of extrapolation from anodic polarization data could overestimate the critical potential of Ag–Au alloys by $\sim$100 mV. Furthermore, morphological investigations confirm the presence of porosity for a potential hold only 10 mV above the critical potential.

The conventional view of morphology evolution in the region below the critical potential is that the alloy surface maintains a stable planar interface while enriching in the more noble constituent. Renner et al. [30] performed atomic scale observations of the initial stages of corrosion of a Cu_3Au (111) single crystal alloy within a sulphuric acid solution by in situ X-ray diffraction (XRD) with picometrescale resolution. They observed the formation of a gold-enriched single crystal layer with thickness of two to three monolayers and an unexpected inverted (CBA-) stacking sequence, below the critical potential. At higher potentials, the protective passivation layer dewets and pure gold islands are formed. STM images further indicate an interlayer exchange of topmost surface atoms during initial dealloying of Cu_3Au (111) single crystal alloy, while scanning Auger electron microscopy (SAEM) data clearly reveal that the surface is fully covered by a continuous Au-rich layer at an early stage. Initiating below this first layer a transformation from stacking reversed toward substrate-oriented Au surface structures is observed close to the critical potential [31]. Below the critical potential, no distinct diffraction signal is evidenced by in situ XRD but atomic force microscopy (AFM) reveals the existence of islands on the surfaces of Cu_3Pd single crystal [32].

Kamundi et al. [33] have found that the dealloying critical potential of (111) oriented alloys is systematically more positive than the one for polycrystalline alloys with identical composition. Thin alloy films (thickness of 20–100 nm) exhibit almost

identical E_c to the bulk samples, whereas spherical particles (diameters ~100 nm) feature consistently lower E_c (by about 0.050–0.100 V). A trend toward even lower E_c (0.300–0.450 V) is illustrated by the dealloying of $Au_xAg_{(1-x)}$ nanoparticles (NPs, diameter 10–15 nm). Moreover, no dealloying threshold applies to $Au_xAg_{(1-x)}$ NPs. Oezaslan et al. [34] reported the particle size dependence of dealloyed morphology for Pt–Co and Pt–Cu alloy nanoparticles with diameters of several to 100 nm (the morphology of "single core–shell nanoparticles," "multiple cores–shell nanoparticles," and "surface pits/nanoscale pores" takes place with increasing particle size). Through Kinetic Monte Carlo simulations, Callejas-Tovar et al. [35] have found that two critical potentials define regions where Pt-based alloy nanoparticles may exist as core–shell, porous, and hollow structures after dealloying. Chen and Sieradzki [36] have recently demonstrated that dealloying of Li from Li–Sn alloys depends on alloy composition, particle size and dealloying rate, and all known dealloyed morphologies evolve including bicontinuous nanoporous structures and hollow core–shell particles. Cui et al. [37] have found that the PtNi octahedra nanoparticles preferentially leach in their facet centers and evolve into "concave octahedra." Li et al. [38] have demonstrated that above the potential corresponding to Ag^+/Ag equilibrium only core–shell structures evolve in the 2–6 nm diameter particles, and dealloying of the 20–55 nm particles results in the formation of porous structures analogous to the behavior observed for the corresponding bulk alloy. Similar results have also been reported for $PtNi_3$ nanoparticles by Rudi et al. [39]. Most recently, Han et al. [40] have found that smaller size, less-oxidative acid treatment and annealing significantly reduced Ni leaching and nanoporosity formation in $PtNi_3$ nanoparticles while encouraged surface passivation.

Petegem et al. [41] studied the evolution of the grain structure, internal strain, and the lattice mis-orientations of NPG during dealloying of bulk (3D) Ag–Au alloy samples by various in situ and ex situ XRD techniques including powder and Laue diffraction. Their experiments revealed that the dealloying process preserves the original crystallographic structure but leads to a small spread in orientations within individual grains. Initially, most grains develop in-plane tensile stresses, which are partly released during further dealloying. Simultaneously, the feature size of the developing nanoporous structure increases with increasing dealloying time.

The formation of NPG by open-circuit dealloying of 100 nm AgAu foils in nitric acid was investigated in situ and in real time by combining synchrotron small angle X-ray scattering (SAXS) and XRD. Several characteristic dealloying stages are observed, Fig. 2.7. First, there is a fast initial dissolution stage with an increase in surface area due to pore and mound formation, which leads to capillary pressure induced strain in NPG. After dissolution is complete, there is rapid coarsening of the quasiperiodic, pore–ligament morphology, together with strong strain anisotropies. Then a slow coarsening stage occurs where the SAXS patterns and the quasiperiodic morphology are self-similar in time. There is a strong correlation between the morphology evolution and strain development, which can be explained by capillary forces [42]. Galinski et al. [43] probed the dominating physical mechanisms of nanoporosity formation during the dealloying process of Pt–Al films, using focused ion beam (FIB) nanotomography and Rutherford backscattering spectroscopy (RBS). The RBS and FIB results show that the porosity evolution has to be regarded

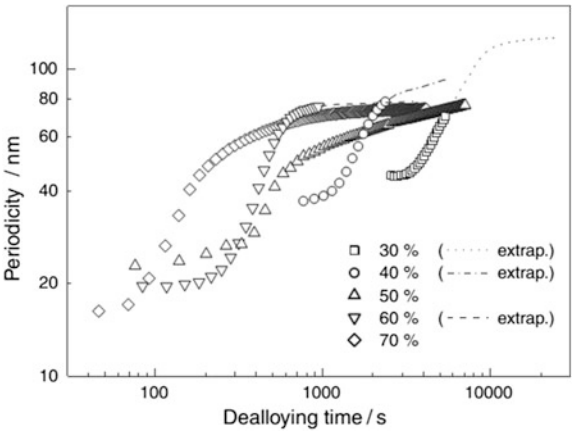

Fig. 2.7 Characteristic length scale of quasiperiodicity in NPG dealloyed with 30–70 % HNO_3 determined from the SAXS correlation peak positions (symbols). *Dashed lines* indicate extrapolated SAXS data as described in the text. (Reproduced from Ref. [42]. Copyright 2011, Wiley-VCH)

as superposition of two independent processes, a linearly propagating diffusion front with a uniform speed and a slower dissolution process in regions which have already been passed by the diffusion front. The experimentally observed front evolution is captured by the Fisher–Kolmogorov–Petrovskii–Piskounov (FKPP) and the slower dissolution is represented by a zero-order rate law which causes a gradual porosity in the thin film. Recently, Ye et al. [44] have found that the dealloying of Au–Ag and Au(Pt)–Ag alloys occurs by two processes: a primary dealloying process that selectively dissolves Ag from the parent alloy and creates a nanoporous (np) structure, and a secondary dealloying process that occurs behind the corrosion front and further dissolves the residual Ag from the nanoligaments. The secondary dealloying can occur during coarsening, and/or when a more anodic potential is applied. With suppressed np structure coarsening in Pt-containing samples, the intrinsic np structure created by the primary dealloying contains small ligament diameter (3–7 nm) and high concentration of residual Ag (~50 at.%), irrespective of the dealloying potentials.

Chen-Wiegart et al. [45] have reported that the dealloying process can be directly imaged by using transmission X-ray microscopy (TXM) for the case of an Ag–30 at.% Au wire dealloyed under free corrosion in nitric acid. The propagation of a sharp dealloying front separating the alloy from nanoporous Au was observed by two-dimensional real time in situ imaging at 30 nm resolution, Fig. 2.8. They have found that the rate of the dealloying front propagation is independent of the dealloying time up to a 3 μm depth, indicating that the dealloying process to this depth is dominated by interfacial effects (i.e., gold surface diffusion and/or silver dissolution) rather than long-range transport effects (i.e., diffusion of acid and corrosion product in and out of the porous layer). Moreover, the dealloying front velocity depends exponentially on the alloy Ag/Au atomic ratio and the acid molar concentration [46]. Upon dealloying via successive voltammetric sweeps between −0.05 and 1.15 V versus standard hydrogen electrode, compressive stress develops in the dealloyed Pt layer at the surface of thin-film PtCu electrodes [47].

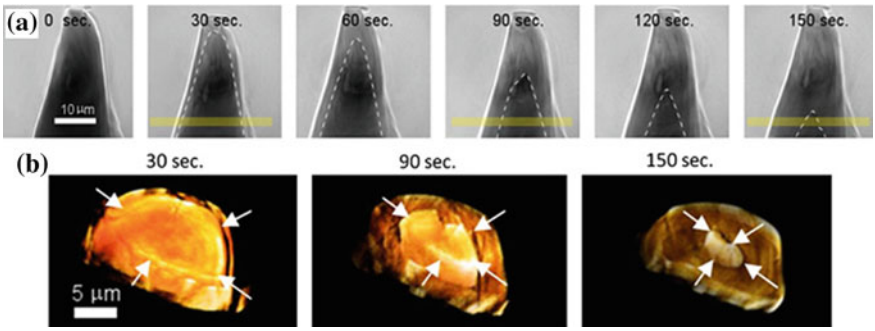

Fig. 2.8 **a** Series of X-ray transmission images showing the dealloying front propagation with ex situ imaging (sample A). The dealloying front is highlighted with a *dashed line*. **b** Cross section of tomographic reconstruction of the selected volume marked in *yellow* in (**a**); the dealloying front is highlighted with *arrows*. (Reproduced from Ref. [45]. Copyright 2013, Elsevier)

It should be noted that the minor dissolution of the more noble element is also possible during dealloying, especially when the electrolyte contains Cl^- or other halide ions. During electrochemical dealloying of brass in aqueous sodium chloride solution, Cu dissolves into the solution to form Cu(I) and Cu(II) complex ions [48]. At appropriately high dealloying potentials, relatively steady chloride compound or chloride complexes can form between chloride ion and the more noble metals included, such as soluble $AuCl_3^-$, $PdCl_2$, $AgCl_2^-$, $CuCl_2^-$ and insoluble AgCl and CuCl during the electrochemical dealloying of Al-based alloys [49]. Moreover, inductively coupled plasma (ICP) measurements also verify the existence of minor Ag ions in the electrolyte after chemical dealloying of Mg–Ag−Pd alloys [50]. In addition, Starr and Buttry [51] have reported that dealloying of the more noble gold atoms from the alloy NPs was also achieved by cyclic voltammetry (CV) in sodium chloride. The silver was oxidized first to cohesive silver chloride, and then gold dealloying to soluble $HAuCl_4$ occurred at higher potentials. Chen et al. [52] developed a novel converse dealloying method to fabricate free-standing nanoporous silver (np–Ag). One remarkable characteristic of the new dealloying method is that inert component (Au) is selectively removed from Au–Ag alloys while active component (Ag) is left undissolved. Thiourea plays a key role in the formation of a free-standing porous Ag framework since it not only leads to anodic dissolution of Au component but also causes the surface passivation of Ag component.

In addition, halide ions also play a significant influence on the formation of nanoporous metals during dealloying of precursors in halide ion-containing solutions. It is generally accepted that the addition of halide ions into the solution could accelerate the surface diffusion of the more noble element during dealloying. It has been found that the electrochemical dealloying mechanism of Al_2Au in the neutral NaCl solution can be explained based upon pourbaix diagram and chloride ion effect [53]. During the dealloying process, a self-acidifying effect is triggered due to the dissolution and instant hydrolysis of Al^{3+}/Al, which is assisted by chloride ions in the electrolyte. The dissolution of Cu to form soluble $CuCl_2^-$ complex also

contributes to the dealloying of $MgCu_2$ and the formation of nanoporous copper [54]. Hakamada and Mabuchi [55] reported the spontaneous formation of NPG prism microassembly with highly dense skins, which was caused by the chloride ion enhanced surface diffusion of gold atoms in concentrated hydrochloric acid. Renner et al. [56] have also argued that chloride additives enhance the surface diffusion and respective morphologies are observed earlier during electrochemical dealloying of Au_3Cu single crystal.

We systematically investigated the electrochemical dealloying of single-phase Al_2Au alloy in sodium halide aqueous solutions at different temperatures [57, 58]. The Al_2Au alloy is passivated in NaF solution but can be dealloyed in NaCl, NaBr, and NaI solutions, leading to typical NPG. The open-circuit potential is susceptible to the halide species, and the amount and pattern of cracks in the obtained NPG as well as the sizes and homogeneity of ligaments are remarkably affected by the halide ions. It has been found that the surface diffusivities of gold adatoms increase with the increase of temperature in a given halide solution, and also increase following the sequence of $Cl^- < Br^- < I^-$ at a given temperature. Besides, the activation enthalpy decreases following the sequence $Cl^- > Br^- > I^-$. The open-circuit potential of the single-phase Al_2Au alloy markedly decreases with increasing electrolyte concentration, as well as the corrosion potential of Al_2Au. The steady-state current density markedly increases, and the dealloying time visibly decreases with increasing chloride ion concentration in the NaCl solutions. There exists a good linear relationship between the surface diffusivities of Au adatoms and the electrolyte concentration, and the activation energy visibly decreases with increasing chloride ion concentration in the electrolyte at the given overpotential. Ankah et al. [59] also found that the additions of halides (Cl^-, Br^-, I^-) have a pronounced effect on the dealloying process of Cu_3Au (111) in acidic solutions and lead to peculiar changes in the resulting surface morphologies.

If multiple phases exist in the alloy, Pugh et al. [60] argued that porosity formation of any individual phase would follow the same requirement for a single phase, and hence typically only the A-rich phase would dealloy (Here A is the less noble element). In this case, dealloying would be isolated to only surface grains unless a mechanism existed for the penetration of the electrolyte throughout the alloy; for example, the A-rich grains form a percolating path through the alloy. As for a two-phase alloy, we have found that the dealloying process depends not only upon the activity difference of the constituent elements, but also on the composition, activity, defect (for example vacancy) concentration and electrochemical properties of each phase in the alloy [49, 61–67]. According to the reactions (being excavated, dealloyed, or retained) of the constitutive phases in a biphasic alloy during dealloying, six types of dealloying are classified, Table 2.1 [49]. Three scenarios (type II, IV, and V) involve the formation of nanoporous structure during dealloying of a two-phase alloy. Moreover, it is suggested positively by type II and IV that the dealloying of bi-phasic alloys is quite versatile and effective in fabricating nanoporous metals with controllable morphologies (bimodal pore size distribution and nanoporous composites). Also in the case of type II and IV, the excavation or dealloying of the less noble phase probably has an obvious catalytic effect on the

Table 2.1 A classification for biphasic alloys (composed of α and β phases) based on the dealloying behaviors of constitutive phases in the 1 M NaCl aqueous solution. (Reproduced from Ref. [49]. Copyright 2010, The Royal Society of Chemistry)

Type number	α	β	Examples
I	Excavated	Excavated	Al–Zn in HCl
II	Excavated	Dealloyed	Al-20 Au, A1-30 Au
III	Excavated	Retained	Al–Sn in dilute HCl (at room temperature)
IV	Dealloyed	Dealloyed	Al-40 Au, Al-40 Cu
V	Dealloyed	Retained	Al-30 Pd
VI	Retained	Retained	$Pt_{40}Ag_{60}$ in HCl

dealloying of the more noble phase. For example, the dealloying of α-Al accelerates the dealloying of Ag_2Al in the biphasic Al-35–50 Ag alloys composed of α-Al and Ag_2Al. Eventually, the single-phase Ag_2Al is totally inert in the same dealloying solution. This catalytic effect is particularly important for the dealloying of bulk samples. As shown in Fig. 2.9a, b, the Al phase can be completely etched away in an alkaline solution like NaOH, leaving large channels. The electrolyte can quickly penetrate into the inner part of the sample through these large channels, and the dealloying front can move forward much faster than the scenario of the homogeneous solid alloy like AuAg. Through this design of the precursor alloys, one could fabricate bulk nanoporous metallic samples with sizes of up to centimeters, Fig. 2.9c. Additionally, strictly speaking, the scenario of type III does not belong to the scope

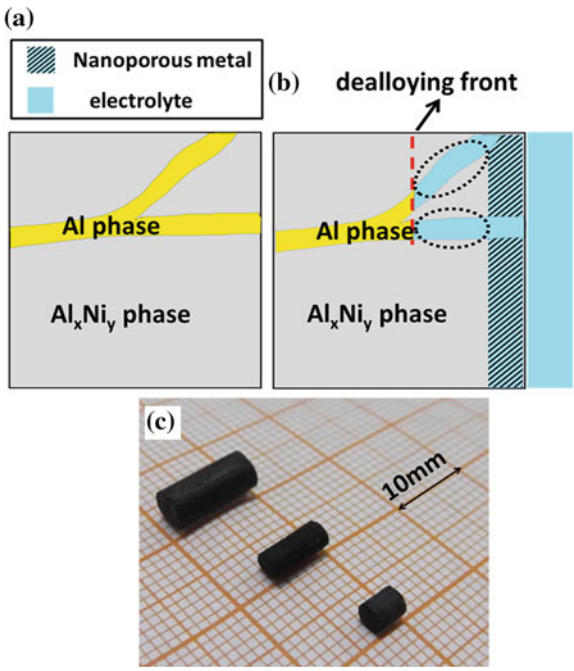

Fig. 2.9 **a**, **b** Schematic illustration of dealloying in two-phase or multiphase precursor alloys (like Al—Ni). **c** Bulk nanoporous Ni rods dealloyed from $Al_{75}Ni_{25}$ in alkaline media

of dealloying-driven nanoporous metals, because no surface diffusion on the atomic scale and no nanoporosity evolution occur during the dealloying process. Although one can obtain nanoporous metals (Fig. 1.7 in Chap. 1) through dealloying of this type of two-phase precursors, the formation of this porous structure is due to one phase simply being excavated out of a two-phase material.

Normally, the minor residual of the less noble element is inevitable in the resultant nanoporous metals formed by dealloying, but less attention has been paid to the retention of the less noble element during dealloying. Recently, Liu et al. [68] have investigated factors controlling the less noble metal retention in nanoporous structures processed by electrochemical dealloying, taking Ag–Au as an example. It has been found that while the dealloying critical potential is generally independent of pH, the dissolution rate is strongly affected by the solution acidity. pH substantially affects Ag retention in both the oxide and alloy forms. They have found that the pH and dissolution rate affect more significantly the amount of Ag retained in the form of oxide (AgO), while the dealloying potential has a stronger impact on Ag trapping. In addition, it is generally accepted that the residual less noble element can not be completely removed but asymptotically reaches a limit at exhaustively long etching times (up to100 h) [23].

At present, although people have known some aspects in dealloying-driven formation of nanoporous metals, the intrinsic physical and chemical mechanisms involved in the dealloying process need to be further clarified using both experiments and computer simulations. For example, it has been found that Cu_3Pt nanoparticles underwent surface dealloying to form core–shell structure under electrochemical conditions, while volumetric dealloying would occur to form a nanoporous structure under chemical dealloying conditions [69]. But the underlying reason for these phenomena is still unclear. On the one hand, people should know how to understand and determine the parting limit and the critical potential of each precursor alloy. On the other hand, people should also unveil some processes possibly occurring during dealloying, including the selective dissolution of the less noble element(s), the surface diffusion/reorganization (or dissolution–redeposition) of the more noble element(s), the penetration of the electrolyte into the precursor, the nucleation/growth of the ligaments, and so forth. Based upon these, novel precursor alloy systems suitable for dealloying could be explored, and nanoporous metallic materials with ideal morphologies/compositions/structures could be designed and fabricated.

2.3 Microstructure and Characterization of Nanoporous Metals

Nanoporous metals possess a unique porous microstructure and combine the properties of both metals and nanostructured materials. In this section, we mainly outline the methods to characterize the microstructures of nanoporous metals.

It is known that the formation of nanoporous metals normally undergoes the surface diffusion and reorganization of the more noble element(s) during dealloying. And thus, phase transformation also takes place in the dealloying process. XRD is the most efficient and also facile method to identify the phase constitution of the precursors and the as-dealloyed samples. For example, Fig. 2.10 shows the phase constitutions of the rapidly solidified Al-based binary precursor alloys and the corresponding nanoporous metals [70]. It can also be seen that digit camera can easily capture the appearance (color) of both the monolithic precursors and the as-dealloyed samples. In addition, it should be noted that the combination of XRD with other methods like TEM and selected area electron diffraction (SAED) can exactly determine the phase constitution of nanoporous metals. Coherent diffraction imaging (CDI) is a method by which the transmission function of a nonperiodic object is recovered from its XRD pattern. X-ray CDI offers nondestructive three-dimensional characterization of electron-dense materials at nanometer length scales beyond the resolution of current x-ray lenses, and access to the full complex refractive index of the material. Kim et al. [71] have demonstrated the use of physically justified object constraints in X-ray Fresnel CDI on NPG, enabling highly reliable imaging of the sample's shape and pore structure.

Normally, the microstructure and morphology of nanoporous metals can be simply characterized by SEM and TEM (see Fig. 1.1 of Chap. 1). It can be clearly seen from SEM/TEM that NPG (taken as an example) appears to be completely irregular in morphology for both empty pore channels and solid metallic ligaments

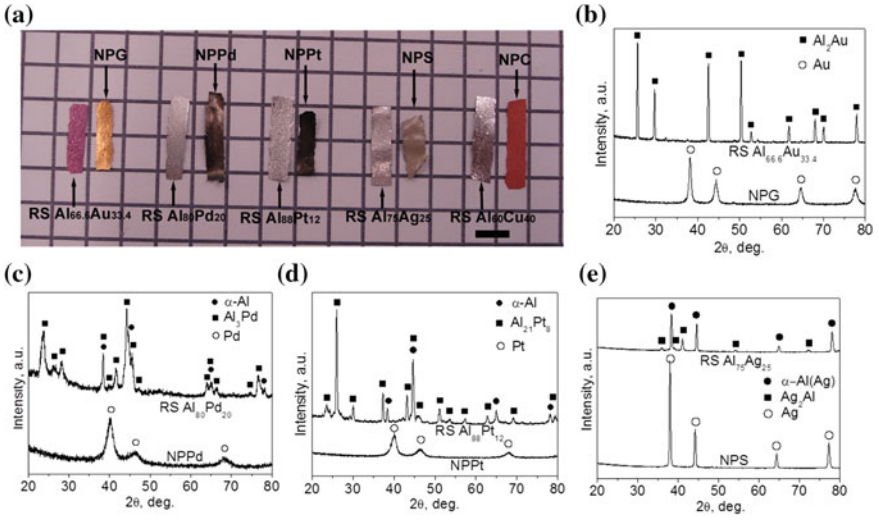

Fig. 2.10 **a** Macrograph of the rapidly solidified (RS) Al_xM_{100-x} (M = Au, Pd, Pt, Ag, and Cu) alloys and corresponding nanoporous metal ribbons. Scale bar, 5 mm. **b–e** XRD patterns of the RS Al_xM_{100-x} (M = Au, Pd, Pt, and Ag) alloys and corresponding nanoporous metal ribbons. a.u.: arbitrary units. **b** $Al_{66.6}Au_{33.4}$ and NPG; **c** $Al_{80}Pd_{20}$ and nanoporous palladium (NPPd); **d** $Al_{88}Pt_{12}$ and nanoporous platinum (NPPt); and **e** $Al_{75}Ag_{25}$ and nanoporous silver (NPS). (Reproduced from Ref. [70]. Copyright 2009, American Chemical Society)

comprising the nanostructure. The distribution of solid gold ligaments and empty pore channels, if assumed as two separate phases, is analogous to the microstructure produced by traditional spinodal decomposition. In addition, the combination of TEM with SAED can determine the phase constitution and crystalline nature (single crystalline or polycrystalline) of nanoporous metals. However, plan-view SEM and TEM cannot probe the internal microstructure nanoporous metals. Fujita et al. [72] employed electron tomography along with a number of algorithms to quantitatively characterize the complex 3D nanoporous structure of NPG (Fig. 1.1c, e in Chap. 1). They found that gold ligaments and nanopore channels are topologically and morphologically equivalent, i.e., they are inverses of each other in three-dimensional space. In addition, through energy dispersive X-ray analyzer (which is normally attached to SEM), the overall composition of nanoporous metals can be determined, but the errors may be as large as ~ 1 at.%.

Besides conventional SEM and TEM, high-resolution TEM (HRTEM) and fast Fourier transform (FFT) have also been utilized to document the microstructure of nanoporous metals. From HRTEM images and corresponding FFT patterns, one can clearly see the lattice features (fringes) of the nanoporous structure within the framework of observation, and further discern the single crystalline or polycrystalline nature of nanoporous metals. For example, NPG dealloyed from Ag–Au or Al–Au alloys generally inherits from the crystalline orientation and grain size of the precursor [70, 73]. One can clearly see lattice fringes extending throughout all of the ligaments shown in the HRTEM image (Fig. 1.13 of Chap. 1). Furthermore, crystal defects sometimes appear in the resultant nanoporous metals due to the stress generated during dealloying, especially potential-driven electrochemical dealloying. Through HRTEM observations, people can obtain the information on lattice defects in nanoporous metals, including dislocations, twins and stacking faults (see Fig. 1.14 of Chap. 1).

By using spherical-aberration-corrected TEM, one can probe the structural information of nanoporous metals on the atomic size. For example, Fujita et al. [74] revealed atomic origins of the high catalytic activity of NPG dealloyed from Ag–Au films through spherical-aberration-corrected TEM and environmental TEM. Figure 2.11 shows the scanning TEM (STEM) images under a high-angle annular dark field (HAADF) mode. The Z-contrast STEM image can well show the porous structure of nanoporous metals (here, NPG, Fig. 2.11a). The curved surfaces with a high density of atomic steps and kinks can be observed from STEM images (Fig. 2.11b–d). Low-index (100) and (110) facets as well as stepped high-index planes, such as (310) and (410), can be recognized from the nanopore surface. Unlike the (111) and (100) surfaces, the (110)-terminated facets do not form ordered terraces (Fig. 2.11d). They further performed in situ environmental HRTEM observations of NPG catalyzing CO oxidation. They found that NPG containing 1.2 at.% Ag begins to show catalytic activity along with significant surface reconstruction (faceting), and higher Ag content (20 at.%) could effectively suppress the faceting dynamics.

With the combination of STEM with EDX (spot analysis, line scanning and area analysis), one can also obtain the compositional information of nanoporous metals,

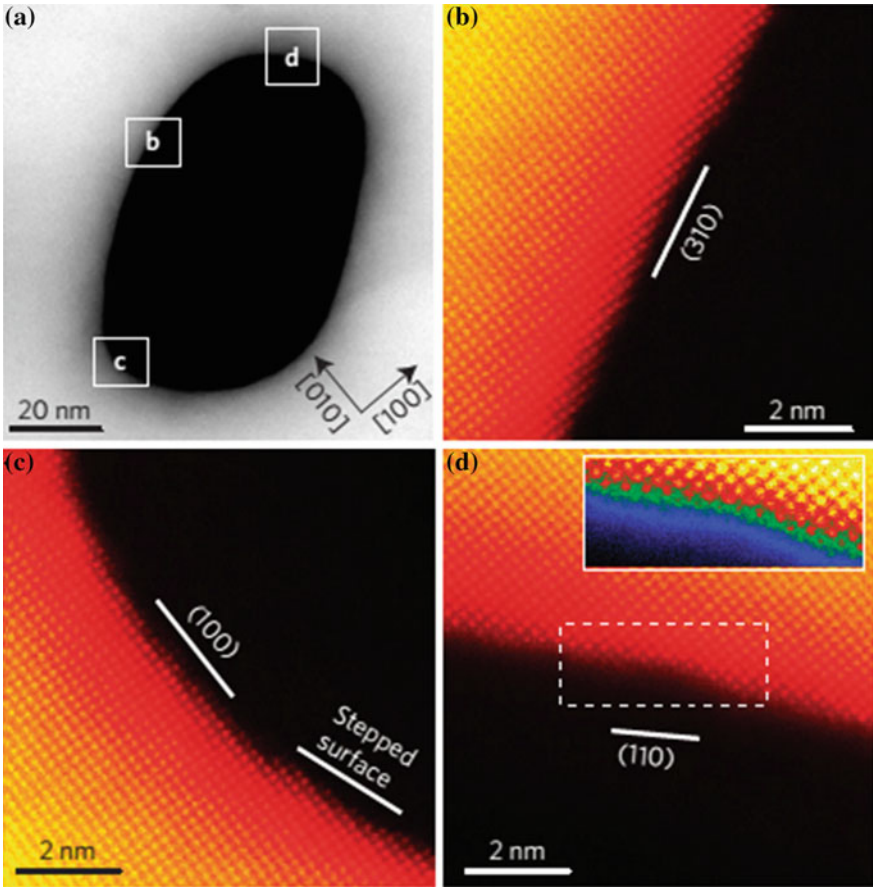

Fig. 2.11 STEM images viewed along [001] of NPG dealloyed from Ag–Au. **a** The labeled *squares* indicate the areas characterized by HAADF-STEM in the following observations. **b** HAADF-STEM image of a high-index (310) plane with atomic kinks. **c** Concave (100) plane area with flat terraces and atomic kinks. **d** Concave (110) plane with a non-level edge. The *Inset* is the color-enhanced image of the area in the *dashed rectangle*. (Reproduced from Ref. [74]. Copyright 2012, Nature Publishing Group)

especially for nanoporous nanostructures (nanoparticles, nanowires or nanotubes). In addition, the morphology and atomic scale elemental distribution of nanoporous metals can be determined by aberration-corrected STEM equipped with electron energy loss spectrometer (EELS). Moreover, STEM 3D tomography reconstruction can be used to directly visualize the three-dimensional porous network of nanoporous metals [69, 75]. For example, Fig. 2.12 shows three-dimensional tomographic reconstruction of a chemically dealloyed nanoparticle (spongy) at two different viewing directions [69]. A series of consecutive slices through the isosurfaces of such nanoparticle clearly show the nanoporous networks of the nanoparticle. Hovden et al. [76] recently proposed a three-dimensional imaging

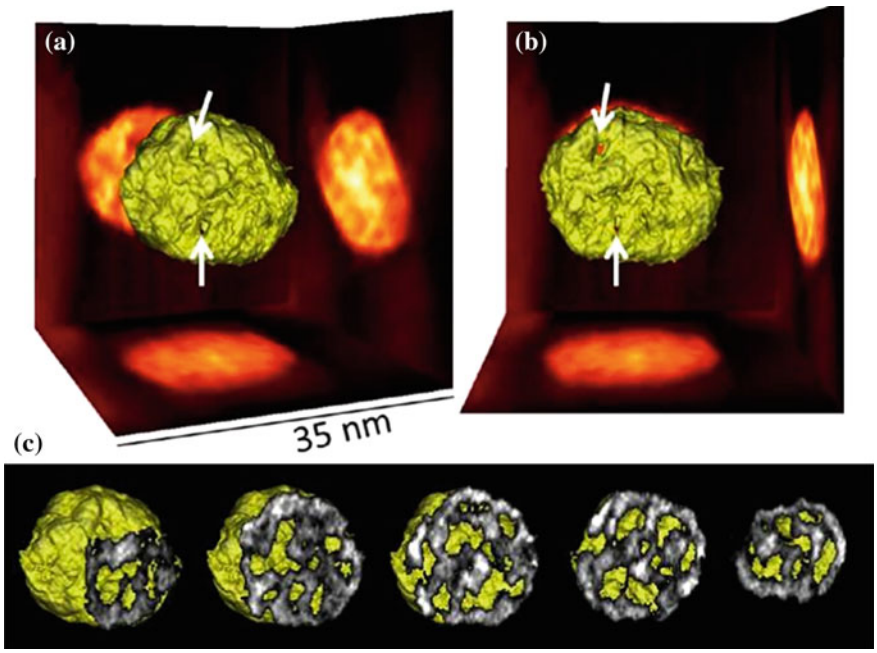

Fig. 2.12 Three-dimensional tomographic reconstruction of a chemically dealloyed nanoparticle (spongy) at two different viewing directions. The *arrows* indicate channels connecting to the exterior surfaces. **c** A series of consecutive slices through the isosurfaces of such nanoparticle, showing the porous networks. (Reproduced from Ref. [69]. Copyright 2012, American Chemical Society)

method by combining through-focal depth sectioning and traditional tilt-series tomography to reconstruct extended objects, with high resolution, in all three dimensions (Fig. 2.13). A through-focal reconstruction over a 390 nm 3D carbon support containing over 100 dealloyed and nanoporous PtCu catalyst particles revealed with sub-nanometer detail the extensive and connected interior pore structure that is created by the dealloying instability.

Corcoran [77] explored the use of small angle neutron scattering (SANS) as potential tools for sorting out the mechanisms involved in porosity formation and characterizing the microstructure of nanoporous metals. Figure 2.14 shows the scattering intensity for dealloying times of 3–21 h. A well-defined peak indicates that the porous structure contains a well-defined average pore size. The average pore size is related to the inverse of the peak position, thus the shifting of the peak to lesser values of Q corresponds to an increasing pore size, i.e., the porosity is coarsening at room temperature during the dealloying process. In addition, STM can not only probe the dealloying process of some single crystal intermetallic compounds (such as Cu_3Au, Au_3Cu, etc.), but also characterize the microstructure of the obtained nanoporous metals [56]. Erlebacher and McCue [78] proposed a hybrid fairing method for geometric characterization of nanoporous metals, and

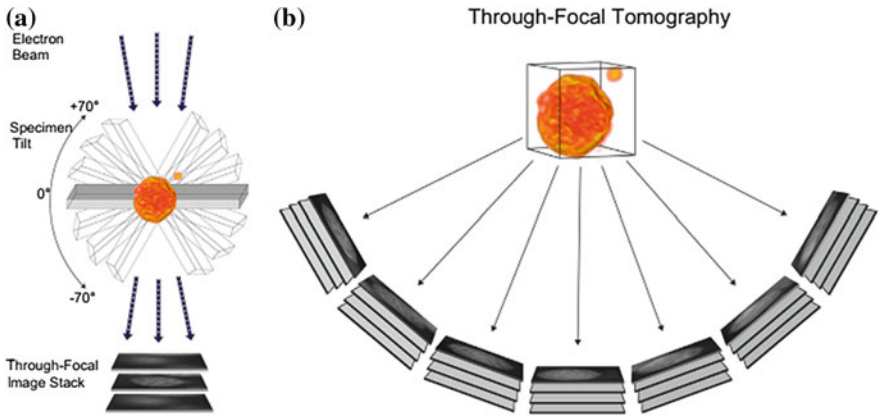

Fig. 2.13 Simplified diagram illustrating through-focal STEM tomography. **a** A stack of images at different focal planes is acquired at one specific tilt. This is repeated over a range of specimen tilts. **b** The through-focal image stacks acquired at every tilt angle contain lateral and depth information allowing for a high-resolution reconstruction of extended objects with fewer tilt angles. (Reproduced from Ref. [76]. Copyright 2014, Elsevier)

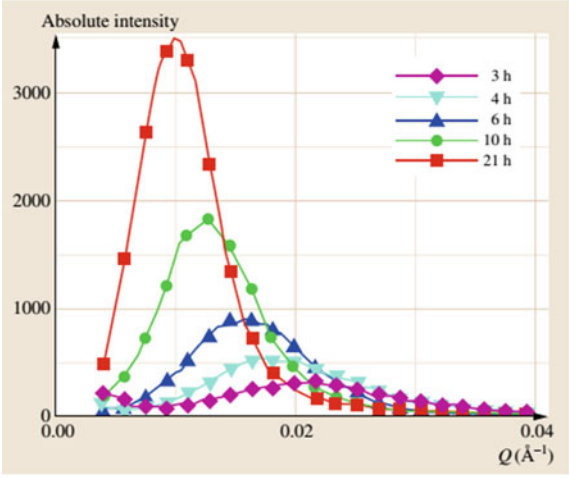

Fig. 2.14 In situ scattering data for the spontaneous corrosion of $Ag_{0.7}Au_{0.3}$ in concentrated HNO_3. The dealloying time associated with each curve is indicated. Adapted from Ref. [77]

found that the method is useful for tracking the morphological evolution of nanoporous metals toward the Wulff shape, in particular to calculate the relative surface fraction of various facet orientations and the interfacial shape distribution.

It has been recognized that the characteristic length scale of nanoporous metals is an important factor that controls their physical, chemical, and mechanical properties. Therefore, a precise measurement of the length scale of NPMs (or even identifying the relevant length scale metric) is essential for modeling the size-related properties and for correctly understanding the relationship between microstructures and properties of nanoporous metals. First, one can roughly determine the average length

scale of nanoporous metals from high-resolution SEM and/or TEM images. For example, the average ligament/channel sizes, defined by the equivalent diameters of ligaments/channels in nanoporous metals, could be determined manually by identifying a minimum of 50 ligaments/channels, making measurements across the shortest distance of each ligament/channel and then averaging [79]. Secondly, the average pore size of the as-dealloyed NPG can also be calculated from the SANS data (the inverse of the peak position) [77]. Third, Fujita et al. [72] proposed a rotational FFT method to evaluate the characteristic length scale of nanoporous metals. The resultant Fourier space spectrum can provide a scattering peak corresponding to the characteristic length scale of the bicontinuous structure. Additionally, the combination of tomographic reconstruction from HAADF-STEM images with 3-D stereological analysis can give quantitative information on the size distribution of both ligaments and nanopores in nanoporous metals [75].

The specific surface area is another important parameter for modulating the microstructures, properties and applications of nanoporous metals. Although developing a standard procedure for the surface area determination is essential for a better understanding of the materials properties influenced by the delocalized surface atoms, there is a lack of general agreement in the characterization of surface area of nanoporous metals. Several methods have been proposed to evaluate the specific surface area of nanoporous metals, and here we summarize as follows. (I) Gas adsorption method [80]. The adsorption isotherms are first obtained through measurements at low temperature (using liquid N_2, normally at 77 K). Thus the specific surface area can be determined by the Brunauer–Emmett–Teller (BET) analysis. The shortcomings of this method include the limited sensitivity, and the need for sample heating in order to obtain accurate measurements. The latter may result in coarsening of nanoporous metals and a decrease of the measured surface area with respect to the actual value. (II) Redox method [81]. The method is applicable to metals (such as Au, Pd, etc.) showing well-developed regions for oxide monolayer formation and reduction. For example, the cathodic peak will appear on the CV curve in the back scan, corresponding to the reduction of Au oxide monolayer which is formed during the forward scan. By calculating the involved charge, the specific surface area can be determined through dividing by the reference charge (390 ± 10 μC cm^{-2} for polycrystalline Au [81]). (III) Hydrogen adsorption/desorption method [81]. The method is used as a rule with a few transition metals (for example, Pt) showing hydrogen adsorption in potential regions prior to massive H_2 evolution. The charge under the voltammetric peaks for hydrogen adsorption or desorption (or associated with the appropriate section of the potential-time curves) corrected for double-layer charging, is assumed to correspond to adsorption of one hydrogen atom on each metal atom of the surface, and the charge associated with a one-to-one H-M correspondence per unit surface area is 210 μC cm^{-2} for polycrystalline Pt. For the methods II and III, one should take care when measuring the specific surface area of Au-based or Pt-based alloys because the addition of other alloying element(s) may change the monolayer nature of Au oxide or hydrogen adsorption/desorption. (IV) The double-layer capacitance method [82]. The double-layer capacitance could be derived by the analysis of electrochemical impedance spectroscopy (EIS). The ratio

between the double-layer capacitance measured on porous and flat electrodes from the same metal correlates directly with the surface area development. EIS is a powerful technique but the recording of impedance spectra is complicated with nanoporous samples and the EI spectra analysis is a complex procedure depending on critical assumptions. (V) Underpotential deposition (UPD) method [82, 83]. The Pb UPD and Cu UPD have been developed to determine the specific surface area of NPG. The specific surface area of nanoporous metals could be evaluated via the formation and stripping of a Pb or Cu monolayer using either CV or chronoamperometry (CA) [82, 83]. The authors also compared the UPD method with other techniques, and found that Cu UPD and Au oxidation/reduction methods yielded surface area values in good quantitative agreement, but estimates based on EIS measurements were 1.5–1.75 times larger. (VI) CO stripping method [84]. In some cases, the CO adsorption/stripping method is used to determine the specific surface area of nanostructured Pd. It is believed that CO could form monolayer adsorption when the Pd electrode is potentially held in the CO saturation electrolyte, and the CO monolayer will be stripped during the subsequent CV scan. Through calculating the involved charge of the CO stripping peak, the specific surface area of the Pd electrode could be determined.

2.4 Microstructural Regulation of Nanoporous Metals

To tune their properties and meet the requirements for various applications, microstructural regulation is a crucial issue for development of nanoporous metallic materials. On the basis of the understanding of the formation mechanisms, kinds of strategies could be utilized for microstructural regulation of nanoporous metals, including design of precursors for dealloying, controlling over the dealloying parameters and post-dealloying treatment, and further modification of nanoporous metals. In the following, we will detailedly discuss these three aspects.

2.4.1 Design of Precursors for Dealloying

Erlebacher [27] has proposed that alloy systems that form porosity upon dealloying share a number of characteristics, and there are four basic common characteristics that an alloy typically possesses if it has a chance of becoming nanoporous during dealloying: (i) the difference in potential required to dissolve the alloy component in its pure form must be separated by a few hundred millivolts, with one element being more noble and the other less noble; (ii) the composition is usually rich in the less noble component (the content of the more noble element is below its parting limit); (iii) the alloy must be homogeneous with no phase separation prior to dissolution. Porosity evolution thus forms dynamically during dissolution and is not due to one phase simply being excavated from a two-phase material; (iv) diffusion of more

noble atoms at the alloy/electrolyte interface must be sufficiently fast. The Ag–Au system is the prototype precursor for dealloying and has received much attention [1]. Based upon the above criteria, many other precursor systems have also been explored, such as Al-based alloys [70], Zn-based alloys [85], Mg-based alloys [64, 86], Mn-based alloys [87], Cu-based alloys [30], Ni-based alloys [88], and so forth.

Composition In general, there exists a parting limit for a precursor alloy suitable for dealloying [27]. According to the above common criteria, the precursors for dealloying-driven nanoporosity evolution normally have the more noble element with the content of less than its parting limit. The dealloying critical potential will increase with increasing content of the more noble element. The higher the more noble element in the precursors (below the parting limit), the better mechanical integrity (the less cracks) of the obtained nanoporous samples would preserve [63]. Sometimes, however, the dilute precursors with the more noble element content well below its parting limit, could be adopted to fabricate nanoporous metals with unique morphologies and compositions. For example, nanoporous Pt–Co alloy nanowires could be synthesized by electrodeposition of Co-rich Pt_1Co_{99} alloy into anodic aluminum oxide (AAO) membranes, followed by a dealloying treatment in a mild acidic medium [89]. Qi and Weissmüller [90] reported an electrochemical dealloying strategy that yields bulk samples of porous gold with a hierarchical microstructure starting from a dilute $Ag_{95}Au_5$ solid solution. Most recently, Qiu et al. [91] fabricated aligned bimetallic Pt–Cu microwires with a three-dimensional nanoporous structure, tunable composition, and high catalytic activity by dealloying a dilute Pt_3Cu_{97} precursor (Fig. 2.15).

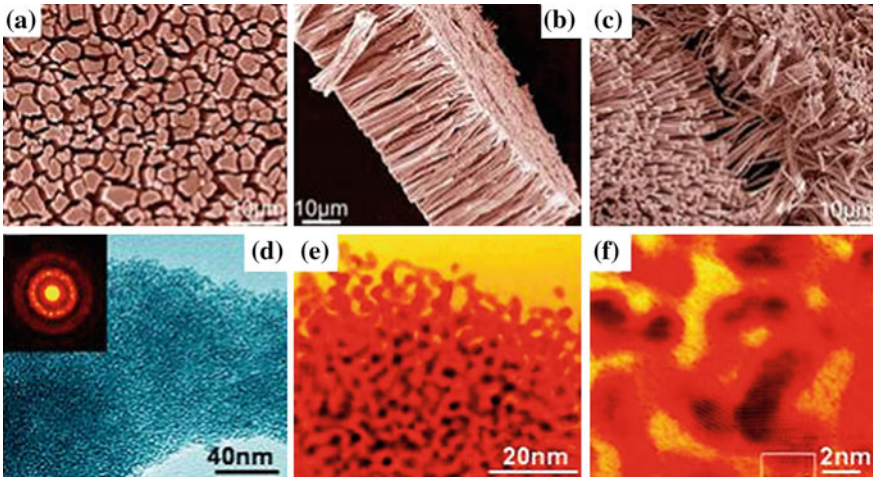

Fig. 2.15 SEM images of the dealloyed sample: **a** plane-view image, **b** section-view image, **c** image of a mildly crushed one. **d** TEM and high-angle annular bright field STEM (**e**, low magnification; **f**, high magnification) images of the np-PtCu microwires. *Inset* in part d is the corresponding SAED image. (Reproduced from Ref. [91]. Copyright 2015, American Chemical Society)

Phase Constitution The precursor alloy may be a single-phase solid solution or intermetallic phase. The single-phase structure is ideal to fabricate nanoporous metals with a homogeneous microstructure. The dealloying of a two-phase or multiphase precursor is complicated, but also provides a versatile and flexible choice to prepare nanoporous metals with multilevel and multiscale morphologies (bimodal pore size distribution [61], composite structure [62], etc.). Moreover, the two-phase microstructure is crucial to the complete dealloying of bulk precursor samples (Fig. 2.9). The two-phase precursors may be comprised of two solid solutions, or two intermetallic phases, or the combination of a solid solution with an intermetallic phase, as summarized in Fig. 2.16. Thus one can design the phase constitution of the precursors in order to obtain nanoporous metals with a desired microstructure. Of course, the scenario will be more complicated for multiphase precursor alloys.

Crystalline Nature In most cases, the precursors for dealloying are crystalline. The widely used Ag–Au alloys (for example, commercially available alloy leaves) are polycrystalline and have a grain size of up to tens of microns. The rapidly solidified Al-based alloy ribbons also have grains with the size of tens of microns [70]. In contrast, single crystalline intermetallic precursors (such as Cu_3Au, Au_3Cu, etc.) are normally adopted to probe the initial corrosion mechanisms during dealloying [30]. Due to the unique microstructure (single phase, no grain boundaries, homogeneous), amorphous alloys (also called as metallic glasses) are another type of precursors for dealloying, such as Pd-based alloys [92], Au-based alloys [92], Ti-based alloys [93], Ag-based alloys [94], and so forth. Moreover, amorphous alloys are normally multicomponent, which are also beneficial to the design and fabrication of nanoporous alloys with better electrocatalytic activities. In addition, quasicrystalline alloys can also be used as precursors for the preparation of nanoporous metallic materials by dealloying. For example, magnetic nanoporous Cu (NPC)/$(Fe,Cu)_3O_4$ composites with tunable magnetism and excellent conductivity were fabricated by dealloying of rapidly solidified Al–Cu–Fe alloys containing

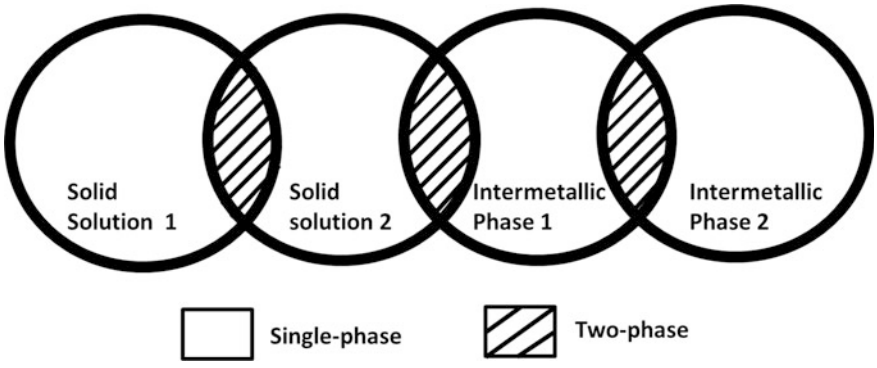

Fig. 2.16 Phase constitution of a two-phase precursor alloy

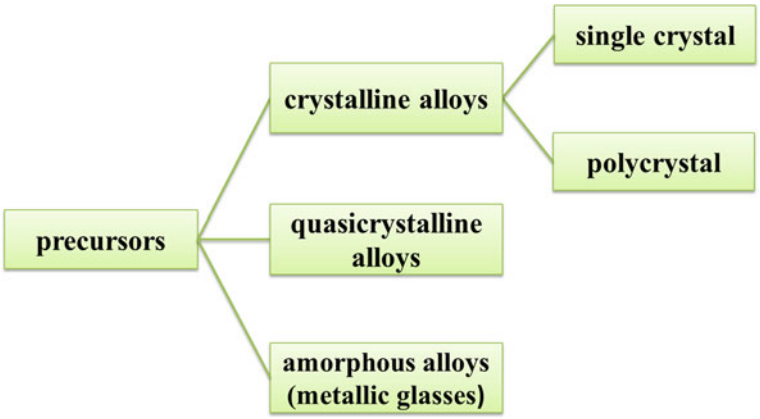

Fig. 2.17 The crystalline/quasicrystalline/amorphous nature of precursors suitable for dealloying

quasicrystalline $Al_{65}Cu_{20}Fe_{15}$ phase [95]. In addition, it has been found that lattice defects (vacancies) in the precursors also play an important role in controlling over the dealloying process and the formation of nanoporous metals [65, 96]. Figure 2.17 summarizes the crystalline/quasicrystalline/amorphous nature of precursors for dealloying.

Addition of the Third Element (Microalloying) It is well recognized that the surface diffusivity of the more noble element along the alloy/solution interface during dealloying has a significant influence on the length scale of ligaments/channels in nanoporous metals [27]. The incorporation of the third element with a lower diffusivity into the precursor alloy could markedly suppress the coarsening of ligaments/channels during dealloying. For example, the nanoporous alloy dealloyed from Ag–Au–Pt precursor has a pore size of less than 5 nm, much smaller than the characteristic length scale (normally above 15 nm) of NPG dealloyed from Ag–Au. Moreover, the addition of Pt to precursor Ag/Au alloys could stabilize the morphology of the nanoporous alloy even in harsh chemical and thermal environments [97]. It has been found that proper elemental doping has no influence on the phase constitution of rapidly solidified Al–Au–Pt, Al–Au–Pd, and Al–Au–Pt–Pd alloys, and all these precursor alloys are composed of a single Al_2Au-type intermetallic compound [Al_2(Au,Pt), Al_2(Au,Pd), and Al_2(Au,Pt,Pd)]. A certain amount of Pt and/or Pd addition exhibits a superior refining effect and the length scale of ligaments/channels in the as-obtained np–Au alloys can reach ~3 nm for the Pt doping or Pt/Pd codoping. Due to the intrinsic catalytic properties, the introduction of Pt and/or Pd into np–Au could generate novel bi/trimetallic nanoporous functionalized alloys with enhanced electrocatalytic activities [98]. Similarly, due to the intrinsic magnetism of Ni and Co, the addition of Ni and/or Co leads to the formation of novel magnetic nanoporous alloys with ultrafine ligament/channel sizes [99]. In the light of the above analysis, the incorporation of element(s) with proper amount and properties into the precursors can not only refine/stabilize the

nanoporous morphology/structure of the as-dealloyed samples, but also lead to the formation of nanoporous alloys/composites with functionalized properties.

Fabrication Methods of Precursors Melting/casting is the most used method to produce the precursor alloys, and the combination with machining/rolling could prepare the precursors with different shapes/sizes (rods, cubes, foils, films, etc.). Rapid solidification (melt spinning) can often be used to produce ribbon-like precursors with thickness of tens of microns [91]. Mechanical alloying (or high-energy ball milling) could be utilized to fabricate precursor powders with multicomponent and sizes of submicron to several microns [100]. Magnetron sputtering is a power technique to produce precursor films with diverse compositions and thicknesses. For example, W–Fe thin-film materials libraries with continuous composition and thickness spreads could be co-deposited by magnetron sputtering processes on thermally oxidized Si wafer substrates, Fig. 2.18 [101]. Electrodeposition, possibly combining with annealing treatment, can also be used to produce precursor films [102, 103]. The Gasar process (metal–gas eutectic unidirectional solidification) can be utilized to fabricate lotus-type, microporous precursor alloys, which could be further dealloyed to form a hierarchically porous structure [104]. In addition, the conventional powder metallurgy processing can also be used for preparation of precursors with regular shapes [105]. It should be noted that dewetting, the normal physical phenomenon, can be used to produce precursor alloys. For example, Nguyen et al. [106] adopted the sputtering–dewetting–dealloying strategy to fabricate site-selective high activity nanoporous Au particles on highly ordered TiO_2 nanotube arrays. Of course, nano-sized precursors (nanoparticles, nanowires, nanotubes, nanocubes, etc.) can be fabricated by versatile methods [69, 89, 107–109].

As described above, the microstructures of the precursors have an important influence on the dealloying process and the formation of nanoporous metals. When designing the precursors, we first choose the constituent elements considering the equilibrium corrosion potential (chemical/electrochemical activity) of pure metal, the parting limit, as well as the diffusivity of the more noble element. The phase

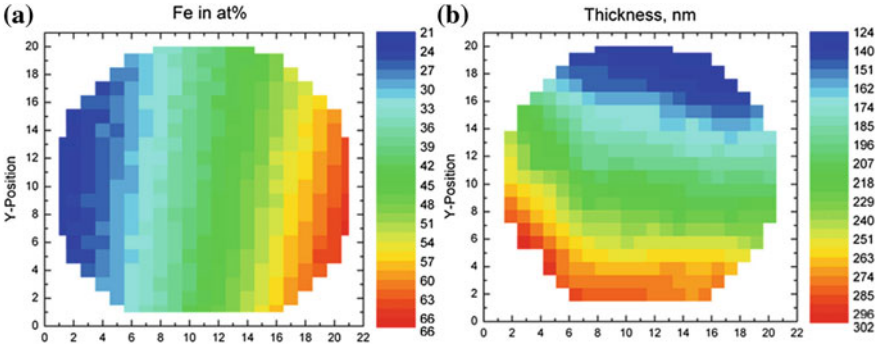

Fig. 2.18 **a** Color-coded composition map (Fe content) of the as-deposited W-Fe materials library and **b** film thickness map of the as-deposited W-Fe materials library. (Reproduced from Ref. [101]. Copyright 2012, Elsevier)

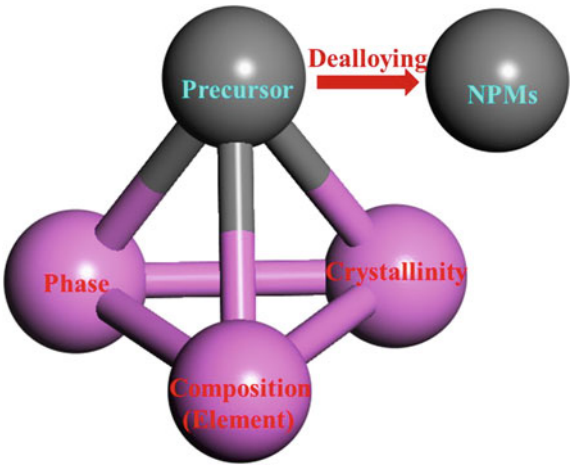

Fig. 2.19 The relationships between the composition (element), phase, and crystallinity of the precursors for dealloying. It can be designated as a novel material polyhedron of the precursor for dealloying

constitution of the precursors is another key issue, depending upon the compositions of the precursors and the processing methods. We should also control over the crystallinity (crystalline, amorphous, quasicrystalline, grain size) of the precursors. Figure 2.19 summarizes the relationships of the above factors (a novel material polyhedron of the precursor for dealloying).

2.4.2 *Control Over the Dealloying Parameters and Post-dealloying Treatment*

It is well recognized that the process parameters obviously affect the dealloying and the formation of nanoporous metals. The parameters include the dealloying solution (kind, concentration), the temperature, the applied potential, the dealloying duration, the dealloying step, and so on. In addition, the post-dealloying treatment (for example, annealing) could also modulate the microstructure/morphology of nanoporous metals. We will discuss these aspects in the following.

Chemical or Electrochemical Dealloying For some precursors like Ag–Au alloys, we can choose chemical or electrochemical dealloying. In both cases, NPG could be obtained. At the same time, the chemical or electrochemical dealloying will result in nanoporous metals with different characteristic length scales, and even with different microstructures. Xu et al. [110] adopted a modified dealloying by etching Ag/Au in concentrated nitric acid under applied anodic potential and obtained NPG with ligament sizes less than 6 nm. Under similar free corrosion conditions, dealloying Ag/Au foil requires extended time, which results in a coarsened structure with ligaments of $\sim$30 nm. Wang et al. [69] found that the electrochemical dealloying of Cu_3Pt nanoparticles led to the formation of a thin Pt skin of ca. 1 nm in thickness with an ordered Cu_3Pt core structure (core–shell), while chemical

leaching of the same precursor gave rise to a "spongy" structure (nanoporous) with no ordered structure being preserved. For Al-based precursors, chemical dealloying can be performed in acidic or alkaline media. Even in neutral electrolytes like NaCl, electrochemical dealloying of Al-based alloys could well proceed, which is important for "green" fabrication of nanoporous metals. For example, nanoporous bimetallic Pt–Au nanocomposites could be produced by chemical dealloying of rapidly solidified Al–Au–Pt precursor in HCl or NaOH [111], and electrochemical dealloying of the same precursor led to bimodal nanoporous bimetallic Pt–Au alloy in a neutral sodium chloride solution [65].

The Dealloying Solution To selectively remove the less noble element(s), we should choose the dealloying solution with proper type and concentration. For the most used Ag–Au precursors, dealloying can be carried out in several solutions, such as concentrated HNO_3, [110] $HClO_4$, [112] neutral $AgNO_3$ solution [113], etc. Snyder et al. [113]. have reported the electrochemical dealloying of silver/gold alloys in neutral pH silver nitrate solution to form NPG, and have found that a small pore ($\sim$5 nm) NPG is formed over a potential regime of 1.3–2.0 V versus normal hydrogen electrode. It is known that the adsorption of anions (such as Cl^-) in the electrolyte can accelerate surface diffusion of the more noble element and thus coarsen the ligaments/channels in the resultant nanoporous structure. Dursun et al. [114] have studied the dealloying of $Ag_{0.7}Au_{0.3}$ and $Ag_{0.65}Au_{0.35}$ alloys in 0.1 M $HClO_4$ with the addition of either 0.1 M KCl, 0.1 M KBr, or 0.1 M KI. Without the addition of halides, a pore size of approximately 8 nm is produced while 17, 16, and 67 nm is measured in the KCl, KBr and KI containing electrolytes. In addition, it has been also found that the length scale of ligaments/channels of nanoporous metals can be modulated by simply changing the dealloying solution (from HCl to NaOH) [70]. The dealloying of Al_2Au in a 20 wt% NaOH solution results in NPG with a characteristic length scale of 10–20 nm, while the dealloying in a 5 wt% HCl solution leads to the formation of coarsened nanoporous structure with ligaments/channels of 60–80 nm [70].

The Dealloying Temperature The low-temperature dealloying treatment is an effective method to tailor the characteristic length scale of nanoporous metals. The lower the dealloying temperature, the slower the surface diffusion of the more noble element(s) is during dealloying. Thus, the smaller length scale of ligaments/channels can be obtained with higher content of the residual active element. By systematically investigating the kinetics of nanopore formation during free corrosion, Qian et al. [115] have experimentally demonstrated that the dealloying process is controlled by the diffusion of gold atoms at alloy/electrolyte interfaces, which strongly relies on the reaction temperatures. Low dealloying temperatures significantly reduce the interfacial diffusivity of gold atoms and result in an ultrafine nanoporous structure with the average pore size of $\sim$7 nm. NPG with an average length scale of $\sim$5.3 nm can be obtained by dealloying the rapidly solidified Al_2Au alloy in alkaline solution at 253 K, but a longer dealloying time is needed for complete dealloying and the residual Al content is a little higher [79]. Similarly, tuning the ligament/channel size of nanoporous copper could be realized by temperature control [116]. In addition, the

high dealloying temperature would coarsen the ligaments/channels of nanoporous metals but simultaneously reduce the cracks. The addition of the third element (like Pt) with lower diffusivity could significantly suppress the temperature-induced coarsening process of ligaments/channels during dealloying [117].

The Applied Potential During electrochemical dealloying, the selection and applying method of the applied potential would have a significant influence upon the formation of nanoporous metals. Normally, to drive the selective dissolution of the less noble element as well as nanoporosity evolution, the applied potential should be higher than the critical potential but lower than the equilibrium corrosion potential of the more noble element(s). The higher the applied potential, the faster the dealloying process proceeds and the less the dealloying duration is needed. But the dealloying could be hardly controlled, and more cracks/defects will be produced in the as-dealloyed samples. Thus, for a given precursor alloy, an appropriate dealloying potential should be applied, to balance the dealloying rate and the dealloying duration. Zhong et al. [118] have found that a complete suppression of crack formation was achieved by application of a high dealloying potential of 1.1 V versus Ag/AgCl for millimeter-sized $Au_{25}Cu_{75}$ samples. NPG films ($\sim$100 nm) with an ultrafine pore size (4–8 nm) could be fabricated by pulse electrochemical dealloying of Ag–Au films, and the pore size is much smaller than NPG obtained by chemical dealloying [119]. Wang et al. [120] have demonstrated that a critical upper limit voltage exists for creating spongy electrocatalysts from Cu_3Pt ordered intermetallic nanoparticles in N_2 purged 0.1 M $HClO_4$ solution. Potential cycles from +0.05 to +1.2 V versus RHE or holding the potential at 1.0 V versus RHE for 3 h resulted in a nanoporous structure, while potential cycles from +0.05 to +1.0 V versus RHE led to the formation of core (Cu_3Pt)–shell (Pt) structure. Okman and Kysar [121] carried out a set of experiments to compare the galvanostatic and potentiostatic dealloying of Ag–Au films. The NPG film obtained by potentiostatic dealloying is severely damaged, but almost no cracks are observed for NPG obtained by galvanostatic dealloying (Fig. 2.20). Vega and Newman [117] investigated the effect of the dealloying potential on the characteristics of different nanoporous structures. The ligament size in NPG increased by reducing the overpotential (Fig. 2.21a, b), which was due to the longer time available for coarsening at a lower current density. The ligament width in NPG increased from 14 nm at 550 mV to approximately 24 nm at 500 mV. The addition of 1 at.% Pt could obviously suppress the ripening process (Fig. 2.21c, d).

The Dealloying Step (Two-Step or Multistep Dealloying) In order to modulate the microstructures/compositions/morphologies of nanoporous metals, multistep dealloying is necessary in some cases. Xu et al. [65] reported the two-step electrochemical dealloying of the rapidly solidified $Al_{75}Pt_{15}Au_{10}$ precursor composed of a single Al_2(Pt, Au) phase with lattice vacancies inside in a neutral sodium chloride solution. It has been found that the dealloying at the low potential of −0.4 V versus Ag/AgCl is associated with the partial dissolution of Al and the disappearance of the vacancies, leading to the formation of the stoichiometric Al_2(Pt, Au). The subsequent dealloying at 0.6 V versus Ag/AgCl is related to the complete

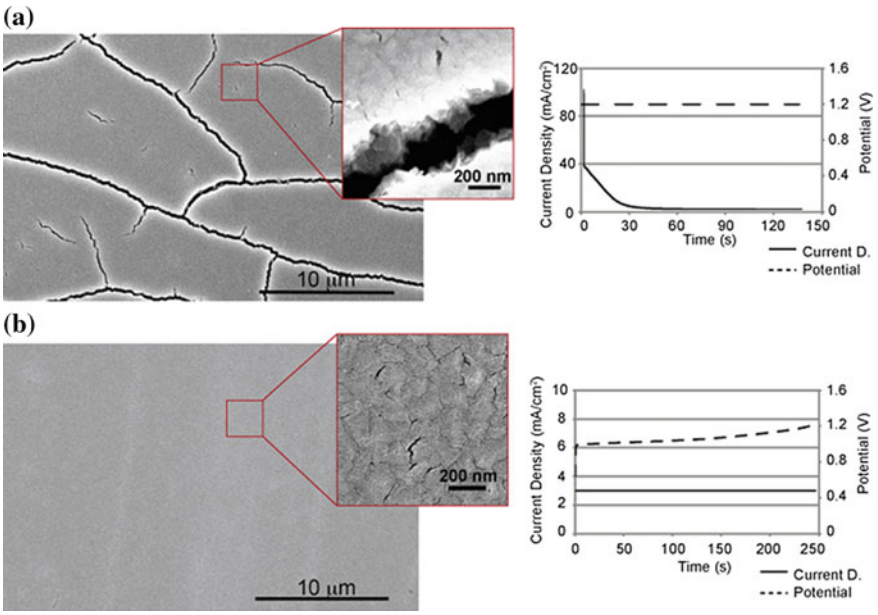

Fig. 2.20 Potential and current history and resulting NPG structure of 1300 nm NPG films from 32 at.% Au precursor alloy: **a** potentiostatic method with stepped potential; **b** galvanostatic method with constant current density of 3 mA/cm^2. (Reproduced from Ref. [121]. Copyright 2011, Elsevier)

dissolution of Al and surface diffusion of Pt/Au, resulting in the formation of the ultrafine nanoporous structure. Qi and Weissmüller [90] reported the fabrication of bulk NPG with a hierarchical microstructure by two-step electrochemical dealloying. The first-step dealloying yields nanoporous Ag–Au alloy as an intermediate product (Fig. 2.22a). After coarsening of the porous alloy to create the large ligaments of the upper hierarchy level (Fig. 2.22b), the second-step dealloying creates the fine ligaments of the lower hierarchy level (Fig. 2.22c). Moreover, the addition of 1 at.% Pt into the Ag–Au precursor could favor the formation of porous gold with a nested network architecture and ultrafine structure through the dealloying–annealing–dealloying strategy [122].

The Effect of Atmosphere on Dealloying Normally, dealloying is performed in air, without considering the influence of atmosphere. More and more investigations demonstrate that the atmosphere may have a visible effect upon the dealloying process. Gan et al. [123] reported the influence of atmosphere (air, N_2) and particle size on the chemical dealloying of $PtNi_3$ nanoparticles (Fig. 2.23). They have found that nanoporosity formation in particles larger than ca. 10 nm is intrinsically tied to a drastic dissolution of Ni when dealloying in air. In contrast, O_2-free acid leaching enabled the suppression of nanoporosity resulting in more solid core–shell particle architectures with thin Pt-enriched shells when dealloying in N_2.

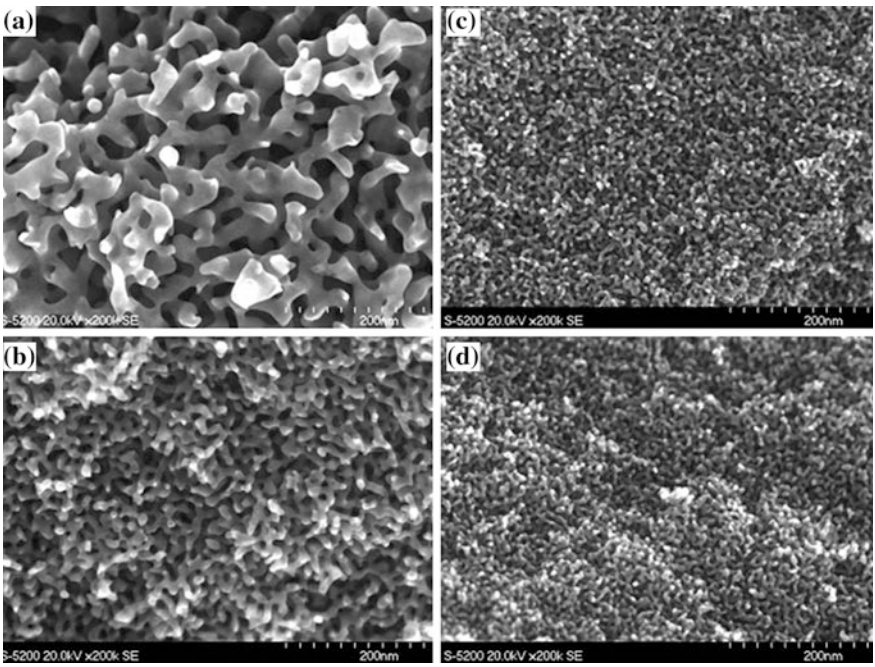

Fig. 2.21 SEM images of freshly formed nanoporous structures at different dealloying potentials: **a** $Ag_{77}Au_{23}$ at 500 mV, **b** $Ag_{77}Au_{23}$ at 550 mV, **c** $Ag_{77}Au_{22}Pt_1$ at 500 mV, **d** $Ag_{77}Au_{22}Pt_1$ at 550 mV. In all cases, the charge density passed and the dealloying temperature were 5 C cm^{-2} and 25 °C respectively. All SEM images were taken approximately in the middle of the dealloyed layer. (Reproduced from Ref. [117]. Copyright 2014, The Electrochemical Society)

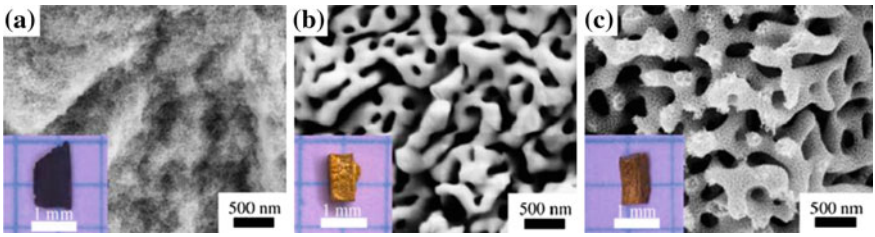

Fig. 2.22 Overview scanning electron micrographs showing microstructure evolution through the consecutive synthesis steps. **a** Fracture surface of as-dealloyed nanoporous $Au_{52}Ag_{48}$ sample after first dealloying step. **b** Fracture surface of annealed sample showing coarsened ligaments. **c** Hierarchical structure formed after second dealloying step. (Reproduced from Ref. [90]. Copyright 2013, American Chemical Society)

Dealloying in Nonaqueous Solutions In most cases, chemical or electrochemical dealloying is performed in aqueous solutions. Actually, the selection of dealloying media is quite flexible. Dealloying also occurs in organic electrolytes, metallic melts, or supercritical fluids. Chen and Sieradzki [36] examined dealloying of Li

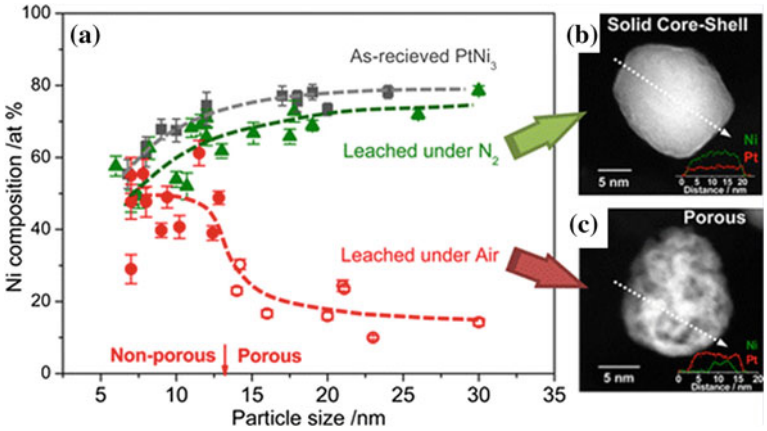

Fig. 2.23 **a** Correlations between particle size, composition, and porosity in the three catalysts. Aberration-corrected HAADF images and STEM-EELS line profiles of **b** N_2–D–$PtNi_3$ catalyst with the size of 18 nm and **c** Air-D–$PtNi_3$ catalyst with the size of 18 nm. (Reproduced from Ref. [123]. Copyright 2013, American Chemical Society)

from Li–Sn alloys in organic electrolytes and show that depending on alloy composition, particle size and dealloying rate, all known dealloyed morphologies evolve including bicontinuous nanoporous structures and hollow core–shell particles. Wada et al. [124, 125] proposed a novel dealloying method employing a metallic melt as the dealloying liquid for preparation of nanoporous metals (Ti, Fe, Cr, et al.). An atomic interaction among alloy components and metallic melt causes specific component to dissolve out from the alloy solid into the melt with self-organizing nanoporous structure by the remaining component. Morrish and Muscat [126] have demonstrated that multiphase AgCu thin films could be dealloyed using a mixture of hexafluoroacetylacetone (hfacH) and H_2O_2 dissolved in supercritical CO_2, leading to the selective dissolution of Cu.

Post-dealloying Treatment To further modulate the compositions, morphologies and microstructures of nanoporous metals, post-dealloying treatment is frequently adopted, such as annealing. As early as in 1992, Li and Sieradzki [127] reported the annealing-induced coarsening of NPG. At present, annealing is still the widely used method to coarsen the ligaments/channels of nanoporous metals to different length scales [128]. Moreover, due to the unique nanoporous structure, the coarsening of ligaments/channels is a self-similar process [129]. The annealing treatment only changes the characteristic length scale of ligaments/channels, but does not alter the topological structure of nanoporous metals. Chen-Wiegart et al. [130] studied the three-dimensional evolution of nanoligaments of NPG created by Ag–Au dealloying during isothermal coarsening by X-ray nanotomography and microbeam Laue diffraction. They have argued that the distribution of orientations for the surfaces of the nanoligaments becomes more anisotropic with coarsening time, with an increasing area of the surfaces having a low surface energy, consistent with the

growth of facets. Moreover, the curvature distribution of the nanoligaments (scaled by their size) also evolves during coarsening. The evolution of both surface orientation and scaled surface curvature indicates that coarsening does not occur in a self-similar manner. Shui et al. [131] have demonstrated that a mild dealloying treatment in acid combined with an annealing treatment could make an effective Pt-rich surface layer when only a little non-noble metal is dissolved from the alloy surface. By exposing freshly dealloyed nanostructures to surprisingly low temperatures in the presence of laboratory air, the Pt segregates to the surface of the ligaments, thanks to its preferential interaction with oxygen; in contrast, in an inert atmosphere (Ar–H_2), Pt mostly remains in the bulk of the ligaments [132].

2.4.3 *Modification of Nanoporous Metals*

To strengthen their functions and potential applications, further modification of nanoporous metallic materials is frequently applied. In this section, we will outline the strategies used to modify nanoporous metals based upon their potential applications.

Modification for Biosensors Enzymatic reactions are crucial for applications of biosensors. Immobilization of enzyme on an appropriate support is a key step for the construction of mediator-free biosensor. Due to the good electrical conductivity, high specific surface area, good biocompatibility and support-free feature, nanoporous metals (especially NPG) are promising electrode materials for immobilization of enzyme. For example, laccase is a multicopper oxidase which contains four copper ions classified into three types (T1, T2, T3) in accordance with their spectroscopic characteristics, is able to oxidize a large number of organic and inorganic substrates with concomitant reduction of molecular oxygen to water, and thus has great potential applications in the fields of biosensors and biofuel cells. Qiu et al. [133] immobilized laccase on NPG (NPG, 100 nm in thickness) for enzyme electrode construction. Direct electrochemistry of laccase on NPG supported by glassy carbon electrode (NPG/GC) was achieved with high efficiency due to the outstanding physicochemical characteristics of the NPG. The laccase-loaded NPG/GC electrode also exhibited a strong electrocatalytic activity toward O_2 reduction and excellent stability. Feng et al. [134] used nanoporous PtCo alloy as an antibody carrier for preparation of a highly sensitive immunosensor for nonenzyme detection of zeranol, Fig. 2.24. Their results show that the immunosensor exhibited a highly sensitive response to zeranol with a detection limit of 13 pg/mL, with zeranol concentration range (0.05–5.0 ng/mL). Ding et al. [135] have demonstrated that the NPG functionalized with cysteamine allows the immobilization of carbon nanotubes on the electrode with the self-assembly technique. The carboxylated carbon nanotubes are further linked with acetylcholinesterase (AChE) for amperometric sensing of pesticides. The immobilized AChE shows excellent activity to its substrate and allows a quantitative measurement of organophosphate pesticides. Hafez et al. [136] have demonstrated that the porous gold surface is more effective

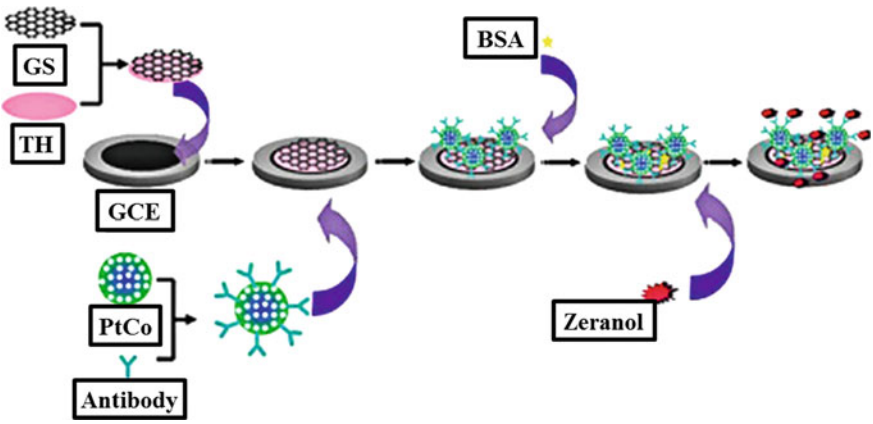

Fig. 2.24 Illustration of fabrication process of modified immunosensor. *GS* graphene sheets; *TH* thionine; *GCE* glassy carbon electrode; *BSA* bovine serum albumin. (Reproduced from Ref. [134]. Copyright 2013, Elsevier)

in adsorption of dodecanethiol as compared to the unetched gold alloy using cyclic voltammetric and time-of-flight secondary ion mass spectrometry (TOF-SIMS) analysis. Liu et al. [137] designed a novel sandwich-type electrochemical immunosensor for sensitive detection of human chorionic gonadotropin (hCG), using nanoporous Pd as a label. Shang et al. [138] fabricated a three-dimensional hybrid film with in- and out-of-plane pores by using porous graphene as framework structure and porous PdCu alloy nanoparticles as building blocks. Based on this hybrid film, they further developed an electrochemical sensor of melamine by further introducing melamine imprinted electropolymer of para-aminobenzoic acid. Yin et al. [139] recently developed all-solid-state polymeric membrane ion-selective electrodes by using a NPG film as solid contact.

Modification for Actuators Nanoporous metallic actuators have shown comparable or even better reversible strain than piezoceramics, and higher strength than conducting polymer. Until now, most attention has been paid to the electrochemical actuation behaviors of nanoporous metals (Au, Pt, Pd, Ag, Ni, etc.) and their alloys (Pt–Au, etc.) in aqueous electrolytes. When being operated in an aqueous electrolyte, however, metallic muscles made of nanoporous metals may suffer from some drawbacks. For example, an aqueous electrolyte prohibits metallic muscles from operating in dry environments and hampers a high actuation rate due to the low ionic conductivity of electrolytes. In addition, redox reactions involved in electrochemical actuation may coarsen the ligaments of nanoporous metals, leading to a substantial loss in performance of the actuator. Detsi et al. [140] reported an electrolyte-free approach to put metallic muscles to work via a metal/polymer interface. By electrochemical oxidative polymerization of aniline from an aqueous solution containing aniline monomers, a nanocoating of polyaniline doped with sulfuric acid was grown onto the ligaments of nanoporous gold (NPG/PANI),

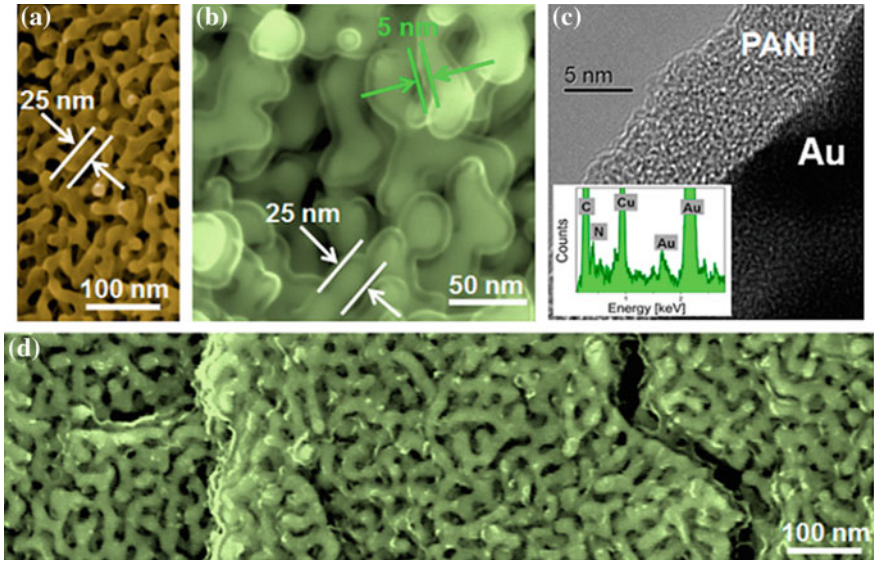

Fig. 2.25 Microstructural characterization of NPG/PANI. **a** Scanning electron micrograph showing the bicontinuous morphology of NPG. **b**, **c** Scanning and transmission electron micrographs showing a ~5 nm thick PANI skin covering the ligaments of NPG. The *Inset* of c displays the EDX spectrum of PANI. C and N come from aniline (C_6H_7N); Cu and Au come, respectively, from the Cu grid used as sample holder and the NPG. **d** Fracture cross section of NPG/PANI. It can be seen that the polymer envelope covering the ligaments is present in the bulk of the composite material. (Reproduced from Ref. [140]. Copyright 2013, American Chemical Society)

Fig. 2.25. Dopant sulfate anions coadsorbed into the polymer coating matrix were exploited to tune the nanoporous metal surface stress and subsequently generate macroscopic dimensional changes in the metal. Strain rates achieved in the single-component nanoporous metal/polymer composite actuator are 3 orders of magnitude higher than that of the standard three-component nanoporous metal/electrolyte hybrid actuator.

Modification for Photocatalysis Photocatalysts have attracted much attention in recent years because they allow highly efficient eco-friendly removal of organic pollutants present in our environment. Among various photocatalytic materials, considerable efforts were focused on the development of visible-light photocatalysts in order to obtain high sun light utilization efficiency. Li and Ding [141] fabricated porous AgCl/Ag nanocomposites with a facile two-step route, which involves the formation of nanoporous silver (NPS) by dealloying AgAl alloys, and a subsequent surface chlorination in a mixed solution containing H_2O_2 and HCl. It was found that porous AgCl/Ag nanocomposites performed very well as efficient and stable visible-light catalysts for the degradation of methylic orange (MO) dye. Yan et al. [142] synthesized porous AgBr@Ag and AgBrI@Ag plasmonic photocatalysts by a multistep route, including a dealloying method to prepare porous Ag, a transformation from Ag to AgBr and AgBrI, and a photoreduction process to form Ag

nanoparticles on the surface of AgBr and AgBrI. Both porous AgBr@Ag and porous AgBrI@Ag showed much higher visible-light photocatalytic activity than cubic AgBr@Ag for the degradation of methyl orange.

Modification for Surface-Enhanced Raman Scattering (SERS) SERS originates from the improved inelastic scattering of the molecules adsorbed on nanostructured metals and alloys. SERS probes bond vibrations of molecules in the proximity of metallic nanostructures. This technique has regained considerable interest stimulated by an explosive development of nanotechnology and superior sensitivity of SERS, in some cases possibly approaching the single molecule detection limit. Although NPG shows good SERS effect [143], the SERS effect could be further enhanced by modification of nanoporous metals. Qian et al. [144] employed a two-step method to create hot spots within hybrid nanostructures, which consist of self-supported NPG films with the absorbed probes and subsequent nanoparticle conjugates without surface agents or mechanical motion, Fig. 2.26. The molecules confined into 1 nm interstice exhibit 2.9×10^7 times enhancement in Raman scattering compared to pure NPG, offering an opportunity to track spatial orientation of single molecule. Zeng et al. [145] have shown that plasmonic resonance can be significantly redshifted by up to 258 nm by the surface modification, which involves the loading of small gold nanoparticles into the pores of NPG disk. In addition, Qian et al. [146] fabricated NPG–alumina core–shell films with fixed gold skeletons and different thicknesses of alumina shells using chemical corrosion and subsequent atomic layer deposition (ALD). A 92 nm redshift of the localized surface plasmon resonance (LSPR) band is attained via its dielectric medium dependence and the comparable decay length with pore size.

Modification for Water Splitting It is known that efficient production of chemical fuels through solar energy is an attractive option to address the global energy challenge. Photoelectrochemical (PEC) water splitting using sunlight offers a promising solution for renewable and clean energy systems. Bak et al. [147] fabricated

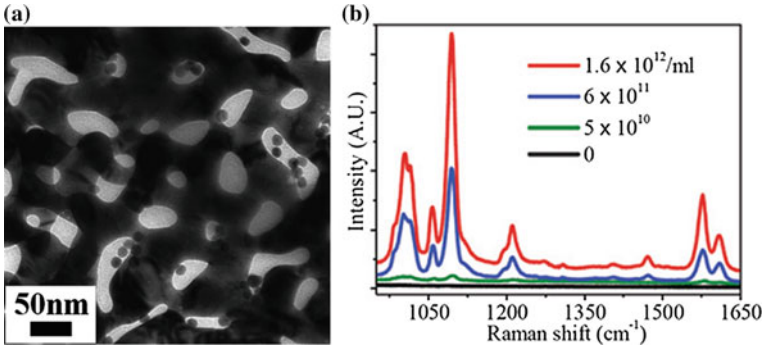

Fig. 2.26 **a** Low magnification TEM image of pure NPG–nanoparticle conjugates by immersing NPG film into gold colloids with 1.6×10^{12}/ml. **b** Typical SERS spectra on pure NPG film and NPG–nanoparticle conjugates. (Reproduced from Ref. [144]. Copyright 2010, The Royal Society of Chemistry)

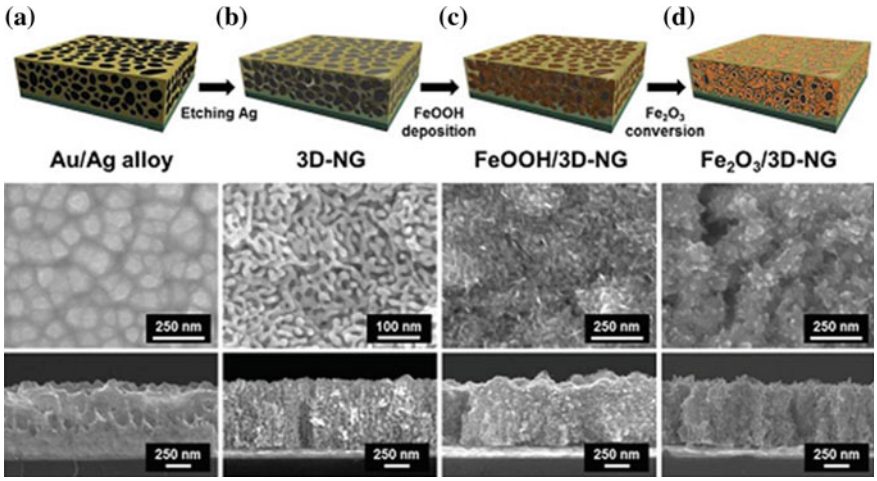

Fig. 2.27 Schematic illustration, top and cross-sectional SEM images of each structure during the fabrication process for 3D α-Fe_2O_3/NG electrodes. **a** $Au_{25}Ag_{75}$ alloy, **b** dealloyed 3D-NG film, **c** β-FeOOH/3D-NG, and **d** α-Fe_2O_3/3D-NG film after annealing. (Reproduced from Ref. [147]. Copyright 2014, The Royal Society of Chemistry)

3D-nanostructured α-Fe_2O_3/nanoporous gold (NG) electrodes in three subsequent procedures, dealloying Au/Ag to produce a conductive 3D-NG electrode, decorating nanocrystalline β-FeOOH onto the nanopores of 3D-NG via a hydrothermal method, and converting β-FeOOH into α-Fe_2O_3, Fig. 2.27. Great enhancement in photoelectrochemical water splitting efficiency could be achieved in hematite assisted by fast and easy transfer of electrons/holes via the 3D-NG electrode. The α-Fe_2O_3/3D-NG electrode exhibits a maximum photocurrent density of 1.6 mA cm^{-2} at 1.5 V versus RHE under AM 1.5 G simulated sunlight illumination via a photocatalytic hydrogen generation reaction, which is two times greater than that of the unmodified α-Fe_2O_3 photoanode.

Modification for Fuel Cells The electrocatalytic activity of nanoporous metals can be further enhanced by surface modification or hybridization at both the anode and the cathode. Wang et al. [148] reported the fabrication of an ultralow-platinum-loading high-performance nanoporous electrocatalyst with nanoengineered surface structures for electrooxidation of formic acid, by means of a well-known Cu underpotential deposition (UPD) mediated process. Monolayer Pt is first deposited onto the ligament surfaces of NPG by in situ redox replacement of $PtCl_4^{-2}$ with monolayer Cu deposited by UPD. Then, an adequate amount of Au is deposited onto the Pt overlayer using the same method, where the amount of deposited Au could be effectively controlled by holding at a specific potential during the Cu UPD process or by repeating Cu UPD and Au replacement cycles. Wang et al. [149] further reported a new type of anode constructed by confining highly active nanoengineered catalysts into an ultrathin catalyst layer with thickness around 100 nm. Specifically, an atomic layer of platinum is first deposited onto NPG leaf to achieve high utilization of Pt and easy accessibility

of both reactants and electrons to active sites. These NPG–Pt core/shell nanostructures are further decorated by a sub-monolayer of Bi to create highly active reaction sites for formic acid electrooxidation. Snyder et al. [150] incorporated a hydrophobic, protic ionic liquid, [MTBD][beti], into the pores of high-surface-area NiPt alloy nanoporous nanoparticles (np-NiPt/C + [MTBD][beti]), and the hybrid materials show enhanced oxygen reduction reaction (ORR) performance. Ke et al. [151] reported Pd-decorated three-dimensional nanoporous Au/Ni foam composite electrodes for H_2O_2 reduction. Here we just show several examples, and the detailed information on modification of nanoporous metals for fuel cells applications will be presented in Chap. 3.

Modification for Supercapacitors It is known that both transition metal oxides and conducting polymers are promising electrode materials for supercapacitors. Transition metal oxides normally suffer from poor electrical conductivity and show limited cycling performance, despite their high theoretical specific capacitance. The optimization of supercapacitor performance, i.e., high power and energy densities, relies on the simultaneous realization of several key structural parameters such as the amount of each individual electrode component, open accessibility by the electrolyte, and the interfacial structure between the electrochemically active material and current collector. Due to the three-dimensional bicontinuous porous structure, good electrical conductivity, and high specific surface areas, nanoporous metals are promising substrates for constructing hybrid electrodes, simultaneously serving as the current collector. Here we just show two examples for these aspects, and the detailed information will be given in Chap. 4. Meng and Ding [152] constructed sub-micrometer-thick all-solid-state supercapacitors with high power and energy densities from polypyrrole (PPy)-decorated NPG. Lang et al. [153] have demonstrated that hybrid structures made of NPG and nanocrystalline MnO_2 have enhanced conductivity, resulting in a specific capacitance of the constituent MnO_2 (~1,145 F g^{-1}) that is close to the theoretical value.

Modification for Lithium Batteries Similarly, active materials can be decorated onto the ligament surface of nanoporous metals for lithium batteries. We know that tin could be used as alternative anode electrodes for lithium ion batteries (LIBs), due to its high electronic conductivity and high theoretical capacity (990 mAh g^{-1} for $Li_{4.4}Sn$, about three times higher than that of graphitic carbon, 372 mAh g_{-1} for LiC_6). However, implementation of metallic tin to LIBs is greatly hampered by its poor cyclability, which can be attributed mainly to pulverization, aggregation, and loss of electrical contact at the electrode, with all of these resulting from the substantial volume changes (over 200 %) during charging and discharging. Yu et al. [154] reported a 3D nanoporous metal-supported nanocrystalline thin tin foil as an alternative anode for rechargeable LIBs with improved electrochemical performance. Zhang et al. [155] have also shown the potential of nanoporous copper as a substrate/collector to deposit a thin tin layer for LIBs. For applications in lithium batteries, the detailed information will be shown in Chap. 5.

2.5 Summary and Conclusions

In summary, we mainly discuss the formation mechanisms, microstructural characterization, and microstructural regulation of dealloying-driven nanoporous metals in this chapter. Although dealloying has a long history, it got renewed attention as novel nanostructured materials for functional applications just at the beginning of this century. Dealloying is a common corrosion process, but involves complex physical and chemical/electrochemical reactions at the alloy/solution interface. Several mechanisms have been proposed to rationalize the formation of nanoporous structures during dealloying, and the main concerns are correlated with the selective dissolution of the less noble element(s) and surface diffusion of the more noble element(s). More in situ/ex situ experiments as well as computer simulations should be explored to further clarify the underlying dealloying mechanisms. Many techniques can be adopted to characterize the microstructures (also compositions and morphologies) of nanoporous metals, and the characteristic length scale and specific surface area are two important issues. The combination of scanning TEM with energy dispersive X-ray analysis can well reveal the morphologies and compositional distribution at the nanoscale and even atomic resolution. And three-dimensional tomographic reconstruction is also powerful to reveal the interior microstructures of nanoporous metals. In the last section of this chapter, we discuss the strategies to regulate the microstructures of nanoporous metals, from three aspects: design of precursors for dealloying, control over the dealloying parameters and post-dealloying treatment, and further modification of nanoporous metals to strengthen their functional applications.

References

1. Erlebacher J, Aziz MJ, Karma A, Dimitrov N, Sieradzki K (2001) Evolution of nanoporosity in dealloying. Nature 410(6827):450–453
2. Forty A (1979) Corrosion micromorphology of noble metal alloys and depletion gilding. Nature 282:597–598
3. Raney M (1925) Method of preparing catalytic material. US Patent 1,563,587
4. Raney M (1940) Catalysts from alloys. Ind Eng Chem 32(9):1199–1203
5. Huber GW, Shabaker J, Dumesic J (2003) Raney Ni–Sn catalyst for H_2 production from biomass-derived hydrocarbons. Science 300(5628):2075–2077
6. Parthasarathi A, Polan NW (1982) Stress corrosion of Cu–Zn and Cu–Zn–Ni alloys: the role of dealloying. Metall Trans A 13(11):2027–2033
7. Pryor M, Giam KK (1982) The effect of arsenic on the dealloying of α-brass. J Electrochem Soc 129(10):2157–2163
8. Cassagne T, Flanagan W, Lichter B (1986) On the failure mechanism of chemically embrittled Cu_3Au single crystals. Metall Trans A 17(4):703–710
9. Sieradzki K, Kim J, Cole A, Newman R (1987) The relationship between dealloying and transgranular stress-corrosion cracking of Cu–Zn and Cu–Al Alloys. J Electrochem Soc 134(7):1635–1639

10. Getsov L, Rybnikov A, Pogrebnyak A, Bavel'skii D (1989) Effect of surface dealloying on the endurance of heat-resistant alloys. Strength Mater 21(2):170–174
11. Buchheit R, Grant R, Hlava P, McKenzie B, Zender G (1997) Local dissolution phenomena associated with S phase (Al_2CuMg) particles in aluminum alloy 2024-T3. J Electrochem Soc 144(8):2621–2628
12. Guillaumin V, Mankowski G (1998) Localized corrosion of 2024 T351 aluminium alloy in chloride media. Corros Sci 41(3):421–438
13. Dimitrov N, Mann J, Vukmirovic M, Sieradzki K (2000) Dealloying of Al_2CuMg in alkaline media. J Electrochem Soc 147(9):3283–3285
14. Pickering H, Swann P (1963) Electron metallography of chemical attack upon some alloys susceptible to stress corrosion cracking. Corrosion 19(11):373t–389t
15. Keir D, Pryor M (1980) The dealloying of copper–manganese alloys. J Electrochem Soc 127 (10):2138–2144
16. Oppenheim IC, Trevor DJ, Chidsey CE, Trevor PL, Sieradzki K (1991) In situ scanning tunneling microscopy of corrosion of silver–gold alloys. Science 254(5032):687–689
17. Pickering H, Wagner C (1967) Electrolytic dissolution of binary alloys containing a noble metal. J Electrochem Soc 114(7):698–706
18. Swann P (1969) Mechanism of corrosion tunnelling with special reference to Cu_3Au. Corrosion 25(4):147–150
19. Forty A, Durkin P (1980) A micromorphological study of the dissolution of silver-gold alloys in nitric acid. Philos Mag A 42(3):295–318
20. Forty A, Rowlands G (1981) A possible model for corrosion pitting and tunneling in noble-metal alloys. Philos Mag A 43(1):171–188
21. Pryor M, Fister J (1984) The mechanism of dealloying of copper solid solutions and intermetallic phases. J Electrochem Soc 131(6):1230–1235
22. Kaesche H (1988) Microtunnelling during selective alloy dissolution and during pitting. Mater Corros 39(4):153–161
23. Sieradzki K, Corderman R, Shukla K, Newman R (1989) Computer simulations of corrosion: selective dissolution of binary alloys. Philos Mag A 59(4):713–746
24. Moffat TP, Fan FRF, Bard AJ (1991) Electrochemical and scanning tunneling microscopic study of dealloying of Cu_3Au. J Electrochem Soc 138(11):3224–3235
25. Sieradzki K (1993) Curvature effects in alloy dissolution. J Electrochem Soc 140(10): 2868–2872
26. Smith A, Tran T, Wainwright M (1999) Kinetics and mechanism of the preparation of Raney® copper. J Appl Electrochem 29(9):1085–1094
27. Erlebacher J (2004) An atomistic description of dealloying. J Electrochem Soc 151(10):C614
28. Wagner K, Brankovic S, Dimitrov N, Sieradzki K (1997) Dealloying below the critical potential. J Electrochem Soc 144(10):3545–3555
29. Dursun A, Pugh DV, Corcoran SG (2005) Probing the dealloying critical potential. J Electrochem Soc 152(2):B65
30. Renner F, Stierle A, Dosch H, Kolb D, Lee T-L, Zegenhagen J (2006) Initial corrosion observed on the atomic scale. Nature 439(7077):707–710
31. Pareek A, Borodin S, Bashir A, Ankah GN, Keil P, Eckstein GA et al (2011) Initiation and inhibition of dealloying of single crystalline Cu_3Au (111) surfaces. J Am Chem Soc 133(45):18264–18271
32. Ankah GN, Meimandi S, Renner FU (2013) Dealloying of Cu_3Pd single crystal surfaces. J Electrochem Soc 160(8):C390–C395
33. Kamundi M, Bromberg L, Fey E, Mitchell C, Fayette M, Dimitrov N (2012) Impact of structure and composition on the dealloying of AuxAg(1–x)alloys on the nanoscale. J Phys Chem C 116(26):14123–14133
34. Oezaslan M, Heggen M, Strasser P (2012) Size-dependent morphology of dealloyed bimetallic catalysts: linking the nano to the macro scale. J Am Chem Soc 134(1):514–524

35. Callejas-Tovar R, Diaz CA, de la Hoz JMM, Balbuena PB (2013) Dealloying of platinum-based alloy catalysts: kinetic Monte Carlo simulations. Electrochim Acta 101:326–333
36. Chen Q, Sieradzki K (2013) Spontaneous evolution of bicontinuous nanostructures in dealloyed Li-based systems. Nat Mater 12(12):1102–1106
37. Cui C, Gan L, Heggen M, Rudi S, Strasser P (2013) Compositional segregation in shaped Pt alloy nanoparticles and their structural behaviour during electrocatalysis. Nat Mater 12(8):765–771
38. Li X, Chen Q, McCue I, Snyder J, Crozier P, Erlebacher J et al (2014) Dealloying of noble-metal alloy nanoparticles. Nano Lett 14(5):2569–2577
39. Rudi S, Gan L, Cui C, Gliech M, Strasser P (2015) Electrochemical dealloying of bimetallic ORR nanoparticle catalysts at constant electrode potentials. J Electrochem Soc 162(4):F403–F409
40. Han B, Carlton C, Kongkanand A, Kukreja R, Theobald B, Gan L, et al (2015) Record activity and stability of dealloyed bimetallic catalysts for proton exchange membrane fuel cells. Energy Environ Sci 8(1):258–266
41. Petegem SV, Brandstetter S, Maass R, Hodge AM, El-Dasher BS, Jr Biener et al (2009) On the microstructure of nanoporous gold: an x-ray diffraction study. Nano Lett 9(3):1158–1163
42. Dotzler CJ, Ingham B, Illy BN, Wallwork K, Ryan MP, Toney MF (2011) In situ observation of strain development and porosity evolution in nanoporous gold foils. Adv Funct Mater 21(20):3938–3946
43. Galinski H, Ryll T, Schlagenhauf L, Rechberger F, Ying S, Gauckler LJ et al (2011) Dealloying of platinum-aluminum thin films: dynamics of pattern formation. Phys Rev Lett 107(22)
44. Ye X-L, Lu N, Li X-J, Du K, Tan J, Jin H-J (2014) Primary and secondary dealloying of Au (Pt)-Ag: structural and compositional evolutions, and volume shrinkage. J Electrochem Soc 161(12):C517–C526
45. Chen-Wiegart Y-cK, Wang S, Lee W-K, McNulty I, Voorhees PW, Dunand DC (2013) In situ imaging of dealloying during nanoporous gold formation by transmission X-ray microscopy. Acta Mater 61(4):1118–1125
46. Chen-Wiegart Y-cK, Wang S, McNulty I, Dunand DC (2013) Effect of Ag–Au composition and acid concentration on dealloying front velocity and cracking during nanoporous gold formation. Acta Mater 61(15):5561–5570
47. Sethuraman VA, Vairavapandian D, Lafouresse MC, Maark TA, Karan N, Sun S et al (2015) Role of elastic strain on electrocatalysis of oxygen reduction reaction on Pt. J Phys Chem C 119(33):19042–19052
48. Martin H, Carro P, Hernández Creus A, Morales J, Fernandez G, Esparza P et al (2000) Interplay of surface diffusion and surface tension in the evolution of solid/liquid interfaces. Dealloying of β-brass in aqueous sodium chloride. J Phys Chem B 104(34):8229–8237
49. Zhang Q, Zhang Z (2010) On the electrochemical dealloying of Al-based alloys in a NaCl aqueous solution. Phys Chem Chem Phys 12(7):1453–1472
50. Ji H, Frenzel J, Qi Z, Wang X, Zhao C, Zhang Z et al (2010) An ultrafine nanoporous bimetallic Ag–Pd alloy with superior catalytic activity. CrystEngComm 12(12):4059
51. Starr CA, Buttry DA (2014) Electrochemical dealloying of gold–silver nanoparticles—selective dissolution of the less and more noble species. In: Leonte OM, Mustain WE (eds) Nanotechnology. ECS transactions 582014. pp 19–26
52. Chen T, Liu Z, Lu W, Zhou X, Ma H (2011) Fabrication of free-standing nanoporous silver by selectively dissolving gold from gold–silver alloys via a novel converse dealloying method. Electrochem Commun 13(10):1086–1089
53. Zhang Q, Wang X, Qi Z, Wang Y, Zhang Z (2009) A benign route to fabricate nanoporous gold through electrochemical dealloying of Al–Au alloys in a neutral solution. Electrochim Acta 54(26):6190–6198
54. Zhao C, Wang X, Qi Z, Ji H, Zhang Z (2010) On the electrochemical dealloying of Mg–Cu alloys in a NaCl aqueous solution. Corros Sci 52(12):3962–3972

55. Hakamada M, Mabuchi M (2006) Nanoporous gold prism microassembly through a self-organizing route. Nano Lett 6(4):882–885
56. Renner FU, Eckstein GA, Lymperakis L, Dakkouri-Baldauf A, Rohwerder M, Neugebauer J et al (2011) In situ scanning tunneling microscopy study of selective dissolution of Au_3Cu and Cu_3Au (001). Electrochim Acta 56(4):1694–1700
57. Zhang Z, Zhang C, Sun J, Kou T (2012) Influence of anion species on electrochemical dealloying of single-phase Al_2Au alloy in sodium halide solutions. RSC Adv 2(10):4481
58. Xu J, Wang Y, Zhang Z (2012) Potential and concentration dependent electrochemical dealloying of Al_2Au in sodium chloride solutions. J Phys Chem C 116(9):5689–5699
59. Ankah GN, Pareek A, Cherevko S, Topalov AA, Rohwerder M, Renner FU (2012) The influence of halides on the initial selective dissolution of Cu_3Au (111). Electrochim Acta 85:384–392
60. Pugh D, Dursun A, Corcoran S (2003) Formation of nanoporous platinum by selective dissolution of Cu from Cu 0.75 Pt 0.25. J Mater Res 18(01):216–221
61. Zhang Z, Wang Y, Qi Z, Lin J, Bian X (2009) Nanoporous gold ribbons with bimodal channel size distributions by chemical dealloying of Al–Au Alloys. J Phys Chem C 113(4):1308–1314
62. Zhang Z, Wang Y, Qi Z, Somsen C, Wang X, Zhao C (2009) Fabrication and characterization of nanoporous gold composites through chemical dealloying of two phase Al–Au alloys. J Mater Chem 19(33):6042
63. Qi Z, Zhao C, Wang X, Lin J, Shao W, Zhang Z et al (2009) Formation and characterization of monolithic nanoporous copper by chemical dealloying of Al–Cu alloys. J Phys Chem C 113(16):6694–6698
64. Zhao C, Qi Z, Wang X, Zhang Z (2009) Fabrication and characterization of monolithic nanoporous copper through chemical dealloying of Mg–Cu alloys. Corros Sci 51(9): 2120–2125
65. Xu J, Zhang C, Wang X, Ji H, Zhao C, Wang Y et al (2011) Fabrication of bi-modal nanoporous bimetallic Pt–Au alloy with excellent electrocatalytic performance towards formic acid oxidation. Green Chem 13(7):1914
66. Wang X, Qi Z, Zhao C, Wang W, Zhang Z (2009) Influence of alloy composition and dealloying solution on the formation and microstructure of monolithic nanoporous silver through chemical dealloying of Al–Ag alloys. J Phys Chem C 113(30):13139–13150
67. Wang X, Wang W, Qi Z, Zhao C, Ji H, Zhang Z (2010) Fabrication, microstructure and electrocatalytic property of novel nanoporous palladium composites. J Alloy Compd 508 (2):463–470
68. Liu Y, Bliznakov S, Dimitrov N (2010) Factors controlling the less noble metal retention in nanoporous structures processed by electrochemical dealloying. J Electrochem Soc 157(8): K168
69. Wang D, Yu Y, Xin HL, Hovden R, Ercius P, Mundy JA et al (2012) Tuning oxygen reduction reaction activity via controllable dealloying: a model study of ordered Cu_3Pt/C intermetallic nanocatalysts. Nano Lett 12(10):5230–5238
70. Zhang Z, Wang Y, Qi Z, Zhang W, Qin J, Frenzel J (2009) Generalized fabrication of nanoporous metals (Au, Pd, Pt, Ag, and Cu) through chemical dealloying. J Phys Chem C 113(29):12629–12636
71. Kim S, Chen YK, Putkunz CT, Dunand DC, McNulty I, McNulty I et al (2011) Use of justified constraints in coherent diffractive imaging. AIP Conf. Proc. 1365:441–444
72. Fujita T, Qian L-H, Inoke K, Erlebacher J, Chen M-W (2008) Three-dimensional morphology of nanoporous gold. Appl Phys Lett 92(25):251902
73. Ding Y, Kim YJ, Erlebacher J (2004) Nanoporous gold leaf:"ancient technology"/advanced material. Adv Mater 16(21):1897–1900
74. Fujita T, Guan P, McKenna K, Lang X, Hirata A, Zhang L et al (2012) Atomic origins of the high catalytic activity of nanoporous gold. Nat Mater 11(9):775–780

75. Rösner H, Parida S, Kramer D, Volkert C, Weissmüller J (2007) Reconstructing a nanoporous metal in three dimensions: an electron tomography study of dealloyed gold leaf. Adv Eng Mater 9(7):535–541
76. Hovden R, Ercius P, Jiang Y, Wang D, Yu Y, Abruna HD et al (2014) Breaking the crowther limit: combining depth-sectioning and tilt tomography for high-resolution, wide-field 3D reconstructions. Ultramicroscopy 140:26–31
77. Corcoran SG (ed) (1999) The morphology of alloy corrosion. In: Proceedings of the symposium on critical factors in localized corrosion III; Citeseer
78. Erlebacher J, McCue I (2012) Geometric characterization of nanoporous metals. Acta Mater 60(17):6164–6174
79. Zhang Z, Wang Y, Wang Y, Wang X, Qi Z, Ji H et al (2010) Formation of ultrafine nanoporous gold related to surface diffusion of gold adatoms during dealloying of Al_2Au in an alkaline solution. Scripta Mater 62(3):137–140
80. Ji C, Searson PC (2003) Synthesis and characterization of nanoporous gold nanowires. J Phys Chem B 107(19):4494–4499
81. Trasatti S, Petrii O (1991) Real surface area measurements in electrochemistry. Pure Appl Chem 63(5):711–734
82. Liu Y, Bliznakov S, Dimitrov N (2009) Comprehensive study of the application of a pb underpotential deposition-assisted method for surface area measurement of metallic nanoporous materials. J Phys Chem C 113(28):12362–12372
83. Rouya E, Cattarin S, Reed M, Kelly R, Zangari G (2012) Electrochemical characterization of the surface area of nanoporous gold films. J Electrochem Soc 159(4):K97–K102
84. Wang X, Wang W, Qi Z, Zhao C, Ji H, Zhang Z (2012) Novel Raney-like nanoporous Pd catalyst with superior electrocatalytic activity towards ethanol electro-oxidation. Int J Hydrogen Energy 37(3):2579–2587
85. Yeh F-H, Tai CC, Huang J-F, Sun I-W (2006) Formation of porous silver by electrochemical alloying/dealloying in a water-insensitive zinc chloride-1-ethyl-3-methyl imidazolium chloride ionic liquid. J Phys Chem B 110:5215–5222
86. Lei W, Briot NJ, Swartzentruber PD, Balk TJ (2014) Magnesium alloy precursor thin films for efficient, practical fabrication of nanoporous metals. Metall Mater Trans A 45(1):1–5
87. Hayes J, Hodge A, Biener J, Hamza A, Sieradzki K (2006) Monolithic nanoporous copper by dealloying Mn–Cu. J Mater Res 21(10):2611–2616
88. Chen LY, Chen N, Hou Y, Wang ZC, Lv SH, Fujita T et al (2013) Geometrically controlled nanoporous PdAu bimetallic catalysts with tunable Pd/Au ratio for direct ethanol fuel cells. ACS Catal 3(6):1220–1230
89. Liu L, Pippel E, Scholz R, Gösele U (2009) Nanoporous Pt–Co alloy nanowires: fabrication, characterization, and electrocatalytic properties. Nano Lett 9(12):4352–4358
90. Qi Z, Weissmüller Jr (2013) Hierarchical nested-network nanostructure by dealloying. ACS Nano 7(7):5948–5954
91. Qiu HJ, Shen X, Wang JQ, Hirata A, Fujita T, Wang Y et al (2015) Aligned nanoporous Pt–Cu bimetallic microwires with high catalytic activity toward methanol electrooxidation. ACS Catal 5(6):3779–3785
92. Yu J, Ding Y, Xu C, Inoue A, Sakurai T, Chen M (2008) Nanoporous metals by dealloying multicomponent metallic glasses. Chem Mater 20(14):4548–4550
93. Dan Z, Qin F, Sugawara Y, Muto I, Hara N (2012) Fabrication of ultrafine nanoporous copper by the minor addition of gold. Mater Trans 53(10):1765–1769
94. Li R, Liu XJ, Wang H, Wu Y, Chu XM, Lu ZP (2014) Nanoporous silver with tunable pore characteristics and superior surface enhanced Raman scattering. Corros Sci 84:159–164
95. Qi Z, Gong Y, Zhang C, Xu J, Wang X, Zhao C et al (2011) Fabrication and characterization of magnetic nanoporous Cu/(Fe, Cu)$3O_4$ composites with excellent electrical conductivity by one-step dealloying. J Mater Chem 21(26):9716
96. Ji H, Zhang C, Xu J, Zhao C, Wang X, Zhang Z (2011) On the vacancy-controlled dealloying of rapidly solidified Mg–Ag alloys. CrystEngComm 13(15):4846

97. Snyder J, Asanithi P, Dalton AB, Erlebacher J (2008) Stabilized nanoporous metals by dealloying ternary alloy precursors. Adv Mater 20(24):4883–4886
98. Wang X, Frenzel J, Wang W, Ji H, Qi Z, Zhang Z et al (2011) Length-scale modulated and electrocatalytic activity enhanced nanoporous gold by doping. J Phys Chem C 115(11):4456–4465
99. Zhang Z, Zhang C, Gao Y, Frenzel J, Sun J, Eggeler G (2012) Dealloying strategy to fabricate ultrafine nanoporous gold-based alloys with high structural stability and tunable magnetic properties. CrystEngComm 14(23):8292
100. Chen X, Jiang Y, Sun J, Jin C, Zhang Z (2014) Highly active nanoporous Pt-based alloy as anode and cathode catalyst for direct methanol fuel cells. J Power Sour 267:212–218
101. Stepanovich A, Sliozberg K, Schuhmann W, Ludwig A (2012) Combinatorial development of nanoporous WO3 thin film photoelectrodes for solar water splitting by dealloying of binary alloys. Int J Hydrogen Energy 37(16):11618–11624
102. Jia F, Yu C, Zhang L (2009) Hierarchical nanoporous gold film electrode with extra high surface area and electrochemical activity. Electrochem Commun 11(10):1944–1946
103. Cherevko S, Kulyk N, Chung CH (2012) Pulse-reverse electrodeposition for mesoporous metal films: combination of hydrogen evolution assisted deposition and electrochemical dealloying. Nanoscale 4(2):568–575
104. Zhang X, Li Y, Liu Y, Zhang H (2013) Fabrication of a bimodal micro/nanoporous metal by the Gasar and dealloying processes. Mater Lett 92:448–451
105. Hyungyung J, Yong-Hun C, Myounggeun C, Jinhan C, Ji Hyun U, Yung-Eun S et al (2014) Novel method of powder-based processing of copper nanofoams for their potential use in energy applications. Mater Chem Phys 145(1–2):6–11
106. Nguyen NT, Altomare M, Yoo J, Schmuki P (2015) Efficient photocatalytic H-2 evolution: controlled dewetting-dealloying to fabricate site-selective high-activity nanoporous Au particles on highly ordered TiO_2 nanotube arrays. Adv Mater 27(20):3208–3215
107. Gu X, Xu L, Tian F, Ding Y (2009) Au–Ag alloy nanoporous nanotubes. Nano Res 2(5):386–393
108. Strasser P, Koh S, Anniyev T, Greeley J, More K, Yu C et al (2010) Lattice-strain control of the activity in dealloyed core–shell fuel cell catalysts. Nat Chem 2(6):454–460
109. Snyder J, McCue I, Livi K, Erlebacher J (2012) Structure/processing/properties relationships in nanoporous nanoparticles as applied to catalysis of the cathodic oxygen reduction reaction. J Am Chem Soc 134(20):8633–8645
110. Xu C, Su J, Xu X, Liu P, Zhao H, Tian F et al (2007) Low temperature CO oxidation over unsupported nanoporous gold. J Am Chem Soc 129(1):42–43
111. Zhang Z, Wang Y, Wang X (2011) Nanoporous bimetallic Pt–Au alloy nanocomposites with superior catalytic activity towards electro-oxidation of methanol and formic acid. Nanoscale 3(4):1663–1674
112. Ruffato G, Garoli D, Cattarin S, Barison S, Natali M, Canton P et al (2012) Patterned nanoporous-gold thin layers: Structure control and tailoring of plasmonic properties. Microporous Mesoporous Mater 163:153–159
113. Snyder J, Livi K, Erlebacher J (2008) Dealloying silver/gold alloys in neutral silver nitrate solution: porosity evolution, surface composition, and surface oxides. J Electrochem Soc 155(8):C464
114. Dursun A, Pugh DV, Corcoran SG (2003) Dealloying of Ag–Au alloys in halide-containing electrolytes. J Electrochem Soc 150(7):B355
115. Qian LH, Chen MW (2007) Ultrafine nanoporous gold by low-temperature dealloying and kinetics of nanopore formation. Appl Phys Lett 91(8):083105
116. Wang Y, Wang Y, Zhang C, Kou T, Zhang Z (2012) Tuning the ligament/channel size of nanoporous copper by temperature control. CrystEngComm 14(24):8352
117. Vega AA, Newman RC (2014) Nanoporous metals fabricated through electrochemical dealloying of Ag–Au–Pt with systematic variation of Au: Pt ratio. J Electrochem Soc 161(1): C1–C10

118. Yi Z, Markmann J, Hai-Jun J, Ivanisenko Y, Kurmanaeva L, Weissmuller J (2014) Crack mitigation during dealloying of Au 25Cu 75. Adv Eng Mater 16(4):389–398
119. Chen AY, Shi SS, Qiu YD, Xie XF, Ruan HH, Gu JF et al (2015) Pore-size tuning and optical performances of nanoporous gold films. Microporous Mesoporous Mater 202:50–56
120. Wang D, Yu Y, Zhu J, Liu S, Muller DA, Abruna HD (2015) Morphology and activity tuning of Cu_3Pt/C ordered intermetallic nanoparticles by selective electrochemical dealloying. Nano Lett 15(2):1343–1348
121. Okman O, Kysar JW (2011) Fabrication of crack-free blanket nanoporous gold thin films by galvanostatic dealloying. J Alloy Compd 509(22):6374–6381
122. Qi Z, Vainio U, Kornowski A, Ritter M, Weller H, Jin H et al (2015) Porous gold with a nested-network architecture and ultrafine structure. Adv Funct Mater 25(17):2530–2536
123. Gan L, Heggen M, O'Malley R, Theobald B, Strasser P (2013) Understanding and controlling nanoporosity formation for improving the stability of bimetallic fuel cell catalysts. Nano Lett 13(3):1131–1138
124. Wada T, Yubuta K, Inoue A, Kato H (2011) Dealloying by metallic melt. Mater Lett 65 (7):1076–1078
125. Wada T, Kato H (2013) Three-dimensional open-cell macroporous iron, chromium and ferritic stainless steel. Scripta Mater 68(9):723–726
126. Morrish R, Muscat AJ (2013) Dealloying multiphase AgCu thin films in supercritical CO_2. J Phys Chem C 117(23):12071–12077
127. Li R, Sieradzki K (1992) Ductile-brittle transition in random porous Au. Phys Rev Lett 68(8):1168
128. Cheng IC, Hodge AM (2014) High temperature morphology and stability of nanoporous Ag foams. J Porous Mater 21(4):467–474
129. Kertis F, Snyder J, Govada L, Khurshid S, Chayen N, Erlebacher J (2010) Structure/processing relationships in the fabrication of nanoporous gold. JOM 62(6):50–56
130. Y-cK Chen-Wiegart, Wang S, Chu YS, Liu W, McNulty I, Voorhees PW et al (2012) Structural evolution of nanoporous gold during thermal coarsening. Acta Mater 60(12):4972–4981
131. Shui J-L, Zhang J-W, Li JCM (2011) Making Pt-shell $Pt_{30}Ni_{70}$ nanowires by mild dealloying and heat treatments with little Ni loss. J Mater Chem 21(17):6225
132. Vega AA, Newman RC (2014) Beneficial effects of adsorbate-induced surface segregation of Pt in nanoporous metals fabricated by dealloying of Ag–Au–Pt alloys. J Electrochem Soc 161(1):C11–C19
133. Qiu H, Xu C, Huang X, Ding Y, Qu Y, Gao P (2008) Adsorption of laccase on the surface of nanoporous gold and the direct electron transfer between them. J Phys Chem C 112 (38):14781–14785
134. Feng R, Zhang Y, Yu H, Wu D, Ma H, Zhu B et al (2013) Nanoporous PtCo-based ultrasensitive enzyme-free immunosensor for zeranol detection. Biosens Bioelectron 42:367–372
135. Ding J, Zhang H, Jia F, Qin W, Du D (2014) Assembly of carbon nanotubes on a nanoporous gold electrode for acetylcholinesterase biosensor design. Sens Actuators B-Chem 199:284–290
136. Hafez AM, Huber A, Wenclawiak BW (2013) Time-of-flight-secondary ion mass spectrometry and cyclic voltammetry studies of self-assembly of dodecanethiol on a nanoporous gold surface. Anal Chem 85(6):3334–3339
137. Liu Y, Guo W, Qin X, Meng X, Zhu X, Wang J et al (2014) Sensitive sandwich electrochemical immunosensor for human chorionic gonadotropin using nanoporous Pd as a label. RSC Adv 4(42):21891–21898
138. Shang L, Zhao F, Zeng B (2014) 3D porous graphene-porous PdCu alloy nanoparticles-molecularly imprinted poly(para-aminobenzoic acid) composite for the electrocatalytic assay of melamine. ACS Appl Mater Interfaces 6(21):18721–18727

139. Yin T, Pan D, Qin W (2014) All-solid-state polymeric membrane ion-selective miniaturized electrodes based on a nanoporous gold film as solid contact. Anal Chem 86 (22):11038–11044
140. Detsi E, Onck P, De Hosson JTM (2013) Metallic muscles at work: high rate actuation in nanoporous gold/polyaniline composites. ACS Nano 7(5):4299–4306
141. Li Y, Ding Y (2010) Porous AgCl/Ag nanocomposites with enhanced visible light photocatalytic properties. J Phys Chem C 114(7):3175–3179
142. Fan Y, Baozhu T, Jinlong Z, Tianqing X, Tingting W (2014) Preparation, characterization, and photocatalytic activity of porous AgBr@Ag and AgBr I@Ag plasmonic photocatalysts. Appl Surf Sci 292:256–261
143. Kucheyev S, Hayes J, Biener J, Huser T, Talley C, Hamza A (2006) Surface-enhanced Raman scattering on nanoporous Au. Appl Phys Lett 89(5):053102
144. Qian L, Das B, Li Y, Yang Z (2010) Giant Raman enhancement on nanoporous gold film by conjugating with nanoparticles for single-molecule detection. J Mater Chem 20(33): 6891–6895
145. Zeng J, Zhao F, Li M, Li C-H, Lee TR, Shih W-C (2015) Morphological control and plasmonic tuning of nanoporous gold disks by surface modifications. J Mater Chem C 3(2):247–252
146. Qian L, Shen W, Shen B, Qin GW, Das B (2010) Nanoporous gold–alumina core–shell films with tunable optical properties. Nanotechnology 21(30):305705
147. Bak C, Kim K, Jung K, Kim J, Jang J (2014) Efficient photoelectrochemical water splitting of nanostructured hematite on a three-dimensional nanoporous metal electrode. J Mater Chem A 2(41):17249–17252
148. Wang R, Wang C, Cai WB, Ding Y (2010) Ultralow-platinum-loading high-performance nanoporous electrocatalysts with nanoengineered surface structures. Adv Mater 22(16):1845–1848
149. Wang R, Liu J, Liu P, Bi X, Yan X, Wang W et al (2014) Ultra-thin layer structured anodes for highly durable low-Pt direct formic acid fuel cells. Nano Res 7(11):1569–1580
150. Snyder J, Livi K, Erlebacher J (2013) Oxygen reduction reaction performance of [MTBD] [beti]-encapsulated nanoporous NiPt alloy nanoparticles. Adv Funct Mater 23(44): 5494–5501
151. Ke X, Xu Y, Yu C, Zhao J, Cui G, Higgins D et al (2014) Pd-decorated three-dimensional nanoporous Au/Ni foam composite electrodes for H_2O_2 reduction. J Mater Chem A 2(39):16474–16479
152. Meng F, Ding Y (2011) Sub-micrometer-thick all-solid-state supercapacitors with high power and energy densities. Adv Mater 23(35):4098–4102
153. Lang X, Hirata A, Fujita T, Chen M (2011) Nanoporous metal/oxide hybrid electrodes for electrochemical supercapacitors. Nat Nanotechnol 6(4):232–236
154. Yu Y, Gu L, Lang X, Zhu C, Fujita T, Chen M et al (2011) Li storage in 3D nanoporous Au-supported nanocrystalline tin. Adv Mater 23(21):2443–2447
155. Zhang S, Xing Y, Jiang T, Du Z, Li F, He L et al (2011) A three-dimensional tin-coated nanoporous copper for lithium-ion battery anodes. J Power Sour 196(16):6915–6919

Chapter 3
Nanoporous Metals for Fuel Cell Applications

Abstract Among various green energy technologies, proton exchange membrane fuel cells (PEMFCs) allow highly efficient direct conversion of chemical energies in chemical fuels to electricity. With low or even zero emissions, fuel cells have been attracting worldwide attention for decades. However, the commercialization of fuel cell technologies has been hampered mainly by the heavy demand on Pt electrocatalysts, which are not only expensive, but resource limited as well. In this chapter, we will discuss the structure and electrochemical properties of dealloyed nanoporous metals with an emphasis on their potential for fuel cell applications. As the first example, nanoporous gold (NPG) can be made into very thin freestanding membranes by etching commercially available white gold leaves in an appropriate electrolyte. This material itself is catalytically active for a series of electrode reactions, and upon further surface functionalization, NPG leaf-based electrocatalysts can demonstrate unique structural advantages that are crucial to fuel cell electrodes, such as high surface area, high electric conductivity, high durability, and high precious metal utilization. After the discussion of Pt–NPG leaves for low Pt hydrogen fuel cells, we will discuss in detail how to rationally design ultralow Pt loading, yet highly active and stable electrocatalysts used for direct formic acid fuel cells (DFAFCs), based on the understanding of electrode reactions at the molecular level and a series of high-precision surface modification techniques. Besides, we will review the recent progresses in the design and processing of nanoporous alloy electrocatalysts. By selecting the proper composition of precursor multielement alloys and suitable dealloying conditions, a wide variety of nanoporous alloy materials can be produced with tunable surface area and chemical states. When coupled with other fabrication techniques, the dealloying method becomes a versatile tool for the construction of nanoporous electrodes for anodic oxidation of small organic molecules or cathodic reaction of oxygen in acidic or alkaline solutions. Finally, we will end this chapter with conclusion and future perspectives.

Keywords Nanoporous metals · Proton exchange membrane fuel cells · Low Pt catalysts · Hydrogen fuel cells · Direct methanol fuel cells · Direct formic acid fuel cells · Oxygen reduction · Dealloying

Y. Ding and Z. Zhang, *Nanoporous Metals for Advanced Energy Technologies*, DOI 10.1007/978-3-319-29749-1_3

3.1 Introduction

Fuel cells represent one of the most attractive energy conversion devices among various electrochemical technologies. Unlike those secondary batteries such as Li-batteries and supercapacitors, fuel cells allow direct and spontaneous conversion of chemical energies in fuels and oxidants to electricity, with only limited amount of by-products such as heat and water. As a high technology that would play a central role in the Hydrogen Era in the twenty-first century, fuel cell is actually a nineteenth century invention. In 1838, nearly 20 years before French physicist Gaston Planté invented the oldest type of rechargeable battery: lead–acid battery, Sir William Grove demonstrated the first H_2/O_2 fuel cell using spongy platinum electrodes and sulfuric acid electrolyte [1]. Fuel cells offer a series of advantages over other energy conversion technologies: (a) It is a zero- or low emission clean energy technology. For systems designed to consume hydrogen fuel, the only by-product is water. (b) It is a highly efficient technology. Typical fuel cell plants are at least twice more efficient than conventional combustion-based power plants. Also because it avoids the use of combustion engines, it can run silently. (c) It is highly stable. Fuel cells can accommodate long-term operation and continuously generate electricity with a constant supply of fuel. (d) It is highly flexible. Modular fuel cells can be designed and stacked to fulfill specific power needs varying from microwatt to megawatt level.

Fuel cells may be classified into many different types according to (i) the operating temperature, (ii) the electrolyte used, (iii) the fuel type, or (iv) the operating mechanism. For example, based on the electrolyte used in a fuel cell, there are polymer electrolyte membrane fuel cells (PEMFCs), alkaline fuel cells (AFCs), phosphoric acid fuel cells (PAFCs), molten carbonate (MCFCs), and solid oxide fuel cells (SOFCs), working under different conditions for different purposes (Fig. 3.1). In this chapter, we will mainly focus on the development of dealloyed nanoporous metals for PEMFC applications, although one may envision them to be a new type of structured electrocatalysts with more general potential.

3.2 Principle and Structure of Proton Exchange Membrane Fuel Cells (PEMFCs)

Polymer electrolyte membrane fuel cells (PEMFCs) sometimes are also called proton exchange membrane fuel cells (PEMFCs), and by coincidence they have the same acronym of PEMFCs. A typical PEMFC includes the following components: (i) bipolar plates that provide fuel supply and also act as the current collector, (ii) electrocatalysts at both anode and cathode to drive the conversion reaction between fuels and oxidants, (iii) electrolyte membrane that acts as an ion-exchanger and separates the anode and cathode. And catalysts and membrane form the heart of a PEMFC, the membrane electrode assembly (MEA). With the current

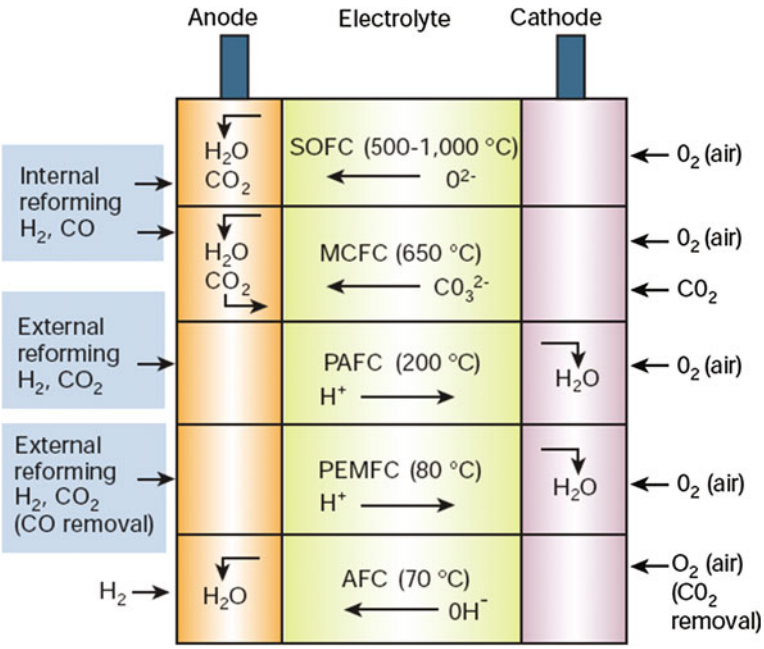

Fig. 3.1 Classification of fuel cells. Reproduced from Nature 2001, 414, 345–352. Copyright 2001, Nature Publishing Group

state-of-the-art technology, an MEA is usually made of a proton exchange membrane sandwiched between two catalyst-coated carbon papers.

Figure 3.2 illustrates a typical structure of a PEMFC. For systems using hydrogen as the fuel, the reaction proceeds in the following way: H_2 is fed to an anode where it is spontaneously separated into protons and electrons, a reaction catalyzed by Pt catalysts. The electrons follow an external circuit to a cathode, performing electrical work, whereas the protons flow to the cathode through a material that conducts protons, but not electrons. Air or oxygen is fed to the cathode where oxygen catalytically combines with the protons and electrons from the anode, again on the catalysts, forming water exhaust. For fuel cells using organic fuels such as methanol and formic acid, CO_2 may be generated on the anode side.

3.2.1 Electrocatalysts

Despite its cost, platinum or platinum-based catalysts are still the most efficient catalysts for most chemical reactions. It was said [2] that "more than 25 % of global industrial output (not just the production of chemicals) depends on heterogeneous catalysis by the Pt metals alone." With regard to the electrochemical reactions in

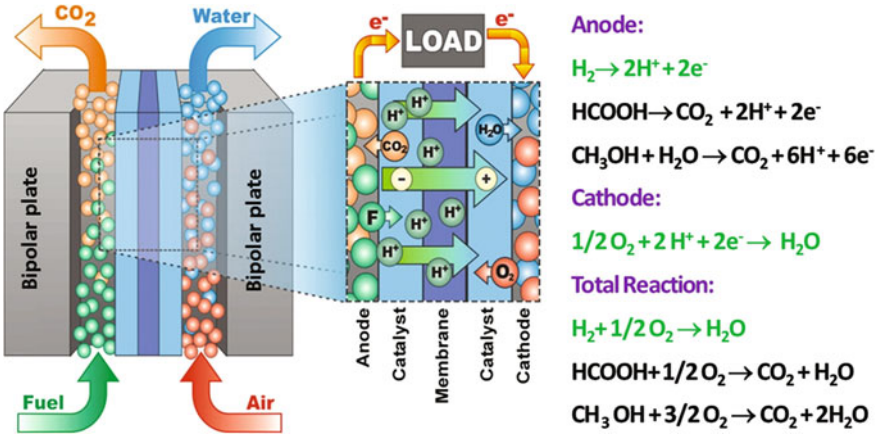

Fig. 3.2 llustrative cartoon of a typical PEM fuel cell. Shown on the *right side* are the typical electrode reactions using common fuels such as hydrogen, methanol, and formic acid

PEMFCs, Pt is active for almost all anode and cathode reactions regardless of what type of fuel is used. For example, Pt is particularly suitable for fuel cells fed with hydrogen and air (oxygen), because it is sufficiently reactive in adsorbing/bonding H_2 and O_2 molecules so as to greatly lower the energy barrier for the dissociation of H–H and O–O bonds to form H(Pt) and O(Pt) intermediates (e.g., $H_2 + 2Pt \rightarrow 2Pt–H$). Furthermore, the bonding of these intermediates to Pt surface is sufficiently weak so it is also capable of effectively releasing these intermediates to form the final product (e.g., $2Pt–H \rightarrow 2Pt + 2H^+ + 2e^-$).

Because the limited Pt reserve on our planet (the Pt world production averages at ~200 tons per year in the past decade), large-scale commercialization of fuel cell technologies has been hampered mainly by the massive usage of Pt-based electrocatalysts. In order to reduce the Pt usage and cost, the current MEA fabrication methodology is primarily based on Pt nanoparticles supported on high surface area carbon materials, frequently denoted as Pt/C. It is therefore not unexpected, that the exploration of low Pt or even non-Pt electrocatalysts has been a research topic of intensive interests in the past decade, and this will continue to be an important R&D activity. For hydrogen fuel cells, technical progresses in MEA fabrication have allowed the significant reduction of the platinum loading from ~2 mg cm^{-2} a decade ago to values below 0.2 mg cm^{-2} without significant impact on their performance and lifetime. For fuels containing trace amount of CO or liquid fuel cells such as direct methanol fuel cells (DMFCs) or direct formic acid fuel cells (DFAFCs), a CO-tolerant catalyst is required. Because the oxidation of adsorbed CO on Pt is slow at temperatures below 100 °C, alloying Pt with transition metals such as Ru, Ir, or Sn to form binary or even ternary alloys is the most common approach to facilitate CO oxidation because these alloy elements provide favorable adjacent lattices for OH-ads formation. Many Pt-based alloy catalysts also show much enhanced intrinsic activity toward oxygen reduction reaction, which will be

discussed in detail in Sect. 3.4.2. In order to further boost the Pt utilization, core–shell nanostructures where the functioning Pt catalytic sites are only exposed on the surface of nanoparticles made of less noble elements are another direction of research efforts. However, whether or not these composite nanostructures can sustain long-term operation, especially under acidic conditions in most PEMFCs, remains unanswered.

3.2.2 *Electrolyte Membrane*

The electrolyte membrane in a PEMFC is a unique class of polymers called ionomers, usually in a thin film form with thickness varying from a few tens to hundreds of microns. Although there are many kinds of ionomers that can fulfill the purpose of proton conduction [3], the most well known and readily available one is a polymer called poly(perfluorosulfonic)acid, with a commercial name of Nafion®.

Nafion®, the first synthetic polymer with ionic properties ever developed, was developed by Dr. Walther Grot [4–6] at DuPont in the late 1960s by modifying Teflon®. The structure of Nafion consists of three regions (Fig. 3.3) [7]: (1) the Teflon-like, fluorocarbon backbone, with hundreds of repeating $–CF_2–CF_2–CF_2–$ units in length; (2) the side chains, $–O–CF_2–CF(CF_3)–O–CF_2–CF_2–$, which connect the molecular backbone to the third region; (3) the ion clusters consisting of sulfonic acid ions, $SO_3^-H^+$.

Because of these structural characteristics, Nafion combines the physical and chemical properties of its Teflon base material with ionic characteristics that give it very unusual properties. Detailed description of the properties of Nafion® can be found at DuPont (www.fuelcells.dupont.com/) or other Nafion® distributors such as Ion Power Inc. (www.ion-power.com/). Listed below are the most important points that make Nafion unparalleled [8].

1. Like Teflon, Nafion is extremely resistant to chemical attack and has relatively high working temperatures up to 190 °C.
2. Unlike Teflon, Nafion is highly ion-conductive due to the bonding of sulfonic acid groups to the polymer matrix.
3. Unlike Teflon, Nafion is highly permeable to water, because the sulfonic acid groups have a very high water of hydration. This character actually has both

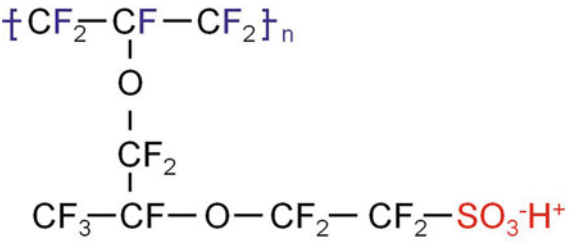

Fig. 3.3 Chemical structure of membrane material, Nafion®, produced by DuPont

positive and negative effects. On the positive side, sulfonic acid groups are permanently attached to the Teflon backbone and cannot move. Only when the membrane becomes hydrated by absorbing water, the hydrogen ions become mobile and can move from SO_{3^-} site to another within the membrane. This is the reason why Nafion is an excellent conductor of hydrogen ions. On the negative side, however, upon absorbing water (so efficiently), Nafion will swell and deform severely, which seriously affects the mechanical and physical stability of the MEA structure.

3.2.3 Fabrication of an MEA

To drive a fuel cell, electrodes must be porous, and catalyst materials must be confined to the narrow region between the electrolyte membrane and the bipolar plate, so that ***a triple-phase boundary*** (TPB) is optimized, where gas agents (H_2, O_2 and water vapor), protons (H^+) and electrons (e^-) can be transferred freely and simultaneously. So the ideal electrode should consist of an inert, conductive, highly porous substrate in the form of thin membrane on which is uniformly coated an atomically thin layer of catalytic materials such as platinum [9]. In this way, precious metal catalyst atoms are most likely to reside on a surface, and not be buried and thus inactive [10, 11].

Conventionally, an MEA is manufactured by the following two methods. In either case, a paste, or ink is used, typically by mixing Pt or platinum group metal nanoparticles with catalyst carrier such as carbon black into a dilute polymer dispersion (other components may also be added to improve the uniformity of the structure). The first method is *Direct Painting*, in that electrode ink is painted or sprayed directly onto polymer membrane at elevated temperature. The second approach is *Hot Pressing*, where the ink is painted onto porous carbon paper to form a composite electrode. These electrodes are then hot pressed onto the polymer membrane [12]. In both cases, platinum nanoparticles and carbon particles are fabricated separately. They are mixed at some point during the manufacturing process, in a way such that Pt nanoparticles are physically attached to the carbon black surface. Carbon is used for this purpose due to its cost-effectiveness, good conductivity and corrosion resistance and also because the interstices between carbon particles can work as a gas flow channel. Pt nanoparticles residing on the surface of the carbon particles and touching nearby polymer electrolyte molecules will catalyze the fuel cell reactions. Being quite effective for most fuel cells, this MEA structure also suffers from serious drawbacks known as the triple phase boundary dilemma [12–14] as summarized by the following conflicts which are the main reasons restricting the performance enhancement of a fuel cell.

1. High activity *versus* high inertness (durability)
2. Electron conductivity *versus* ion/proton conductivity (insulation)
3. High compact density (high power) *versus* high porosity (mass transport)

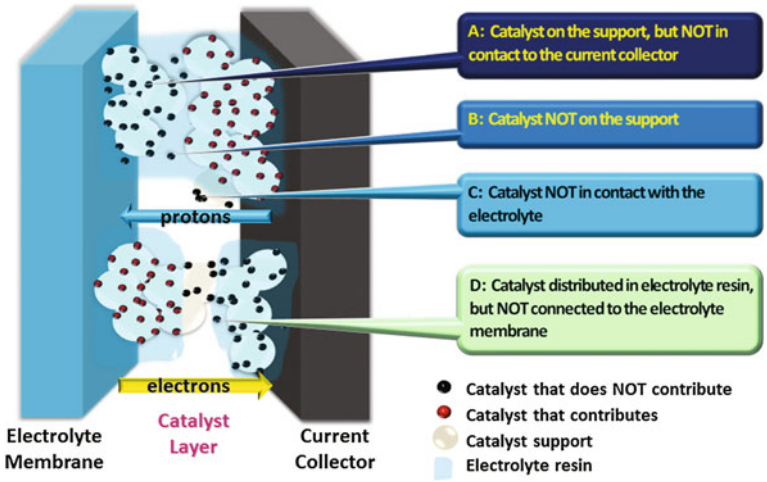

Fig. 3.4 Illustrative cartoon of a typical MEA (anode side)

4. Low Pt loading
5. Resistive to poisoning
6. Low manufacturing cost.

Shown in Fig. 3.4 is a cartoon for a half MEA which illustrates how a typical catalyst structure looks like on the anode side. Sitting on the left side is the electrolyte membrane which collects and transports protons. And on the right side is the current collector (bipolar plate). In the middle is the catalyst layer where we find a mixed slurry of supported Pt particles and electrolyte resin such as Nafion ionomer. From this picture, we may realize immediately even though these Pt-based nanoparticles may have been uniformly dispersed on carbon support, a significant portion of catalysts actually do not contribute to the reaction (marked by black spots). For example, over the entire area A, although Pt nanoparticles are on the carbon support, they are not in contact to the current collector. In area B, some Pt nanoparticles have lost contact to the support during mixing and processing. In area C, these Pt nanoparticles are not in good contact with the electrolyte. And for those catalysts distributed in the electrolyte resin (area D), if they are not in ultimate contact to the electrolyte membrane, they cannot function either. It is therefore not unexpected that many electrocatalysts show substantially enhanced activity during electrochemical half-cell tests as compared to the commercial Pt/C catalysts, while their successful implementation into real fuel cells is scarcely seen. Finally, because those catalyst nanoparticles are only weakly adsorbed to the carbon support, there is a strong tendency for them to agglomerate over time under operating conditions, thereby reducing their active surface area and limiting device lifetime. It should be emphasized that all those structural drawbacks and predictions have been experimentally observed and confirmed using electron microscopy such as TEM (Fig. 3.5).

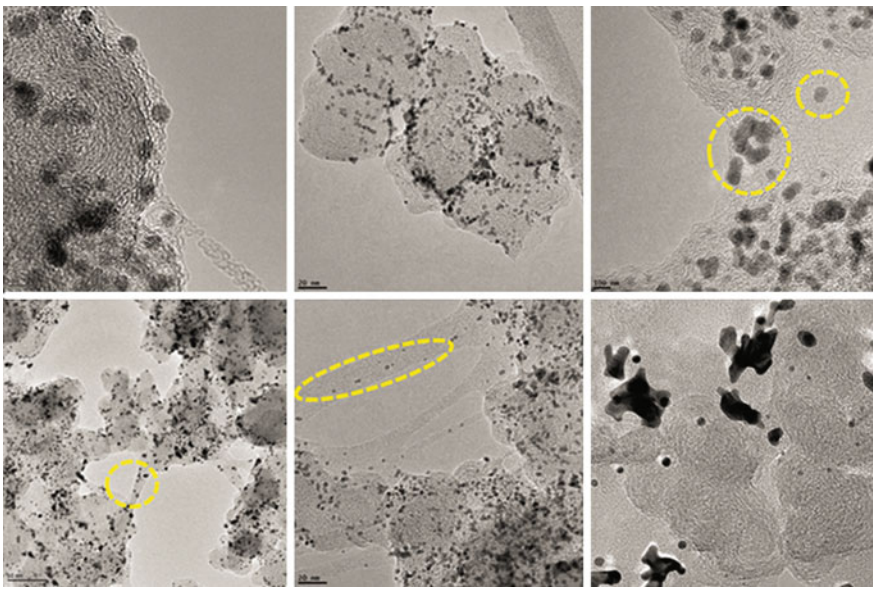

Fig. 3.5 TEM images of the actual electrocatalyst layer within an MEA. *Black spots* are Pt nanoparticles whereas *grayish* particles are carbon black. Most Pt nanoparticles are not in ideal conditions as expected. Adapted from http://www.hydrogen.energy.gov/pdfs/review10

3.3 Fuel Cell Electrodes Based on Nanoporous Gold (NPG)

In the past decade, the great demand in energy and environmental technologies has resulted in rush in fuel cell communities to pursue various nanostructured electrodes or electrocatalysts, with tailored size or dimension, structural uniformity and dispersity, crystallographic morphology, and surface configuration, aiming at increasing the catalytic activity and precious metal efficiency [15, 16]. For example, core–shell nanostructured catalysts have been developed to improve the precious metal utilization [17, 18], while morphologically controlled nanocatalysts have also received particular interests in the light of the possibility that different crystal surfaces have distinct activities [19]. However, as discussed above, for actual implementation in real fuel cells, these nanocrystal catalysts have to undergo further processing by adsorbing onto high surface area conducting substrates such as carbon black to facilitate the catalyst dispersion, and fuel diffusion. As the catalyst nanoparticles are only physically adsorbed on the carbon support, they tend to aggregate to form larger nanoparticles or even lose contact to support under the operation conditions [20]. Moreover, the large contact resistance between carbon particles aroused from the incorporation of poorly conductive polymer electrolyte such as Nafion® when preparing the MEA leads to the increase of internal resistance in catalytic layer and decrease of overall cell performance. Due to their cost-effectiveness and excellent chemical stability, nanostructured

carbon materials have received tremendous research interests, and typical examples include ordered nanoporous carbon [21], carbon nanotube [22], films of fullerene [23], and more recently graphene. In comparison, few attentions have been paid to nanoporous metals, which actually provide much more flexibility and functionalities than carbon support materials.

In this chapter, the authors will summarize some of the inspiring studies regarding the processing of dealloyed nanoporous metals for fuel cell applications. In particular, emphasis will be placed on a unique NPG membrane material called nanoporous gold leaf (NPGL), which shows extraordinary structural properties as compared to the carbon black as a catalyst support material. While many people may argue that gold is not a potentially applicable material as a catalyst support, this is objectively not the case. In the review by Steele and Heinzel [9], gold is noted as a potentially better catalyst support than carbon black because based on the same structure configuration, gold has at least 500 times better conductivity than that of graphite [24], is more stable, and corrosion resistant. However, the problem has been how to make a porous gold structure with a manufacturing cost comparable to that of carbon black based technology. If one can design and fabricate an ultrathin porous gold membrane with high enough surface area to load sufficient catalytically active elements such as Pt to drive the fuel cell, gold may no longer be a cost-limiting factor. Indeed, NPG membranes of thickness around 100 nm contain less than 0.1 mg Au per square centimeter. The raw material therefore only costs less than 0.4 US cent cm^{-2} gold, which is at least ten times less expensive than the polymer electrolyte membranes used in PEM fuel cells.

3.3.1 Structural Properties of NPG

As introduced in previous chapters, nanoporous metals could be made into any kind of form depending on the shape and geometry of the pristine alloys. In 2004, Ding and Erlebacher reported that the commercially available 12 carat white gold leaves (Ag/Au alloys, 50/50 wt%) can be readily dealloyed in nitric acid to form large scale, freestanding NPG membranes (Fig. 3.6) [25]. And the samples can be easily transferred from one solution to the other by a glass slide or a graphite roller, which eases the fabrication of high-quality large area NPG membrane-based electrode with tailorable surface functionalities for a wide variety of applications. Depending on the dealloying conditions, the entire etching process can complete within a few seconds, and prolonging the reaction time may coarsen the structure. Accordingly, other originally white colored alloy leaves would turn into freestanding copper colored and translucent thin membranes made of almost pure gold. Compared with the pristine alloy leaf, the NPG leaf is more brittle, but still could be transferred from one solution to another for rinsing or decoration upon gentle operation.

As mentioned previously the formation of nanoporous structure is associated with atomic corrosion and diffusion at the interface between alloy and electrolyte. The grain structure of NPG leaf is primarily determined by the pristine white gold

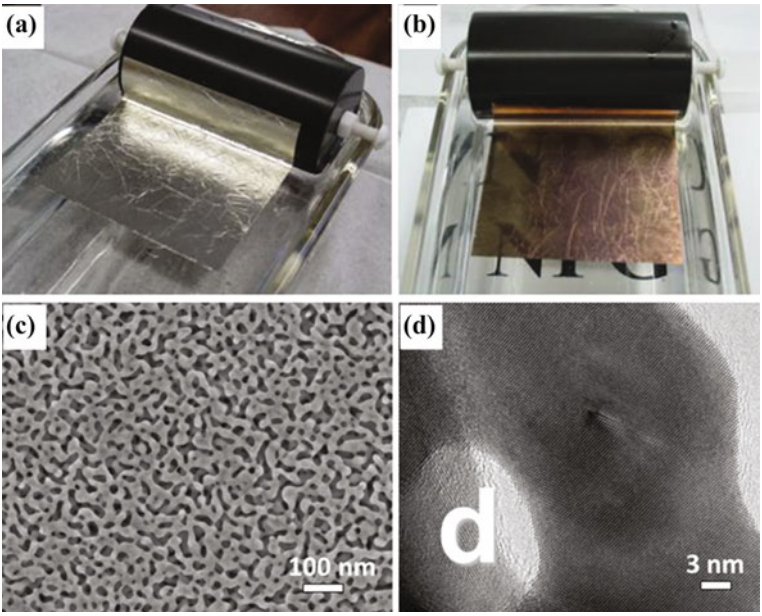

Fig. 3.6 Optical images of white gold leaf before (**a**) and after (**b**) dealloying in nitric acid. Leaf samples can be transferred easily from one liquid surface to another with a graphite roller. SEM (**c**) and HRTEM (**d**) images of an NPGL sample feature a random uniform spongy morphology. Reproduced from Adv Mater 2004, 16, 1897. Copyright 2004, Wiley-VCH

leaf which has large lateral grain dimension on the order of 10 μm. But considering that the pore and ligament size of NPG can be made down to several nanometers, almost three magnitudes smaller than the lateral grain dimension, one would expect an unusual single crystalline yet porous grain structure for NPG leaf. This unique single crystal feature can be demonstrated by electron diffraction and high resolution transition electron microscopy (HRTEM) observation. As shown by a typical SEM image in Fig. 3.6c, the structure is composed by interconnected ligaments with sizes at about 15 nm. From the HRTEM image shown in Fig. 3.6d, {200} lattice fringes are found to extend continuously from one ligament across the pore to another. This unique single crystal feature of NPG leaf is markedly different from traditional porous metal structures based on controlled aggregation of nanoparticles, which renders the material with superior electrical conductivity [26] and mechanical rigidity which are highly desired for electrocatalysis and fuel cell applications.

NPG leaf possesses several distinct structure features which make it unique as compared with traditional nanoparticle-based catalysts. First, as the NPG leaf is dealloyed from highly corrosive regent, the ligament surface is free of contaminations such as surfactants and organic surface passivating species which are commonly seen in traditional nanoparticles made via wet chemical methods. And this structural advantage is of particular importance for catalysis. Second, the whole structure is interconnected with highly conductive ligaments and open pore

channels, which is highly desired for electrocatalysis as electrons could be transported from any reaction sites on the ligament surface to current collector easily. This feature is also markedly different from that in nanoparticle-based catalysts, where functioning nanoparticles have to be isolated from each other to avoid aggregation and each be dispersed on conducting substrates such as carbon black. It can be imagined that a significant portion of nanoparticles would be under non-optimized conditions and eventually become inoperative. Finally, as the grain size in NPG leaf is typically about 3 orders of magnitude larger than the length scale of ligaments ($\sim$10 μm vs. $\sim$10 nm), this 3D nanoporous structure should consist of different kinds of crystal facets exposed on the ligament surfaces, forming favorable reaction sites for catalysis and electrocatalysis.

With these unique structural properties, NPG itself can be an interesting electrocatalyst used for potential energy-saving and electrochemical sensing technologies. Methanol electrooxidation in alkaline solution is the first reaction examined using NPG electrode [27]. With stronger chemisorption of OH^- ions on the NPG surface than on bulk gold surface, NPG shows much enhanced catalytic activity toward methanol electrooxidation. Although this reaction is performed on thick NPG foils, these results have been reproduced on NPG leaves with different ligament sizes. The ultrathin yet robust enough NPG in the leaf form makes it very easy to be assembled into an MEA. Zeis et al. [28]. examined the fuel cell performance using NPG leaf as the cathode, and observed a surprisingly high open circuit of $\sim$850 mV. Without any hydrogen peroxide detected in the output of fuel cell, the most possible reaction mechanism is suggested to be a two-step four-electron reduction process in which oxygen is first reduced to hydrogen peroxide, and then further reduced to water. Further experiments on rotating ring disk electrochemistry (RRDE) demonstrate that the reduction of oxygen to hydrogen peroxide on NPG leaf is similar to results on planar gold electrode. However, the reduction of hydrogen peroxide to water is quite different (Fig. 3.7). In contrast to the small reduction currents on planar gold electrode, the reduction current on NPG is much enhanced. As the reduction of hydrogen peroxide was highly catalyzed by NPG, the reduction of oxygen becomes the rate determining step. Under the fuel cell operation conditions, the hydrogen peroxide

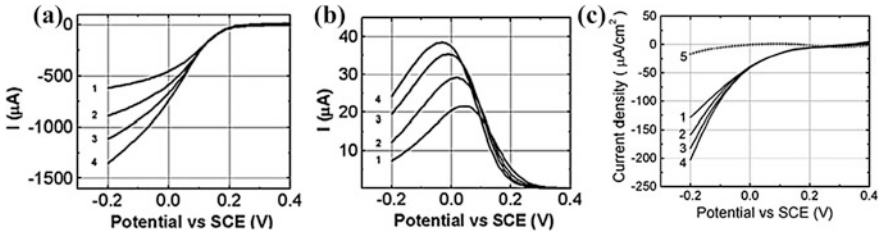

Fig. 3.7 **a** Disk and **b** ring currents during oxygen reduction on NPG at various rotation rates (*1*) 400, (*2*) 900, (*3*) 1600 and (*4*) 2500 rpm. **c** Disk currents during peroxide reduction on and NPG at various rotation rates (*1*) 400, (*2*) 900, (*3*) 1600 and (*4*) 2500 rpm. Curve (*5*) is the disk current during the peroxide reduction on bulk, planar gold at ω = 1600 rpm. Reproduced from J Catal 2008, 253, 132. Copyright 2008, Elsevier

once formed would then be further reduced to water mediated by NPG leaf catalyst. This is why the open circuit potential can reach as high as 850 mV. It is suggested that the high density of steps on ligament surface of NPG leaf contribute to the high catalytic activity toward hydrogen peroxide reduction.

3.3.2 *Functionalization of NPG Electrodes*

Although NPG shows high catalytic activity toward several electrochemical reactions, mostly in alkaline solutions, gold is still much less active as compared with platinum group metals in most cases especially in acidic solution. Considering NPG leaf is highly conductive, corrosion resistive, modification of NPG surfaces with catalytically active metals such as Pt is a realistic strategy to highly effective electrocatalysts which could bypass the intrinsic weaknesses of traditional nanoparticle-based catalysts such as carbon corrosion at high potential and the weak interaction between nanoparticle catalysts and carbon substrate.

Various techniques have been developed to decorate NPG structures, and the most employed ones include: electroless plating and electrochemical plating (Fig. 3.8). Both approaches involve a similar electrochemical mechanism of metal ions reduction and a subsequent heterogeneous coating onto desired substrate, NPG.

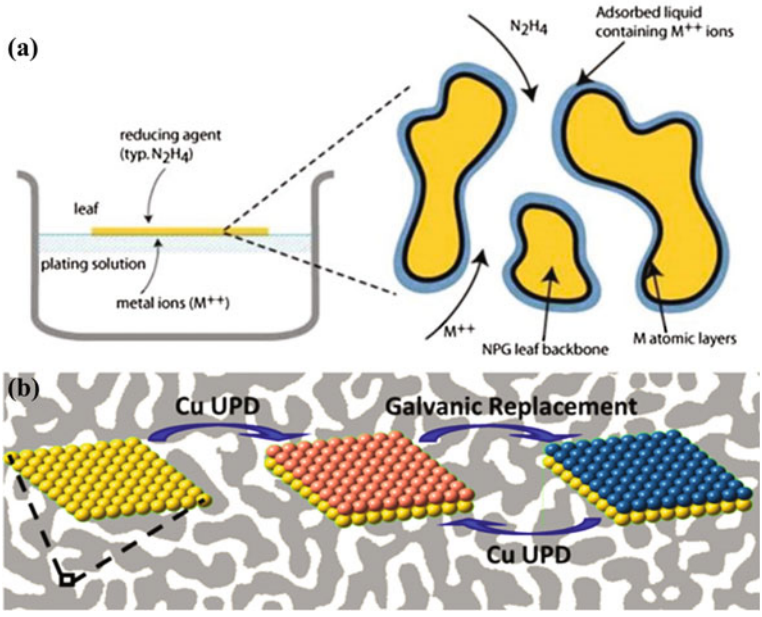

Fig. 3.8 Schematic illustrations of **a** electroless plating and **b** copper UPD-Mediated electrochemical plating method. Reproduced from J Am Chem Soc 2004, 126, 6876. Copyright 2004, ACS and Langmuir, 2009, 25, 561. Copyright 2009, ACS

The electroless plating method was first developed by Ding and Erlebacher to plate NPG leaf with silver to make NPG with bi-modal porous structures. It was soon demonstrated that a wide variety of materials, including metals and oxides, could also be plated onto NPG leaves using this method and the resulted nanocomposites show great potential for electrocatalysis, fuel cell, Li-battery, and supercapacitor applications. More details will be covered in the respective chapters later on. The electroless plating method is actually a gas–electrolyte–substrate interfacial plating technique. The plating procedure can be illustrated in Fig. 3.8a. NPG leaf is placed on the surface of plating solution and reducing agent (typically N_2H_4) is introduced from air above. When reducing gas approaches and dissolves into the thin wetting layer of plating solution within the porous leaf, the redox reaction takes place. As the reducing agent vapor and metal ions are separately supplied from each side of the leaf, the redox reaction is essentially confined in the very thin porous layer of the nanostructure [29].

With this method, platinum can be deposited onto the whole ligament surfaces of NPG leaf in minutes at room temperature in the absence of any structural directing agents or surfactants. The Pt loading (deposition amount) can be easily monitored by controlling the time of reaction which can be terminated by removing the vapor of reducing agent. Typically, the calculated Pt layer (based on the loading and surface area of NPG leaf) reaches 1 monolayer after several minutes. The plating is self-limiting and saturates at a loading of approximately 0.05 mg cm^{-2} after about 200 min.

As the electroless plating process is governed by the redox reaction of metal ions and reducing reagents which depends significantly on the reaction parameters such as temperature, concentration, and the combination of metal ions and reducing reagents of choice. It is also nearly inevitable that some reducing gas will be dissolved into the solution and react with the metal ions, leading to the deterioration of the whole plating system. In contrast, electrochemical method allows precise control of the reducing process by finely tuning the potential applied to electrodes. However, traditional electrochemical deposition methods can not be easily applied to the plating of NPG leaf, as the crystal nucleation on the high curvature surfaces and mass transportation in the porous structure would greatly affect the plating process.

In 2009, Ding and coworkers reported that the well developed Cu underpotential deposition (UPD) electrochemistry could be applied to coat foreign metals such as Pt and Pd on NPG leaf with remarkable structural uniformity and precision (Fig. 3.8b) [30]. The deposition potential and time are the two key parameters that influence the completeness of UPD layer and consequently the quality of Pt layer. Typically, the optimized deposition condition in 0.5 M H_2SO_4 solution containing 0.5 mM Cu^{2+} ions is holding the potential at 0.24 V versus RHE for 120 s where a complete monolayer of Cu could be deposited on NPG leaf. The galvanic replacement of the monolayer Cu with solution containing Pt^{2+} ions results in the monolayer deposition of Pt on NPG. As Cu can also form UPD layer on Pt, this process can then be repeated to deposit more Pt on NPG in a layer-by-layer mode. With this method, one can not only investigate the structure–property relationship

of NPG-supported Pt catalysts, but also design and fabricate other artificial nanocatalysts with tailored functionalities.

3.3.3 *Structure and Electrochemical Properties of Pt–NPG*

The catalytic activity and stability of electrocatalysts are often influenced by the catalyst surface and the interfacial structure between catalyst and support. The microstructures of Pt-plated NPG leaves have been investigated by electron microscopy techniques such as SEM, TEM, and HRTEM. Figure 3.9 shows TEM and HRTEM images of porous gold leaves before and after platinum plating for varying lengths of time. The three-dimensional bi-continuous porous structure can be seen in NPG leaf with a pore size around 15 nm (Fig. 3.9a). The single crystal

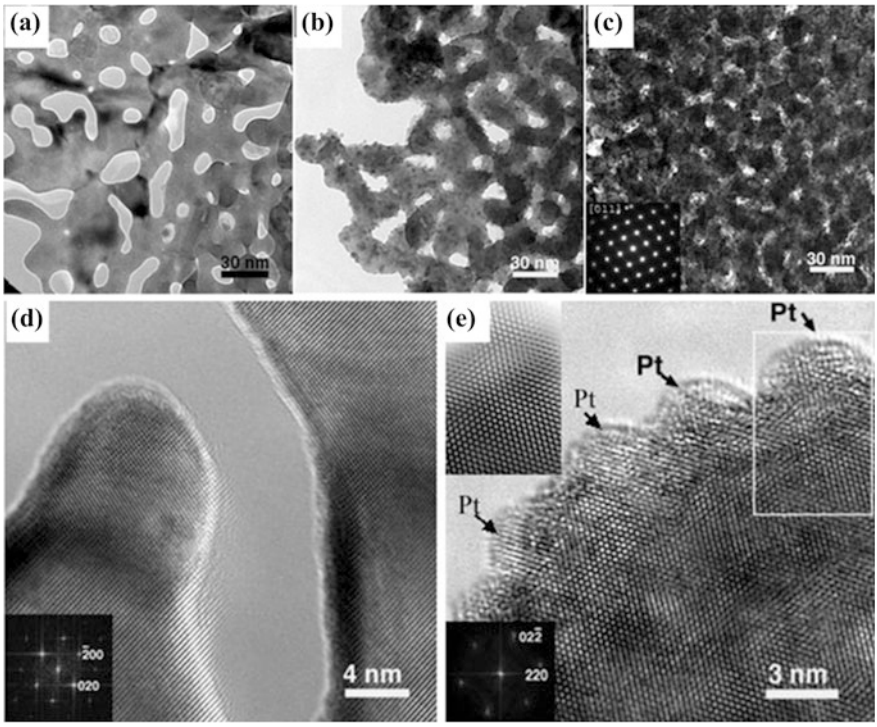

Fig. 3.9 **a** Bright field TEM images of **a** NPG leaf; **b** Pt–NPG samples after plating for 24 min; and **c** Pt–NPG samples after plating for 192 min. The inserted electron diffraction pattern in **c** shows the single crystal nature of the Pt–NPG composites, indicating a coherent crystallographic relationship between plated Pt nanoparticles and the gold substrate. **d** HRTEM image of NPG leaf. **e** HRTEM image of Pt–NPG plated for 24 min showing a coherent crystal relationship between Pt nano-islands and Au matrix. Reproduced from J Am Chem Soc 2004, 126, 6876. Copyright 2004, ACS

nature of the NPG substrate can also be clearly seen from a high-resolution transmission electron microscope (HRTEM) image as shown in Fig. 3.9d, where lattice fringes extend continuously from one ligament to the other by viewing the image at grazing incidence along ⟨200⟩ directions. Upon plating, it looks as if the NPG surfaces have been covered by a uniform dispersion of Pt nanoparticles. These nanoparticles have a very narrow size distribution between 2 and 4 nm (Fig. 3.9b, c). Interestingly, the single crystal character of the support is retained in Pt-plated NPG leaf. Even with the relatively high platinum loading (0.05 mg cm^{-2}) in the 192-min sample, electron diffraction still yields single crystal diffraction patterns with only slight diffuse streaks along ⟨110⟩ directions from this composite nanostructure (see the inserted pattern in Fig. 3.9c). This observation indicates a coherent crystallographic relationship between deposited Pt and the NPG substrate, evidence for an epitaxial growth mode of Pt on the NPG substrate rather than adsorption of individual Pt nanoparticles. Indeed, HRTEM observations with atomic resolution confirm this coherent relationship. As shown in Fig. 5.2b, those Pt nanoparticles are actually *nano-islands* in hemispherical shape. Two sets of lattice fringes ⟨110⟩ extend continuously from gold to platinum. The relationship can be determined as: $\langle 110\rangle_{Au}//\langle 110\rangle_{Pt}\langle 110\rangle_{Au}$ and $\{111\}_{Au}//\{111\}_{Pt}$. In addition, slight lattice distortion is found at the interface between Pt and Au and is highlighted in the inset Fourier-filtered image. These nano-islands are generally 3 nm in diameter with a height of just a few atomic layers. Despite the different deposition method, the structures of Pt–NPG leaves using Cu UPD-mediated method are quite similar. During the first two cycles of Pt deposition, Pt appears to cover the NPG surface in a layer-by-layer mode, and further deposition will lead to the formation of Pt nanoclusters of size 2–3 nm [30].

With the above-mentioned structure advantages, Pt–NPG leaf should be very suitable for electrocatalytic applications. The surface structures of Pt–NPG leaves made by different methods have been investigated by cyclic voltammetry (CV) in 0.5 M H_2SO_4 and the results are shown in Fig. 3.10. Both plating methods result in complete cover of Au by Pt overlayer which is proved by the disappearance of gold oxide reduction peak especially for higher Pt loading samples. However, at low Pt loading, the difference of two fabrication methods is quite obvious. The Cu UPD-mediated method shows better control for the plating layer which is demonstrated by nearly complete inhibition of gold oxide reduction signal even after one layer of Pt plating. While the sample made by the electroless method shows significant gold reduction peak even after 2 min plating and the complete coverage of Au by Pt could be achieved after 8 min plating which equals more than one layer of Pt. From the CV curves, one can see that the surface area of Pt increases with the increase of Pt loading, although the utilization of Pt shows an opposite trend. In addition, the platinum oxide reduction peaks demonstrate a positive shift with the increase of Pt loading. This phenomenon should be caused by the electronic interaction between Au and Pt which induces improved adsorption of oxygen on Pt surface, as demonstrated by both density functional theory (DFT) simulations [31] and electrochemical experimental results [32].

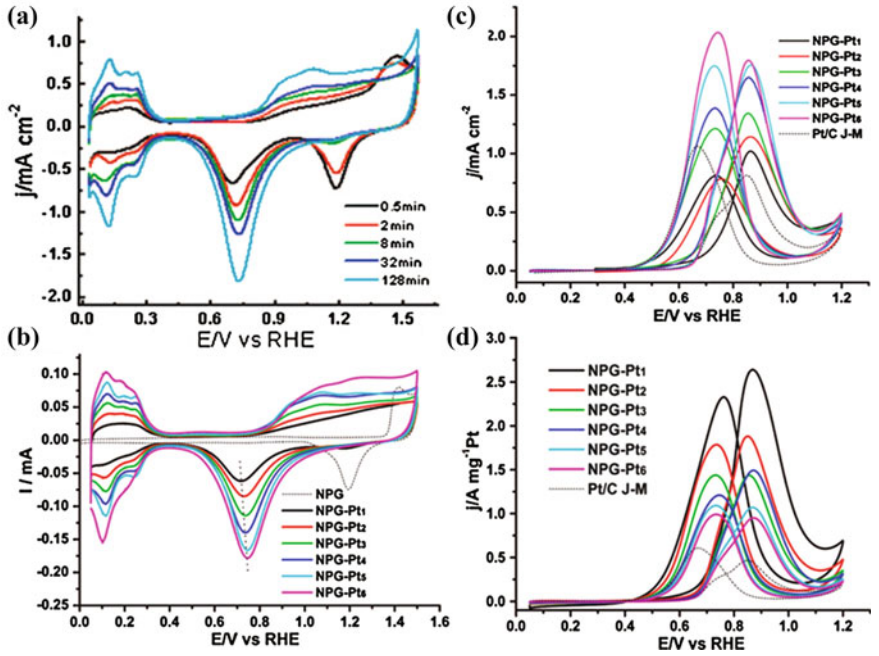

Fig. 3.10 Cyclic voltammograms (CVs) of Pt–NPG leaves made by **a** electroless and **b** Cu UPD-mediated methods with different Pt loadings. **c** and **d** are ECSA- and Pt mass specific catalytic activities of different Pt–NPG leaves made by Cu-UPD method in 0.5 M H_2SO_4 + 1.0 M CH_3OH. Reproduced from Langmuir 2009, 25, 561. Copyright 2009, ACS & Chem Mater 2007, 19, 5827. Copyright 2007, ACS

The electrocatalytic activity of Pt–NPG leaves toward methanol oxidation is investigated by CV in 0.5 M H_2SO_4 + 1.0 M CH_3OH mixed solution. Despite the different fabrication method, two types of nanocomposites show rather similar electrocatalytic performance and Fig. 3.10c, d depicts the CV profile for samples made by the Cu UPD-mediated method. The catalytic activities have been normalized to ECSA (electrochemically active surface area) and Pt mass loading which are critical for the understanding of catalytic performance from fundamental and technological point of view, respectively. As shown in Fig. 3.10c, the ECSA-specific activities of Pt–NPG leaves increases with the increase of Pt loading and are all superior to commercial Pt/C catalyst revealed by the enhanced current densities. The increased catalytic activities with the increase of Pt mass loading should be caused by the decrease of electronic perturbation of Pt surface by underlayer gold substrate that has been discussed above. The improved catalytic activities of samples with higher Pt loading compared with Pt/C catalyst must be caused by their different surface configuration. In Pt–NPG, epitaxial Pt nano-islands are essentially linked together and form an extended overlayer structure with comparatively less compressive stress as often seen in spherical Pt nanoparticles of

similar size. This is somewhat consistent to the observation by T. Frelink and coworkers that larger Pt nanoparticles show improved catalytic activity toward methanol electrooxidation as compared with smaller ones [33].

The Pt mass specific catalytic activities of Pt–NPG leaves catalysts are shown in Fig. 3.10d. With much improved Pt utilization (close to 100 % for the sample with one deposition layer), all Pt–NPG leaf samples show much enhanced mass specific activity as compared with the Pt/C catalyst. The highest enhancement factor is about 7 for sample with one deposition layer. With the increase of Pt layer, the Pt mass specific activities decrease which is reasonable considering the decreased Pt utilization value.

With higher energy density and much lower toxicity, ethanol is also believed to be an attractive fuel option [34]. The catalytic activities of Pt–NPG leaves toward ethanol electrooxidation are investigated by CV in 0.5 M H_2SO_4 + 1.0 M C_2H_5OH mixed solution. The ECSA and Pt mass specific activities are shown in Fig. 3.11 with those of Pt/C catalyst for comparison. It is expectable the Pt mass specific activities are all much higher than the commercial catalyst. However, different from

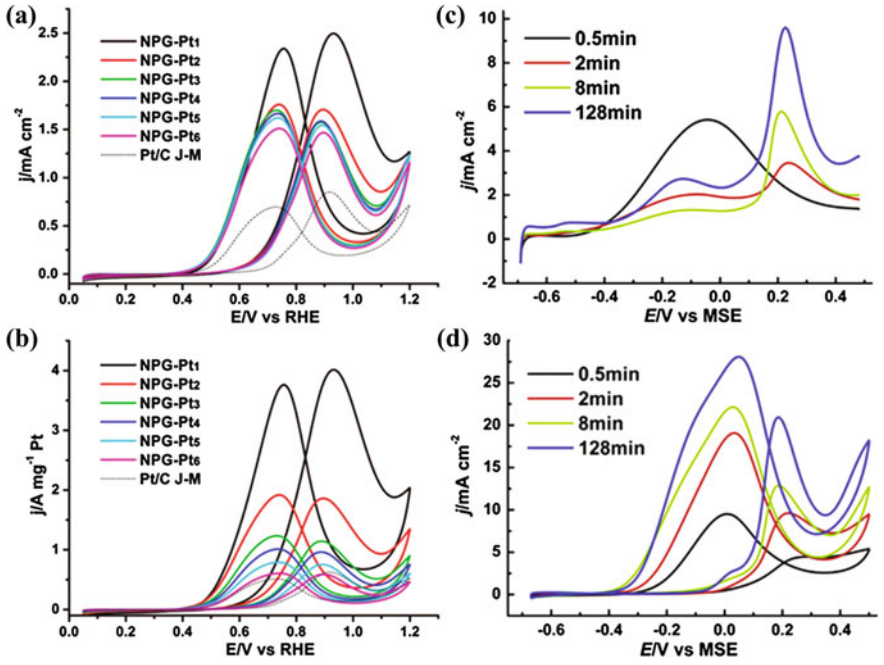

Fig. 3.11 **a**, **b** ECSA- and Pt mass specific catalytic activities of Pt–NPG leaves with different Pt loadings made by Cu-UPD method in 0.5 M H_2SO_4 + 1.0 M C_2H_5OH; **c**, **d** Electrochemical catalytic activities of Pt–NPG leaves made by electroless method with different Pt loadings in 0.1 M $HClO_4$ + 0.1 M HCOOH and 0.1 M $HClO_4$ + 0.1 M HCHO mixed solutions. Reproduced from Langmuir, 2009, 25, 561. Copyright 2009, ACS and Electrochem Commun 2008, 10, 1494. Copyright 2008, Elsevier

methanol electrooxidation, Pt–NPG leaf sample with one Pt deposition layer shows much enhanced catalytic activity even compared with samples with more Pt deposition layers. The decrease of ECSA-specific catalytic activities with the increase of Pt loading imply the electronic perturbation of Pt by underneath gold substrate should facilitate ethanol electrooxidation. The different response of oxidation kinetic between methanol and ethanol to the electronic perturbation of Pt should be caused by the quite different reaction paths and this phenomenon deserves further investigation.

The electrooxidation reactions of formic acid and formaldehyde are often investigated on one hand to understand the oxidation mechanism of small organic molecules fundamentally and on the other hand to develop new type fuel cells with alternative fuel options. The catalytic activities of Pt–NPG leaf toward formic acid and formaldehyde electrooxidation are investigated by CV in 0.1 M $HClO_4$ + 0.1 M HCOOH and 0.1 M $HClO_4$ + 0.1 M HCHO mixed solutions [35]. As expected, the formaldehyde oxidation currents increase with the increase of Pt loading which is caused by the improved electrochemical surface area of Pt. The electrooxidation of formic acid is quite different. At higher Pt loading, the oxidation currents increase with the increase of Pt loading. However, for low Pt loading sample, only one oxidation peak appears at lower potential which is totally different from that for high Pt loading samples, where there are two broad anodic peaks. The distinct voltammetric behavior for low Pt loading samples is caused by the switch of the reaction path of formic acid electrooxidation on small Pt ensembles and will be discussed later in detail.

Despite the promising electrochemical performance discussed above, the stability of Pt–NPG nanocomposites should be addressed before discussing their potential application in fuel cells. The structure evolution of Pt–NPG leaf has been investigated at different elevated temperature [36]. It has been found that the porous structure could be retained after annealing at 300 °C for 48 h, which is markedly different from that of bare NPG which would undergo significant coarsening at this temperature even for a couple of minutes. The stabilization effect of Pt on NPG leaf should be ascribed to the relatively slow diffusion rate of Pt as compared with Au. Interestingly, although the porous structure maintains very well upon low temperature (below 300 °C) annealing, careful structural analyses with HRTEM still reveal quite dramatic surface structure evolution details. After annealing at 150 °C, the growth of Pt islands is already seen. The situation is much more apparent if the temperature is raised to even higher temperature of 300 °C where all Pt nano-islands are found flattened out on the surface of NPG substrate. Coupled with surface sensitive electrochemical characterization techniques, this surface structure evolution is ascribed to the atomic interdiffusion between Pt islands and Au substrate. This interdiffusion process changes the originally core–shell typed Au–Pt nanostructure into the eventual Au–Pt surface alloys at temperature down to about 150 °C.

3.3.4 NPG-Based Electrodes in PEM Fuel Cells

To function in fuel cells, traditional nanoparticulate Pt/C catalyst is processed by first mixing with an ionomer solution such as Nafion which acts as binder and proton carrier to form a catalyst ink. The catalyst suspension is then brushed or sprayed onto a gas diffusion layer (GDL) to form catalyst layer which is in turn hot pressed onto each side of a solid electrolyte membrane to form an MEA. By substituting traditional nanocatalysts with nanoporous metals such as Pt–NPG leaves, particular structural advantages can be achieved in a conceptually new design of MEAs (Fig. 3.12).

(1) The utilization of catalytically active materials such as Pt can be significantly improved. As demonstrated above, monolayer type Pt–NPG electrodes can be readily produced, where all Pt atoms are accessible by reactants and can contribute to the catalytic reaction.
(2) The highly conductive NPG substrate greatly facilitates the electron transportation from surface Pt through the interconnected porous structure to the current collector.
(3) NPG substrate is more corrosion-resistive as compared with carbon, which would contribute to the electrochemical stability of the composite catalyst under the harsh operation conditions.
(4) The open and tunable porous structure allows fast diffusion of fuel molecules to the entire framework.

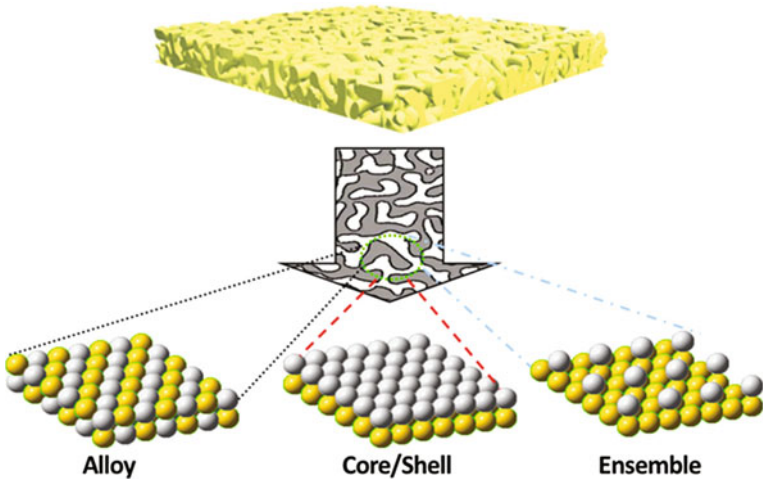

Fig. 3.12 Schematic illustrations of the NPG-based fuel cell electrodes which offer particular structural flexibility for high performance fuel cells

(5) Unlike the weak interaction between Pt nanoparticles and carbon support, the strong metallic bond between Pt and NPG substrate can stabilize the Pt nanoparticles from detaching from the substrate.
(6) The surface chemistry of the nanoelectrodes can be optimized, ranging from core–shell structures, surface nanoalloys, and even well-defined surface ensembles for superior performance (examples will be given in the following sections when discussing DFAFCs).
(7) By reducing the catalyst layer thickness from tens of microns down to sub-micron scale, the overall MEA structure can be greatly simplified.

3.3.4.1 NPG-Based Electrodes in Hydrogen Fuel Cells

A functional hydrogen fuel cell employing Pt–NPG electrodes was reported first by Ding and Erlebacher in 2004 [29]. To make the cell, two pieces of Pt–NPG leaves are collected from the water solution surface onto a sheet of Nafion 112 polymer electrolyte, one on each side. Upon air-drying, the sandwich structure is heated at 120 °C for 2 min to form a completed MEA. This heating step serves to pull ionomer into the pores of the Pt–NPG leaf, improving adhesion between the Nafion and the electrode and also creating pathways for proton conduction from within the electrode to the ionomer. In this way the region of triple-phase contact of the fuel cell containing active catalyst is confined to within a 100 nm thick layer. The MEA is sandwiched between two pieces of Toray carbon paper, and this structure is in turn sandwiched between two graphite current collecting plates on which gas flow channels have been machined into an area of 1 cm^2 (Fig. 3.13).

Figure 3.14 shows two polarization curves for two MEA samples running with H_2 and O_2 bubbled through water at room temperature and atmospheric pressure. Although those cells are not tested under optimized operating conditions, typical *I–V* curves are characterized by an open circuit voltage near 1.0 V, a short circuit

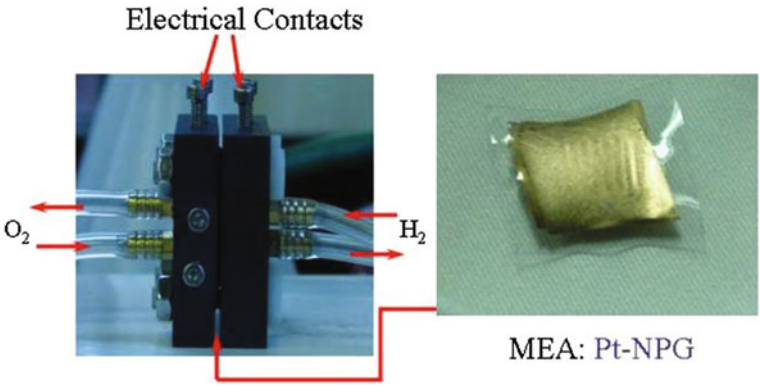

Fig. 3.13 Digital pictures of the testing cell and a typical Pt–NPG based MEA

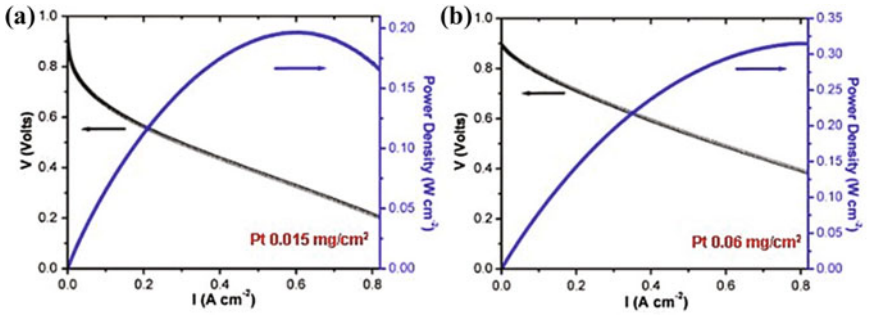

Fig. 3.14 Cell voltage and power density versus current density for two Pt–NPG based hydrogen fuel cells. The MEAs have a Pt loading of 0.015 mg/cm^2 **a** and 0.06 mg/cm^2 **b** respectively on each electrode side

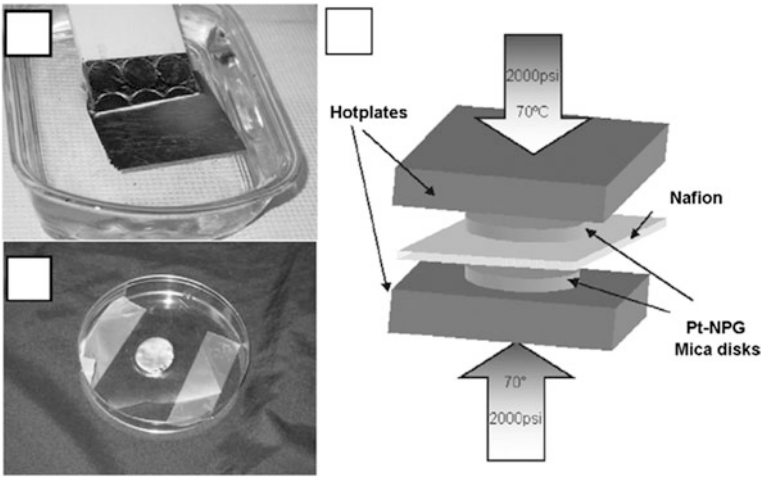

Fig. 3.15 Process of MEA fabrication with NPG leaves. **a** Transfer of Pt–NPG leaf with mica sheets; **b** The stamping procedure to make the MEA; and **c** Final MEA. Reproduced from J Power Sour 2007, 165, 65. Copyright 2007, Elsevier

current density higher than 0.8 A cm^{-2}, and a maximum power density around 0.20 W cm^{-2}. On a per gram basis, these two sample cells generated 6.67 and 2.86 kW/g of Pt, which compares favorably to the performance of then industrial state-of-the-art, which typically generate a peak power near 1.0 W cm^{-2} with loading of 0.5 mg of Pt cm^{-2} on each electrode (a specific power of order 1.0 kW g^{-1}) [1].

Based on the same materials, Zeis et al. developed a more reliable technique to make such an MEA [37]. As shown in Fig. 3.15, Pt–NPG leafs floating on water surface are first caught by a mica sheet from underneath. After drying in air, the samples on mica sheets are hot pressed onto each side of a moisturized Nafion film.

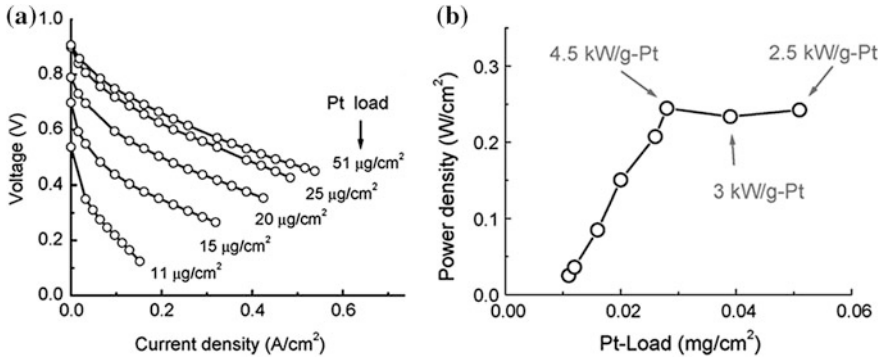

Fig. 3.16 **a** Charge density corresponding to adsorbed hydrogen on Pt–NPG leaf MEAs versus Pt loadings; and **b** Electrochemically active surface area versus Pt loadings. ECSA of a commercial MEA (0.5 mg cm^{-2}) was also shown for comparison. Reproduced from J Power Sour 2007, 165, 65. Copyright 2007, Elsevier

It is reported that MEAs prepared at 70 °C demonstrated the highest and reproducible performance.

The prepared Pt–NPG leaf-based MEAs are then sandwiched between two pieces of Teflon treated carbon cloth and then fixed between two stainless steel current collection plates for test and characterization in hydrogen fuel cells. The fuel cell performance with Pt–NPG leaves is shown in Fig. 3.16. It is obvious that the open circuit potentials increase with the Pt loading and the highest value approaches ~0.9 V. Compared with the commercial Pt/C catalyst, this value is about 0.1 V lower which may be caused by the kinetic losses at the cathode side at such low Pt loadings. The maximum power densities as the function of Pt loadings are shown in Fig. 3.16b. The curve follows the trend of electrochemical surface areas which increase at low Pt loading and remain unchanged upon further increasing the loading. Further increasing the electrochemical surface area may be a potential direction to increase the fuel cell performance. Although the fuel cell performances are inferior to that of commercial Pt/C catalyst, the Pt specific activity (2.5–4.5 kW/g-Pt) is typically within a factor of two of what is reported for many state-of-the-art fuel cells [37].

3.3.4.2 NPG-Based Electrodes in Direct Formic Acid Fuel Cells

Compared with hydrogen fuel cells, direct liquid fuel cells show great potential to support portable electronic devices and off-grid facilities. Compared with methanol, formic acid has received increasing attention recently due to its advantages of being nonflammable, less toxic, higher electromotive force, and lower fuel crossover [38, 39]. However, the commercialization of DFAFCs has been hampered by the massive usage of precious metals such as Pt and Pd, which is typically on the order of several milligrams per square centimeter area at anode. It is particularly

challenging for the development of DFAFC anodes because Pt seems to be the only metal that can tolerate the acidic cell operation conditions while exhibiting certain activity toward formic acid oxidation (FAO). Even more unfortunate is the spontaneous decomposition of formic acid molecules to CO-like intermediates which poison the Pt catalysts, and deteriorate the cell performance. An ideal anode electrode in DFAFCs should then simultaneously fulfill the following desired properties: high Pt utilization, high catalytic activity toward formic acid electrooxidation and excellent durability against CO poisoning.

In order to rationally design such a catalyst, one should first be aware of the working mechanism on the electrode at the molecular level. It is commonly accepted that formic acid electrooxidation takes place on Pt via a dual-path mechanism [40]. The first path is to form carbon monoxide intermediate by dehydration and further to be oxidized to CO_2. As the oxidation of CO takes place at higher potential, it thus acts as the poisoning species and passivates the Pt catalyst surfaces at low potential. The other path is to form CO_2 via active intermediate which is believed to be formate and has also been demonstrated by time resolved surface enhanced infrared absorption (SEIRA) spectroscopy by Osawa and coworkers [41]. However, the dual-path mechanism was recently challenged by R. Behm et al. who believed there should be at least another path to explain the apparent difference of the ratio between formate band intensity and faradic current at different potentials, although they have no direct spectroscopic evidence yet [42]. Therefore they proposed a triple path mechanism which is shown in Fig. 3.17a. Although the exact mechanism is still under debate [43], it is quite clear and accepted that the desired direct reaction path requires small Pt ensembles [44] which is also consistent to reported experimental results that adsorbed atoms on Pt could facilitate the reaction [45] and simulation results that at least three adjacent Pt atoms are needed in order to proceed via the unfavorable dehydration path to form CO (see Fig. 3.17b) [44].

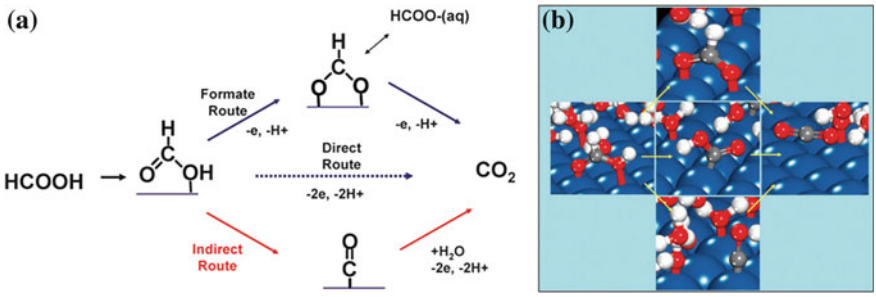

Fig. 3.17 **a** Reaction paths involved in formic acid electro-oxidation; **b** DFT calculated surface ensembles required for the direct oxidation path (*center*), the indirect path through CO (*bottom*) and the formate path (*top*) for the oxidation of formic acid over Pt(111) to CO_2 at a constant potential of 0.5 V. Reproduced from Faraday Discuss 2008, 140, 363. Copyright 2008, The Royal Society of Chemistry

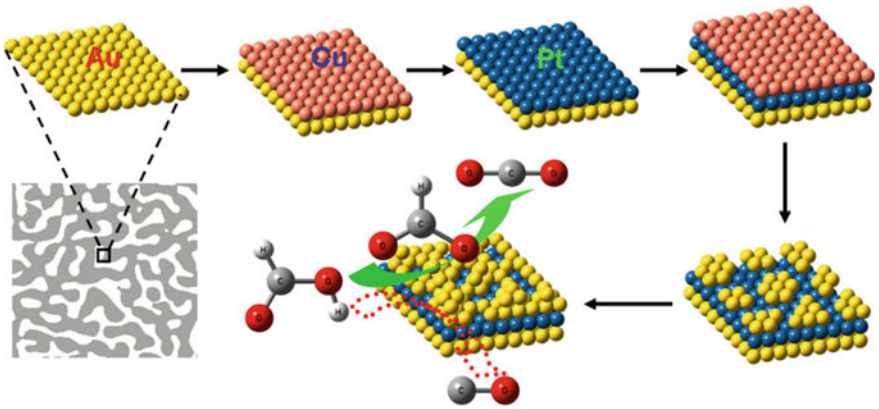

Fig. 3.18 Schematic illustration of the fabrication procedure of gold covered monolayer Pt catalyst on NPG leaf

Guiding by the understanding of the desired structure, Wang and Ding proposed a novel strategy to prepare highly active and stable catalysts for formic acid electrooxidation [46]. The preparation procedure can be illustrated by a carton in Fig. 3.18. Monolayer Pt is first deposited onto the ligament surface of NPG leaf using Cu UPD-mediated method to achieve very high Pt utilization. Then sub-monolayer Au clusters are deposited further onto the monolayer Pt covered NPG leaf in order to divide the continuous surface into surface ensembles that are small enough to facilitate the desired direct oxidation path. With monolayer structure, the Pt loading in this kind of materials is only 2 μg cm^{-2} of geometric area. As the monolayer Pt has been divided into small ensembles, it should be very active for formic acid electrooxidation. And also because of the protection of outer layer Au, the monolayer Pt should be stabilized against dissolution which guarantees the durability of the low Pt loading catalyst.

The formic acid electrooxidation results of these catalysts are shown in Fig. 3.19. The CV profile of NPG-Pt_1 sample shows a peak at 0.9 V with a shoulder at lower potentials between 0.4 and 0.7 V. The result is similar with that of bulk Pt surface which means the whole Pt surface is severely poisoned by CO intermediate. After a little amount of gold deposition, the peak current density at 0.9 V decreases and the shoulder evolves into a new peak at about 0.6 V. Further depositing gold on the surface results in a much enhanced current density at lower potential of 0.5 V and nearly complete suppression of peak at higher potential of ~0.9 V. Because CO could not be oxidized at such low potential, the much enhanced current density should only be ascribed to the direct oxidation of formic acid molecules at CO-free sites. These results provide clear evidence that the catalytic reaction path of formic acid electrooxidation has been changed from an indirect path on monolayer Pt surface to a direct one on gold covered monolayer Pt surface. In terms of the Pt mass specific activity, the current density at 0.5 V reaches 7.966 A mg^{-1} for the NPG–Pt_1–Au_2 sample, which is almost 140 times higher than that of Pt/C at the

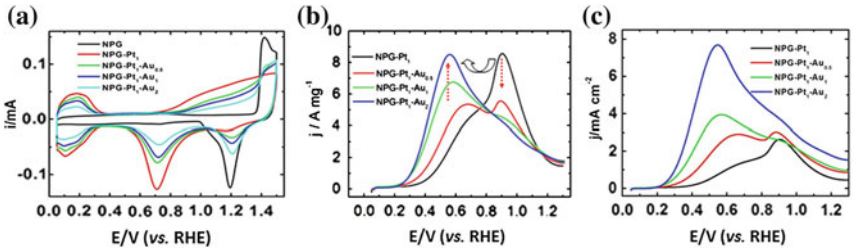

Fig. 3.19 **a** Electrochemical CV curves for NPG–Pt_x–Au_y catalysts in 0.5 M H_2SO_4; **b** Pt mass-specific and **c** ECSA-specific CV curves for NPG–Pt_x–Au_y catalysts in 0.1 M $HClO_4$ and 0.05 M HCOOH (only forward segments were shown for clarity). Reproduced from Adv Mater 2010, 22, 1845. Copyright 2010, Wiley-VCH

same potential (0.057 A mg^{-1}). It should be further emphasized that for this particular sample, a significant number of surface Pt sites ($\sim$62 % for NPG–Pt_1–Au_2) have been blocked with less-active Au atoms, indicating an extraordinary improvement of the intrinsic activity of thus-designed surface (Fig. 3.19c).

To understand the detailed mechanism of the catalytic activity improvement, time resolved SEIRA spectroscopy is used to monitor the intermediate on the electrode surface during the potential cycling and the results are shown in Fig. 3.20. From the spectra, we can see there is a little CO formation on gold covered Pt surface which is far less compared with bulk Pt surface. To determine the coverage of CO during formic acid electrooxidation, the spectra are compared with that of monolayer CO covered surface, which provides a CO coverage of about 16 % for the new catalyst, indicating a structural perfectness of better than 80 % on this high surface area electrode. These results demonstrate that after Au deposition, the monolayer Pt surface has been separated into small ensembles most of which are small enough to suppress the formation of CO poisoning intermediate but large and active enough to facilitate the direct reaction path. To provide a clear picture for the reaction path changing, NPG–Pt_1–Au_1 electrode is first covered by monolayer CO, and then tested for formic acid electrooxidation. As shown in Fig. 3.20c, there is no anodic current below 0.8 V during the first CV segment because the surface has been totally poisoned by CO. After CO oxidation, there is tremendous anodic current onset around 0.2 V during the third CV segment which could be ascribed to formic acid electrooxidation at gold covered Pt surface via the direct path.

Being highly effective, the above-mentioned electrocatalysts still contain a majority of Pt atoms not accessible by the fuel molecules due to the coverage of surface Au clusters. More recently, Wang and Ding developed a molecular self-assembly/electrodeposition (MSA-ED) method that allows high dispersion of atomically small Pt ensembles onto NPG surface, a nearly ideal formic acid electrocatalyst that allows simultaneous fulfillment of perfect Pt utilization and perfect Pt intrinsic activity [47]. They found that $PtCl_6^{2-}$ ions could form a stable monolayer structure on the ligament surface of NPG leaf, a phenomenon very similar to those of platinate complex ions adsorbed on the single crystalline Au

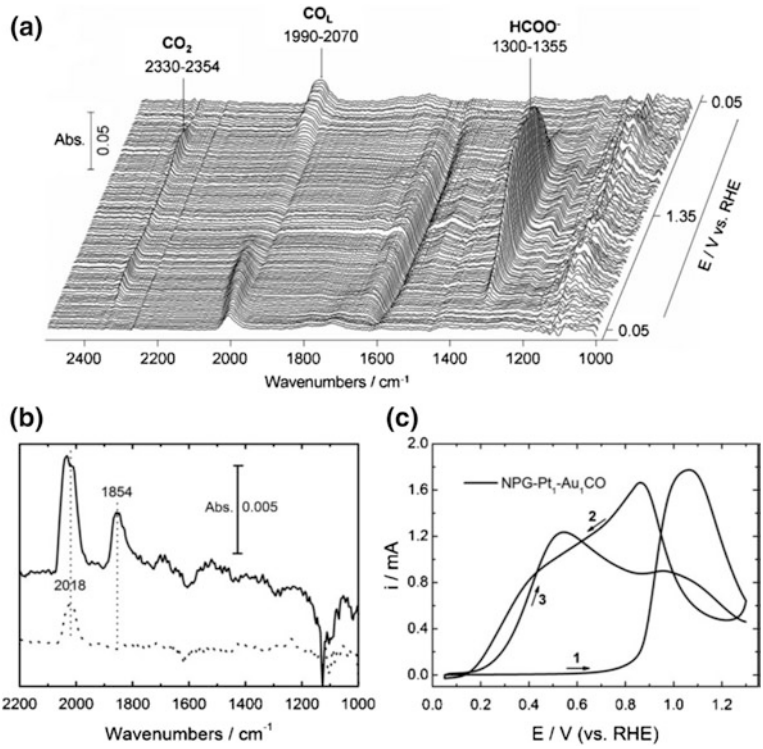

Fig. 3.20 **a** Series of SEIRA spectra for the Si–Au–Pt_1–Au_2 electrode (made via a similar fabrication procedure with NPG–Pt_1–Au_2 catalyst) acquired simultaneously with the CV cycling between 0.05 and 1.35 V; **b** Comparison of SEIRA spectra for a Si–Au–Pt_1–Au_2 electrode in 0.1 M HClO4 + 0.05 M HCOOH (*dotted line*) and pre-dosed with monolayer CO (*solid line*) in 0.1 M HClO4; **c** Electrochemical response of NPG–Pt_1–Au_1 electrode (pre-adsorbed with monolayer CO) in 0.1 M $HClO_4$ + 0.05 M HCOOH. Reproduced from Adv Mater 2010, 22, 1845. Copyright 2010, Wiley-VCH

(111) electrode [48]. Upon electroreduction, these self-assembled $PtCl_6^{2-}$ ions could be reduced and deposited onto the surface of NPG. Because each $PtCl_6^{2-}$ complex ion occupies the surface area of seven sub-layer Au atoms, ideally the surface Pt coverage will be $\sim$14 % (Fig. 3.21a). Surprisingly, the measured Pt coverage on NPG is in excellent agreement with this value. It should be noted that the similar experiments on single crystalline electrodes or bulk Au foils would not achieve the same goal because thus-produced Pt atoms are highly mobile to form larger ensembles or clusters. However, HRTEM characterization reveals a unique structure of NPG, with the ligament surfaces mostly terminated with {111} facets, showing sub-nanometer-sized steps (Fig. 3.21b). The presence of small steps on the NPG surface is believed to be beneficial to inhibiting the diffusion of Pt atoms and trapping them on the surface of the NPG, forming very small ensembles, the most favorable sites for FA molecule oxidation.

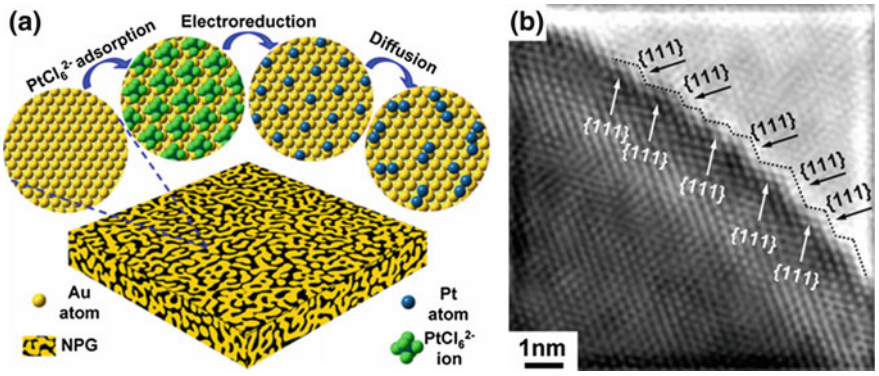

Fig. 3.21 **a** Schematic illustration of the fabrication procedure of dispersed Pt atoms or small ensembles on NPG. **b** HRTEM image of NPG ligament. The surface steps are illustrated by *dashed lines*. Reproduced from Chem Sci 2014, 5, 403. Copyright 2014, ACS

The success of this unique surface modification technique is confirmed by the comparison of their formic acid electrooxidation activities with the commercial Pt/C catalysts. As shown in Fig. 3.22b, for the Pt/C catalyst, there is only a small oxidation current at potentials below 0.8 V in the forward scan, as the surface is almost totally passivated by CO. When the poisoning CO molecules start to be oxidized, there is a steep increase in the anodic current at about 0.8 V. In contrast, NPG–Pt_1 exhibits completely different electrochemical responses in this potential range, which are characterized by a dramatic negative shift in onset potential to below 0.2 V and huge anodic peaks at around 0.5 V, indicative of successful inhibition of the formation of the poisoning CO intermediates due to the selection of the direct reaction path. At this potential, the NPG–Pt_1 catalyst shows a peak current density of 21.7 A mg^{-1} at a sweep rate of 50 mV s^{-1}, which is approximately 380 times higher than that of the Pt/C catalyst (0.057 A mg^{-1}).

These novel electrodes have been tested in actual single fuel cells. For comparison purposes, all fuel cells use the same type of Pt/C cathode (2.2 mg cm^{-1}) made by the standard MEA fabrication technique. Figure 3.22d shows the current–voltage and current–power polarization curves of NPG–Pt catalysts with different Pt loading. Although the Pt loading is typically orders of magnitude lower than the commercial Pt/C catalysts (2.2 mg Pt cm^{-2}), the NPG–Pt 0.013 mg catalyst shows both higher open circuit voltage and maximum power output with impressive stability. Specifically, its maximum power reaches 61 mW cm^{-2}, which is 1.5 times of Pt/C 2.2 mg catalyst (40 mW cm^{-2}). If one normalizes the apparent maximum power to the amount of Pt used on anode, the NPG-Pt 0.013 mg sample exhibits a 260-fold enhancement in specific power efficiency (4.7 vs. 0.018 W mg^{-1}). Once again, the tremendous performance enhancement should be mainly attributed to the nearly optimized Pt ensemble structure involved in the NPG–Pt structure. Besides, these electrodes also show excellent durability which may be attributed to the

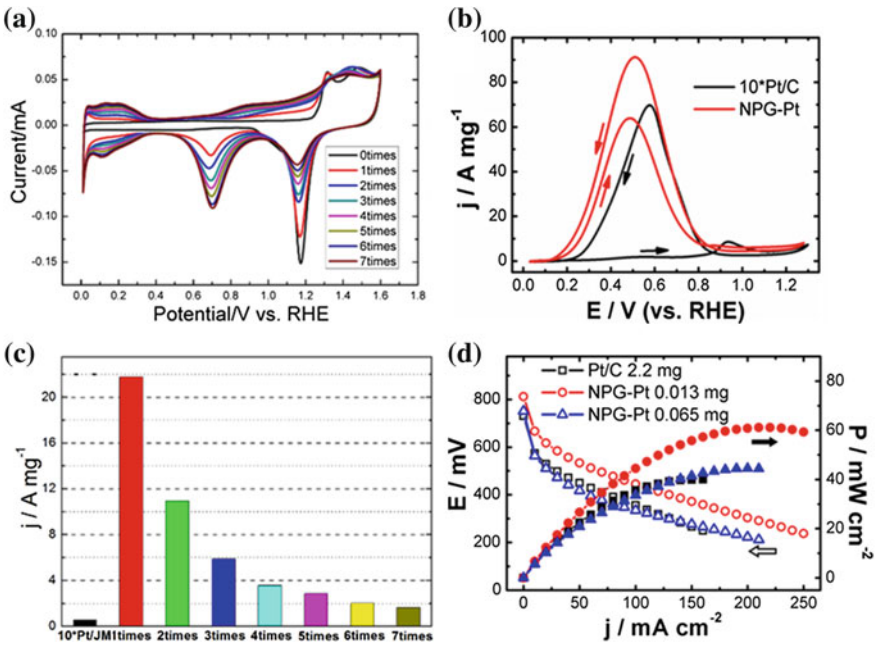

Fig. 3.22 **a** CV curves of NPG and NPG–Pt electrodes prepared for 1–7 deposition cycles (*black-brown*) in 0.1 M $HClO_4$. The ordered changes in hydrogen adsorption/desorption, Pt and Au oxidation/reduction can be clearly seen. **b** Pt mass specific catalytic activities of NPG–Pt_1 and Pt/C (magnified by 10-fold for clarity) in 0.5 M H_2SO_4 + 1 M HCOOH. **c** Pt mass specific catalytic activities of NPG–Pt electrodes prepared for 1–7 deposition cycles and Pt/C. **d** Current–voltage and current–power polarization curves for Pt/C 2.2 mg, NPG–Pt 0.013 mg, and NPG–Pt 0.065 mg anode catalysts in DFAFC single cells. Reproduced from Chem Sci 2014, 5, 403. Copyright 2014, ACS

strong bonding between Pt surface ensembles and Au substrate, and an electric stabilization effect by Au.

Previous approaches focus on the optimization of ensemble structure of Pt with an aim to maximizing its intrinsic activity toward direct oxidation of fuel molecules such as formic acid, and under these conditions NPG's primary role is to provide a chemically stable, electrically conductive, high surface area porous scaffold. It is well known that alloying Pt with other elements such as Bi is an effective route to dramatically improve the catalytic activity by changing the reaction paths or facilitating the removal of CO poisoning intermediates [49]. Based on this concept, Wang and Ding designed NPG leaf supported Pt/Bi catalysts by firstly forming monolayer Pt covered NPG via the previously noted Cu UPD-mediated deposition, and then electrochemically coating sub-monolayer Bi species further on top (Fig. 3.23) [50]. By confining high density, ultrahigh reactive sites into an ultrathin catalyst layer, they demonstrated a high performance DFAFC anode with extremely low Pt loading down to 3 μg per cm^{-2}. Electrochemical CV showed very high

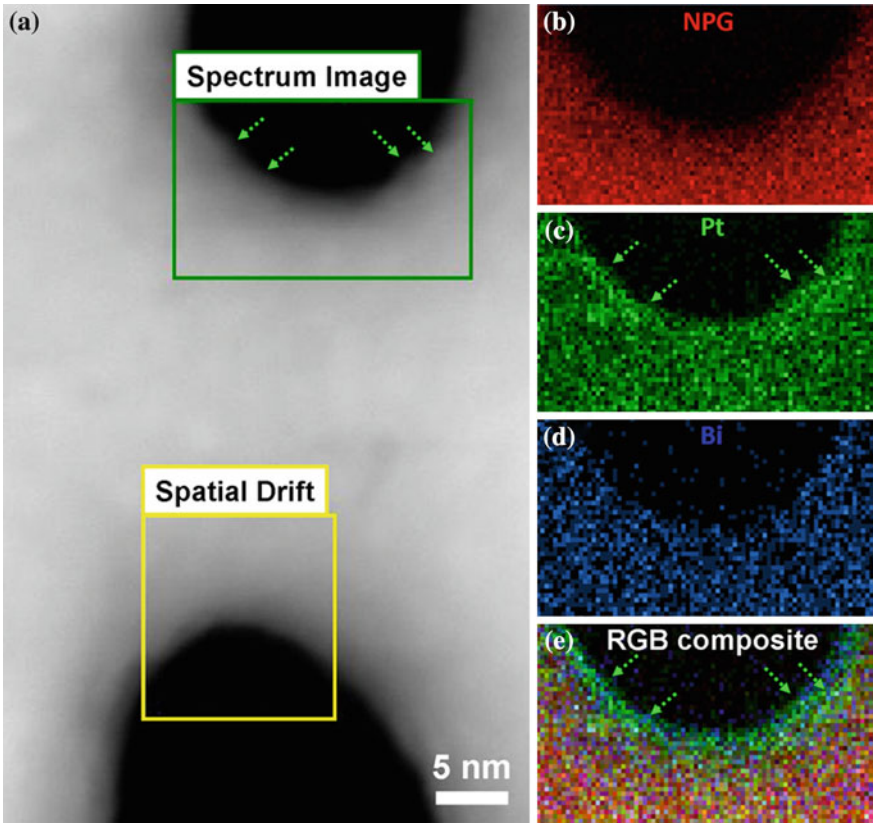

Fig. 3.23 HAADF TEM image of NPG–Pt–Bi catalyst and the corresponding EDS mappings. **a** HAADF TEM image. **b** EDS mapping for Au. **c** EDS mapping for Pt. **d** EDS mapping for Bi. **e** EDS mapping overlay for Au, Pt and Bi

electrochemical performance of NPG–Pt–Bi toward formic acid electrooxidation, and at 0.6 V the NPG–Pt–Bi catalyst could exhibit over 570-fold enhancement in Pt mass specific activity as compared with the Pt/C catalyst (103.4 vs. 0.18 A mg^{-1}) under the same testing conditions. This value is so far the highest ever achieved on DFAFC anodes.

Figure 3.24a compares the current–voltage (C–V) and current–power (C–P) polarization curves of NPG–Pt–Bi catalysts with different Pt loadings and a commercial Pt/C electrode as the control. Typically, the NPG–Pt–Bi based anodes show both higher open circuit voltage and maximum power output. For example, the sample with 3 micrograms Pt loading already exhibits larger maximum power than the Pt/C catalyst (44 vs. 40 mW cm^{-2}). The maximum power output for NPG–Pt–Bi 0.02 mg catalyst is $\sim$80 mW cm^{-2}, which is twice of that for Pt/C catalyst although the catalyst layer is only 100 nm thick for this specific sample. By normalizing the performance to the amount of Pt used on anodes, the specific

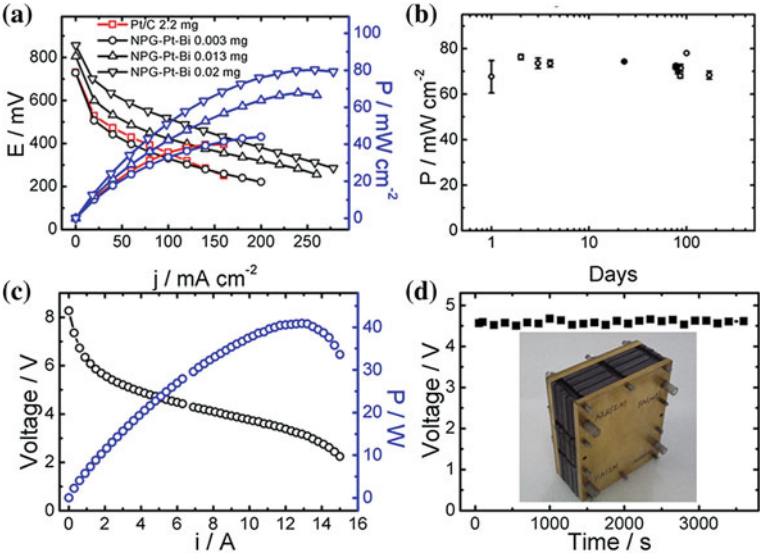

Fig. 3.24 Single-cell performances of NPG–Pt–Bi and Pt/C based MEAs. **a** C–V and C–P polarization curves for Pt/C catalyst (*red*) with 2.2 mg Pt loading and NPG–Pt–Bi samples with Pt loading of 0.003, 0.013 and 0.02 mg per cm^2 in the anode. **b** Durability test of NPG–Pt–Bi 0.09 mg catalysts. **c** C–V and C–P polarization curves for a 10-cell stack (each cell: 6 cm × 8 cm, with Pt loading of 0.09 mg cm^{-2}) using NPG–Pt–Bi catalysts as anodes. **d** Voltage–time curves at a constant current density of 100 mA cm^{-2}. Insert is a digital photo of this stack

maximum power densities of NPG–Pt–Bi samples are in the range of 4–14.7 W mg^{-1} with the highest value for the catalyst with 3 micrograms Pt. In contrast, the data in literatures are typically in the range of 10–280 mW mg^{-1}, indicating two orders of magnitude improvement in specific power efficiency for these new electrodes. It has to be emphasized that even when the mass of NPG substrate is considered, the anode specific power density normalized to the *total* precious metal loading reaches 667 mW mg^{-1} for the NPG–Pt–Bi catalyst which is still much higher than the reported ones. The fuel cell performance can also be boosted to over 160 mW cm^{-2} by testing the cell under more vigorous conditions. These nanoelectrodes also demonstrate surprisingly good durability. Repeatedly operating this fuel cell in long time period of over 6 months (each for more than 4 h) always generates a power density around 70 mW cm^{-2}, indicating the excellent durability of this catalyst (Fig. 3.24b). And these fuel cell catalysts can also tolerate common fuel impurities including CH_3OH, $HCOOCH_3$ and CH_3COOH at concentration as high as 500 ppm.

To further demonstrate their applicability for DFAFCs, multicell stacks were assembled by using the NPG-Pt–Bi based MEAs. From Fig. 3.24c, the maximum power density achieves 40.9 W at a current of 12.9 A, indicating an area specific power density of 85 mW cm^{-2} which is a little higher than that in a single cell. This may be caused by the slight increase in temperature during stack operation. When

the fuel cell stack is operated at 4.8 A, there is almost no voltage decline over 10 h period which again proves its high stability and reliability (Fig. 3.24d) [50].

3.4 Processing of Nanoporous Alloys and Composites

As a facile and green technique to produce nanoporous (NP) metals, dealloying method has been widely used to prepare NP alloy electrocatalysts, by selectively dissolving the more active component out of binary, ternary, quaternary, or even quinary alloys. The preparation route commonly consists of the following steps. Firstly, the multicomponent alloys with controlled compositions are melted or milled from the respective pure source metals under protective atmosphere if necessary. Secondly, dissolution of Al from precursor alloys is carried out in alkaline or acidic solutions (Fig. 3.26) at ambient temperature. Thirdly NP alloys with pre-determined molar ratios are generated by washing and drying the collected powder or foil products. The combination of dealloying with underpotential deposition (UPD), displacement reaction, or other surface modification techniques would obviously offer more flexibility in designing multicomponent nanoporous structures. Owing to the unique three-dimensional bi-continuous ligament/channel structure with high active surface area and good permeability, which are all highly desired characteristics for the electrocatalytic reactions, various NP alloys and composites, especially those with platinum or platinum group metals have been developed as the anode or cathode materials for fuel cell catalysis.

3.4.1 NPM-Based Anode Catalysts

In fuel cells, oxidation reactions of H_2 and small organic molecules are conducted on anodes. Up to now, Pt and Pt-based catalysts are still the most employed electrode materials for low temperature fuel cells. However, the successful application of Pt and Pt-based catalysts as anode materials still requires the further improvement of their activity, durability, and cost-effectiveness. Firstly, low anode activity not only restricts the fuel cell power output, but also causes other problems, e.g., fuel crossover which will bring in the mixed potentials on cathode side and lower the overall utilization efficiency. Secondly, the durability of traditional Pt-based catalysts is challenged by nanoparticle aggregation during operation due to their weak adsorption to the carbon support, and most significantly by catalyst poisoning due to the strong adsorption of CO-like species arising from residual CO in reforming gas or partial oxidation of small organic fuels such as methanol. Finally, there is always strong demand for decreasing the Pt usage due to its low abundance. Therefore, constructing Pt-based alloys or composites by adding non-precious metals to enhance the Pt utilization efficiency, or developing non-platinum electrocatalysts with outstanding electrocatalytic activities at no or low cost of their durability is highly pursued in fuel cell community.

During the early stages of practice, AuAg alloys are the most investigated model systems to study how different dealloying parameters affect the structure formation and evolution of the resulted NPG. However, NPG produced under normal conditions often exhibits pore or ligament size larger than 10 nm, due to the relatively large surface diffusivity of gold element. Apparently, the addition of elements with low surface diffusivity into alloy precursors can effectively refine the ligaments and channels of nanoporous metals (or alloys). This prediction was first realized by Erlebacher and coworkers who discovered the addition of Pt to precursor Ag/Au alloys effectively stabilizes the morphology of the porous metals formed [51]. As Pt possesses much slower surface diffusion rates than Au, during dissolution, Pt embedded in exposed terraces should segregate to the edges of the growing islands, stabilizing them, ultimately reducing the scale of porosity as well as leading to a Pt-rich shell. Based on the similar concept, Ding and coworkers proposed that dealloying can be extended to multicomponent alloy systems to fabricate nanoporous alloys with tailorable alloy composition and pore/ligament dimension. For example, selective etching of Cu from Au/Pt/Cu alloy precursors results in the formation of three-dimensional bi-continuous porous network structures with uniform pores and ligaments less than 10 nm (Fig. 3.25) [52]. Moreover, nanoporous Au/Pt alloys have a single-phase cubic structure with relatively uniform and pre-determined compositions across the samples, and they also exhibit composition dependent electrocatalytic activity toward anodic oxidation of fuel molecules such as methanol and formic acid. Zhang et al. reported almost at the same time that the addition of the third element Pd into Mg–Ag results in the formation of an ultrafine nanoporous $Ag_{80}Pd_{20}$ alloy which exhibits superior catalytic activity toward electrooxidation of ethanol [53].

Due to its amphoteric properties and excellent alloy formation capability, Al has been widely chosen to prepare nanoporous alloys. It is found that elemental doping has no influence on the phase constitution of rapidly solidified Al–Au–Pt, Al–Au–Pd, and Al–Au–Pt–Pd alloys, and all these precursor alloys are composed of a single Al_2Au-type intermetallic compound [Al_2(Au,Pt), Al_2(Au,Pd) and Al_2(Au,Pt,Pd)]. Ultrafine NPG alloys with ligaments/channels less than 10 nm can be fabricated by dealloying Al_2Au-based precursors under free corrosion conditions. When performing dealloying in 20 wt% NaOH solution, a certain amount of Pt or/and Pd addition offers superior refining effect and the length scale of ligaments/channels in the as-obtained np-Au alloys can reach $\sim$3 nm after Pt doping or Pt/Pd co-doping. When performing dealloying in 5 wt% HCl solution, the anti-coarsening capacity of Pt doping is more remarkable than that of Pd doping. In addition, the amount of doping can also affect the anti-coarsening ability of ligaments/channels in the as-obtained NP alloys [54]. Up to now, transition metals that have been used to alloy with Pt and Pd, with an aim to decrease the precious metal loading and to enhance their intrinsic activity or durability, include Cu [55–62], Fe [63–66], Co [67, 68], Ni [68, 69], and Au [70–72]. For example, NP-PtPd alloy [73, 74] with ligament size $\sim$5 nm can be straightforwardly prepared by chemically dealloying Pt–Pd–Al ternary alloys in alkaline or acidic solution (Fig. 3.26). What's more, hierarchical bi-model NP alloys with higher porosity can also be constructed via the selective

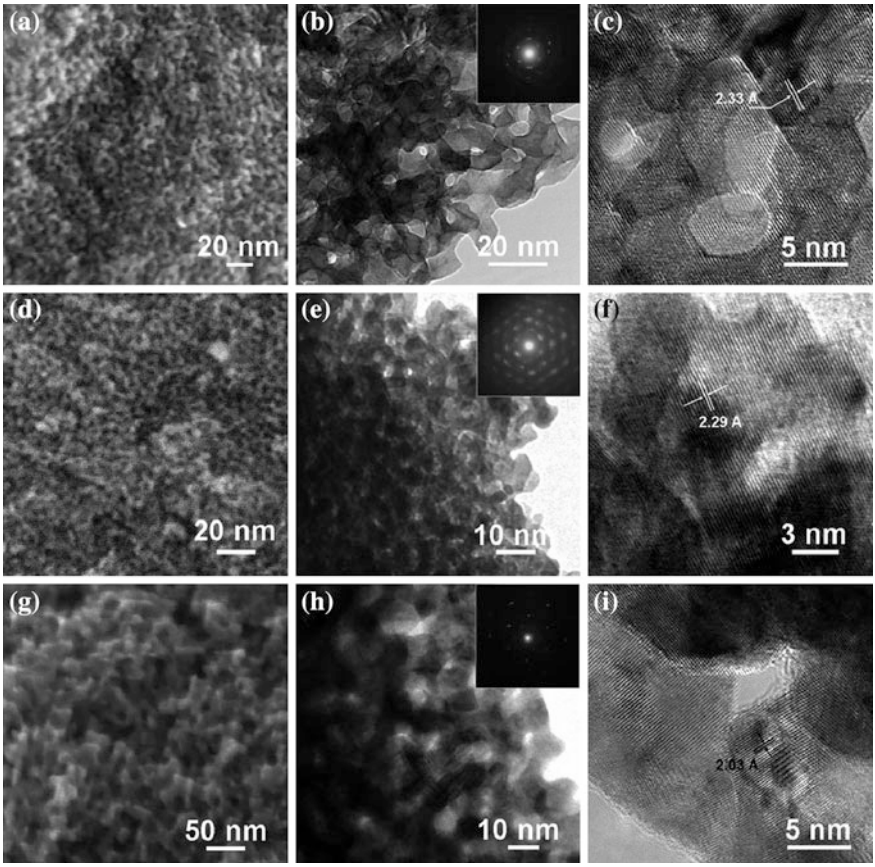

Fig. 3.25 SEM, TEM, and HRTEM images of nanoporous Au/Pt alloys by dealloying **a**, **b**, **c** $Au_{10}Pt_{10}Cu_{80}$, **d**, **e**, **f** $Au_4Pt_{16}Cu_{80}$ and **g**, **h**, **i** $Au_{16}Pt_4Cu_{80}$ alloys, respectively. Reproduced from Phys Chem Chem Phys 2010, 12, 239–246. Copyright 2010, The Royal Society of Chemistry

dissolution of more active component in the NP alloys (Fig. 3.27), or via a two-stage electrochemical corrosion process from rapidly solidified ternary alloys (Fig. 3.28). For example, by dealloying in alkaline solution, NP-PtCu alloy (Fig. 3.27a) can be readily obtained from Pt–Cu–Al precursor alloy. What's more, via the controllable dissolution of Cu in acidic solution, hierarchical bi-model NP PtCu alloy (Fig. 3.27b) can be constructed upon further corrosion of the NP-PtCu alloy. Similarly, bi-modal NP-PtAu alloy [71, 72] can be facilely fabricated by electrochemically etching the Pt–Au–Al ternary alloy in a sodium chloride solution. With the built-in voids in the rapidly solidified $Al_{75}Pt_{15}Au_{10}$ precursor, the corrosion proceeds in two stages. During the first stage under a lower potential, an island channel structure forms by localized corrosion of the interspace between ribbons. A bi-model NP-PtAu alloy with dual pore size distribution of $\sim$100 and $\sim$3.5 nm is finally achieved upon further potentiostatic dealloying at a higher potential.

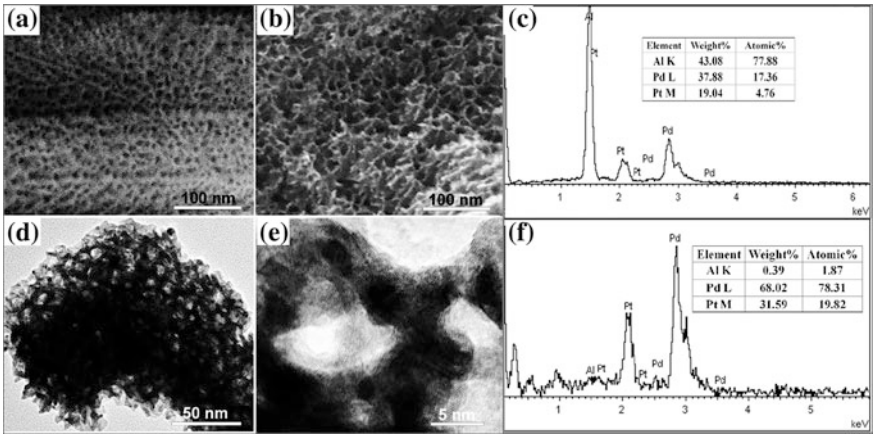

Fig. 3.26 **a** Surface SEM, **b** cross section SEM and **d**, **e** TEM images of NP–PtPd sample. EDS spectra of **c** PtPdAl and **f** NP–PtPd alloy (*right*). Reproduced from J Mater Chem A, 2014, 2, 8875. Copyright 2014, The Royal Society of Chemistry

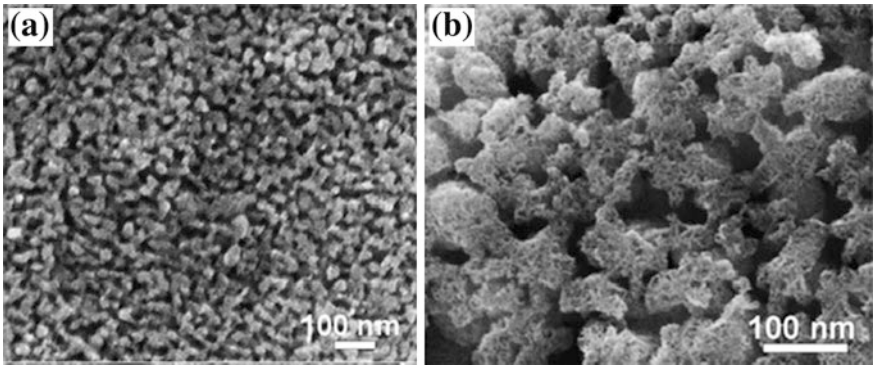

Fig. 3.27 SEM images of the sample **a** after first dealloying the PtCuAl alloy in 1 m NaOH; **b** the HNP-PtCu sample after being dealloyed in acidic solution. Reproduced from ChemPlusChem 2014, 79, 107–113. Copyright 2014, Wiley-VCH

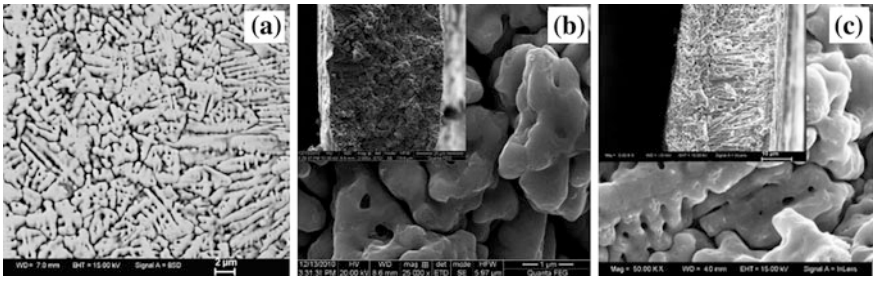

Fig. 3.28 SEM pictures of **a** $Al_{75}Pt_{15}Au_{10}$ precursor alloy, **b** sample after dealloying at −0.4 V versus Ag/AgCl and **c** sample after dealloying at 0.6 V versus Ag/AgCl. Reproduced from Green Chem 2011, 13, 1914–1922. Copyright 2011, The Royal Society of Chemistry

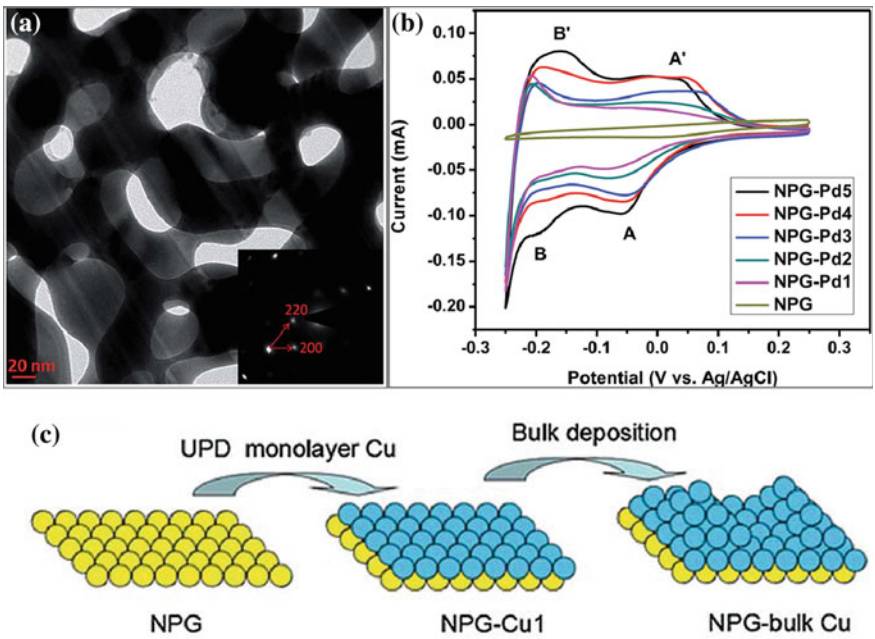

Fig. 3.29 **a** TEM image of the NPG-Pd_2 film. *Inset* Corresponding SAED pattern; **b** CVs of the NPG and NPG-Pd_x electrodes in the 0.5 M H_2SO_4 solution at the scan rate of 50 mV s^{-1}; **c** schematic of Cu deposition on the NPG surface. Reproduced from RSC Adv, 2015, 5, 19409–19417. Copyright 2015, The Royal Society of Chemistry

Obviously, NP alloys with more than two components can be readily obtained by melting more elements in the precursor alloys and processing under corrosive conditions [56]. In addition, the combination of various preparation technologies, such as UPD, replacement reaction, and dealloying, allows the fabrication of more complicated nanostructures [70]. For example, core–shell structured NP Au–Pd films have been obtained by repeating Cu-UPD and Pd–Cu replacement on NPG surface (Fig. 3.29). By controlling the applied potential and time, monolayer Cu can be deposited onto the NPG surface, which can in turn react with palladium salts to coat a monolayer of Pd on NPG. And this process can be repeated to coat more Pd layers on NPG, a process essentially the same as Pt-NPG discussed in section 3.3.3.

The incorporation of transition metals into Pt-based electrocatalysts allows the modification of the intrinsic catalytic activity of Pt surface atoms through different mechanisms which may be broadly classified as structural factors, inhibition by anion adsorption, electronic factors, and surface sensitive factors [75]. For example, NP-PtCu alloy with a molar ratio of 3:1 and ligament size $\sim$3 nm, exhibits greatly enhanced catalytic activity toward methanol oxidation as compared with the commercial Pt/C catalyst [55] (Fig. 3.30). Theoretical calculations indicate that

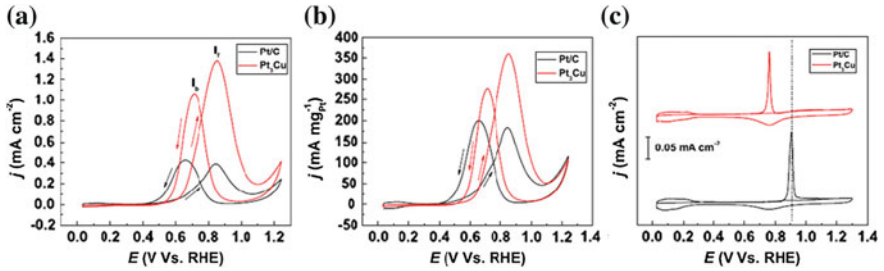

Fig. 3.30 **a** ECSA- and **b** mass-normalized CV curves for methanol electrooxidation of NP-Pt_3Cu and Pt/C catalysts in 0.5 M H_2SO_4 + 0.5 M CH_3OH solution. **c** Electrochemical CO-stripping curves in 0.5 M H_2SO_4 solution. Reproduced from J Power Sour 2015, 279, 334–344. Copyright 2015, Elsevier

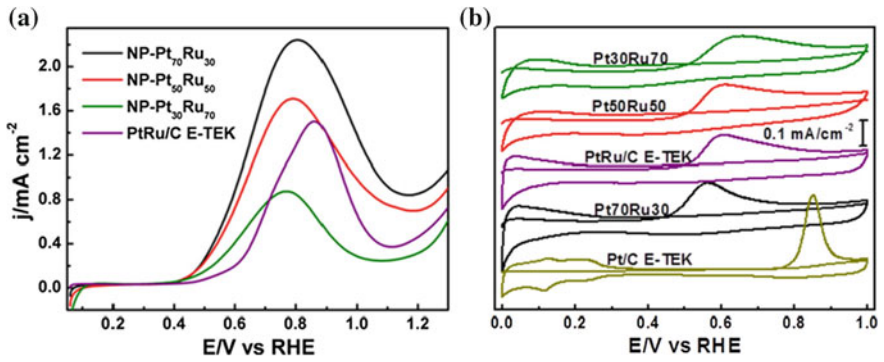

Fig. 3.31 **a** Voltammetric curves of NP-PtRu alloys and PtRu/C catalyst for methanol electrooxidation in mixed 0.5 M H_2SO_4 + 1.0 M CH_3OH solution. Scan rate: 20 mV/s. **b** Electrochemical CO-stripping curves for NP-PtRu alloys, E-TEK Pt/C and PtRu/C catalysts in 0.5 M H_2SO_4 solution. Scan rate: 50 mV/s. Reproduced from Langmuir 2010, 26(10), 7437–7443. Copyright 2010, ACS

alloying with Cu modifies the electronic distribution of Pt, which effectively weakens the CO adsorption, results the improved reaction kinetics for methanol oxidation.

Due to the simplicity of the dealloying process and the possible synergetic mechanisms between Pt and the alloyed elements, recently there appears a rush in research interests to screen various nanoporous Pt-based alloys, such as nanoporous PtRu [76], PtCu [55–57, 59], PtFe [64, 66] PtPd [57, 73, 74], and so on. PtRu nanoparticles are the most well-known anode material for methanol fuel cells and a metal ratio of 1:1 has been recognized as the most favorable composition due to a bifunctional mechanism. Ding and coworkers reported in 2010 that selective etching of Al from ternary PtRuAl source alloys generates three-dimensional NP-PtRu alloys with a single-phase face centered cubic crystalline structure and

uniform surface and bulk bimetallic ratio [76]. With characteristic structural dimensions less than 5 nm, these high surface area bimetallic nanostructures show distinct electrocatalytic performance as the Ru content varies within the structure. Interestingly, NP-$Pt_{70}Ru_{30}$ shows the highest specific activity as well as the most negative onset potential among all samples toward methanol oxidation. NP-$Pt_{50}Ru_{50}$ is found to possess a similar specific activity to the commercial E-TEK $Pt_{50}Ru_{50}$/C catalyst, but its onset and peak potentials are about 70 mV more negative. CO-stripping experiments demonstrate that the adsorption of CO is the weakest on NP-$Pt_{70}Ru_{30}$, and further increasing the Ru content actually shifts the CO-stripping peak to a more positive potential (Fig. 3.31). Therefore, the overall sequence for CO tolerance is found to be: NP-$Pt_{70}Ru_{30}$ > NP-$Pt_{50}Ru_{50}$ ≈ $Pt_{50}Ru_{50}$/C > NP-$Pt_{30}Ru_{70}$ > Pt/C.

Besides the construction of Pt-based anode materials, a great deal of investigations have been devoted to non-platinum electrocatalysts. As a cheaper metal, Pd catalysts also exhibit remarkable activity and hence hold great potential for fuel cell technologies [77–79]. Electrochemical measurements indicate that dealloyed nanoporous Pd catalysts with ultrafine ligaments of size 3–6 nm exhibit considerable catalytic activities toward electrooxidation of methanol, formic acid and ethanol in alkaline solutions. Accordingly, Pd-based nanoporous alloys, such as Pd–Cu [58, 61], Pd–Ni [69, 80] and so on [67, 70, 81], have been successfully prepared by dealloying and utilized as anode materials for alcohol or FAO reactions. For example, NP Pd–Cu alloys with different molar ratios can be fabricated by dealloying Pd–Cu–Al ternary alloys and are electrochemically evaluated for FAO [61]. Upon electrochemical potential cycling in 1.0 M H_2SO_4 solution, the anodic peak of Cu gradually disappears, indicative of the dissolution of Cu element on the anode surface. And eventually, a unique structure of Pd-shell covered NP $Pd_{75}Cu_{25}$ alloy is formed (Fig. 3.32). By optimizing the Pd/Cu molar ratios and the structure of surface active sites, thus-produced NP $Pd_{50}Cu_{50}$ alloy anode shows superior FAO activity due to a more favorable direct oxidation pathway. DFT calculations indicate that, the *d*-band center of Pd shifts negatively by alloying with

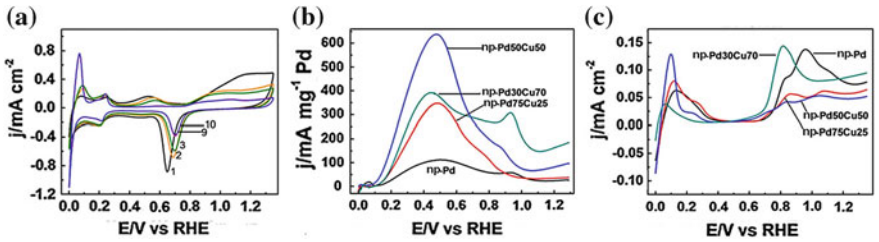

Fig. 3.32 CVs of np-$Pd_{75}Cu_{25}$ at different scan cycles in 1.0 M H_2SO_4 solution **a**; mass current densities in 0.1 M $HClO_4$ + 0.1 M HCOOH solution **b**; electrochemical stripping curves after 1 h of formic acid oxidation in 0.1 M $HClO_4$ + 0.1 M HCOOH solution under 0.1 V versus RHE (**c**). Reproduced from J Power Sour 199 (2012) 124–131. Copyright 2012, Elsevier

Cu, which results in the weakened CO adsorption and enhanced catalytic activity for FAO.

In addition, electrocatalytic activities of Pd-based catalysts are also strongly affected by the promoters and supporting materials. And transition metal oxides are effective promoters or appropriate supporting materials for Pd-based anode catalysts. For example, Zhang and coworkers reported ultrafine NP PdFe/Fe_3O_4 catalysts by dealloying Pd–Fe–Al ternary alloys, which exhibit excellent electrocatalytic activities toward the oxidation of methanol and ethanol, due to the dual function from Fe_3O_4 and Fe [63].

3.4.2 NPM-Based Cathode Catalysts

3.4.2.1 Principles of Oxygen Reduction Reactions (ORR)

The reduction of oxygen plays a key role in electrochemical reactions, and improved understanding of the reaction principles the current fuel cell researches [82]. However, the understanding of the principles of ORR remains incomplete, even on well-established catalysts such as Pt. Due to the recent progress of modern spectroscopic techniques, such as in situ infrared spectroscopy, it is well accepted there are certain critical steps during oxygen reduction, and detailed analyses of these steps determine whether reduction proceeds to the two-electron products H_2O_2 or HO_2^-, or takes place to a more desired four-electron product H_2O.

The initial steps of the ORR process are the physisorption of di-oxygen on electrode surface, and the formation of the chemisorbed OOH intermediates in acid solution, accompanied by one electron transferring from the electrode to O_2. The following steps are generally believed as the *parallel* and *series* pathways (Fig. 3.33). The *parallel* pathway involves dissociation of the oxygen and its subsequent reduction to water via the intermediate atomic O, while the *series* pathway involves the formation of H_2O_2, which can be a final product or an intermediate, eventually turning also to water. From Fig. 3.33, it can be seen that, the high chemical potential intermediate atomic oxygen in the *parallel* pathway would require catalyst surfaces which can significantly reduce the chemical

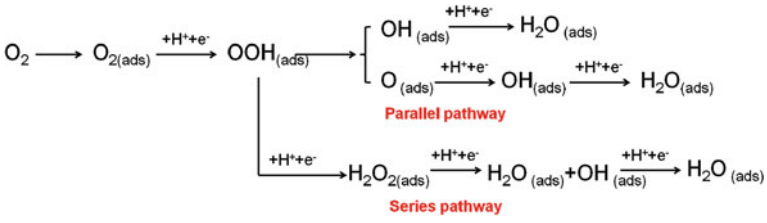

Fig. 3.33 Typical pathways of oxygen reduction reaction

potential. However, such a pathway has only been suggested for a few metals such as Pt, Pd, and Ag. Most other materials, including carbons, metals, and oxide covered metals, tend to follow a *series* reduction pathway , eventually turning to a peroxide product. In the *series* pathway, peroxide tends to desorb into the solution or decompose into water and di-oxygen. Whilst in fuel cells, in order to obtain maximum efficiency and to avoid corrosion of carbon supports, membrane and other materials by peroxide, it is desired to achieve a *parallel* reduction.

According to the theoretical calculation and experiment research on model electrodes, Pt and Pt-based materials are still the most active electrocatalysts for ORR in fuel cells.

3.4.2.2 Nanoporous Pt-Based Alloy Cathode Catalysts

Oxygen reduction operated on cathode is the key reaction that occupies the majority of precious metal usage in PEMFCs, due to its sluggish reaction dynamics, which seriously limits the cell performance. At present, the most practiced commercial Pt/C cathode catalysts still suffer the drawbacks of catalyst aggregation and leaching, relatively low intrinsic activity, and deactivation due to CO poisoning.

By DFT calculations, Nørskov et al. [83] revealed a volcano-type relationship of various metals toward ORR, which shows excellent consistency with the experimental results. Figure 3.34 separately plots the trends of ORR activity as a function of O and OH binding energy, which clarify why Pt is the best catalysts for ORR among various elements. However, at high potentials the adsorbed oxygen becomes too stable due to the high Pt-O binding energy. Upon decreasing the potential, the stability of adsorbed oxygen weakens and the oxygen reduction reaction may proceed, whilst the lowered potential value is suggested to be the overpotential on

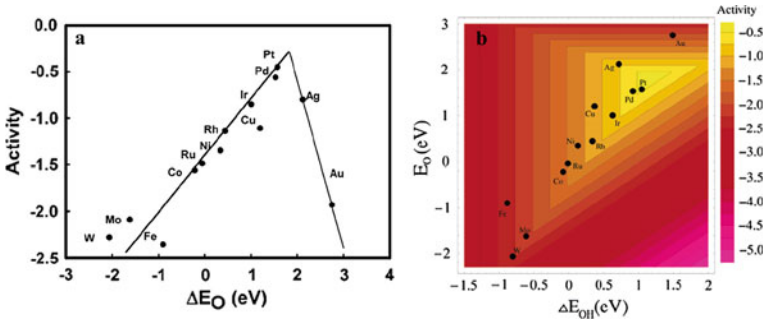

Fig. 3.34 **a** Trends in oxygen reduction activity plotted as a function of the oxygen binding energy. **b** Trends in oxygen reduction activity plotted as a function of both O and OH binding energy. Reproduced from J Phys Chem B 2004, 108, 17886–17892. Copyright 2004, ACS

Pt electrode. Apparently, alloying with other elements to achieve lower oxygen binding energy would a realistic strategy to increase the ORR activity of Pt electrocatalysts, and at the same time to lower the Pt usage.

An interesting early work related to nanoporous Pt-based catalysts is the nanotubular mesoporous platinum NMP by epitaxially casting nanoporous gold membrane molds by Ding and Erlebacher [84]. Freestanding NPG membranes of 100 nm thick, used as molds by dealloying from Au–Ag precursor alloy, are epitaxially coated with Pt overlayers with an average thickness of about 1 nm by a chemical reduction process, then annealed at a moderate temperature to smooth out the surface for a uniform coating, and finally completely dissolved the gold away in aqueous gold etchant. Thereafter, nanotublar mesoporous Pt shell of 1-nm thick could be generated which retains single crystalline feature within individual grains and the bi-continuous void space of the original NPG but adding a second, tubular void region where the gold has been prior to etching (Fig. 3.35). NMP with atomically thin tube walls, hence a very high surface area and total surface free energy, exhibits favorable thermal stability, stable at 125 °C for at least 24 h, entirely different from Pt nanoparticles, which suggests the applicability for low temperature fuel cells. Furthermore, it must be reminded that, this fabrication method is not limited to any particular size and shape of sample, because the mold NPG is a three-dimensional bi-continuous mesoporous metal with a tunable ligament size on the order 10–100 nm with the crystallographic coherence extending to the scale of the grains of the Au/Ag alloy.

According to the theoretical achievements and facile dealloying method in preparing nanoporous structure, Pt-based alloys with 3D-transition metals, Fe, Co, Ni, etc., are of particular interest, for enhanced intrinsic activity, specific activity, durability and lower Pt amount for ORR [75, 85–89].

A notable research for dealloyed Pt-based nanoparticle catalysts is the fabrication of core–shell Pt and PtCo nanostructures by voltammetric surface dealloying of carbon supported PtCo and PtCuCo nanoparticles, respectively [85, 86, 90]. The synthesis of the electrocatalysts is a two-step process involving the preparation of carbon-supported Cu-rich precursor alloys by a conventional impregnation-reductive annealing method, followed by electrochemical dissolution of Cu. The CV profiles suggest that at the end of the dealloying process, the $Pt_{25}Cu_{75}$ precursor alloy changes into a Pt–Cu alloy with an essentially pure Pt surface, i.e., a core–shell structure consisting of a pure Pt shell and a Pt–Cu alloy core (Fig. 3.36). As to the mechanism for the enhanced ORR catalytic activity compared with Pt/C, a reactivity–strain relationship is proposed to provide guidelines for tuning electrocatalytic activity. Platinum-rich shell with smaller lattice parameter exhibits compressive strain, modifies the *d*-band structure of the Pt atoms, and thereby weakens the adsorption energy of intermediates as compared to unstrained Pt, and would finally result in an increase in the catalytic activity, which was consistent with the

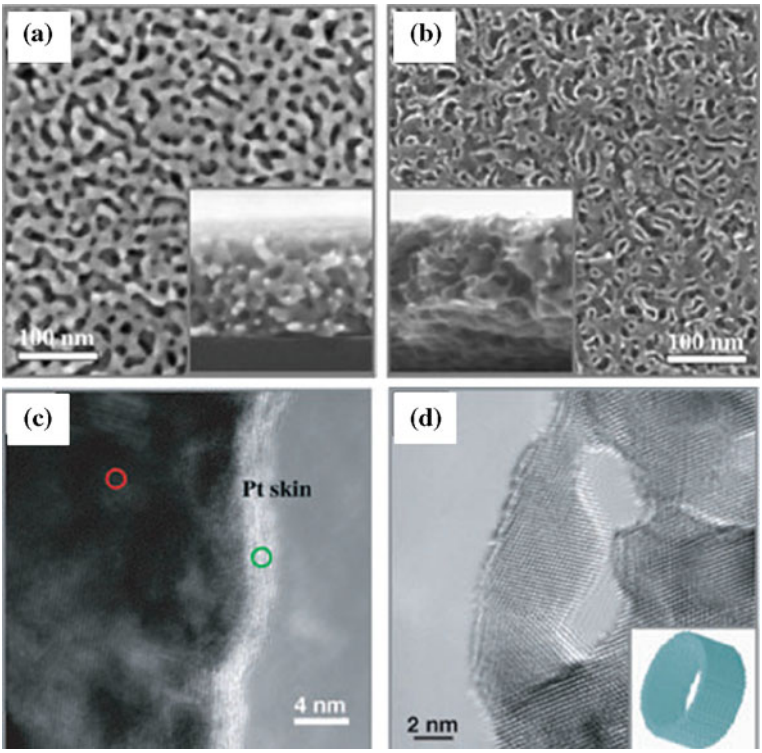

Fig. 3.35 **a** Plan-view and cross section *Inset* SEM images of NPG. **b** Plan-view and cross section *Inset* SEM images of NMP. **c** HREM images of Pt/NPG and NMP. **a** A uniform skin of heteroepitaxial Pt on nanoporous gold was made by platinum deposition followed by thermal annealing at 3008C for 30 min. **d** Side-view of a tube opening of NMP. Lattice distortion and dislocations are observed. The *Inset* is an atomistic model consistent with the projection of the tube opening shown in (**d**). Reproduced from Angew Chem Int Ed 2015, 44, 4002-4006. Copyright 2005, Wiley-VCH

DFT-based predictions. A unique feature of is proposed to provide dealloyed catalysts is the facile experimental control over the extent of dealloying and the particle composition, providing that the noble and the non-noble constituents can be adjusted in the alloy precursor, such that both expansive and compressive strain can be achieved to control the strengthening or weakening of surface bonds. This enables continuous tuning of catalytic activity.

In recent years, dealloying method has been used to produce support-free nanoporous Pt-based alloys. Xu and coworkers have successfully constructed nanoporous PtPd, PtCu, PtFe and PtTi cathode catalysts using chemical dealloying method from ternary alloys [59, 64, 73, 91]. NP Pt–M alloys with different

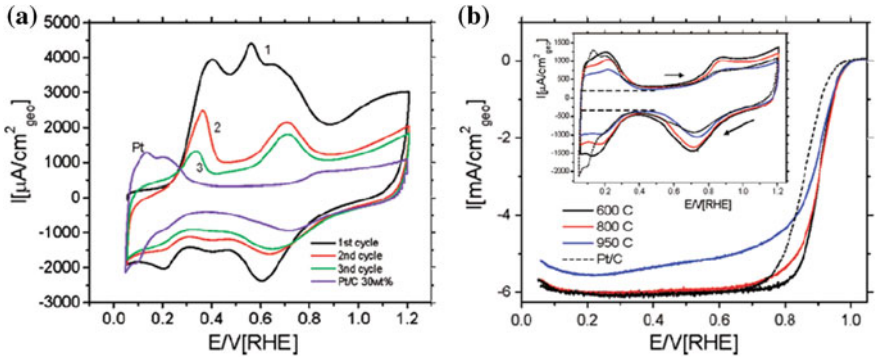

Fig. 3.36 **a** Initial three cyclic CV profiles (1, 2, 3) of a $Pt_{25}Cu_{75}$ precursor catalyst (annealed at 600 °C) during electrochemical dealloying at 100 mV/s. For comparison, the CV of a Pt standard catalyst is shown in *blue*. **b** Sweep voltammetry of dealloyed $Pt_{25}Cu_{75}$ catalysts, annealed at 600 °C (*black*), 800 °C (*red*), 950 °C (*blue*), compared to Pt (*dotted*). The *Inset* shows the cyclic voltammograms of the catalysts in O_2 free electrolyte. The *horizontal black dotted line* indicates the positive and negative capacitance currents. *Arrows* indicate scan directions. Reproduced from J Am Chem Soc 2007, 129, 12624–12625. Copyright 2007, ACS & Angew Chem Int Ed 2007, 46, 8988–8991. Copyright 2007, Wiley-VCH

bimetallic ratios, comprised of nanoscale ligament–channel structure with uniform ligament size, can be fabricated by mild dealloying of PtMAl precursor alloys, which often exhibit much higher specific and mass activities toward ORR in comparison to commercial Pt/C. More importantly, alloying with those elements surprisingly stabilizes the catalytic activity as evidenced by almost no loss of the electrochemical surface area of Pt and ORR activity upon long–term operation. Almost at the same time, Zhang and coworkers also synthesized NP PtCu or multicomponent PtRuCuOsIr alloy cathode catalysts by using a similar method [55, 56].

Among NP Pt-based alloy cathodes, catalysts with Pt/M molar ratio of 3 have been frequently investigated owing to their predicted high activity and stability toward ORR [87–89]. By using the ultrahigh vacuum preparation and characterization techniques on Pt3M alloy model systems, Markovic and coworkers illustrated a fundamental relationship (Fig. 3.37) in electrocatalytic trends on Pt_3M (M=Ni, Co, Fe, Ti, V) surfaces between the experimentally determined surface electronic structure and activity for the oxygen reduction reaction, which also exhibits the 'volcano type' behavior, where the maximum catalytic activity is governed by a balance between adsorption energies of reactive intermediates and surface coverage by spectator species.

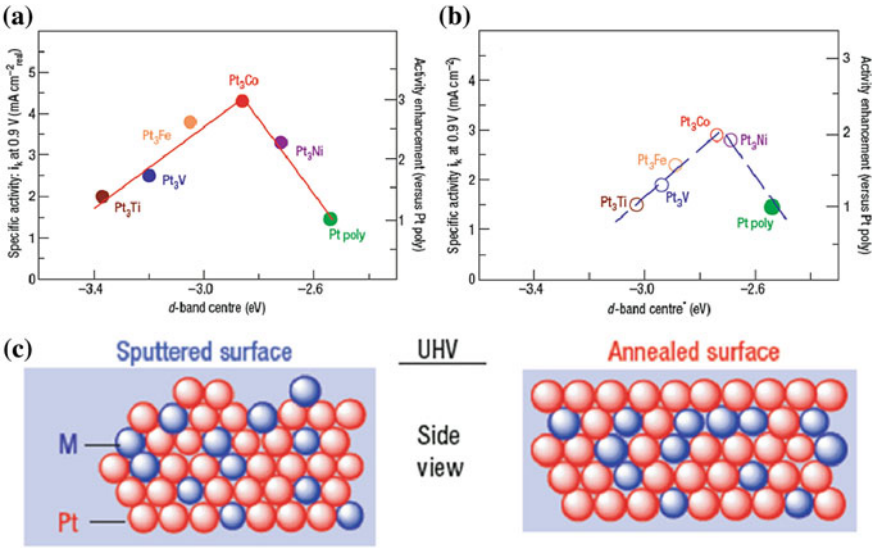

Fig. 3.37 Relationships between experimentally measured specific activity for the ORR on Pt_3M surfaces in 0.1 M $HClO_4$ at 333 K versus the *d*-band center position for the Pt-skin (**a**) and Pt-skeleton (**b**) surfaces. **b** shows the *d*-band centre values* established in UHV, which may deviate in the electrochemical environment due to dissolution of non-Pt atoms. **c** Schematic model for Pt_3M and Pt skin surfaces. Reproduced from Nature Mater 2007, 6, 241–247. Copyright 2007, Nature Publishing Group

3.4.2.3 Nanoporous Pt–Ni Cathode Catalysts

Since Markovic found that Pt_3Ni (111) skin surface exhibits outstanding catalytic activity that has ever been detected for ORR [89], much research interests have focused on developing efficient PtNi alloy catalysts. With a Pt outer surface and Ni-rich second atomic layer, synergetic effect between Pt and Ni would induce the shift of *d*-band center of the surface Pt atoms, which results in a weakened interaction between Pt and intermediate oxide species, freeing more active sites for O_2 adsorption and therefore improving the ORR dynamics.

Ding et al. [92] successfully prepared core–shell structured NP-PtNi alloy catalysts with an open bi-continuous spongy morphology, by sequentially leaching out the more active one in a highly controllable manner from PtNiAl ternary alloys (Fig. 3.38). The obtained core–shell structures are comprised of Pt_1Ni_1 and Pt_6Ni_1 alloy cores, and nearly pure nanoporous Pt surface with the ligament size $\sim$3 nm. Polarization curves of NP Pt_1Ni_1 and Pt_6Ni_1 alloys together with Pt/C for ORR display very encouraging performance, that NP-Pt_1Ni_1, and NP-Pt_6Ni_1 alloys exhibite much higher half-wave potentials at 0.897 and 0.916 V, respectively, which are 31 and 50 mV more positive than that of Pt/C catalyst (0.866 V), indicating dramatically improved reaction kinetics for ORR at lower overpotentials. Furthermore, those two samples also show better stability than Pt/C catalyst.

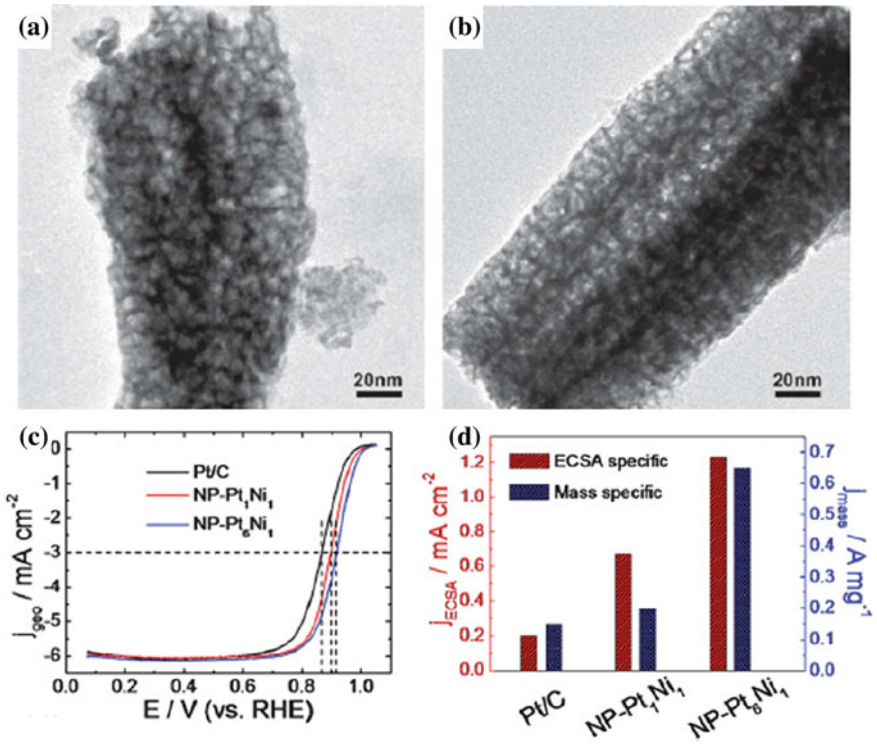

Fig. 3.38 **a**, **b** TEM images of NP-Pt_1Ni_1 and NP-Pt_6Ni_1. **c** ORR polarization curves for NP-Pt_1Ni_1 and NP-Pt_6Ni_1 and Pt/C. **d** The ECSA and Pt mass specific kinetic current densities for Pt/C, NP-Pt_1Ni_1, and NP-Pt_6Ni_1 at 0.9 V. Reproduced from Energy Environ Sci 2012, 5, 5281–5286. Copyright 2012, The Royal Society of Chemistry

According to the former literatures about PtNi alloy catalysts, surface strain and the energetic effect between Ni and Pt may account for the observed performance improvement. In addition, the unique nanoporous structure also plays a vital role of easy transport of electrons and medium molecules along these interconnected skeletons and bi-continuous hollow channels. What needs to be noticed is that this preparation methodology can be easily extended to other NP alloy series, and one will expect that a whole new family of multicomponent alloy nanostructures will soon be explored.

A creative approach to further boost the ORR performance of NP alloy cathode catalysts is reported by from Erlebacher and coworkers, who introduce a novel concept of metal-ionic liquid composites for ORR [93–95]. Core–shell Pt_3Ni@Pt alloy with nanoporous Pt shell is first obtained via electrochemical dissolution of Ni on the alloy surface, and then a tailored geometric and chemical formula is used to further improve ORR catalytic activity by adding a special ionic liquid with hydrophobic, high oxygen solubility, and protic ionic liquid properties. The

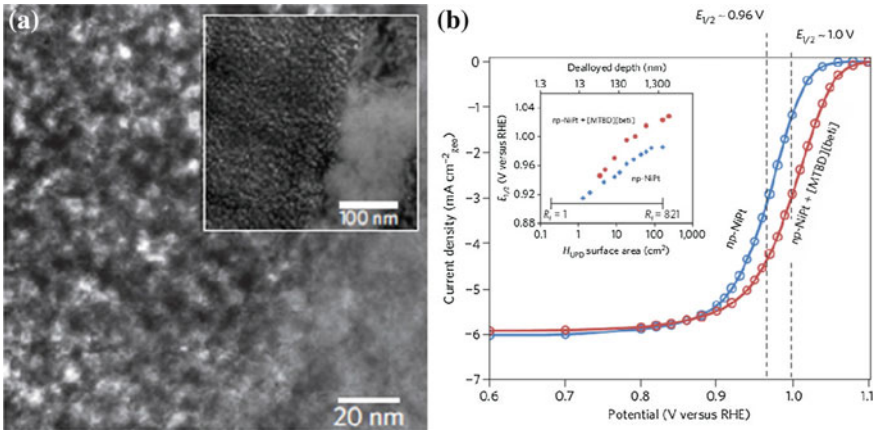

Fig. 3.39 **a** TEM of a wedge slice of a NiPt foil dealloyed in $0.05MNiSO_4$ at 2.1 V versus RHE after residual surface oxide has been reduced in $0.1MH_2SO_4$; *Inset* is a lowermagnification view showing a sharp interface between the porous dealloyed region (*left*) and undealloyed metal (*right*). b Potentiostatic ORR curves and half-wave as a function of roughness factor. Reproduced from Nature Mater 2010, 9, 904–907. Copyright 2010, Nature Publishing Group

experiment results suggest that, by the enhancement of both the intrinsic activity of the nanoporous electrode and the engineered high O_2 solubility within the pores, which biases the reaction toward completion, this unique nanocomposite can exhibit very high activity for the ORR (Fig. 3.39). In addition, by tracking nucleation in solvothermal method, a facile method is developed to control the PtNi nanoparticles size, composition, and simultaneously maintain uniform particle size distribution. What is the most important for this work is the new material synthesis strategy for high surface area catalysts that leverage both the surface reactivity of the component materials and the geometric environment in which these components are assembled.

3.4.2.4 Nanoporous Non-Pt Cathode Catalysts

Besides the fabrication of Pt-based cathode materials, great efforts have been devoted to alternative non-Pt catalysts with high catalytic activity, good CO-tolerant and low cost. As a cheaper metal, Pd catalysts hold great potential for fuel cell technologies. However, owing to the poor activity and stability of pure Pd materials, Pd-based alloys with transition metals have been constructed for ORR.

Accordingly, Pd-based nanoporous alloys, such as PdCu [60, 96, 97], PdFe [65], PdCo and so on [67, 80, 81], have been successfully fabricated by dealloying and utilized as cathodes for ORR. For instance, nanotubular mesoporous PdCu bimetallic electrocatalysts with hierarchically hollow structures are fabricated through a simple galvanic replacement by using dealloyed nanoporous copper

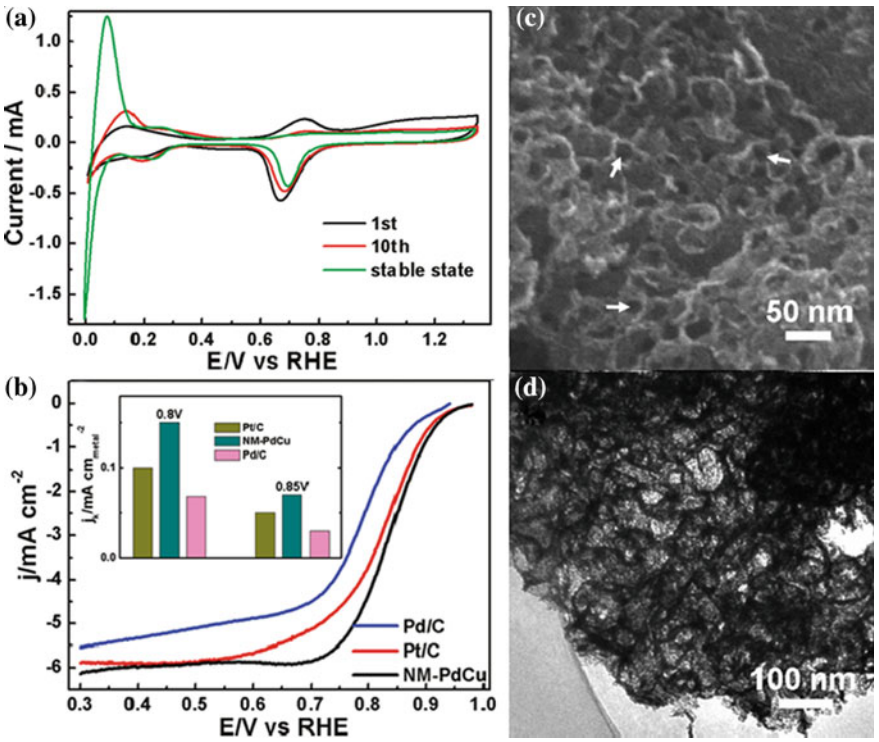

Fig. 3.40 **a** Cyclic voltametric curves (CVs) of NM-PdCu sample in 0.1M$HClO_4$ solution. Scan rate: 20 mV s^{-1}. **b** Polarization curves for the ORR on NM-PdCu and Pd/C, Pt/C nanoparticles in an O_2-saturated 0.1 M$HClO_4$ at room temperature at 1600 rpm. Scan rate: 5 mV s^{-1}. *Inset* is the specific activity for NM-PdCu, Pt/C, and Pd/C catalysts at 0.8 and 0.85 V, respectively. **c**, **d** SEM and TEM (HRTEM) images of nanotubular mesoporous PdCu bimetallic nanostructure. Reproduced from Chem Mater 2009, 21, 3110–3116. Copyright 2009, ACS

(NPC) as both the template and reducing agent and electrochemical evaluated for ORR (Fig. 3.40) [96]. PdCu bimetallic material is obtained by immersing NPC dealloyed from $Cu_{25}Al_{75}$ alloy in K_2PdCl_4 aqueous solution for galvanic replacement. The reaction process can be monitored by UV–vis absorption spectroscopy and finally a unique nanotublar mesoporous structure is formed with a tube diameter $\sim$60 nm and shell thickness $\sim$4 nm. Upon electrochemical potential cycling in 0.1 M $HClO_4$ solution, disappearance of the Cu dissolution peak suggests the formation of nearly pure Pd-skin on the catalyst surface. The ORR polarization curves for NM-PdCu, Pd/C, and Pt/C catalysts obviously indicate that NM-PdCu catalyst exhibits a half-wave potential of 0.840 V, which is nearly 60 mV more positive in comparison with that of the commercial Pd/C catalyst (0.78 V), presenting a greatly enhanced ORR activity.

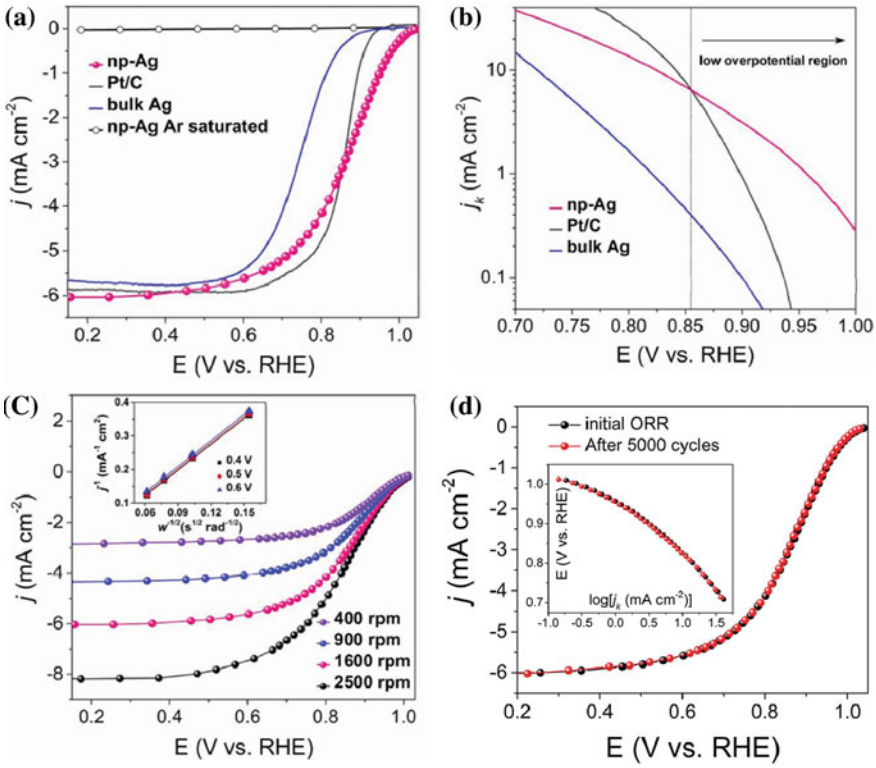

Fig. 3.41 **a** ORR polarization curves of np-Ag, Pt/C, and bulk polycrystalline Ag. The polarization curve of np-Ag was also measured in Ar-saturated electrolyte. Rotation rate: 1600 rpm. **b** The corresponding Tafel plots. **c** ORR polarization curves at different rotation rates. The *Inset* shows the corresponding Koutecky–Levich plots at different potentials. **d** ORR curves and *Inset* corresponding Tafel plots of np-Ag before and after 5000 potential cycles between 0.6 and 1.0 V versus RHE. Reproduced from Adv Energy Mater 2015, 5, 1500149. Copyright 2015, Wiley-VCH

In addition, electrochemical reduction of oxygen in alkaline environment is of tremendous importance for many electrochemical devices that are directly related to efficient energy conversion and storage applications. NP Ag catalyst [98] has been successfully prepared by dealloying and evaluated for electrochemical ORR in alkaline solution (Fig. 3.41). A higher ORR activity than the state-of-the-art Pt/C catalysts is demonstrated at low overpotential region and better stability in the alkaline electrolyte. The NP-Ag catalyst provides a promising alternative to replace Pt-based catalysts in alkaline media without scarifying any ORR activity.

Low loading, high stability and high active Pt catalyst is still a big challenge for PEMFC technology. Compared with Pt/C, nanoporous metal cathodes with higher activity and durability are most likely to be candidates for the next generation of

automotive fuel cell catalysts. In the technical level, in order to achieve lower cost and higher performance fuel cell catalysts, the most probable solution might be porous metal membrane catalysts with single atomic or sub-nanometer Pt group metal overlayer coating, with controllable crystal surfaces. Of course, the demonstrated performance of NPM catalysts in half-cell electrochemical or single-cell tests has to be confirmed in larger scale, standard evaluation systems, before concluding if they can indeed meet the actual requirements of either light duty portable electronic devices or heavy duty automotive applications.

3.5 Summary and Outlook

In the past two decades, tremendous progresses have been made in nanomaterial field and it is now quite routine to employ highly controllable chemical or physical approaches to produce various nanostructures, with tailored size or dimension, structural uniformity and dispersity, crystallographic morphology, and surface configuration. These technologies allow the enhancement of the intrinsic catalytic activity and precious metal utilization of the electrodes. In order to function in real fuel cells, these nanoparticulate catalysts have to undergo further processing by adsorbing onto high surface area conducting substrates such as carbon black to facilitate the catalyst dispersion, and fuel diffusion. As the catalyst nanoparticles are only physically adsorbed on the carbon support, they tend to aggregate to form larger nanoparticles or even lose contact to support under the operation conditions. Moreover, the large contact resistance between carbon particles aroused from the incorporation of poorly conductive polymer electrolyte such as Nafion® when preparing the MEA leads to the increase of internal resistance in catalytic layer and decrease of overall cell performance.

In comparison, dealloyed nanoporous metals represent a new class of high surface area *structured* nanoelectrodes, as characterized by their clean and readily accessible surfaces, highly conductive open framework structure for free transport of medium molecules and electrons, and tunable surface chemistry which is particularly desirable for electrocatalysis. Being support free and particle free, nanoporous metals completely eliminate the support corrosion problem and particle aggregation/sintering problem, can therefore provide a mechanically rigid scaffold for grafting catalytically active species.

Preliminary investigations in this field have already revealed some encouraging results not commonly seen from traditional nanoparticle electrocatalysts, such as ultralow Pt loading hydrogen fuel cells and DFAFCs by using Pt or Pt-based alloys coated NPG leaves as the electrodes. However, this has to be related to the relatively simple and fast oxidation kinetic of hydrogen on Pt and recently clarified formic acid electrooxidation mechanism. This is why the progress in exploring similarly active NPG-based nanoelectrodes for direct methanol, ethanol and/or

glucose fuel cells is comparatively slow. Except for NPG-based electrocatalysts, the implementation of nanoporous metals and alloys for actual fuel cells has not been realized. The main difficulty would be the development of cost-effective methods to produce high quality, multicomponent alloy thin films. The nanoporous alloys so far screened are mostly made from melt-spun alloy foils which have a thickness of tens of microns or above, and thus are not compatible to any MEA fabrication techniques.

Despite the advantages and disadvantages mentioned above, the overall advancement in this area is still in its infancy. As a relatively new class of materials, the majority of their structural properties and applications remain unexploited, and their applicability in important technologies such as fuel cells is mainly practiced in a traditional engineering manner, rather than based on a rational system level. In-depth researches, especially those with comprehensive knowledges, skills and resources will lead to more groundbreaking discoveries, and dealloyed nanoporous metals will certainly have a bright future in advanced energy technologies.

References

1. Larminie J, Dicks A (2003) Fuel cell systems explained, 2nd edn. Wiley, Hoboken, p 2003
2. Lambert RM (1997) Introduction to heterogeneous catalysis. In: Lambert RM, Pacchioni G (eds) Chemisorption and reactivity on supported clusters and thin films, 1997. Kluwer Academic Publishers, Netherlands
3. Yamada M, Honma I (2004) A biopolymer composite material as an anhydrous proton-conducting membrane. Angew Chem Int Ed 43(28):3688–3691
4. Grot WG (1972) CF2 = CFCF2CF2SO2F and derivatives and polymers thereof. U. S. Patent 3, 718, 627
5. Grot WGG SA (2004) Fuel cell membranes. U. S. Patent, 6, 733, 914
6. Grot, GW (1994) Perfluorinated ion-exchange polymers and their use in research and industry. Macromol Symposia 82:161–172
7. Srinivasan S (2006) Fuel cells: from fundamentals to applications. Springer, Berlin
8. Information from websites: http://www.fuelcells.dupont.com/ and http://www.ion-power.com/
9. Steele BCH, Heinzel A (2001) Materials for fuel-cell technologies. Nature 414:345–352
10. Anderson ML, Stroud RM, Rolison DR (2002) Enhancing the activity of fuel-cell reactions by designing three-dimensional nanostructured architectures: catalyst-modified carbon-silica composite aerogels. Nano Lett 2:235–240
11. Wilson MS et al (1993) Surface area loss of supported platinum in polymer electrolyte fuel cells. J Electrochem Soc 140:2872–2877
12. Alkire RC et al (1997) Advances in electrochemical science and engineering, vol 5. Wiley, New York
13. Campbell CT, Parker SC, Starr DE (2002) The effect of size-dependent nanoparticle energetics on catalyst sintering. Science 298(5594):811–814
14. Blom DA et al (2003) Preparation of cross-sectional samples of proton exchange membrane fuel cells by ultramicrotomy for TEM. J Electrochem Soc 150(4):A414
15. Xia Y et al (2009) Shape-controlled synthesis of metal nanocrystals: simple chemistry meets complex physics? Angew Chem Int Ed 48(1):60–103
16. Tao AR, Habas S, Yang P (2008) Shape control of colloidal metal nanocrystals. Small 4 (3):310–325

17. Sasaki K et al (2010) Core-protected platinum monolayer shell high-stability electrocatalysts for fuel-cell cathodes. Angew Chem Int Ed 49(46):8602–8607
18. Shao MH et al (2010) Pt monolayer on porous Pd–Cu alloys as oxygen reduction electrocatalysts. J Am Chem Soc 132:9253–9255
19. Wang C et al (2008) A general approach to the size- and shape-controlled synthesis of platinum nanoparticles and their catalytic reduction of oxygen. Angew Chem Int Ed 47 (19):3588–3591
20. Borup R et al (2007) Scientific aspects of polymer electrolyte fuel cell durability and degradation. Chem Rev 107:3904–3951
21. Joo SH et al (2001) Ordered nanoporous arrays of carbon supporting high dispersions of platinum nanoparticles. Nature 412:169–172
22. Wang C et al (2004) Proton exchange membrane fuel cells with carbon nanotube based electrodes. Nano Lett 4:345–348
23. Vinodgopal K et al (2004) Fullerene-Based carbon nanostructures for methanol oxidation. Nano Lett 4:415–418
24. Information from http://www.webelements.com
25. Ding Y, Kim YJ, Erlebacher J (2004) Nanoporous gold leaf:"ancient technology"/advanced material. Adv Mater 16:1897–1900
26. Fujita T et al (2008) Unusually small electrical resistance of three-dimensional nanoporous gold in external magnetic fields. Phys Rev Lett 101(16):166601
27. Zhang J et al (2007) Nanostructured porous gold for methanol electro-oxidation. J Phys Chem C 111:10382–10388
28. Zeis R et al (2008) Catalytic reduction of oxygen and hydrogen peroxide by nanoporous gold. J Catal 253(1):132–138
29. Ding Y, Chen M, Erlebacher J (2004) Metallic mesoporous nanocomposites for electrocatalysis. J Am Chem Soc 126:6876–6877
30. Liu P et al (2009) Facile fabrication of ultrathin Pt overlayers onto nanoporous metal membranes via repeated Cu UPD and in Situ redox replacement reaction. Langmuir 25(1):561–567
31. Pedersen MØ et al (1999) How a gold substrate can increase the reactivity of a Pt overlayer. Surf Sci 426:395–409
32. Du B, Tong Y (2005) A coverage-dependent study of Pt spontaneously deposited onto Au and Ru surfaces: direct experimental evidence of the ensemble effect for methanol electro-oxidation on Pt. J Phys Chem B 109:17775–17780
33. Frelink T, Visscher W, Van Veen JAR (1995) Particle size effect of carbon-supported platinum catalysts for the electrooxidation of methanol. J Electroanal Chem 382: 65–72
34. Kowal A et al (2009) Ternary Pt/Rh/SnO_2 electrocatalysts for oxidizing ethanol to CO_2. Nat Mater 8:325–330
35. Ge X et al (2008) Structure dependent electrooxidation of small organic molecules on Pt-decorated nanoporous gold membrane catalysts. Electrochem Commun 10(10):1494–1497
36. Ge X et al (2009) Tailoring the structure and property of Pt-decorated nanoporous gold by thermal annealing. J Phys Chem C 113(17): 7379–7384
37. Zeis R et al (2007) Platinum-plated nanoporous gold: an efficient, low Pt loading electrocatalyst for PEM fuel cells. J Power Sour 165(1):65–72
38. Yu X, Pickup PG (2008) Recent advances in direct formic acid fuel cells (DFAFC). J Power Sour 182(1):124–132
39. Ricea C et al (2002) Direct formic acid fuel cells. J Power Sour 111:83–89
40. Capon A, Parsons R (1973) The oxidation of formic acid at noble metal electrodes. J Electroanal Chem 45:205–231
41. Samjeske G et al (2006) Mechanistic study of electrocatalytic oxidation of formic acid at platinum in acidic solution by time-resolved surface-enhanced infrared absorption spectroscopy. J Phys Chem B 110:16559–16566
42. Chen YX et al (2006) Kinetics and mechanism of the electrooxidation of formic acid–spectroelectrochemical studies in a flow cell. Angew Chem Int Ed 45(6):981–985

43. Osawa M et al (2011) The role of bridge-bonded adsorbed formate in the electrocatalytic oxidation of formic acid on platinum. Angew Chem Int Ed 50(5):1159–1163
44. Neurock M, Janikb M, Wieckowski A (2008) A first principles comparison of the mechanism and site requirements for the electrocatalytic oxidation of methanol and formic acid over Pt. Faraday Discuss 140:363–378
45. Lopez-Cudero A et al (2009) Formic acid electrooxidation on Bi-modified polyoriented and preferential (111) Pt nanoparticles. Phys Chem Chem Phys 11(2):416–424
46. Wang R et al (2010) Ultralow-platinum-loading high-performance nanoporous electrocatalysts with nanoengineered surface structures. Adv Mater 22(16):1845–1848
47. Wang R et al (2014) Dispersing Pt atoms onto nanoporous gold for high performance direct formic acid fuel cells. Chem Sci 5(1):403–409
48. Uosaki K et al (1997) Adsorption of hexachloroplatinate complex on Au(111) electrode. An in situ scanning tunneling microscopy and electrochemical quartz microbalance study. Langmuir 13:594–596
49. Uhm S et al (2008) A stable and cost-effective anode catalyst structure for formic acid fuel cells. Angew Chem Int Ed 47(52):10163–10166
50. Wang R et al (2014) Ultra-thin layer structured anodes for highly durable low-Pt direct formic acid fuel cells. Nano Research 7(11):1569–1580
51. Snyder J et al (2008) Stabilized nanoporous metals by dealloying ternary alloy precursors. Adv Mater 20(24):4883–4886
52. Xu C et al (2010) Dealloying to nanoporous Au/Pt alloys and their structure sensitive electrocatalytic properties. Phys Chem Chem Phys 12(1):239–246
53. Ji H et al (2010) An ultrafine nanoporous bimetallic Ag–Pd alloy with superior catalytic activity. CrystEngComm 12(12):4059
54. Wang X et al (2011) Length-scale modulated and electrocatalytic activity enhanced nanoporous gold by doping. J Phys Chem C 115(11):4456–4465
55. Sun J et al (2015) Enhanced methanol electro-oxidation and oxygen reduction reaction performance of ultrafine nanoporous platinum–copper alloy: experiment and density functional theory calculation. J Power Sour 279:334–344
56. Chen X et al (2015) Multi-component nanoporous platinum–ruthenium–copper–osmium–iridium alloy with enhanced electrocatalytic activity towards methanol oxidation and oxygen reduction. J Power Sour 273:324–332
57. Chen X et al (2014) Highly active nanoporous Pt-based alloy as anode and cathode catalyst for direct methanol fuel cells. J Power Sour 267:212–218
58. Chen S et al (2012) Co-delivery of genes and drugs with nanostructured calcium carbonate for cancer therapy. RSC Advances 2(5):1820
59. Xu C et al (2014) A hierarchical nanoporous PtCu alloy as an oxygen-reduction reaction electrocatalyst with high activity and durability. ChemPlusChem 79(1):107–113
60. Zhang H et al (2013) Nanoporous PdCu alloys as highly active and methanol-tolerant oxygen reduction electrocatalysts. Int J Hydrogen Energy 38(24):10029–10038
61. Xu C et al (2012) Nanoporous PdCu alloy for formic acid electro-oxidation. J Power Sour 199:124–131
62. Xu C et al (2011) Fabrication of nanoporous Cu–Pt(Pd) core/shell structure by galvanic replacement and its application in electrocatalysis. ACS Appl Mater Interfaces 3(12): 4626–4632
63. Zhang Z et al (2013) Ultrafine nanoporous PdFe/Fe_3O_4 catalysts with doubly enhanced activities towards electro-oxidation of methanol and ethanol in alkaline media. J Mater Chem A 1(11):3620
64. Duan H, Hao Q, Xu C (2014) Nanoporous PtFe alloys as highly active and durable electrocatalysts for oxygen reduction reaction. J Power Sour 269:589–596
65. Han B, Xu C (2014) Nanoporous PdFe alloy as highly active and durable electrocatalyst for oxygen reduction reaction. Int J Hydrogen Energy 39(32):18247–18255
66. Xu C et al (2012) Hierarchical nanoporous PtFe alloy with multimodal size distributions and its catalytic performance toward methanol electrooxidation. Langmuir 28(3):1886–1892

67. Xu C et al (2013) A nanoporous PdCo alloy as a highly active electrocatalyst for the oxygen-reduction reaction and formic acid electrooxidation. Chem Asian J 8(11):2721–2728
68. Xu C et al (2012) Nanoporous PtCo and PtNi alloy ribbons for methanol electrooxidation. Int J Hydrogen Energy 37(14):10489–10498
69. Qi Z et al (2011) Novel nanocrystalline PdNi alloy catalyst for methanol and ethanol electro-oxidation in alkaline media. J Power Sour 196(14):5823–5828
70. Yan X et al (2015) Atomic layer-by-layer construction of Pd on nanoporous gold via underpotential deposition and displacement reaction. RSC Adv 5(25):19409–19417
71. Xu J et al (2011) Fabrication of bi-modal nanoporous bimetallic Pt–Au alloy with excellent electrocatalytic performance towards formic acid oxidation. Green Chem 13(7):1914
72. Zhang Z, Wang Y, Wang X (2011) Nanoporous bimetallic Pt-Au alloy nanocomposites with superior catalytic activity towards electro-oxidation of methanol and formic acid. Nanoscale 3(4):1663–1674
73. Duan H, Xu C (2015) Nanoporous PtPd alloy electrocatalysts with high activity and stability toward oxygen reduction reaction. Electrochim Acta 152:417–424
74. Xu C, Hao Q, Duan H (2014) Nanoporous PdPt alloy as a highly active electrocatalyst for formic acid oxidation. J Mater Chem A 2(23):8875
75. Gasteiger HA et al (2005) Activity benchmarks and requirements for Pt, Pt-alloy, and non-Pt oxygen reduction catalysts for PEMFCs. Appl Catal B 56(1–2):9–35
76. Xu C et al (2010) Nanoporous PtRu alloys for electrocatalysis. Langmuir 26(10):7437–7443
77. Wang X et al (2012) Novel Raney-like nanoporous Pd catalyst with superior electrocatalytic activity towards ethanol electro-oxidation. Int J Hydrogen Energy 37(3):2579–2587
78. Wang X et al (2010) Electrochemical catalytic activities of nanoporous palladium rods for methanol electro-oxidation. J Power Sour 195(19):6740–6747
79. Wang X et al (2009) High catalytic activity of ultrafine nanoporous palladium for electro-oxidation of methanol, ethanol, and formic acid. Electrochem Commun 11(10):1896–1899
80. Xu C et al (2013) Nanoporous PdNi alloy as highly active and methanol-tolerant electrocatalyst towards oxygen reduction reaction. J Mater Chem A 1:13542–13548
81. Liu Y, Xu C (2013) Nanoporous PdTi alloys as non-platinum oxygen-reduction reaction electrocatalysts with enhanced activity and durability. ChemSusChem 6(1):78–84
82. Gewirth AA, Thorum MS (2010) Electroreduction of dioxygen for fuel-cell applications: materials and challenges. Inorg Chem 49(8):3557–3566
83. Nørskov JK et al (2004) Origin of the overpotential for oxygen reduction at a fuel-cell cathode. J Phys Chem B 108(46):17886–17892
84. Ding Y et al (2005) Epitaxial casting of nanotubular mesoporous platinum. Angew Chem Int Ed 44(26):4002–4006
85. Koh S, Strasser P (2007) Electrocatalysis on bimetallic surfaces modifying catalytic reactivity for oxygen reduction by voltammetric surface dealloying. J Am Chem Soc 129:12624–12625
86. Srivastava R et al (2007) Efficient oxygen reduction fuel cell electrocatalysis on voltammetrically dealloyed Pt–Cu–Co nanoparticles. Angew Chem Int Ed 46(47):8988–8991
87. Stamenkovic VR et al (2007) Trends in electrocatalysis on extended and nanoscale Pt-bimetallic alloy surfaces. Nat Mater 6(3):241–247
88. Stamenkovic VR et al (2006) Effect of surface composition on electronic structure, stability, and electrocatalytic properties of Pt-transition metal alloys: Pt-skin versus Pt-skeleton surfaces. J Am Chem Soc 128(27):8813–8819
89. Stamenkovic VR et al (2007) Improved oxygen reduction activity on Pt_3Ni via increased surface site availability. Science 315:493–497
90. Koh PS et al (2010) Lattice-strain control of the activity in dealloyed core–shell fuel cell catalysts. Nat Chem 2:454–460
91. Duan H, Hao Q, Xu C (2015) Hierarchical nanoporous PtTi alloy as highly active and durable electrocatalyst toward oxygen reduction reaction. J Power Sour 280:483–490
92. Wang R et al (2012) Nanoporous surface alloys as highly active and durable oxygen reduction reaction electrocatalysts. Energy Environ Sci 5(1):5281–5286

93. Snyder J et al (2010) Oxygen reduction in nanoporous metal-ionic liquid composite electrocatalysts. Nat Mater 9:904–907
94. Snyder J, Livi K, Erlebacher J (2013) Oxygen reduction reaction performance of [MTBD][beti]-encapsulated nanoporous NiPt alloy nanoparticles. Adv Funct Mater 23(44):5494–5501
95. Benn E, Uvegi H, Erlebacher J (2015) Characterization of nanoporous metal-ionic liquid composites for the electrochemical oxygen reduction reaction. J Electrochem Soc 162(10): H759–H766
96. Xu C et al (2009) Nanotubular mesoporous PdCu bimetallic electrocatalysts toward oxygen reduction reaction. Chem Mater 21(14):3110–3116
97. Yang R et al (2013) Dealloyed $PdCu_3$ thin film electrocatalysts for oxygen reduction reaction. J Power Sour 222:169–176
98. Zhou Y et al (2015) Oxygen reduction at very low overpotential on nanoporous Ag catalysts. Adv Energy Mater 5(13): 1500149

Chapter 4
Nanoporous Metals for Supercapacitor Applications

Abstract Supercapacitors have received great attentions among various energy storage devices both in academic and practical applications. They show high power densities and can be fully discharged or charged in seconds which are suitable for large instantaneous current densities. The performance is highly dependent on the specific surface area and conductivity of the electrode materials. Nanoporous metals-based electrode materials with a large internal surface area and excellent conductivity have been widely investigated in supercapacitors. In this chapter, we summarize the research progress of pure nanoporous metals, pseudo-capacitive materials (metal oxides, conductive polymer)/nanoporous metals composites in supercapacitors. By introducing nanoporous structures into electrode materials, the 3D bicontinuous porous structure and the high conductivity of the nanoporous metal-based framework benefit the electron–proton transport and electrolyte permeation, giving rise to ultrahigh specific capacitance. The pseudo-capacitive materials can also be deposited on the nanoporous metals by surface oxidize/oxyhydroxide. The surface oxyhydroxide and the internal nanoporous metal framework form a homogeneous and stable hybrid structure. The mixed-valence oxyhydroxide composite has been prepared by dealloying ternary Ni–Cu–Mn alloy. This hybrid composite electrode exhibits an ultrahigh specific capacitance of 627 F/cm^3 and a very large operating potential window of 1.8 V in an aqueous electrolyte. The MnO_2/NPG composite electrode gives a high specific capacitance of 601 F/g even based on the total mass of gold and MnO_2. The conductive polymer/NPG composites have been developed into all-solid-state supercapacitor electrode and gives excellent electrochemical performance. Asymmetric capacitors based on nanoporous metal electrodes have also been fabricated to further improve the performance of supercapacitors. All of the related works have been reviewed in this chapter. The summary part of this chapter gives a brief prospective and the roadmap in the field of nanoporous metals-based electrode materials about toward a practical supercapacitor.

Keywords Nanoporous metals · Pseudo-capacitive · Supercapacitor · Metal oxides · Deposition · All-solid-state supercapacitor · Asymmetric capacitor

Y. Ding and Z. Zhang, *Nanoporous Metals for Advanced Energy Technologies*, DOI 10.1007/978-3-319-29749-1_4

4.1 Introduction

Among various energy storage systems, supercapacitors, also called electrochemical double-layer capacitors (EDLCs) or ultra-capacitors, have attracted intense attention in the past few years. Compared with traditional secondary batteries, supercapacitors are an interesting type of power devices that can be fully charged and discharged in seconds. More specifically, their energy densities ($\sim$5 Wh kg^{-1}) are lower than those of common batteries, but much higher power delivery or uptake ($\sim$10 kW kg^{-1}) can be achieved for shorter period (a few seconds) [1]. Figure 4.1 shows the Ragone plot of power against energy density for various energy storage systems [2]. Due to their particular operation behaviors, supercapacitors may complement or replace batteries in special situations, such as uninterruptible power supplies and load-leveling. A more recent example is the use of electrochemical double-layer capacitors in emergency doors (16 per plane) on an Airbus A380, proving that in terms of performance, safety, and reliability the electrochemical capacitors are definitely ready for large-scale implementation [2]. Table 4.1 highlights the performance comparisons of supercapacitors, batteries, and traditional capacitors.

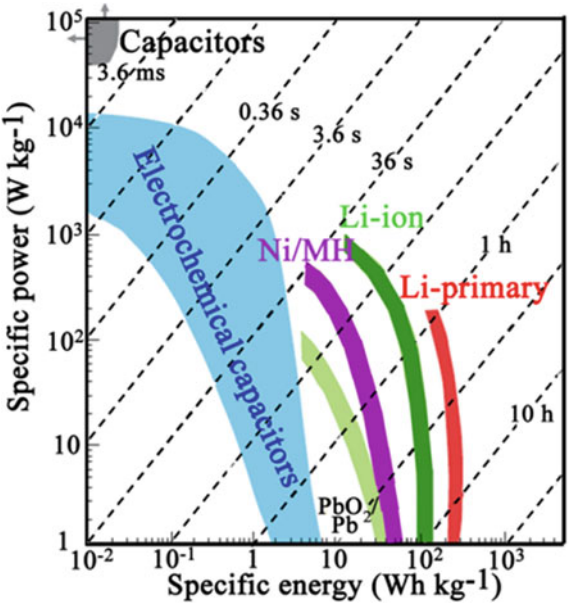

Fig. 4.1 Specific power against specific energy, also called a Ragone plot, for various electrical energy storage devices. If a supercapacitor is used in an electric vehicle, the specific power shows how fast one can go, and the specific energy shows how far one can go on a single charge. *Times* shown are the time constants of the devices, obtained by dividing the energy density by the power (Reproduced from Ref. [2]. Copyright 2008, Nature Publish Group.)

Table 4.1 Comprehensive performance comparisons of supercapacitors, batteries, and traditional capacitors

Parameter	Supercapacitors	Batteries	Traditional capacitors
Cycle life	>100,000	500–2000	>500,000
Charge-discharge efficiency	0.90–0.95	0.7–0.85	1.0
Charge time (s)	1–30	0.3–3 h	10^{-6}–10^{-3}
Discharge time (s)	1–30	1–5 h	10^{-6}–10^{-3}
Energy density (Wh kg^{-1})	1–10	20–100	<0.1
Power density (W kg^{-1})	1000–2000	50–200	>10,000

Supercapacitors have been considered as one of the ideal energy storage devices due to their high power densities, long cycle life, and wide range of working temperature [3, 4]. The development history of supercapacitors has experienced a long period. During the mid-eighteenth century when the physics of "static electricity" was revealed and investigated, various "electrical machines" started to be invented, such as the Electrophorus and the Wimshurst machine (Excellent examples of these, as well as Leyden jars, can be seen in the Museum of Science in Florence) [1]. The utilization of this principle to store electrical energy for practical purposes, as in a voltaic cell or battery of cells, was first realized as an original development by Becker at General Electric Corp. in 1957 (US Patent 2,800,616) [5]. This patent describes electrical energy storage by means of the charge held in the interfacial double layer in a porous carbon material perfused with an aqueous electrolyte. In 1971, NEC (Japan) developed aqueous electrolyte capacitors under the energy company SOHIO's license for power saving units in electronics, and this application can be considered as the starting point for actual implementation of electrochemical capacitors in commercial devices [6]. A different principle was realized in mid-1970s by B. Conway in Ottawa, then under contract with Continental Group, who proposed that the electrochemical redox process in certain precious metal oxide electrodes might be used for energy storage, a phenomena known as pseudo-capacitance [3]. And a prototype pseudo-capacitor device was disclosed in a Canadian Patent (No. 1,270,296) issued to D. Craig at Hooker Corp [3]. Since then, supercapacitors have attracted much more attentions and developed quickly.

4.2 Energy Storage Mechanisms of Supercapacitors

4.2.1 Supercapacitor Compositions

Supercapacitors are comprised of two electrodes (anode and cathode), an electrolyte, a conducting charge path for operation, and a separator that electrically isolates the two electrodes. These four components are then packaged together and

can function as a conventional capacitor. In most EDLCs both positive and negative electrodes are made of the same materials.

4.2.1.1 Electrode

The electrode is mainly composed of the electrochemically actives material (the electrode material), the conductive agent, the binder, and the current collector. Each element plays a unique role to the final performance of the supercapacitor. In particular, the electrode materials are of central importance in deciding the specific capacitance, which can be optimized by choosing high surface area, electrically conducting materials. It is therefore not unexpected that researches in this community focus mainly on the development and processing of functional electrode materials. Typical electrode materials include carbon materials [7, 8] conducting polymers [9] and metal oxides [2]. Sometimes, the conductive agents may be pre-integrated into the electrode structures to form multi-composition multifunctional composites in order to improve the performance of the electrodes. The graphite and carbon black are the commonly used conductive agents, although they exhibit certain capacitance properties themselves. The binder often includes PVDF or PTFE. The current collector is the ultimate source for electron collection and charge flow during electrode reactions, and it also functions as the supporter of the active materials.

4.2.1.2 Electrolyte

Besides the electrode materials, the supercapacitor performance also depends very much on the electrolyte. This is because the temperature range which the electrolyte can stably exist directly decides the operating conditions of supercapacitors. And the decomposition voltage of the electrolyte also decides the working voltage (or potential) of the supercapacitors. Therefore, the electrolyte should possess the advantages of high conductivity, high decomposition voltage, wide working temperature range, safe and nontoxic, excellent chemical stability, and so on. Commonly, they can be classified into two categories: solid electrolyte and liquid electrolyte, among which liquid electrolytes are most widely used, and can be further classified into organic electrolyte and aqueous ones.

The aqueous electrolyte has the advantages of high conductivity, small molecular diameter, easy infiltration within the micropores, and low price. And they can be sorted into acid, alkaline, and neutral electrolyte. The most popularly used acid electrolyte is H_2SO_4 aqueous solution, which contains three major advantages including high conductivity, high ions concentration, and low equivalent series resistance. But it also suffers several disadvantages: (1) the electrolyte is corrosive; (2) non-noble metal materials cannot be used as the current collector; (3) H_2SO_4 aqueous solution will get easily divulged once the supercapacitor is extruded, which

may cause serious handling and environmental issues. Alkaline electrolytes such as KOH and LiOH aqueous solutions are also commonly used. Metal oxide electrode materials usually exhibit higher capacitance in the alkaline electrolyte. The corrosion of alkaline electrolyte is comparatively weak to the acid electrolyte. However, alkaline electrolyte often diffuses quickly which results in the difficulty in sealing. The neutral electrolytes containing potassium, sodium, or lithium salts is safe for handling, but the capacitance of metal oxide electrode materials is relatively low in the neutral electrolyte. Another limit for using aqueous electrolytes is their low decomposition voltage (the water-splitting potential is 1.229 V) and narrow operation temperature range (0–100 °C). These issues pose main disadvantages for the performance enhancement and actual application of aqueous supercapacitors.

Similarly, organic electrolyte solutions are also composed of electrolyte and solvent, both of which are organic. The most studied electrolyte cations are of the R_4N^+ type, such as Me_4N^+, Et_4N^+, Bu_4N^+, and Me_3EtN^+. And the common anions include ClO_4^-, BF_4^-, PF_6^-, AsF_6^-, and so on. The solvents usually include ethylene carbonate (EC), butyrolactone (BL), dimethylformamide (DMF), propylene carbonate (PC), acetonitrile (AN), and so on. The decomposition voltages of organic electrolytes are much higher which is beneficial to obtaining high energy density. Moreover, the operating temperature range of organic electrolytes is relatively wide due to their high chemical and electrochemical stability. Finally, organic electrolytes also have a few disadvantages of weak ions transportation and high cost.

4.2.1.3 Membrane

The membrane is used primarily to avoid the direct contact (short circuit) between anode and cathode, while providing open channels for the transportation of electrolyte ions. Therefore, they must be chemically and mechanically stable, insulating, porous, and in thin film form. The most used membranes are porous polymer films, such as glass fiber, polypropylene film, and agar film.

4.2.2 Supercapacitor Categories

As mentioned above, depending on the charge storage mechanism as well as the active materials used, supercapacitors can be classified into two general categories: electrochemical double-layer capacitors (EDLCs) and pseudo-capacitors. The energy storage mechanisms of the EDLCs and pseudo-capacitors will be introduced in detail below.

4.2.2.1 Energy Storage Mechanisms of the EDLCs

The double layer at the electrode surface forms and relaxes almost instantaneously. It has a time constant, or time of formation, of about 10^{-8} s. Therefore, the structure of the double layer has the capability to respond rapidly to potential changes in the same time frame. The process involves only a charge rearrangement, not a chemical reaction. The rapid response to change is in contrast to the situation involved in the redox electrode reactions in other batteries and fuel cells. The key to reaching high capacitance by charging the double layer is in using high specific surface area, electrically conductive electrodes. Graphitic carbon satisfies all of the requirements for this application, including high conductivity, electrochemical stability and open porosity. Activated, templated, and carbide-derived carbon, carbon fabrics, nanotubes [10], and nanohorns have also been tested for EDLC applications. And the activated carbons are the mostly widely used materials today, because of their high specific surface area and moderate cost. The capacitance of activated carbon reaches 100–200 F g^{-1} in organic electrolytes. This value can exceed 150–300 F g^{-1} in aqueous electrolytes, but at a lower cell voltage because the electrolyte voltage window is limited by water decomposition (Fig. 4.2).

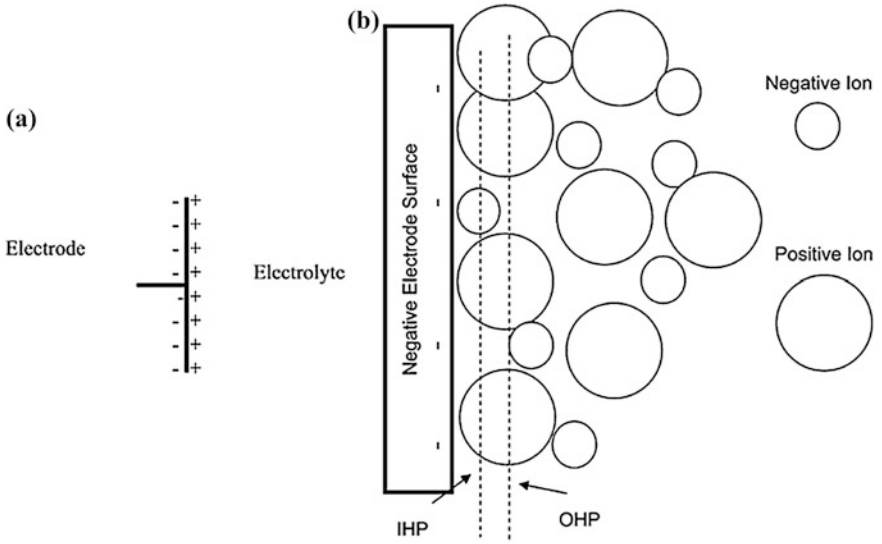

Fig. 4.2 **a** Simple Helmholtz model of the electrical double layer. It is essentially a picture of a conventional capacitor. **b** Depiction of the electrical double layer at the surface of the negative electrode showing the outer Helmholtz plane (OHP) and the inner Helmholtz plane (IHP). The inner Helmholtz plane (IHP) refers to the distance of closest approach of specially adsorbed ions and solvent molecules to the electrode surface. The outer Helmholtz plane (OHP) refers to the distance of ions, which are oriented at the interface by coulomb forces (Reproduced from Ref. [1]. Copyright 2004, American Chemical Society.)

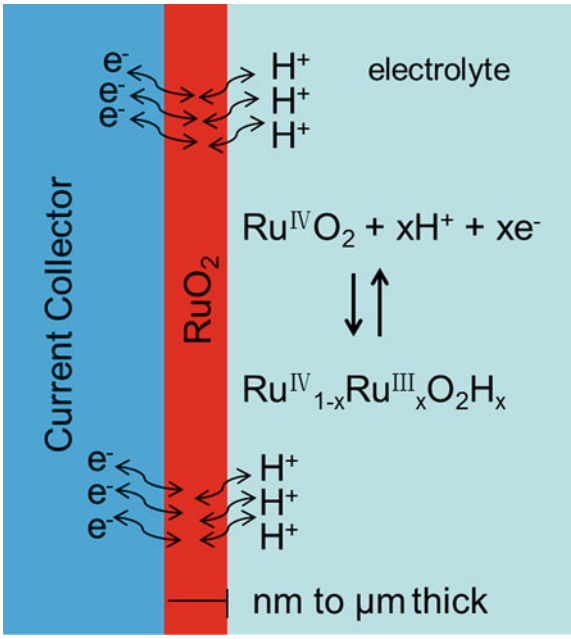

Fig. 4.3 Schematic of the charge storage mechanisms via redox reactions based pseudo-capacitance (Adapted from Ref. [11].)

4.2.2.2 Energy Storage Mechanisms of Pseudo-capacitors

A second group of supercapacitors, known as pseudo-capacitors or redox supercapacitors, (as shown in Fig. 4.3) take advantage of fast and reversible surface or near-surface reactions for charge storage purpose [11]. Given the nature of the Faradaic process (redox reactions) involved in energy storage, pseudo-capacitors can increase specific capacitance and energy density but at some cost of power density and cycle life when compared to EDLCs, because its response to environmental variations such as electro-potential is much slower. Metal oxides as well as electrically conducting polymers are examples of pseudo-capacitive active materials.

Trasttil and Buzzanca [12] and Conway [13] found that noble metal oxides such as RuO_2 exhibited the similar capacitance characteristics, while their capacitance was much higher than the carbon materials. Afterwards, PRI and Giner corporation studied RuO_2 and RuO_2/C capacitors which were applied to the laser weapon and the missile guidance system. RuO_2 is a widely studied pseudo-capacitive material thanks to their high theoretical specific capacitance (1358 F g^{-1}) and good electric conductivity (3×10^2 S cm^{-1}). When electrochemically cycled in acidic aqueous electrolytes, they exhibit distinct oxidation states accessible within a voltage window of $\sim$1.2 V. The pseudo-capacitive behavior of RuO_2 is generally ascribed to a series of fast and reversible electron transfer reactions coupled with adsorption of protons on the surface of RuO_2 electrodes (as shown in Fig. 4.3) where Ru oxidation states can change from (II) up to (IV). But due to its high price, RuO_2-based

power device may only be used in cost-insensitive applications such as space flight and aviation, military, and so on. Therefore, design and development of the cheap transition metal oxides and conducting polymers are imperative. The most commonly known pseudo-capacitive metal oxides include manganese oxide (MnO_x) [14], iron oxide (Fe_3O_4) [15], nickel oxide (NiO) [16], and others. Lee and Goodenough [17] firstly reported the capacitance-like behavior for MnO_2 when it was electrochemically cycled in 2 M KCl aqueous electrolyte, which has so far catalyzed a great deal of interest in exploring MnO_2 as an active material for EC applications. The theoretical specific capacitance is 1370 F g^{-1}. But this value has rarely been achieved in experiments mainly due to its poor electric conductivity ($\sim 10^{-6}$ S cm^{-1}), which limits the rate capability for high power performance and thus hinders its wide applications in energy storage systems. Typical conducting polymers for redox pseudo-capacitance are polyanilines, polythiophenes, polypyrroles, and so on. These π-conjugated conducting polymers with various heterocyclic organic compounds have shown high gravimetric and volumetric pseudo-capacitance in various nonaqueous electrolytes with operating voltages of ~ 3 V. However, their capacitive performances are limited by high electric resistance and low cycling stability. Particularly, the attainable energy density is often an order of magnitude lower than their theoretical assessment.

4.3 The Advantages of Nanoporous Metals as Electrodes for Supercapacitors

Recently, dealloyed nanoporous metals with a large internal surface area and an excellent conductivity have also been studied as both the EDLCs and supports for pseudo-capacitive materials, such as metal oxides and polymers. For example, by utilizing the excellent conductivity, large internal surfaces, and open porosity of nanoporous gold (NPG), Lang et al. [18] successfully incorporated pseudo-capacitive MnO_2 and PANI into NPG and fabricated novel hybrid electrodes for supercapacitors with a high energy density. Meng and Ding [19] documented the fabrication of an ultrathin flexible, all-solid-state supercapacitor based on PPy-decorated NPG membranes. The symmetric supercapacitor thus produced offers large specific capacitance, power density, and energy density, and exhibits almost identical performance at various curvatures. There are several advantages of nanoporous metals as electrodes for supercapacitors:

1. Unique structure. Among various nanostructured materials, nanoporous metals made by dealloying possess some of the most intricate and random 3D morphologies. Nanoporous metals appear to be completely irregular in morphology for both empty pore channels and solid metallic ligaments comprising the nanostructure. The distribution of solid ligaments and empty pore channels is analogous to the microstructure produced by traditional spinodal decomposition. In remarkable contrast to other porous materials, the porosity of nanoporous

metals may be easily adjusted over a wide range of length scales, where the primary degree of control is simple bench-top postprocessing at room temperature by immersion in electrolytes or thermal annealing at moderate temperatures. The nanoporous gold possesses large surface area, interconnected metal ligaments, high porosity, and excellent electric conductivity. These fascinating structural properties enable nanoporous materials to exhibit high electrochemical/mechanical stability and advantages for enhancing ion and electron transport kinetics in the electrode materials. That is, well interconnected porous channels not only allow rapid ion transport in the electrodes but also provide extremely large specific surface area of electrode/electrolyte interface to ensure the sufficient redox reaction during charge/discharge processes, facilitating the full use of large pseudo-capacitance.

2. High conductivity. Hu et al. [20] recently invented a series of flexible energy storage devices by coating paper or textiles with single-walled carbon nanotubes (SWNTs), and the sheet resistance of the resultant films could reach a low level of $\approx 0\ \Omega\ sq^{-1}$. Meng and Ding [19] reported that the sheet resistivity measurements show impressively small values of 2.5 and 4.4 $\Omega\ sq^{-1}$ for bare NPG and NPG-PPy leaves, respectively, which are comparable to those with carbon nanotubes, although the thickness of the electrode can be two orders of magnitude smaller. Since the electrical conductivity of nanoporous metals (Au or Cu) is $\sim$3–5 orders of magnitude higher than that of carbon materials, nanoporous metals are expected to dramatically enhance the electronic and ionic conductivity of pseudo-capacitive materials for high specific capacitance. The 3D interconnected Au network with ultrahigh electrical conductivity harnesses the electron transport by remarkably decreasing the internal resistance of assembled devices.

Therefore, the unique architecture and the high conductivity of the nanoporous metal-based electrode materials are beneficial to enhancing the charge transport, giving rise to ultrahigh specific capacitance (often approaching their theoretical values), low rate dependence, and long cycling life.

4.4 Nanoporous Metals and Self-grown Components for Supercapacitors

The bicontinuous porous structure in electrodes significantly increases the specific surface area and enlarges the interface of electrode/electrolyte, which enhance the electrochemical performance of supercapacitors. Pure nanoporous metals and surface oxidized/oxyhydroxidized nanoporous metals have been directly investigated as electrodes in supercapacitors. In this section, we briefly introduce the bare nanoporous metals electrodes and surface oxidized/oxyhydroxidized nanoporous metals electrodes for supercapacitor applications.

4.4.1 Pure Nanoporous Metals as Electrodes

Nanoporous gold (NPG), which can be produced by dealloying $Ag_{65}Au_{35}$ ribbons in 70 % HNO_3, has been investigated as electrodes of supercapacitors [21]. The dealloyed NPG exhibits a bicontinuous nanoporous structure which consists of quasi-periodic nanoporous channels as shown in Fig. 4.4a. The uniform nanoporous structures are observed all over the dealloyed sheet. The supercapacitor devices are composed by two NPG sheets separated by a piece of cotton paper. The schematic diagram of the fabricated supercapacitor is shown in Fig. 4.4b. In this research, both 2 M KOH aqueous solution and ionic liquid have been investigated as electrolyte and the corresponding CV curves at different scan rates are displayed in Fig. 4.4c, d. The supercapacitors with ionic liquid electrolyte show improved operating voltage range (about 2 V) compared to that of KOH aqueous electrolyte (about 1 V). These results demonstrate that the high electric conductivity combined with the high surface area of NPG contributes for the good device performance both in aqueous and ionic liquid electrolytes. The electrochemical performance of NPG can

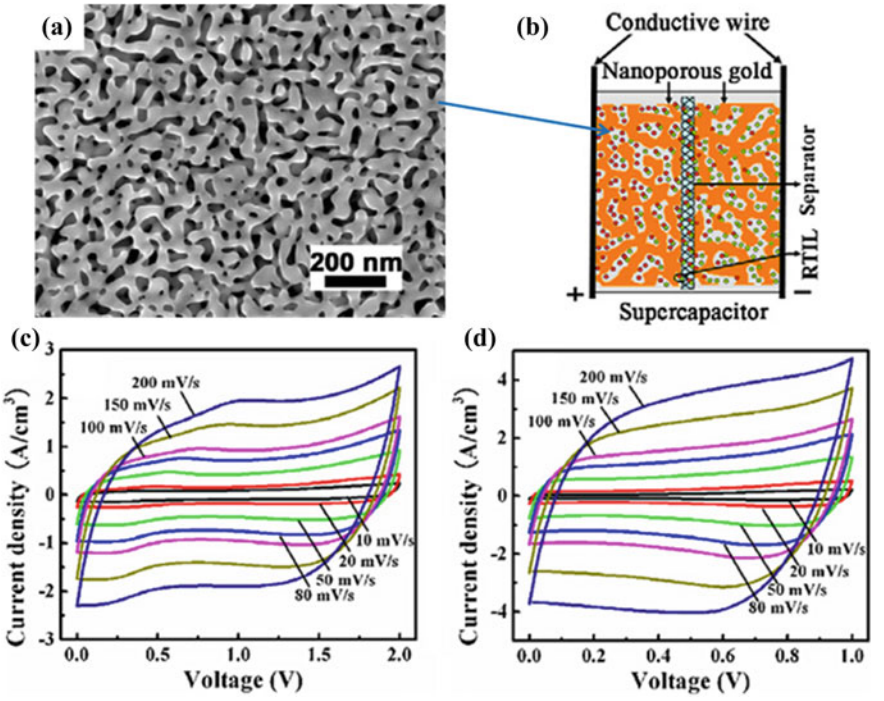

Fig. 4.4 **a** Representative SEM images of a NPG electrode from *top view*, **b** schematic diagram of the supercapacitor assembled with NPG as both electrodes and current collectors, and a piece of cotton paper as separator. **c** Cyclic voltammetry of the NPG-based supercapacitors in a DEME-TFSI ionic liquid at room temperature and **d** in a 2 M KOH aqueous electrolyte (Adapted from Ref. [21].)

be further enhanced by enlarging the nanoporosity of NPG and optimizing the electrolytes.

Nanoporous Ni has also been studied as electrodes both in normal organic electrolyte propylene carbonate and ionic liquid electrolyte as shown in Figs. 4.5 and 4.6 [22, 23]. The porous Ni electrode is fabricated by dealloying Ni–Al alloy in alkaline solutions. The post heat treatment should be taken with great caution due to the high reactivity of nanoporous Ni in air. The surface oxidation of nanoporous Ni undoubtedly increases the electrochemical resistance and deteriorates the capacitor performance. The microstructure of thus produced nanoporous Ni can be appreciated by a TEM image shown in Fig. 4.5a. The irregular distributed dark and light patterns demonstrate that the pores are surrounded by Ni grains. The chaotic distribution of pores is originated from the diffusion of Ni atom and the subsequent aggregation of the resulting Ni particles to grains. The pore distribution is determined from the N_2 adsorption/desorption isotherm as shown in Fig. 4.5b, which features a multimodal porous structure with characteristic pore dimension around 5, 30, and 80 nm. The heat treatment and gas conditions apparently affect the pore

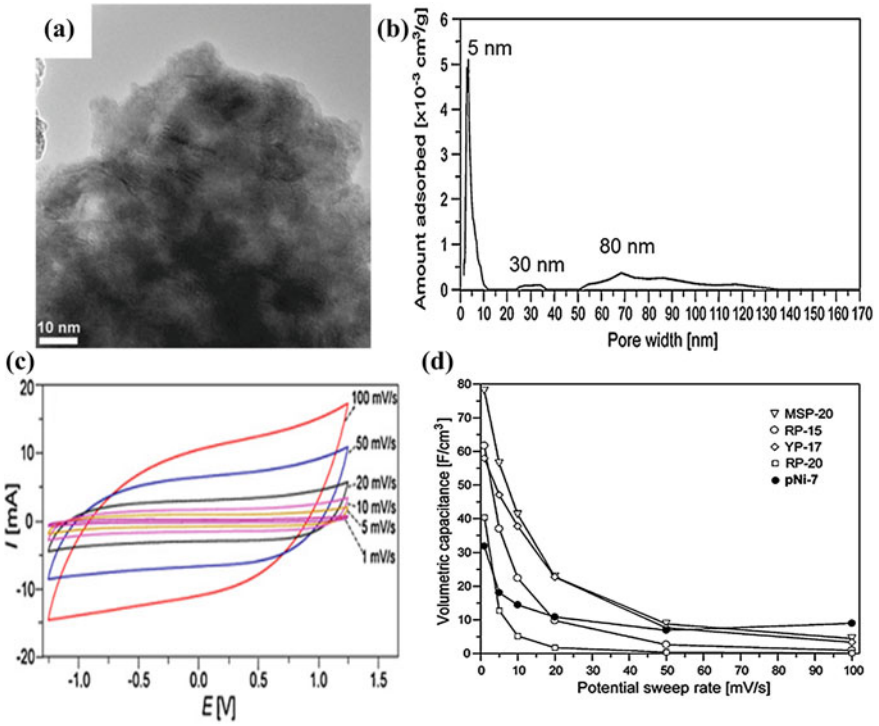

Fig. 4.5 **a** Typical TEM images of porous Ni material, **b** pore-size distribution of porous, **c** cyclic voltammetary curves of porous Ni electrodes at the potential-sweep rate of 100–1 mV/s, **d** potential-sweep-rate dependence of volumetric capacitance of porous Ni and the commercial active carbons (Adapted from Ref. [22].)

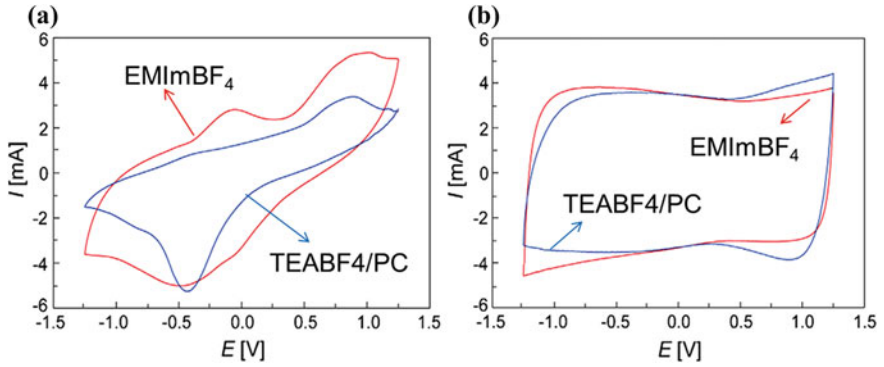

Fig. 4.6 **a** Cyclic voltammetry curves of poroous electrode prepared without heating and air-contact, **b** a high-capacitance-type activated carbon, MSP-20, in TEABF4/PC (*blue line*) and $EMImBF_4$ ionic liquid (*red line*). The CV curves were measured at 1 mV/s in a three-electrode system (Adapted from Ref. [23].)

distributions. By drying the dealloyed slurry under Ar flow at 120 °C for 2 h, the dominant pore size lies in the range of 2–10 nm in combined with some larger size mesopores and macropores. The capacitor performance of nanoporous Ni electrode is shown in Fig. 4.5c. The profiles show rectangular shape and exhibit capacitor characteristic behaviors. The rectangular shape deviation becomes marked at the faster sweep rates. The volumetric total capacitance of the nanoporous Ni and other commercial active carbons are compared as shown in Fig. 4.5d. Nanoporous Ni shows abrupt capacitance decrease in the low sweep-rate region, whereas it becomes almost constant at sweep rate higher than 20 mV/s. The corresponding capacitance retention is ~4.9 times higher than those of the active carbon materials. The enhanced performance is mainly associated with the special porous structure.

The supercapacitor performance of nanoporous Ni with an average pore size of 7.2 nm is examined as shown in Fig. 4.6 [23]. Both $TEA{\cdot}BF_4$/PC and $EMIm{\cdot}BF_4$ are used as the electrolytes. The working-potential range of ionic liquid is broader than that in PC-solvated ion system, and the calculated volumetric total capacitance reaches 67.4 F/cm^3, which is twice of that in $TEA{\cdot}BF_4$/PC. In comparison, the MSP-20 active carbon sample only finds slight increase of the current in the ionic liquid.

4.4.2 *Surface Oxidized/OxyHydroxidized Nanoporous Metals as Electrodes*

3D nanoporous metals hold a unique combination of a highly conductive network and a bicontinuous open porous structures, which promise their utilization in supercapacitors. Metal oxides as thin coating layers onto various nanoporous metal

substrates thus become a rational electrode structure for high performance supercapacitors, benefiting from their synergistic effects. For example, nanoporous Ti with a TiO_2 coating layer has been proposed by dealloying of nitinol followed by heat treatment [24]. In this special structure, the pore channels can be well maintained for efficient electrolyte penetration, while the good conductivity of the metal framework can be well reserved. The capacitive performance of the fabricated electrode is investigated by cyclic voltammetry and as shown in Fig. 4.7, nanoporous TiO_2 shows a capacitance of 7.01 mF, which is better than that of TiO_2 nanotubes. Moreover, the curve of the nanoporous TiO_2 presents as a well rectangular shape compared with the TiO_2 nanotube sample. The schematic diagram of these two types of supercapacitors is shown in Fig. 4.7b. In the diagram of the nanoporous Ti/TiO_2 electrode, there is a very thin dielectric layer of TiO_2. However, in the ordered TiO_2 nanotube, the electrons transport is only in a vertical direction along the nanotubes to the bottom of electrode, which is comparatively inefficient for charge/discharge route. In addition, the nanoporous structure and very thin TiO_2 layer promise the shorter electrons transmission path, and thus, the faster charge/discharge process.

The oxyhydroxide also shows superior performance as an electrode in supercapacitors [25]. To enlarge the surface area, promote the electrode conductivity and electrolyte penetration, the oxyhydroxide/nanoporous metals have been prepared by

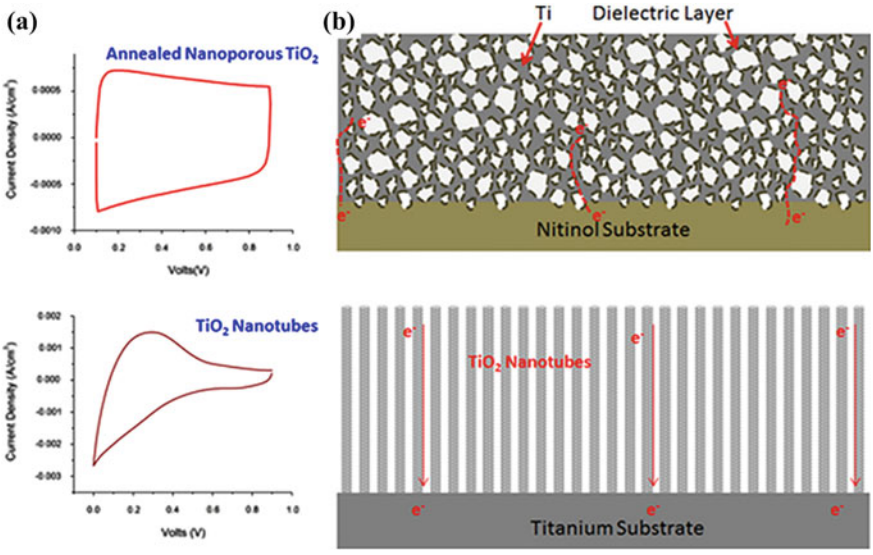

Fig. 4.7 **a** Cyclic voltammetry curves of annealed nanoporous Ti/TiO_2 (*top*) and ordered TiO_2 nanotubes (*bottom*); **b** schematic diagrams of structures comparison with dealloyed nanoporous TiO_2 and TiO_2 nanotubes: the upper diagram shows the Ti/TiO_2 nanoporous structure, the *gray part* is titanium and the *dash line* represents the very thin dielectric layer of TiO_2; the *bottom diagram* shows the ordered TiO_2 nanotube (*light gray*) on titanium substrate (*dark gray*) (Adapted from Ref. [24].)

electrochemical polarization of the dealloyed nanoporous metals. The surface oxyhydroxide and the internal nanoporous metal framework form a homogeneous composite structure. In the resultant electrode, the oxyhydroxide grows on the surface of the nanopore channels, forming a stable hybrid nanoporous structure. The $(Ni_aMn_bMn_c)O_d(OH)_e$ *f* H_2O based on nanoporous Ni–Mn binary alloy have been synthesized by dealloying Ni–Mn in $(NH_4)_2SO_4$ solution and followed by electrochemical polarization in a 1 M KOH solution at 0.8 V [25]. The channels of the nanoporous metals have been retained very well even after polarization treatment as shown in Fig. 4.8a. The rock-salt oxyhydroxide phase can be confirmed as the inset figure. The distribution of the face-centered-cubic (*f.c.c.*) metal substrate and rock-salt oxyhydroxide phases have been determined by the inverse fast fourier

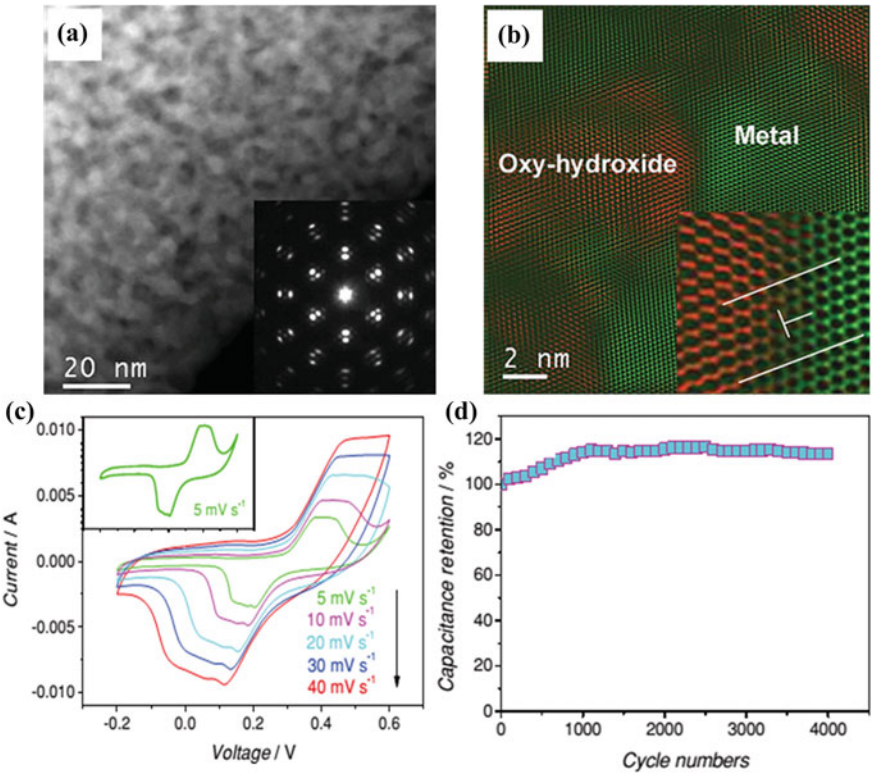

Fig. 4.8 Microstructure and chemistry of the nanoporous self-grown Ni–Mn oxyhydroxide@NPM electrode. **a** STEM-HAADF image showing nanoporous structure. The *inset* is the selected area electron diffraction pattern taken from this sample. **b** IFFT-STEM atomic image displaying the distribution of the self-grown oxyhydroxide and metal substrate. The *inset* is the zoom-in micrograph shows the mismatch dislocations at the oxyhydroxide/metal interface. **c** Cyclic voltammogram curves at different scan rates. The *inset* is a slow-scan curve with well-defined redox reaction peaks. **d** The cycling stability of the electrode by charge/discharge testing at a current density of 5 A/cm^{-3} (Reproduced from Ref. [25]. Copyright 2014, Wiley-VCH.)

transform (IFFT) of a high-resolution STEM-HAADF image as shown in Fig. 4.8b. The two phases have a coherent crystallographic relation with a small lattice mismatch. This result demonstrates the successful growth of the oxyhydroxide on the metal surface during the polarization progress.

The capacitance performance of the self-grown oxyhydroxide/nanoporous metals are studied in a three-electrode system in 1 M KOH solution. The cyclic voltammetry curves of the composite electrode are tested in the voltage range of −0.2 to 0.6 V at varied scan rates from 5 to 40 mV/s. As shown in Fig. 4.8c, there is a pair of well-defined redox peaks at 0.2 and 0.4 V, which is associated with the reversible reactions of Ni^{2+}/Ni^{3+} and OH^- anions. The separation of reduction and oxidation peaks increases with the increasing of scan rates, suggesting the redox reversibility of the hybrid electrode is kinetically associated with a rate-controlling process. There is also a rectangular-shape area in the CV curves which accounts for about 18 % of the total capacitance. The surface area is dependent on the amount of Mn in the final electrode composites. A maximum specific capacitance reaches up to 505 F cm^{-3} at a current density of 0.5 A cm^{-3}, which is 3–10 times higher than the best reported values achieved from highly porous carbon materials and pseudo-capacitor electrodes. The cycle performance is evaluated by the charge/discharge test as shown in Fig. 4.8d. The capacitance gradually increases at the first 1000 cycles, demonstrating the gradually activation of Mn–Ni oxyhydroxide electrode. It keeps nearly constant even up to 4000 cycles. This high cyclic stability of the hybrid electrode is associated with the intrinsic chemical bonding between 3D current collector and oxyhydroxide. The residual tensile strain at the epitaxial oxide/metal interface benefits to alleviate the mechanical failure from the metal substrate during cycling.

To further improve the specific capacitance and working-potential range, mixed-valence oxyhydroxide ($Ni^{II}_aCu^{I}_bCu^{II}_cMn^{II}_dMn^{IV}_e$) $O_f(OH)_gH_2O$ has been prepared by dealloying ternary Ni–Cu–Mn alloy [26]. This hybrid composite electrode exhibits an ultrahigh specific capacitance of 627 F cm^{-3} at a current density of 0.25 A cm^{-3} and a very large operating potential window of 1.8 V in an aqueous electrolyte. The typical fabrication process of the composite electrode is shown in Fig. 4.9a. The nanoporous alloy has a monolithic *f.c.c.* structure as confirm by X-ray diffraction in Fig. 4.9b. The rock-salt-type oxide can be observed and a mixture of MnO and NiO in the final electrode composite. The nanoporous ternary alloy is obtained by dealloying the $Ni_{15}Cu_{15}Mn_{70}$ (at.%) in 1 M $(NH_4)_2SO_4$ solution at −0.70 V (vs. Ag/AgCl). The most active metal Mn is partially leached off to form the porous structure. The nanoporous alloy is further polarized in 1 M KOH solution at 0.9 V to oxidize the ternary alloy. The metal ligament size can be reduced to about 3.4 nm after the formation of a stable oxide layer. The nanopores channels are almost filled by a leaky polarization product with pore sizes smaller than 1 nm (Fig. 4.9c).

The electrochemical performance of the nanoporous oxyhydroxide-based electrode is evaluated by cyclic voltammetry in 1 M KOH electrolyte at a voltage range of 0–1.8 V at varied scan rates. All of the redox reactions are fully reversible in this

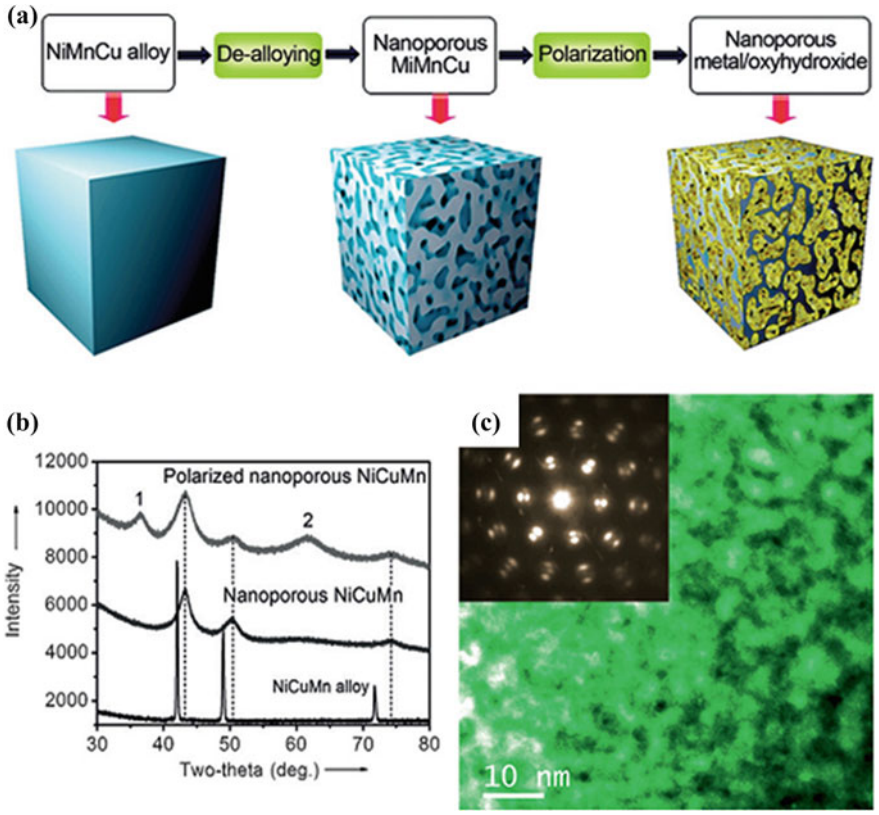

Fig. 4.9 **a** Illustration of the fabrication process of the oxyhydroxide supported by interconnected metal skeletons; **b** XRD spectra of the precursor NiCuMn alloy, dealloyed nanoporous NiCuMn, and electrochemically polarized nanoporous NiCuMn. **c** STEM micrograph of the electrochemically polarized nanoporous NiCuMn alloy. The *inset* is the SAED pattern (Reproduced from Ref. [26]. Copyright 2015, Wiley-VCH.)

wide voltage range. It is well known that the improved operation working potential windows of oxides or oxyhydroxides, or mixture of Mn and Ni oxides is no more than 1.1 V in aqueous electrolytes. Herein, this large working potential window of NiCuMnOOH is mainly from the introduction and stabilization of the effective redox reactions in the cathodic potential region by the synergetic alloying effect of Ni, Cu, and Mn ions. The obvious charge/discharge plateaus in Fig. 4.10b are associated with the redox reactions. This result is consistent with the CV curves. The maximum volumetric capacitance is measured to be ca. 627 F cm^{-3} at a low current density of 0.25 A cm^{-3}, which is among the best values achieved in supercapacitors so far. With the increase of current density, the volumetric capacitance gradually decreases due to the low utilization efficiency of the active oxyhydroxide at high rates. To evaluate the resistance of the fabricated composites

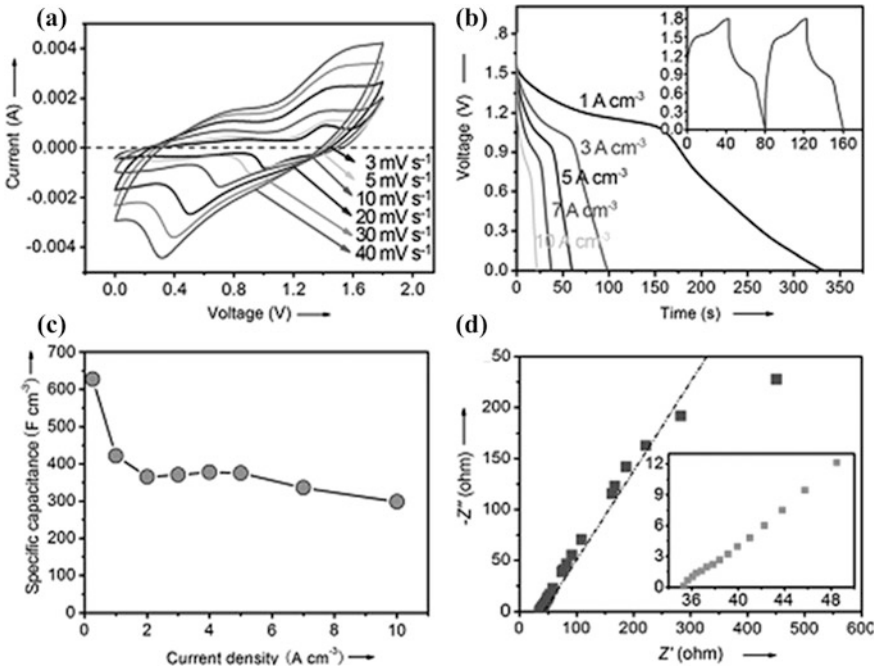

Fig. 4.10 Supercapacitor performance of the oxyhydroxide electrode tested by a two-electrode configuration in 1 m KOH electrolyte. **a** Cyclic voltammograms at scan rates from 3 to 40 mV/1. **b** Discharge curves at different current densities. The *inset* shows typical charge/discharge curves. **c** The specific volumetric capacitances of the electrode versus current density. **d** Nyquist diagram of electrochemical impedance spectroscopy of the oxyhydroxide-based supercapacitor device. The inset is the enlarged high-frequency region (Reproduced from Ref. [26]. Copyright 2015, Wiley-VCH.)

electrode, the electrochemical impedance spectroscopy, as shown in Fig. 4.10d, features the very small radius of the semi-circle in the high-frequency region, indicating the low charge transfer resistance at the electrode/electrolyte interface. The low intrinsic resistance is most likely associated with the highly conductive metallic skeletons.

4.5 Active Materials Modified Nanoporous Metals for Supercapacitors

4.5.1 MnO_2/Nanoporous Metal Composites

Among various electrode materials, MnO_2 has drawn great attentions due to its high capacitance ($\sim$1145 F/g) for storing electrical charge while inexpensive resources

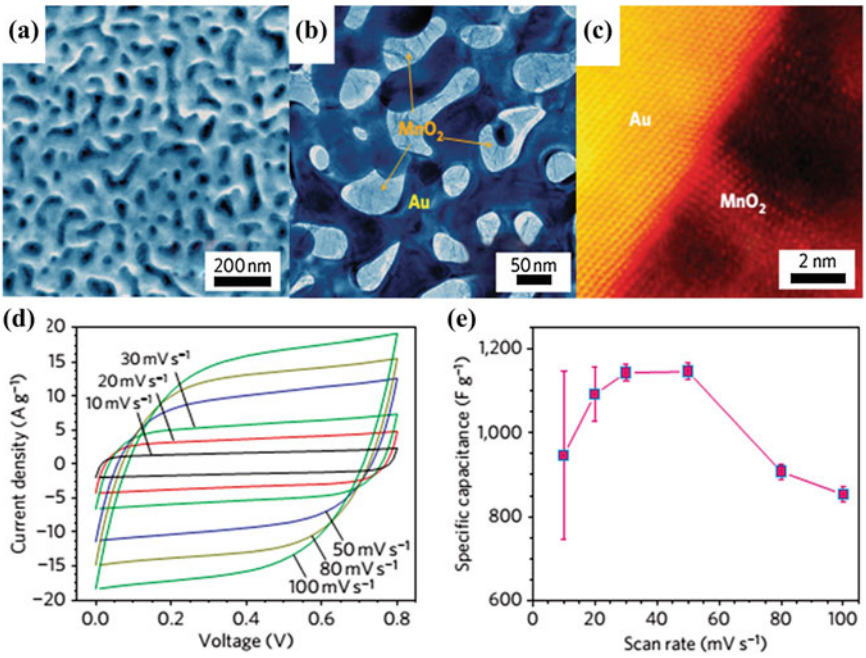

Fig. 4.11 Microstructure characterization. **a** SEM image of a nanoporous gold/MnO_2 film and MnO_2 nanocrystals were uniformly plated onto the gold without changing the nanoporosity. **b** Bright-field TEM image of the nanoporous gold/MnO_2 hybrid. **c** High-angle annular dark-field STEM image taken from a gold/MnO_2 interface region. **d** Cyclic voltammograms (current density vs. voltage) for a nanoporous gold/MnO_2 electrode (plating time, 20 min) at six different scan rates between 10 and 100 mV/s. **e** Corresponding specific capacitance of the plated MnO_2 versus scan rate. All data are taken in a 2 M Li_2SO_4 solution at room temperature (Reproduced from Ref. [18]. Copyright 2011, Nature Publishing Group)

and not harmful to the environment. However, the poor conductivity of MnO_2 (10^{-5}–10^{-6} S cm^{-1}) limits the charge/discharge rates. By accommodating MnO_2 into skeletons as nanoporous gold, nanoporous copper, the resulted nanohybrids show substantially enhanced performance as supercapacitor electrodes [27]. Tremendous efforts have also been committed to optimize the MnO_2/nanoporous metal electrode structures. Thick MnO_2 layer electrode and chip supercapacitor have been constructed [28].

MnO_2 can be adopted into a 100-nm thick MnO_2/NPG composite electrode by a two-step fabrication process [18]. First, the NPG substrate is obtained by dealloying $Ag_{65}Au_{35}$ in HNO_3, and then plating nanocrystalline MnO_2 into the nanoporous. The bicontinuous nanoporous structure which consisting of quasi-periodic gold ligaments and nanopore channels can be appreciated by an SEM image in Fig. 4.11a. The loading mass of MnO_2 can be adjusted by controlling the plating time. TEM images of hybrid electrode displays that the nanopores are filled with nanocrystalline MnO_2 with a grain size of $\sim$5 nm (in Fig. 4.11b). The gold/MnO_2

interfaces are further confirmed by scanning TEM as shown in Fig. 4.11c. The nanocrystalline MnO_2 grows epitaxially on the gold ligament surfaces, forming a chemically bonded metal/oxide interface.

The prepared hybrid electrodes are assembled into two electrodes symmetry supercapacitor by using 2 M Li_2SO_4 aqueous electrolyte. Cyclic voltammograms show a perfectly symmetrical rectangular shape. This is due to both the surface electrosorption of Li^+ cations and the fast, reversible successive surface redox reactions of MnO_2 by means of intercalation/de-intercalation processes of the protons according to the reactions. This supercapacitor is charged and discharged at a pseudo-constant rate over the entire voltammetric cycles. With the increasing of MnO_2 mass loading, there is significant improvement of capacitance. A high specific capacitance of 601 F/g (based on the total mass of gold and MnO_2) can be achieved for the 20 min MnO_2-plated electrodes, which is much higher than the values for MnO_2/carbon composites. The hybrid electrode also shows superior rate performance as investigated by cyclic voltammetry over the range 10–100 mV s^{-1} (Fig. 4.11d). The extremely high volumetric capacitance of 1160 F/cm^3 has been obtained at a scan rate of 50 mV/s. Moreover, the capacitance remains quite high under repeated charge/discharge cycles, retaining about 80 % of its initial value after 500 cycles at this scan rate. Figure 4.11e summarizes the corresponding specific capacitance of the plated MnO_2 versus electrodes at low discharge current densities and scan rates. The maximum value of 1145 F/g is about 84 % of the maximum theoretical value of 1370 F/g at a scan rate of 50 mV/s. This excellent performance is associated with the porous metal/oxide structure, in which the nanocrystalline MnO_2 grows coherently onto the internal surface of the highly conductive nanoporous gold, allowing easy and efficient access of both electrons and ions so as to afford a fast redox reaction at high scan rates.

The nanoporous copper (NPC)-based composite electrode has also been fabricated [29]. To prepare NPC, $Cu_{52.5}Hf_{40}Al_{7.5}$ alloy ribbons are corroded in 0.5 M HF. The MnO_2/NPC composites are synthesized by dropping 0.1 M $KMnO_4$ aqueous solution to ethanol with the presence of NPC substrate. Figure 4.12a illustrates the fabrication process of hybrid composites, in which MnO_2 layer is directly deposited on the ductile NPC substrate. The homogeneous deposition of MnO_2 on the NPC surface has been confirmed by SEM as shown in Fig. 4.12b. The composite electrodes with different MnO_2 ratios have been investigated in supercapacitors. Cyclic voltammogram curves are performed by three-electrode cells equipped with 0.5 M Na_2SO_4 electrolyte. Figure 4.12c shows the CV curves of the pure NPC, pure MnO_2 and MnO_2/NPC composites with different weight ratios. The pure NPC electrode shows negligibly low capacitance. The signal and the closed area of CV curves for the MnO_2/NPC composite electrode are remarkably enhanced as compared to that for the pure MnO_2 powders fabricated under the same conditions. Moreover, the current response increases greatly as the weight ratio of NPC to MnO_2 increases. The values of the specific capacitance of MnO_2/NPC composites with different weight ratios and cycle numbers are calculated and shown in Fig. 4.12d. The specific capacitance of 80 wt% NPC is larger than that of the 50 % composite at the same scan cycle. In both electrodes, the capacitance of the

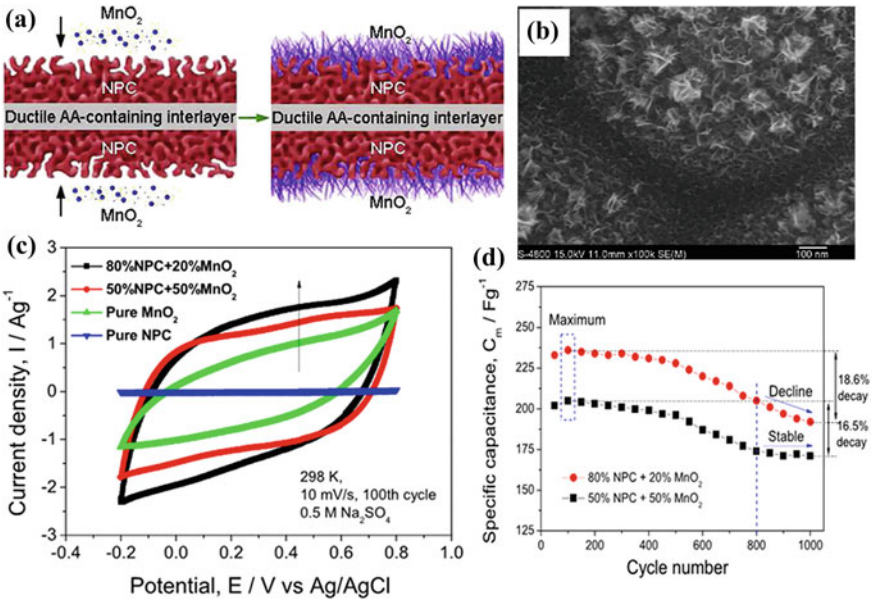

Fig. 4.12 **a** The fabrication process of the MnO_2/nanoporous copper composites, **b** SEM image of MnO_2/nanoporous copper composite with 80 wt% nanoporous copper, **c** CV curves of monolithic nanoporous copper, pure MnO_2 and MnO_2/NPC composites with different weight ratios in 0.5 M Na_2SO_4 solution, **d** cycling performances of MnO_2/nanoporous copper composite (Adapted from Ref. [29].)

composites reaches the maximum value at the 100th cycle and then decreases with further increasing cycles. This composite electrode shows good mechanical integrity and bendability, which promise its potential utilizations in flexible devices.

To further improve the mass loading of MnO_2 in the electrode composite, a novel sandwich electrode has been designed by utilizing the open porosity of dealloyed NPG [28]. The fabricated hybrid electrode presented as a sandwich structure and the NPG sheet acts a current collector and provides good electronic/ionic conductivity for realization of the high pseudo-capacitance of MnO_2. The deposition of MnO_2 is finished in an aqueous solution containing 0.2 M $Mn(CH_3COO)_2$ and 0.2 M Na_2SO_4. MnO_2 films are electrodeposited on both sides of a NPG sheet using a three-electrode system. The electroplated film is comprised of MnO_2 thin sheet with a thickness of about several nanometers. The schematic diagram of a symmetric supercapacitor cell assembled using two MnO_2/NPG/MnO_2 sandwich electrodes is shown in Fig. 4.13a. Here the cotton paper is soaked with 2 M Li_2SO_4 electrolyte to function as a separator. The inset is the photo of a real device with the MnO_2 loading of about 200 g/cm^2 for each sandwich electrode. The CV curves keep rectangular shape even at high scan rates (Fig. 4.13b). The specific capacitance remains at about 580 F/g as in Fig. 4.13c. The electrochemical impedance (EIS) measurements (Fig. 4.13d) demonstrate the resistance of hybrid

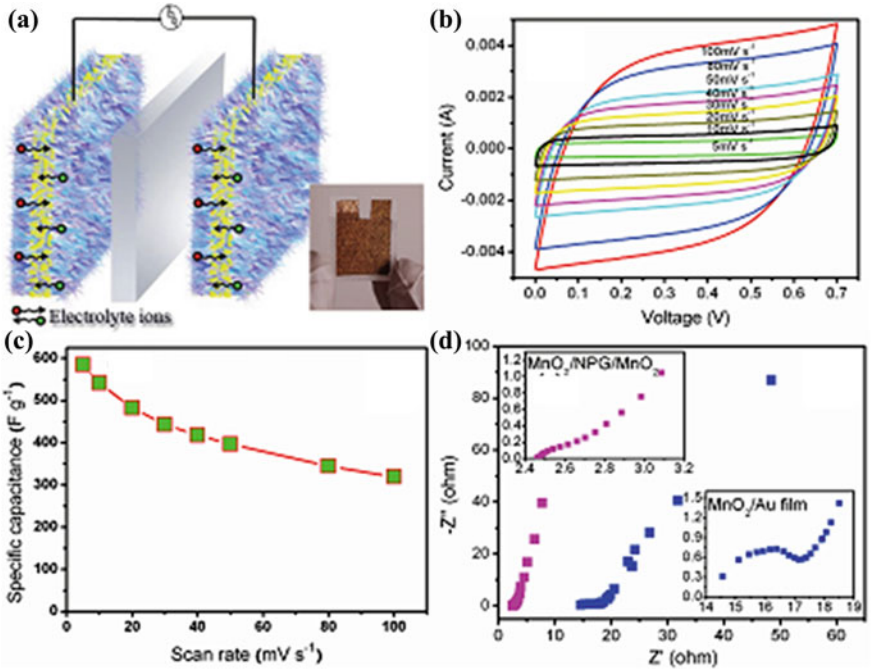

Fig. 4.13 **a** Schematic and optical images of the supercapacitor device using the sandwich electrodes, **b** CV curves of the device at different scan rates from 5 to 100 mV/s and **c** the corresponding specific capacitances of the electrode versus scan rates, **d** Nyquist plot of the devices assembled by MnO_2/NPG/MnO_2 electrodes and MnO_2/Au electrodes with similar loading mass (Reproduced from Ref. [28]. Copyright 2013, Wiley-VCH)

electrodes. The sandwich electrode shows a very small radius of R_{ct}, indicating high efficiency of charge transport with the electrolyte. This value has been significantly reduced compared with the resistance of MnO_2/gold film. The fully open porosity of NPG possesses ultrahigh charge transfer at the three-phase interfaces of active MnO_2, electrolyte and NPG. These results verify that the active MnO_2 deposited on the sandwich electrodes can be fully utilized for redox reaction with high charge storage efficiency.

MnO_x is also electrodeposited on Pt decorated NPG to further enhance its electrochemical performance [30]. Figure 4.14a illustrates the fabrication process of MnO_x/NPG and MnO_x/Pt@NPG hybrid electrodes. NPG is fabricated by normal dealloying method and Pt@NPG is prepared by electrodeposited Pt nanoparticles on the NPG membrane. Figure 4.14b and c show the surface morphology of fresh NPG and Pt@NPG. The bicontinuous structure is characterized by quasi-periodic gold ligaments and nanopore channels with a characteristic length of about 41 nm. Pt nanoparticles are uniformly distributed on the NPG and with a size of about 3 nm. The fabricated MnO_x/Pt@NPG hybrid electrode shows higher electrochemical performance than MnO_x/NPG for supercapacitors operated in 1 M

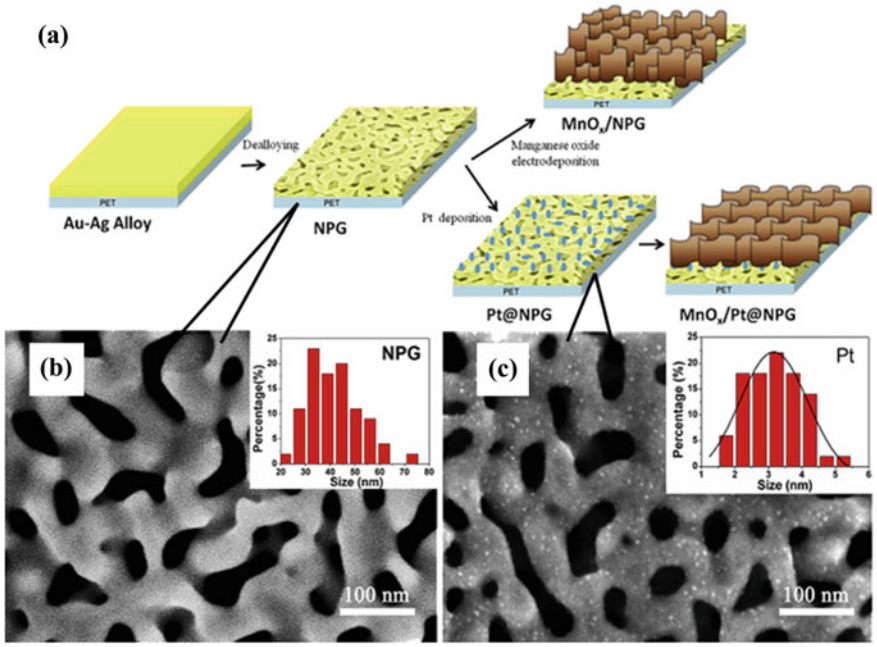

Fig. 4.14 **a** Schematic illustration of the fabrication process of the MnO_x/NPG and MnO_x/Pt@NPG hybrid electrodes. SEM images of **b** NPG membrane and **c** Pt@NPG membrane. The *inset* of **b** indicates the size distributions of nanoporous channels of the NPG membrane with the mean and standard deviation values of 41 ± 11 nm. The *inset* of **c** indicates the size distributions of Pt nanoparticles with the mean and standard deviation values of 3 ± 1 nm (Adapted from Ref. [30].)

Na_2SO_4 aqueous electrolyte. The specific capacitance of MnO_x/Pt@NPG is 775 F/g at 1 A/g, which is about twice larger than that of MnO_x/NPG electrodes with 404 F/g at 1 A/g. In this electrode structure, the Pt nanoparticles not only facilitate the formation of manganese oxide nanosheets, but also improve the conductivity of hybrid electrodes.

On-chip supercapacitors are promising energy storage devices for a variety of applications such as sensor and wearable electronics. The MnO_x/NPG hybrid electrodes with hundreds-nm-thickness are fabricated into all-solid-state interdigitated micro supercapacitors. The MnO_x/NPG films are used as active storage electrodes in interdigitated device architectures that include polyvinyl alcohol (PVA)/H_2SO_4 gel as the electrolyte [31]. The schematic diagram of device fabrication process is shown in Fig. 4.15a and the photo of prepared NPG supported MnO_x/NPG supercapacitor device is shown in Fig. 4.15b. The gel electrolyte is directly dropped on the hybrid electrode and dried in vacuum to remove residual water. This kind of devices exhibit good electrochemical performance with power density of 3.4 W/cm^3 and energy density of 50 μWh/cm^3. The capacitance retention

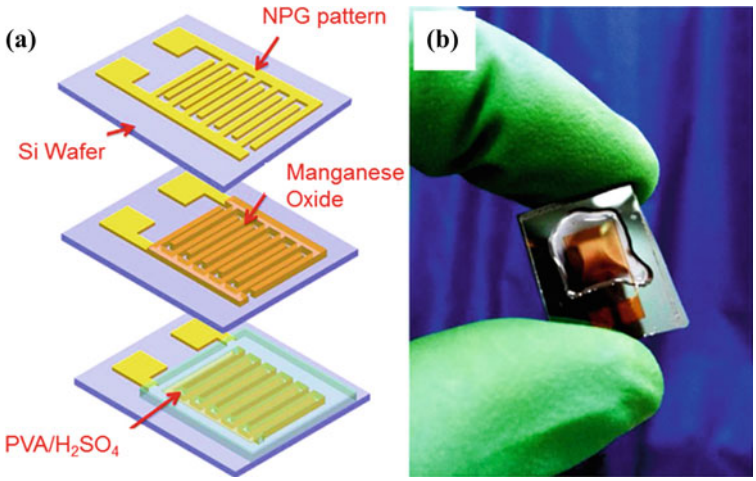

Fig. 4.15 **a** Schematic diagram of the fabrication process of NPG/manganese oxide nanowires based on-chip supercapacitor, **b** optical photographs of the fabricated NPG/manganese oxide nanowires-based supercapacitor device (Adapted from Ref. [31].)

after long-term cycles is about 81 %, and it also shows very quick response to the alternating current with the response time less than 4 ms.

A hierarchical MnO_2/NPG hybrid micro-pseudo-capacitor has also been proposed for on-chip supercapacitor and fabricated by micro-electro-mechanical technique [32]. Figure 4.16a schematically demonstrates its structure. The entire device, with dimensions of 3.95 * 5.45 mm, is settled on a glass substrate and consists of 16 microelectrodes organized in an interdigital planar geometry. Every eight out of the 16 electrodes, made of NPG and MnO_2, form either the cathode or anode and the gap between two electrodes is 50 μm (Fig. 4.16b). The microstructure of fabricated MnO_2/NPG electrode is shown in Fig. 4.16c. It can be clearly observed that the flocculent MnO_2 has been successfully plated into the nano-pore channels of NPG.

The electrochemical performance of all-solid-state microdevices have been examined by CV curves. The specific capacitance of MnO_2 is about 10–30 F/g higher than that in liquid electrolyte at the same current density. The high salt concentration in gel electrolyte resulted in the improved performance. A stack capacitance up to 99.1 F/cm^3, corresponding to an energy density of 6.74 mWh/cm^3, which is among the highest records (Fig. 4.17).

4.5.2 Metal Oxides/Nanoporous Metal Composites

Pseudo-capacitive metal oxides, including MnO_2, $Ni(OH)_2$, RuO_2 and SnO_2, have been widely investigated and incorporated into mutil-dimensional conductive

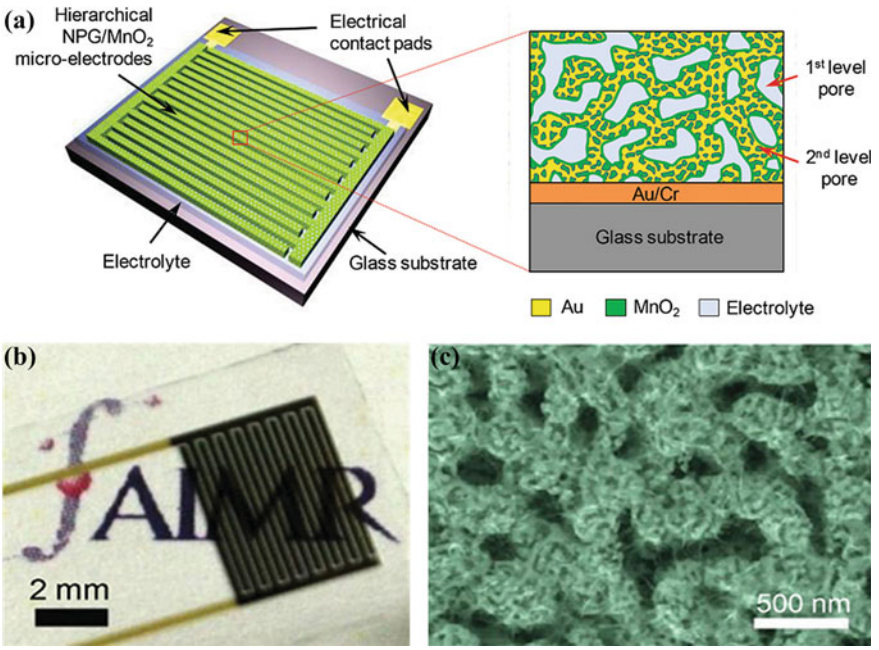

Fig. 4.16 Design of the hierarchical NPG/MnO_2 MPCs. **a** Schematic of the microdevice. Hierarchical NPG/MnO_2 microelectrodes were grown on planar Au/Cr templates that have been previously fabricated into an interdigital configuration. **b** A digital photograph of the microdevice. **c** SEM image of the hierarchical NPG/MnO_2 composites with a MnO_2 plating time of 11 min. (Reproduced from Ref. [32]. Copyright 2015, Wiley-VCH)

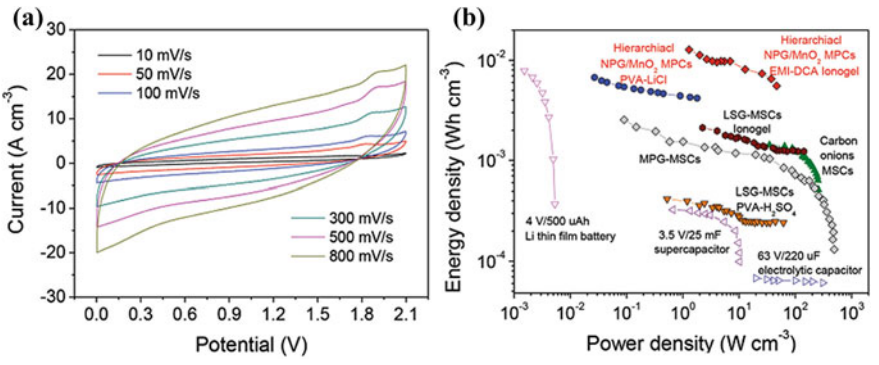

Fig. 4.17 Electrochemical performance of the solid-state hierarchical NPG/MnO_2 MPCs in EMI-DCA ionogel electrolyte. **a** Cyclic voltammogram profiles of the MPCs at various scan rates between 10 and 800 mV/s. **b** Ragone plot (energy density versus power density) of the hierarchical NPG/MnO_2 MPCs. Other MSCs reported and commercially available energy storage systems are shown for comparison (Reproduced from Ref. [32]. Copyright 2015, Wiley-VCH.)

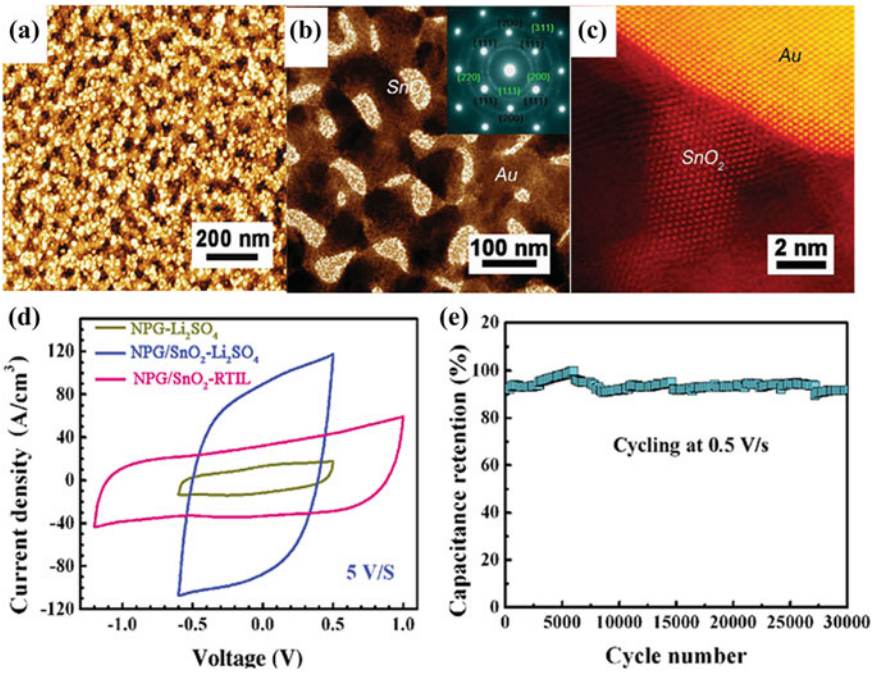

Fig. 4.18 **a** Morphology and chemical analysis for NPG plated with and without SnO_2 nanoparticles, top-view SEM images. **b** TEM micrograph of NPG/SnO_2 electrode. The *inset* shows the selected area electron diffraction pattern of SnO_2 nanoparticles in NPG. **c** High-angle annular dark-field STEM images of the NPG/SnO_2 composite. **d** Electrochemical data for the NPG/SnO_2 electrode. Typical cyclic voltammograms of bare NPG and NPG/SnO_2 films in Li_2SO_4 and RTIL, respectively, at the scan rate of 5 V/s. **e** Cycling stability of supercapacitor devices with NPG/SnO_2 electrodes at the low scan rate of 0.5 V/s (Reproduced from Ref. [35]. Copyright 2014, Wiley-VCH.)

framework with an aim to achieving high energy density with retained charging/discharging rate and high specific power [33]. Besides MnO_2, other metal oxides have also decorated by nanoporous metals to enhance their electrochemical performance.

The SnO_2/NPG composite electrode can be fabricated by electrode liquid/gas plating method [8]. NPG is obtained by a normal chemical dealloying method in concentrated HNO_3. SnO_2 nanoparticles are plated on the clean NPG films in 2 mM $SnCl_4$ aqueous solution at room temperature under the gas reagent of hydrazine N_2H_4. The loading amount of SnO_2 can be accurately controlled by the plating time and the best capacitive performance of composite electrodes is achieved at the optimal plating time of about 12 h. Figure 4.18a legibly reveals the optimal SnO_2 loading on the surface of NPG film. The deposition of SnO_2 nanoparticles can be more clearly observed in Fig. 4.18b, and the size distribution is in the range of

5–10 nm. Both NPG substrate and the deposited SnO_2 exhibit a crystalline nature as evidenced by the selected area electron diffraction pattern (inset of Fig. 4.18b). The Au (110) and rutile SnO_2 (111), (200), (220), and (311) diffraction rings can be easily found. The SnO_2 nanoparticles epitaxially grow on the stepped surfaces of gold ligaments as illustrated in Fig. 4.18c. The fascinating nanoporous structure of SnO_2 probably originates from the epitaxial growth of SnO_2 nanoparticles at selected sites of the curved NPG surface with quasi-periodic surface atomic steps. The hierarchical nanoporosity offers outstanding advantages in enhancing ionic and electronic conductivity of pseudo-capacitive SnO_2. The ultrafine pore channels of SnO_2 not only allow rapid ion transport in the composite electrodes but also provide an extremely large specific interface between SnO_2 nanoparticles and electrolytes, facilitating the full realization of the pseudo-capacitance of SnO_2. Moreover, the highly conductive gold network as backbones chemically bonding with SnO_2 nanoparticles promotes the electron transport of the composite electrodes.

The ruthenium dioxide (RuO_2) is also a promising candidate for supercapacitor electrode because of its ultra-large theoretical capacitance and high electrical conductivity (10^5 S/cm). However, supercapacitors based on agglomeration of RuO_2 nanoparticles often exhibit unsatisfying performance. By using NPG as both support and current collector, the RuO_2 particles have been electroplated on NPG substrate [34]. The fabrication process is schematic illustrated in Fig. 4.19a. The NPG attached to the polyethylene terephthalate as the working electrode is immersed in 5 mM $RuCl_3$ electrolyte and hydrous RuO_2 is electroplated onto the ligament surface of NPG [27, 34]. The morphology of the fabricated electrode composite is shown in Fig. 4.19b. The low crystalline RuO_2 deposited on the porous of NPG and the loading amount increases with the plating cycle number. The RuO_2/NPG composite electrodes are fabricated into three-electrode system to investigate the capacitance performance by using 0.5 M H_2SO_4 as electrolyte. Figure 4.19c exhibits the CV curves with different plating cycles. By controlling the same scan rate of 100 mV/s, the current intensities decrease gradually with the RuO_2 plating cycles from 15 to 40, while the current density of 50 cycles sample drops. The specific capacitance slightly reduces with increasing loading amount up to 40 cycles. Thus, the composite electrode with 40 cycles of plating should be the optimized composites. The high capacitive performance of 1500 F/g is achieved at a scan rate of 10 mV/s. The specific capacitance gradually decreases but can still retain a high value of around 1100 F/g at the scan rate of 1000 mV/s, which demonstrates the good rate performance. It can be clearly seen in Fig. 4.19d. By varying the discharge current density from 20 to 170 A/g, the specific capacitance decreases from about 1450 to 1150 F/g. This excellent rate performance is realized by combination of high capacitance of RuO_2 and highly conductivity of NPG.

The AgO/NPG composite electrode has also been prepared by a simple two-step partial dealloying-stripping process [36]. This novel fabrication process involves a partial electrochemical dealloying step and a following oxidation step as shown in Fig. 4.20a. The TEM image of AgO/Au composite electrode is displayed in Fig. 4.20b. It should be noted that a floccule AgO layer is tightly attached to the porous framework surface. The capacitive performance is examined in a

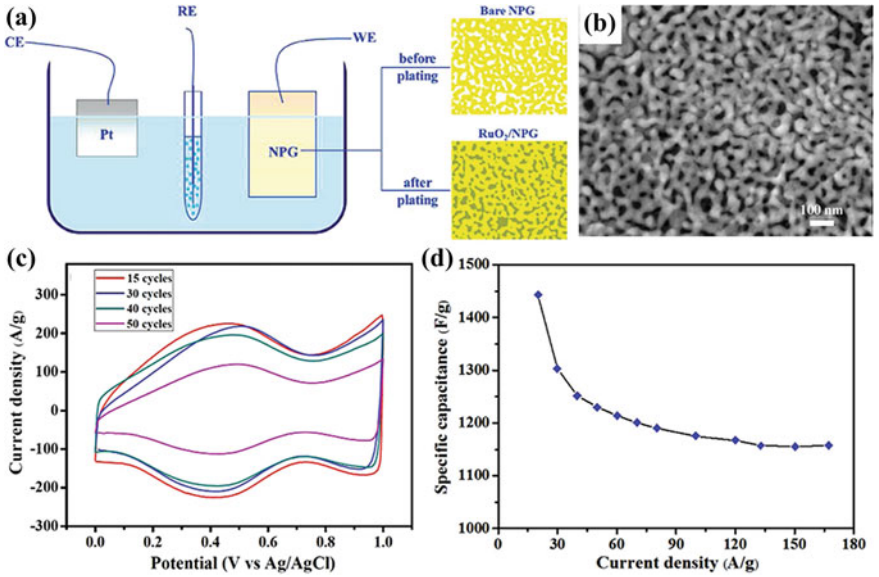

Fig. 4.19 **a** Schematic diagram of the fabrication process of RuO_2/NPG hybrid composites by an electroplating method using a three-electrode electrochemical cell. **b** SEM images of RuO_2/NPG composites with plating 40 cycles. **c** Cyclic voltammetry curves of RuO_2/NPG electrodes with different RuO_2 loading amounts in a 0.5 M H_2SO_4 electrolyte. **d** Specific capacitance of the RuO_2/NPG electrode with 40 plating cycles at different current densities (Reproduced from Ref. [34]. Copyright 2013, Wiley-VCH.)

three-electrode system in aqueous electrolyte. It delivers a specific capacitance of ~80 F/g at a current density of 5 A/g. The cycle stability is studied over 10,000 charge/discharge cycles at 5 A/g, as shown in Fig. 4.20c. There is only small degradation at the initial cycles from 82 to 77 F/g. It corresponds to the activation process which may be derived from the complete adsorption and desorption of electrochemical species. It keeps stable until the end of the cycling. The excellent performance can be mainly attributed to the electrochemical double-layer mechanism.

4.5.2.1 Polymer/Nanoporous Metal Composites

Conductive polymers have received great attentions as electrodes for pseudo-capacitors due to their high theoretical capacitance values [19]. However, the high electric resistance and low cycling stability have limited the practical applications of this kind of materials. Particularly, the obtained energy density is often an order of magnitude lower than their theoretical assessment. By utilizing the conductive nanoporous metal framework, conductive polymer-based electrode materials have been incorporated and excellent performance has been achieved.

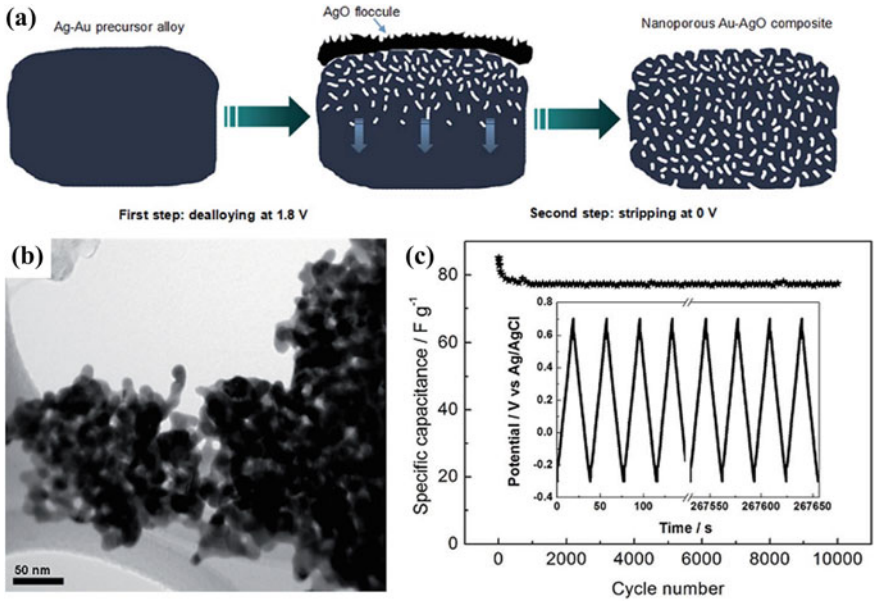

Fig. 4.20 **a** Schematic diagram for the fabrication process of the AgO/NPG composite. **b** TEM images of AgO/NPG composite electrode. **c** Cycling performance of AgO/NPG at a current density of 5 A/g, *inset*, the corresponding charge-discharge profile (Reproduced from Ref. [36]. Copyright 2015, The Royal Society of Chemistry.)

As one of the first examples in this area, an ultrathin flexible all-solid-state supercapacitor is designed and fabricated based on the polypyrrole (PPy)/NPG composite electrode [19]. The total thickness is less than one micrometer. The detailed fabrication process is demonstrated in Fig. 4.21a. The NPG leaves serve as both electrode support and current collector, and a gel poly(vinyl alcohol) contained $HClO_4$ as both electrolyte and separator. The bicontinuous open porosity feature of NPG is observed from the SEM image in Fig. 4.21b. The pore/ligament size is around 30 nm. After electropolymerization, a rough layer about 8 nm is clearly seen on the entire surface of the NPG leaves (Fig. 4.21c). Compared with the bare NPG, the pore and ligament sizes become evidently smaller and wider. Nevertheless, the original porous remains unchanged. The color changed from shining brownish to dark-green after the formation of PPy thin films as displayed in Fig. 4.21e, f. The total thickness of the assembled supercapacitor is about 600 nm which include the solid electrolyte separator. The Ragone plot shown in Fig. 4.21h demonstrates the volumetric power (P) and energy (W) of the device. The single PPy/NPG electrode exhibits very high volumetric power (283 W cm^{-3}) and energies (19 mWh cm^{-3}). For the entire supercapacitor including both the electrolyte and electrodes, the volumetric power, and energy of the flexible supercapacitor device are estimated to be 56.7 W cm^{-3} and 2.8 mWh cm^{-3}, respectively. The fast capacitive response of

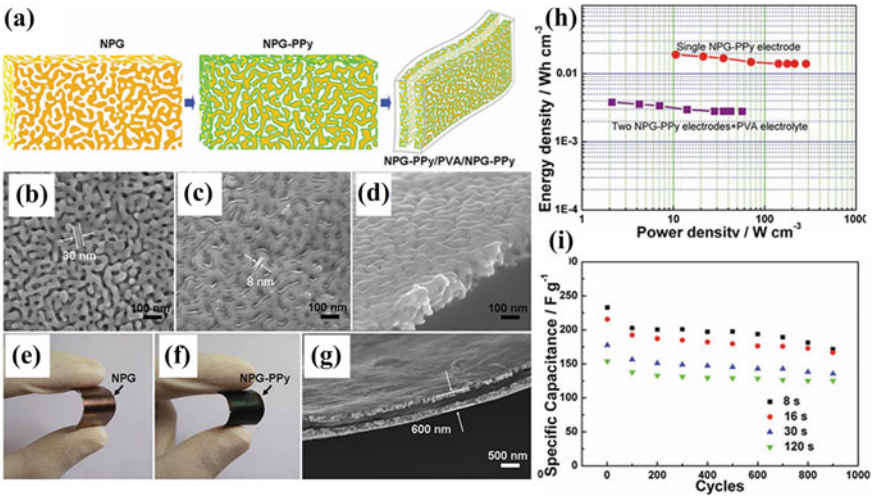

Fig. 4.21 **a** Schematic illustration of the fabrication process of the ultrathin flexible solid state supercapacitor. **b**, **c** SEM images of NPG and NPG/PPy. **d** SEM side view of NPG/PPy. **e**, **f** Digital pictures of macroscopic NPG and NPG/PPy thin membranes. **g** SEM cross sectional image of the as-designed symmetric supercapacitor device. **h** The Ragone plots of the NPG/PPy electrode and the supercapacitor. **i** Dependences of the capacitances of various NPG/PPy composites on the charge–discharge cycles at a current density of 4.4 A/g (Reproduced from Ref. [19]. Copyright 2011, Wiley-VCH.)

the solid state supercapacitor further indicates the efficient ion and electron transport within the porous nanocomposite. The cycle performance with different polymerizing times is shown in Fig. 4.21i. Shorter polymerizing time sample exhibits the high specific capacitance. It can be ascribed to the jammed ionic transferring channels within the network.

PPy/NPG composite electrodes have also been fabricated by anodic oxidation by cyclic voltammetry with a potential window ranging from −0.2 to 0.9 V [37]. The microstructure of the prepared electrode showed in Fig. 4.22a, b demonstrate that the polymer uniformly covers the internal surfaces of the ligaments. The PPy layers display bright contrast as the shell while the gold skeleton shows dark contrast. A 50 nm thickness of PPy layer can be observed. This structure feature with open porosity promises the good conductivity of the PPy/NPG composite and the effective rapid ion transport between the electrolyte ant the composite. The supercapacitor performance of the PPy/NPG electrode is examined in a three-electrode system in 1 M $HClO_4$ aqueous solution. The CV curves shown in Fig. 4.22c describe a symmetrical and near rectangular shape. The energy density of up to about 100 Wh/kg along with the power density of up to 57 kW/kg of the PPy/NPG-based supercapacitor. It is comparable to that of the NiMH batteries. It

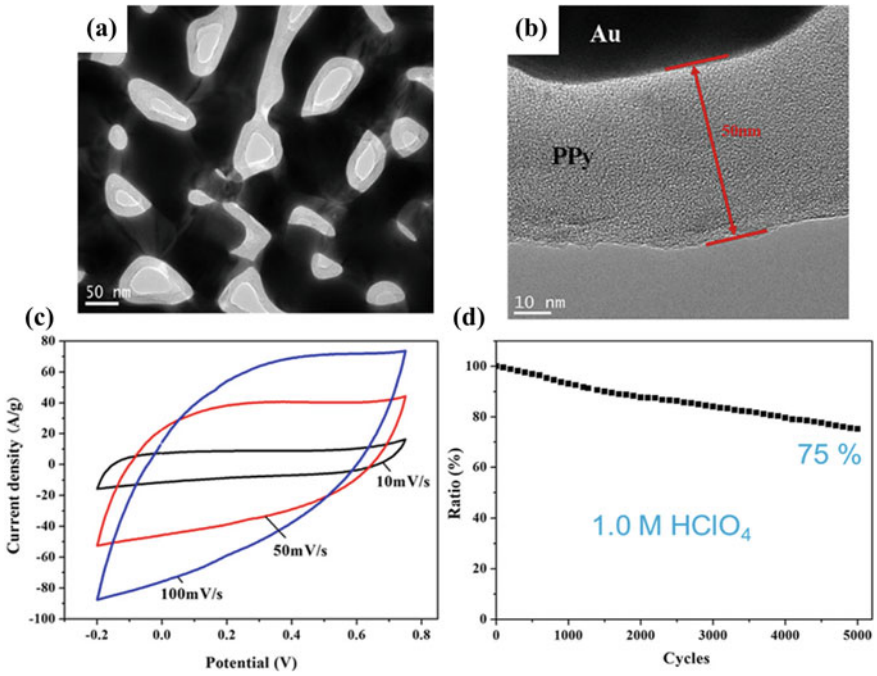

Fig. 4.22 **a** Microstructure of PPy/NPG composite with 15 cycle PPy loading. **b** HRTEM image of the interfacial structure of PPy/NPG, revealing that the amorphous PPy bonds well with the metal ligaments. **c** Electrochemical performances of the PPy/NPG hybrid electrode with the PPy coating loaded by 15-cycle electrochemical polymerization, cyclic voltammograms at different scan rates in 1 M $HClO_4$. **d** Capacitance retention ratio of the PPy/NPG electrode from the 1st to the 5000th cycle at a scan rate of 100 mV/s in 1 M $HClO_4$ acid solutions (Adapted from Ref. [37].)

also shows high capacitance and maintains about 85 % after 3000 cycles (Fig. 4.22d).

This electrochemical polymerization method can also expand to the synthesis of PANI/NPG electrode composite [38]. Figure 4.23a shows quasi-periodic gold ligaments and nanopore channels with the characteristic length of about 30-40 nm. After polymerization, the surface PANI layer can be obtained clearly from the TEM image in Fig. 4.23b. Interfacial analysis revealed by high-resolution demonstrates the intimate interaction between Au and PANI via the formation of chemical bonds. This unique interfacial structure ensures the occurrence of the PANI/Au charge transfer. The thickness of the PANI layer can be easily controlled by the plating cycles. Electrochemical performance is evaluted in two electrode supercapacitors. With gel electrolyte containing of H_2SO_4, all-solid-state device has been fabricated as shown in Fig. 4.23c. There is only small capacitance decay (18 %) compared with that aqueous ones (43 %) as the discharge current densities decreases from 1 to

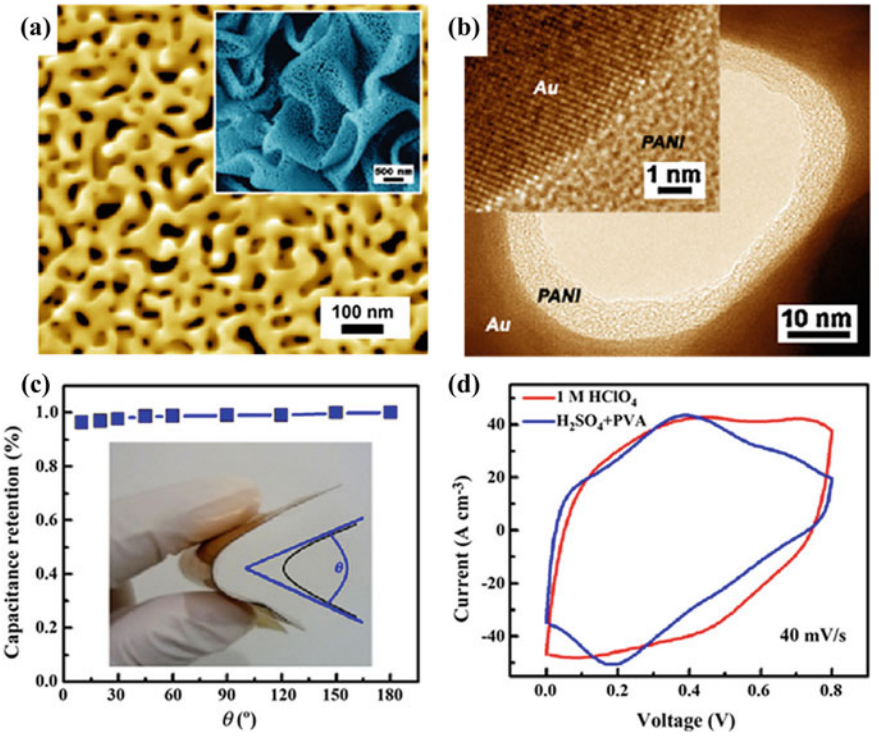

Fig. 4.23 **a** SEM image of NPG. Inset: the wrinkled films illustrating that NPG films exhibit excellent flexibility; **b** representative TEM micrograph of NPG/PANI composite electroplated for 3-cycle electroplating. *Inset* High-resolution TEM image of Au/PAIN interface. **c** Bend angle dependence of capacitance retention. Inset: digital picture showing all-solid-state devices with excellent flexibility. **d** Comparison of cyclic voltammograms of supercapacitors devices in the H_2SO_4-PVA gel electrolyte and 1 M $HClO_4$ solution. The scan rate is 40 mV/s (Reproduced from Ref. [38]. Copyright 2012, Elsevier.)

80 A/cm^3. Moreover, the entire all-solid-state device exhibits the superior mechanical flexibility. The macroscopic bend of the all-solid-state device from 180 to 10° does not remarkably influence and capacitance retention. With normal aqueous electrolyte, there are only smaller improvements as shown in Fig. 4.23d.

4.5.3 Asymmetric Capacitors Based on Nanoporous Metal Electrodes

The operational voltages of normal two-electrode supercapacitor devices are limited to 1 V due to the electrolysis potentials of aqueous electrolytes. In order to obtain

high cell voltages, nonaqueous electrolytes, including ionic liquids and organic solutions, have been investigated. An alternative approach to achieve a high cell voltage in aqueous electrolytes is to use an asymmetric electrode configuration, for example, two active materials with complementary working potential windows as anode and cathode, respectively [39]. With this configurations, the cells can be operated at a high voltage, up to about 2.0 V, leading to enhanced energy density and power density. The specific capacitance of an asymmetric cell is determined from:

$$1/C_{\text{supercapacitor}} = 1/C_{\text{positive}} + 1/C_{\text{negative}}$$

It is apparent that the overall specific capacitance of an asymmetric cell essentially depends on the electrode with a smaller specific capacitance. Therefore, to achieve a high energy density from an asymmetric supercapacitor, the paired electrodes are expected to have an identical high specific capacitance and complimentary working potential windows.

Asymmetric supercapacitors have been constructed based on nanoporous framework electrode materials. Based on metal oxide pseudo-capacitors materials, novel RuO_2@NPG//$Co(OH)_2$/NPG asymmetric supercapacitor with a high specific capacitance and wide operation potential window have been fabricated [39]. The schematic illustration of fabrication process is displayed in Fig. 4.24a. The RuO_2/NPG and $Co(OH)_2$/NPG composites fixed on polyethylene terephthalate (PET) plate are used as both electrodes and current collectors. The cotton paper soaked in 1 M NaOH aqueous electrolyte was used as separator. The electrochemical performance of RuO_2/NPG or $Co(OH)_2$/NPG electrode are studied by CV in a standard three-electrode electrochemical analyzer at room temperature. The RuO_2/NPG and $Co(OH)_2$/NPG electrodes can reach specific capacitances of 1300 and 1800 F/g, respectively, which provide comparatively high specific capacitances in relation to metal oxide/carbon electrodes. Figure 4.24b shows the CV curves of the asymmetric supercapacitor at varied scan rates from 10 to 200 mV/s. The maximum potential window can be achieved from 0 to 1.6 V in this aqueous electrolyte. The specific capacitance of the asymmetric supercapacitor is 340 F/g based on both electrodes. The energy storage performance of the asymmetric supercapacitor is evaluated by the energy density and power density as displayed in the Ragone plot in Fig. 4.24c. The energy density of about 120 Wh/kg and power density of 70 kW/kg have been obtained, which is much higher than those of symmetric supercapacitors based on RuO_2/NPG or $Co(OH)_2$/NPG electrode because of the wider operating voltage window.

Flexible asymmetric pseudo-capacitors have also been assembled by PPy/NPG and MnO_2/NPG electrodes [40]. Both of the PPy/NPG and MnO_2/NPG composite electrodes are prepared by an electrochemical plating method, and the mass loading of PPy and MnO_2 can be adjusted by the plating time. The schematic of the

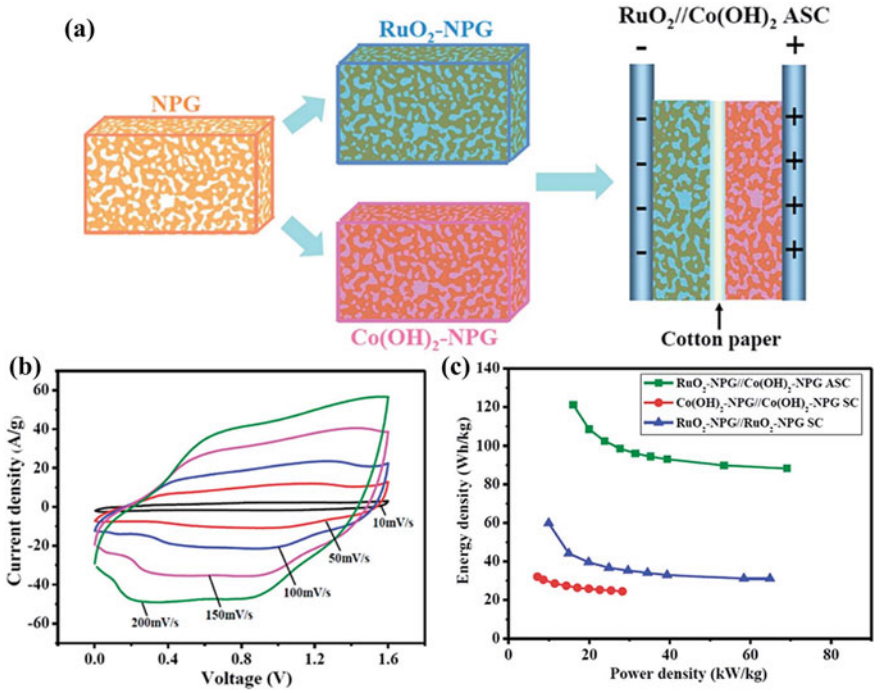

Fig. 4.24 **a** Assembly schematic of the RuO_2–NPG//$Co(OH)_2$–NPG asymmetric supercapacitor. **b** Electrochemical capacitance of in 1 M NaOH electrolyte, cyclic voltammetry curves at different scan rates. **c** Energy density versus power density plots of the symmetric supercapacitors (Reproduced from Ref. [39]. Copyright 2014, The Royal Society of Chemistry.)

assembly and photograph of the PPy@NPG//MnO_2@NPG flexible asymmetric supercapacitor are shown in Fig. 4.25 a and b, whereas their CV curves in 1 M $LiClO_4$ electrolyte are described in Fig. 4.25c. The potential window of the PPy/NPG electrode spans from −0.5 to 0.5 V while that of the MnO_2/NPG electrode spans between 0 and 0.8 V. The different voltage window determines the ratio of the mass loading in two different electrodes. Figure 4.25d shows the CV curves of optimized asymmetric supercapacitor with different potential windows. The maximum potential window can be achieved from 0 to 1.8 V in aqueous electrolyte. The high specific capacitance of about 193 F/g based on the mass of both electrodes was obtained, and both high energy and power density from a single supercapacitor cell.

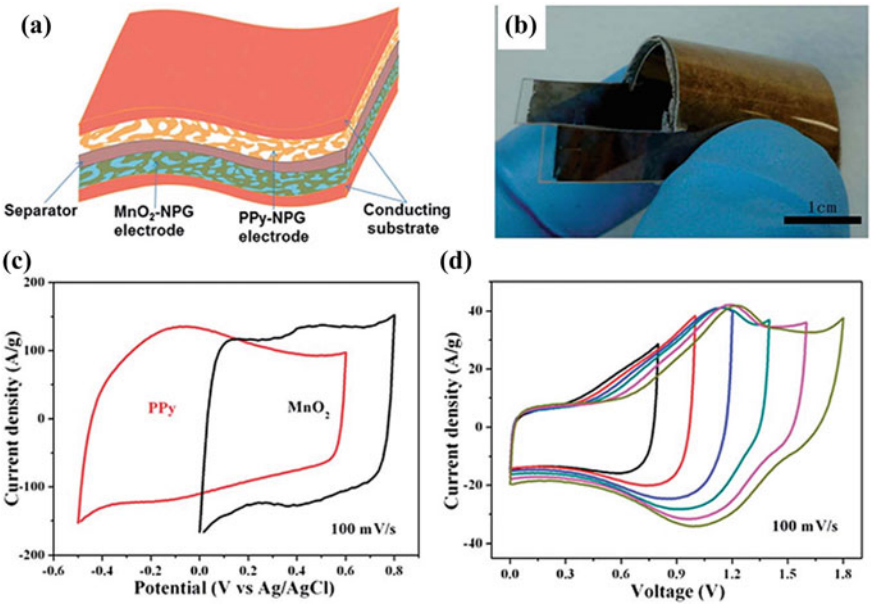

Fig. 4.25 **a** Assembly schematic of the PPy–NPG//MnO_2–NPG asymmetric supercapacitor. **b** Photograph of a PPy–NPG//MnO_2–NPG asymmetric supercapacitor. **c** CV curves of PPy–NPG and MnO_2–NPG electrodes in different potential windows, which were measured by using a three-electrode system in a 1 M $LiClO_4$ aqueous solution. **d** CV curves of the optimized PPy–NPG//MnO_2–NPG asymmetric supercapacitor measured in different potential windows in a 1 M $LiClO_4$ aqueous solution. Scan rate: 100 mV/s (Reproduced from Ref. [40]. Copyright 2014, The Royal Society of Chemistry.)

4.6 Summary and Outlook

The nanoporous metal based composite electrodes have been widely investigated in supercapacitor and gained great success. With unique three-dimensional bicontinuous structures, nanoporous metals can serve as both supports of active materials and current collectors. Benefited from good electron conductivity and electrolyte penetrability, high energy density and power density can be readily obtained. However, before they are feasible for actual applications, critical technological challenges should be overcome which include:

1. Reducing the cost and weight of the nanoporous metal frameworks. Most of the reports so far are based on nanoporous noble metals or late transition elements. Their high cost undoubtedly poses unfavorable economic concerns while their heavy weight limits their practical applications from a system viewpoint. It is thus highly urgent to develop nanoporous non-noble, light weight metals that are still mechanically robust and electrochemical stable for further functionalization for supercapacitor applications.

2. Improving the porosity of the structure to allow higher mass loading of active materials. High porosity nanostructures, especially those with narrow ligaments and large open channels can incorporate more active materials without sacrificing their specific surface area. Besides, multimodal structures [41] may provide additional benefits of facilitating mass transfer and improving mechanical rigidity at no cost of surface area decrease. Technological improvement in these areas allows anchoring of more active materials and thus improves the specific capacity of the whole device.
3. Increasing the operation voltage window. A wide voltage window to 1.8 V has been observed in aqueous electrolyte [26]. This encourages us to further optimize the components and surface oxidation properties of nanoelectrodes, for example, by accommodation of the electrochemical properties of metal substrates, surface active species, and the electrolytes within the whole framework, to realize a much enhanced supercapacitor performance.
4. Optimizing the active electrode components for asymmetric supercapacitors. The asymmetric supercapacitors usually exhibit large working voltage window due to the different operation voltage range of the respective active materials. By carefully design and preparation of composite electrodes with large potential difference, the resulted asymmetric supercapacitors would hold better electrochemical performance.

Finally, special technologies such as wearable electronic devices require particular development of challenging technologies, such as flexible, all-solid-state, transparent, and durable power devices. As a unique high power density power source, supercapacitors may also find new solutions and applications in these next-generation technologies.

References

1. Winter M, Brodd RJ (2004) What are batteries, fuel cells, and supercapacitors? Chem Rev 104 (10):4245–4269
2. Simon P, Gogotsi Y (2008) Materials for electrochemical capacitors. Nat Mater 7(11):845–854
3. Burke A (2000) Ultracapacitors: why, how, and where is the technology. J Power Sour 91 (1):37–50
4. Miller JR, Simon P (2008) Materials science—electrochemical capacitors for energy management. Science 321(5889):651–652
5. Becker HL (1957) Low voltage electrolytic capacitor. United States Patents, 2,800,616[P]. 1957-07-23
6. Kotz R, Carlen M (2000) Principles and applications of electrochemical capacitors. Electrochim Acta 45(15–16):2483–2498
7. Wang DW, Li F, Liu M, Lu GQ, Cheng HM (2008) 3D aperiodic hierarchical porous graphitic carbon material for high-rate electrochemical capacitive energy storage. Angew Chem Int Ed 47(2):373–376

8. Zhang Y, Feng H, Wu XB, Wang LZ, Zhang AQ, Xia TC et al (2009) Progress of electrochemical capacitor electrode materials: a review. Int J Hydrogen Energy 34(11): 4889–4899
9. Wang K, Wu HP, Meng YN, Wei ZX (2014) Conducting polymer nanowire arrays for high performance supercapacitors. Small 10(1):14–31
10. Futaba DN, Hata K, Yamada T, Hiraoka T, Hayamizu Y, Kakudate Y et al (2006) Shape-engineerable and highly densely packed single-walled carbon nanotubes and their application as super-capacitor electrodes. Nat Mater 5(12):987–994
11. Yu GH, Xie X, Pan LJ, Bao ZN, Cui Y (2013) Hybrid nanostructured materials for high-performance electrochemical capacitors. Nano Energy 2:213–234
12. Trasatti S, Buzzanca P (1971) Ruthenium oxide: a new interesting electrode material, solid state structure and electrochemical behavior. J Electroanal Chem 29:1–5
13. Conway BE (1991) Transition from supercapacitor to battery behavior in electrochemical energy storage. J Electrochem Soc 138(6):1539–1548
14. Toupin M, Brousse T, Belanger D (2004) Charge storage mechanism of MnO_2 electrode used in aqueous electrochemical capacitor. Chem Mater 16(16):3184–3190
15. Wang L, Ji HM, Wang SS, Kong LJ, Jiang XF, Yang G (2013) Preparation of Fe_3O_4 with high specific surface area and improved capacitance as a supercapacitor. Nanoscale 5(9):3793–3799
16. Lang JW, Kong LB, Wu WJ, Luo YC, Kang L (2008) Facile approach to prepare loose-packed NiO nano-flakes materials for supercapacitors. Chem Commun 35:4213–4215
17. Lee HY, Goodenough JB (1999) Supercapacitor behavior with KCl electrolyte. J Solid State Chem 144(1):220–223
18. Lang XY, Hirata A, Fujita T, Chen MW (2011) Nanoporous metal/oxide hybrid electrodes for electrochemical supercapacitors. Nat Nanotechnol 6(4):232–236
19. Meng FH, Ding Y (2011) Sub-micrometer-thick all-solid-state supercapacitors with high power and energy densities. Adv Mater 23(35):4098–4102
20. Hu LB, Pasta M, La Mantia F, Cui LF, Jeong S, Deshazer HD et al (2010) Stretchable, porous, and conductive energy textiles. Nano Lett 10(2):708–714
21. Lang XY, Yuan HT, Iwasa Y, Chen MW (2011) Three-dimensional nanoporous gold for electrochemical supercapacitors. Scripta Mater 64(9):923–926
22. Kobayashi N, Ogata H, Park KC, Takeuchi K, Endo M (2013) Investigation on capacitive behaviors of porous Ni electrodes for electric double layer capacitors. Electrochim Acta 90:408–415
23. Kobayashi N, Sakumoto T, Mori S, Ogata H, Park KC, Takeuchi K et al (2013) Investigation on capacitive behaviors of porous Ni electrodes in ionic liquids. Electrochim Acta 105: 455–461
24. Chen PC, Hsieh SJ, Zou J, Chen CC (2014) Selectively dealloyed Ti/TiO_2 network nanostructures for supercapacitor application. Mater Lett 133:175–178
25. Kang JL, Hirata A, Qiu HJ, Chen LY, Ge XB, Fujita T et al (2014) Self-grown Oxy-Hydroxide@ nanoporous metal electrode for high-performance supercapacitors. Adv Mater 26(2):269–272
26. Kang JL, Hirata A, Chen LY, Zhu SL, Fujita T, Chen MW (2015) Extraordinary supercapacitor performance of a multicomponent and mixed-valence oxyhydroxide. Angew Chem Int Ed 54(28):8100–8104
27. Chen LY, Kang JL, Hou Y, Liu P, Fujita T, Hirata A et al (2013) High-energy-density nonaqueous MnO_2@nanoporous gold based supercapacitors. J Mater Chem A 1(32): 9202–9207
28. Kang JL, Chen LY, Hou Y, Li C, Fujita T, Lang XY et al (2013) Electroplated thick manganese oxide films with ultrahigh capacitance. Adv Energy Mater 3(7):857–863
29. Wang ZF, Liu JY, Qin CL, Liu L, Zhao WM, Inoue A (2015) Fabrication and new electrochemical properties of nanoporous Cu by dealloying amorphous Cu–Hf–Al–alloys. Intermetallics 56:48–55

30. Zeng ZG, Zhou HJ, Long X, Guo EJ, Wang XH (2015) Electrodeposition of hierarchical manganese oxide on metal nanoparticles decorated nanoporous gold with enhanced supercapacitor performance. J Alloy Compd 632:376–385
31. Zeng ZG, Long X, Zhou HJ, Guo EJ, Wang XH, Hu ZY (2015) On-chip interdigitated supercapacitor based on nano-porous gold/manganese oxide nanowires hybrid electrode. Electrochim Acta 163:107–115
32. Han JH, Lin YC, Chen LY, Tsai YC, Ito Y, Guo XW et al (2015) On-chip micro-pseudocapacitors for ultrahigh energy and power delivery. Adv Sci 2:1500067
33. Lu Q, Chen JG, Xiao JQ (2013) Nanostructured electrodes for high-performance pseudocapacitors. Angew Chem Int Ed 52:1882–1889
34. Chen LY, Hou Y, Kang JL, Hirata A, Fujita T, Chen MW (2013) Toward the theoretical capacitance of RuO_2 reinforced by highly conductive nanoporous gold. Adv Energy Mater 3 (7):851–856
35. Lang XY, Hirata A, Fujita T, Chen MW (2014) Three-dimensional hierarchical nanoporosity for ultrahigh power and excellent cyclability of electrochemical pseudocapacitors. Adv Energy Mater 4(10):1301809
36. Xu JL, Wang CD, Liu JB, Xu S, Zhang WJ, Lu Y (2015) Facile fabrication of a novel nanoporous Au/AgO composite for electrochemical double-layer capacitor. RSC Adv 5 (49):38995–39002
37. Hou Y, Chen LY, Zhang L, Kang JL, Fujita T, Jiang JH et al (2013) Ultrahigh capacitance of nanoporous metal enhanced conductive polymer pseudocapacitors. J Power Sour 225:304–310
38. Lang XY, Zhang L, Fujita T, Ding Y, Chen MW (2012) Three-dimensional bicontinuous nanoporous Au/polyaniline hybrid films for high-performance electrochemical supercapacitors. J Power Sour 197:325–329
39. Chen LY, Hou Y, Kang JL, Hirata A, Chen MW (2014) Asymmetric metal oxide pseudocapacitors advanced by three-dimensional nanoporous metal electrodes. J Mater Chem A 2(22):8448–8455
40. Hou Y, Chen LY, Liu P, Kang JL, Fujita T, Chen MW (2014) Nanoporous metal based flexible asymmetric pseudocapacitors. J Mater Chem A 2(28):10910–10916
41. Ding Y, Erlebacher J (2003) Nanoporous metals with controlled multimodal pore size distribution. J Am Chem Soc 125(26):7772–7773

Chapter 5
Nanoporous Metals for Li Battery Applications

Abstract Electrode materials with nanoporous structures have been widely investigated and gained great success in Li-ion batteries and Li-air batteries. Compared with normal electrodes, they usually show improved electrochemical performance which are mainly originated from the following aspects: (1) 3D bicontinuous architectures provide high surface areas readily accessible by carrier charges and electrolyte; (2) porous structure at nanometer scale allows the reducing of the Li-ion diffusion length between the electrolyte and the electrode, and also the diffusion pathway inner the active materials; (3) the residual space in the electrode composite can accommodate large volume expansion during discharging–charging processes. In this chapter, the research progress of nanoporous electrode materials both in Li-ion batteries and Li-air batteries are summarized. As in Li-ion batteries, nanoporous framework can be adopted as a 3D scaffold, upon which various electrode materials have been deposited, including metals, alloys, metal oxides, metal sulfides, and insertion materials. The large volume expansion accommodation ability and good conductivity of 3D framework promise the improved battery performance. By introducing the nanoporous gold and metal oxides/nanoporous gold as cathode in Li-air battery, ultrastable cycle performance can be achieved which is rarely seen in traditional materials. In addition, novel nanoporous metals can also be fabricated by electrochemical delithiation from Li-metals alloys, corresponding to a charging mechanism in Li-ion battery. This phenomenon has been explored to be a versatile template-free method for the synthesis of not only transition metals but also metal oxides with large surface area and pronounced nanoporosity. The conclusion part of this chapter briefly summarized the mechanism of performance improvement by nanoporous metals framework and also point out the new research direction of nanoporous metal-based electrodes.

Keywords Nanoporous metals · Electrode · Li-ion battery · Li-air battery · Volume expansion · Conductivity

Y. Ding and Z. Zhang, *Nanoporous Metals for Advanced Energy Technologies*, DOI 10.1007/978-3-319-29749-1_5

5.1 Introduction

Environment deterioration and global warming are becoming hot topics of discussion all over the world since the past few decades, because we are excessively dependent on the fossil fuels in the current energy consumption system, which account for approximately 68 % of the electrical energy produced [1]. To cope with the ever-increasing energy demand and decreasing of fossil energy reserves, it is highly urgent to increase the percentage of renewable energy utilizations. However, the intermittent generation of renewable energy requires the development of rechargeable batteries to store the electricity. In addition, the applications of hybrid electric vehicle (HEV) and electrical vehicle (EV) are also highly dependent on the performance of energy storage devices. Among various state-of-the-art batteries, Li-ion batteries (LIBs) currently predominate the market of energy storage devices, as characterized by their higher energy density (210 Wh/kg or 650 Wh/L), which exceeds most traditional secondary batteries [1]. LIBs have gained great success in portable electronic devices since its commercialization by Sony in early 1990s. However, the first generation LIBs are approaching their theoretic performance limits, which hampers their application in new energy storage fields, especially for HEV/EV and smart grids, which ask for simultaneous fulfillment of high energy and power densities, high durability as well as low overall fabrication cost [1]. Therefore, tremendous R&D efforts are placed on the exploration of new energy storage materials for traditional LIBs and new battery concepts, which can meet the standards of high energy, high power, abundant resources, high safety, and environmental friendliness [2, 3].

5.2 Operation Principles and Structure of LIBs

A typical LIB unit is composed of cathode and anode which are separated by an electrolyte-soaked separator. The battery performance can be characterized by E (Wh/kg or Wh/L), the amount of electrical energy delivered per unit of weight or volume, which is a function of cell voltage U (V) and capacity Q (Ah/kg). Both U and Q are correlated with the chemical systems of electrode materials. Accordingly, two ways can be achieved in order to improve the battery performance: (1) to enlarge the working potentials of the cell by choosing cathodes with higher oxidation potentials and anodes with lower reduction potentials; (2) by developing new electrode materials with higher capacities [1]. In addition, the diverse interface contact, which includes the electrode/electrolyte interface, the contact between electrode materials and current collector, also profoundly influences the battery performance. In typical commercialized LIBs, the Li-ions shuttle between the $LiCoO_2$ cathode and graphite anode during charge/discharge process as shown in Fig. 5.1. During the charging process, the Li-ions that are extracted from $LiCoO_2$ cathode will pass across the separator in electrolyte, migrate and insert into the graphite anode, with the whole process balanced by electron transfer through the

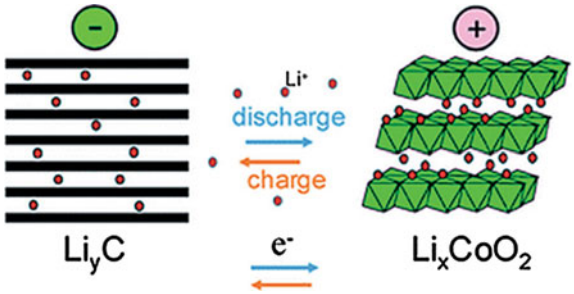

Fig. 5.1 The operation principle of a typical lithium-ion battery. Lithium ions migrate back and forth between the anode and cathode through the electrolyte upon discharging/charging, and the charge balance is fulfilled by electron transfer through the outer electrical circuit (Reproduced from Ref. [4]. Copyright 2012, Wiley-VCH.)

external circuit. And during discharging, a reverse Li-ion extraction/intercalation process will occur at the anode and cathode. The oxidation/reduction equilibrium potentials of cathode/anode materials during electrochemical reactions determine the working potential of batteries. The potential difference of $LiCoO_2$ and graphite is nearly 4.0 V, which is much higher than the traditional batteries such as lead acid battery (1.9 V) and NiMH battery (1.2 V).

To improve the battery performance, the predominate research efforts are focused on developing new cathode materials with high working potentials ($LiNi_{0.5}Mn_{1.5}O_4$), high durability and low cost ($LiFePO_4$), large capacities (Li rich layered oxides), new anode materials with large capacities (silicon, metal oxides), zero-strain $Li_4Ti_5O_{12}$, etc. [1]. The feasibility of a battery is highly dependent on the diverse interfaces between various components inside the battery. For example, Li-ions migrate at different rates across electrode materials of different particle sizes, morphology and orientation even in the same electrolyte, which directly determines its rate capability, a key parameter to evaluate the power density [5, 6]. Therefore, it is of great significance to optimize the various interface structures during battery engineering, which typically include the electrode/electrolyte interface, electrode/current collector interface, and the interface between different electrode particles. Materials with nanoporous structures, either as electrodes or current collectors, have the genuine potential to improve the rate capability of LIBs, because they allow significant decrease of the Li-ion diffusion distance between particles, and can also improve interface properties. The introduction of nanoporous metal (NPM) based materials into LIBs, benefits not only the improvement in energy and power, but also the electrode kinetics, cycle stability, and the cost. Recently, rapid progress has been achieved by the exploration of various functional NPM structures for LIBs. Moreover, they also show superior performance in advanced rechargeable batteries such as Li-air batteries (LABs). In this chapter, we review the recent progresses in NPM-based electrode materials and current collectors in LIBs, and also discuss some emerging investigations as electrodes in new energy storage devices of LABs.

5.3 Advantages of Nanoporous Metal Materials for LIBs

Nanoporous metals (NPMs), a class of functional materials with unique structural properties of mechanical rigidity, electrical conductivity and nanoscale aperture, show great promise in energy storage devices such as supercapacitors, LIBs, and LABs [1]. When adopting as electrodes or current collectors in LIBs or LABs, the following advantages can be recognized for NPMs:

1. The bicontinuous structural feature endows the composite electrodes with high tolerance toward the volume expansion during discharge/charge process, thereby improving the cycle stability. The insertion/desertion of Li-ions into metal-based anodes is always accompanied by pulverization, loss of electrical contact at the electrode due to the substantial volume change (over 200 % for Sn) [7]. This enormous volume expansion of electrode will result in the crack and peeling off from the current collector, which in turn leads to the capacity loss and battery fading. By introducing novel nanoporous configuration, the electrode materials are encapsulated in the porous network, which provides effective buffer against such large volume expansion. Therefore, the composite electrodes usually display significantly enhanced durability and prolonged cycle life.
2. The reduced particle size can significantly improve the rate performance by decreasing the Li-ion diffusion distance within the particles. During the entire Li-ion diffusion route, the solid-state diffusion of Li in host materials is the rate determining step which influences the power density of the battery. The diffusion rate is in inverse ratio to the diffusion length square [1]. From the traditional microscale electrode materials to the nanometer particles, a reduction length from several μm to about 50 nm, the diffusion rate can increase by more than three orders of magnitude. This is also one of the driving forces for the development of nanoscale electrodes in other electrode materials for rechargeable batteries.
3. The open porous structure can facilitate the permeating of electrolyte into the electrodes, which is beneficial to the formation of well-defined electrode/electrolyte interface. Compared with the bulk electrode surface, the surface of NPM-supported electrode can be well infiltrated and accessed more easily by Li-ions. The high surface area network structure thus ensures a significant portion of Li-ions stored in the near surface region of the electrodes. By optimizing the specific current density at the interface of particles and electrolyte, it helps maintain a high capacity at high charge/discharge current densities [1].
4. The limited space promotes the preferential materials growth in certain crystal directions with better rate and cycle performance [8]. Nanostructured electrode materials with exposed highly reactive crystal planes can demonstrate promising properties, including higher Li-ion insertion/desertion rates. However, it remains greatly challenging to concurrently obtain nanostructured active materials with

both highly exposed crystal facets, and efficient ion/electron pathways. With the help of NPM scaffolds, the electrode may exhibit a preferential crystalline growth mode. The favorable crystal orientation of electrode materials could contribute to the efficient and rapid pathways for ion diffusion while NPM scaffolds guarantee the rapid electron transport. In this way, the high-rate and high-capacity Li storage properties may be achieved simultaneously.

5. The high conductivity and excellent electrochemical/mechanical stability of NPMs benefit the highly reversible reactions for the formation/decomposition of Li_2O_2 in advanced Li-O_2 batteries [1]. Taking nanoporous gold (NPG) as an example, there will be no electrode corrosion problems which are one of the limiting factors that prohibit the applications of carbon based electrode materials in high-voltage Li-O_2 batteries. NPMs can also be decorated by other catalysts due to their natural chemical affinity for oxides. By effectively reducing the electron diffusion length, the otherwise insulating oxides can fully exhibit their electrocatalytic activities toward the cathodic reactions. Finally, NPM electrodes also show good compatibility toward the non-aprotic electrolytes, which eases the development of new battery systems.

5.4 Nanoporous Metal Materials as Electrodes of LIBs

By introducing porous structures into electrodes, the charge transport and volume expansion tolerance can be enhanced simultaneously. These NPMs can be constructed as novel electrode materials themselves, or be adopted as unique 3D scaffolds, where various electrode materials can be deposited, including metals, alloys, metal oxides, metal sulfides, and insertion materials. In the following sections, we will introduce nanoporous electrodes and NPM-based electrodes decorated with different active materials.

5.4.1 Electrode Materials with Nanoporous Structures

Li alloy-based materials have attracted particular attention due to their ability to reversibly react with large amount of Li per formula unit. The theoretical capacity of tin is 990 mAh g^{-1} for $Li_{4.4}Sn$, which is three times higher than that of graphite (372 mAh g^{-1} for LiC_6). However, its practical application is hampered by the poor cyclability because of the large volume expansion/contraction during the discharge/charge process. Recent research progresses demonstrate that the porous electrode materials can effectively accommodate the volume expansion, provide specific electrochemical interface and plenty of electrolyte channels. Therefore, porous electrode materials can readily show enhanced cycle and rate performance.

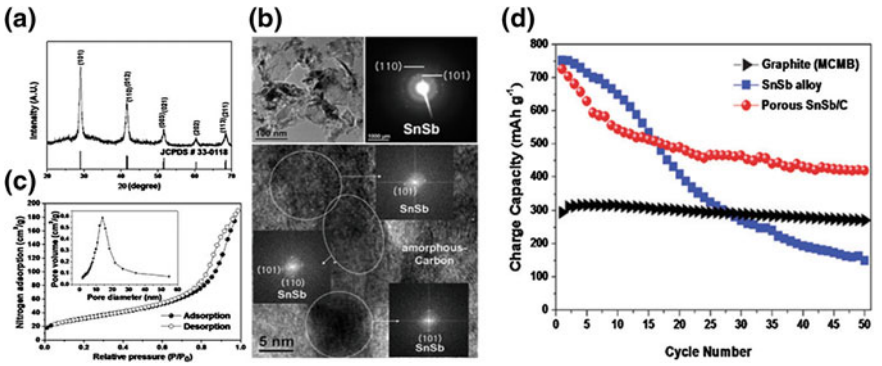

Fig. 5.2 Characterization of porous SnSb/C nanocomposites. **a** XRD pattern; **b** TEM bright-field and HRTEM images with the corresponding lattice spacing; **c** Nitrogen adsorption isotherm; **d** comparison of the cycle performances of various electrodes (MCMB graphite, SnSb alloy, and porous SnSb/C nanocomposites electrodes) between 0 and 2.0 V (vs. Li/Li^+) at a cycling rate of 100 mA g^{-1} (Reproduced from Ref. [9]. Copyright 2011. The Royal Society of Chemistry.)

In this context, porous structured SnSb/C nanocomposites [9], porous Sn/SnSb [10], nanoporous Sn–SnO_2–TiO_2 composite films [11], nanoporous Si with Al_2O_3 coating layer [12], nanoporous Ge [13], and porous dendritic Ni–Sn anodes [14] have been reported to possess favorable battery performance.

The SnSb/C electrode composites are fabricated by a simple physiochemical route [9]. First, the SnSb/$MgCl_2$/C composite precursor is prepared by high energy mechanical milling and then $MgCl_2$ is removed to expose the pore channels. As shown in Fig. 5.2, the average crystallite size of SnSb in the porous electrode composites locates in the range of 10–15 nm. The electrochemical reaction mechanism of the porous SnSb/C can be summarized as: SnSb + 7.25Li ↔ Li_3Sb + $Li_{4.25}Sn$. To further understand the performance improvement by the porous structure, the cycle performance of commercial graphite, SnSb alloy, and porous SnSb/C nanocomposites electrodes are evaluated at a current of 100 mA/g as shown in Fig. 5.2d. This porous SnSb/C electrode composites show quite stable capacity retention of approximately 420 mAh/g over 50 cycles, which is higher than that of the commercial graphite. The good electrochemical performance of high capacity and stable cyclability is mainly associated with the pore structure to accommodate the volume expansion generated during cycling, as well as the blocking effect for the agglomeration of active SnSb nanocrystallites during cycling by the amorphous carbon matrix.

Porous Sn/SnSb negative electrodes are fabricated by electroreduction of SnO_2–SbO_2 in 1 M H_2SO_4 aqueous solution [10]. The removal of oxygen from the electrode intrinsically results in homogeneous pore channels which can accommodate the volume change during lithiation. The porosity of the Sn/SnSb negative electrode can be further adjusted by pore-forming in the parent electrode with NH_4HCO_3. The porosity is estimated about 29 % in the metallic product. In the first cycle, the discharge and charge capacities are 1600 and 800 mAh/g (Fig. 5.3a),

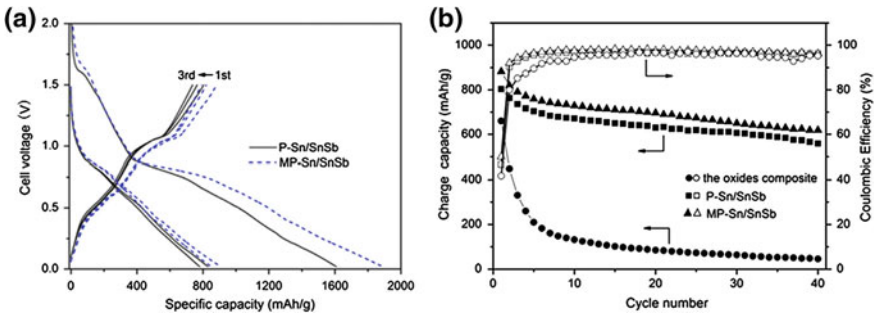

Fig. 5.3 **a** Voltage profiles of the P–Sn/SnSb and MP–Sn/SnSb electrodes at 100 mA/g (each for the first three cycles); **b** cycling performances of the SnO_2–Sb_2O_3 composite, the P–Sn/SnSb and MP–Sn/SnSb electrodes at 100 mA/g between 0.02 and 1.5 V (cell voltage) (Reproduced from Ref. [10]. Copyright 2014, Elsevier.)

respectively. The irreversible loss is usually attributed to the formation of SEI (solid electrolyte interface) film. The coulombic efficiency of 97 % illustrates highly reversible Li-alloying/dealloying of the porous Sn/SnSb. This material also shows improved cyclic capacity retention. At a current density of 100 mA/g, the capacity retention is still over 70 % after 40 cycles (Fig. 5.3b).

Electrodeposition technique has been adopted to fabricate highly porous dendritic Ni–Sn [14] and nanoporous Sn–SnO_2–TiO_2 [11] on Cu foil as anodes for LIBs. In preparation of the Ni–Sn metal foam, Cu foil is used as the current collector and conductive substrate for the electrodeposition in aqueous solution containing 0.2 M $NiCl_2$, 0.015–0.05 M $SnCl_2$ and 1 M H_2SO_4. The electrodeposition of the Sn–TiO_2 composite films is conducted in a mixed ethanol–water bath containing 0.04 M $SnCl_2$, 0.02–0.04 M $TiCl_3$, and 0.08 M H_2O_2, with different volumetric EtOH/H_2O ratios.

The morphology of fabricated $Ni_{50}Sn_{50}$ alloy foam is illustrated in Fig. 5.4a, b. The porous and dendrites structures can be observed, whose morphology depends on the concentrations of the metal ions during the synthesis process. The voltage profiles as anode for LIBs at 1 C rate are shown in Fig. 5.4c. A clear potential plateau is shown at around 0.5 V versus Li/Li^+ in the first cycle, which is caused by the lithiation of Sn to form the Li_xSn alloy. The capacities gradually increase to 530 mAh/g and remain stable. The highly porous structure of the Ni–Sn anode contributes to excellent cycle life stability, providing facile accessibility to Li^+ ions. The volumetric voids also act as mechanical bumpers preventing the structural disruption of Ni–Sn anodes.

The synthesis conditions have tremendous effects on the electrochemical performance of nanoporous Sn–SnO_2–TiO_2 composites film. The discharge capacity is 1069 mAh/g in the initial cycle. The enhanced discharge capacity and improved retention of the Sn–SnO_2–TiO_2 composite films can be attributed to their

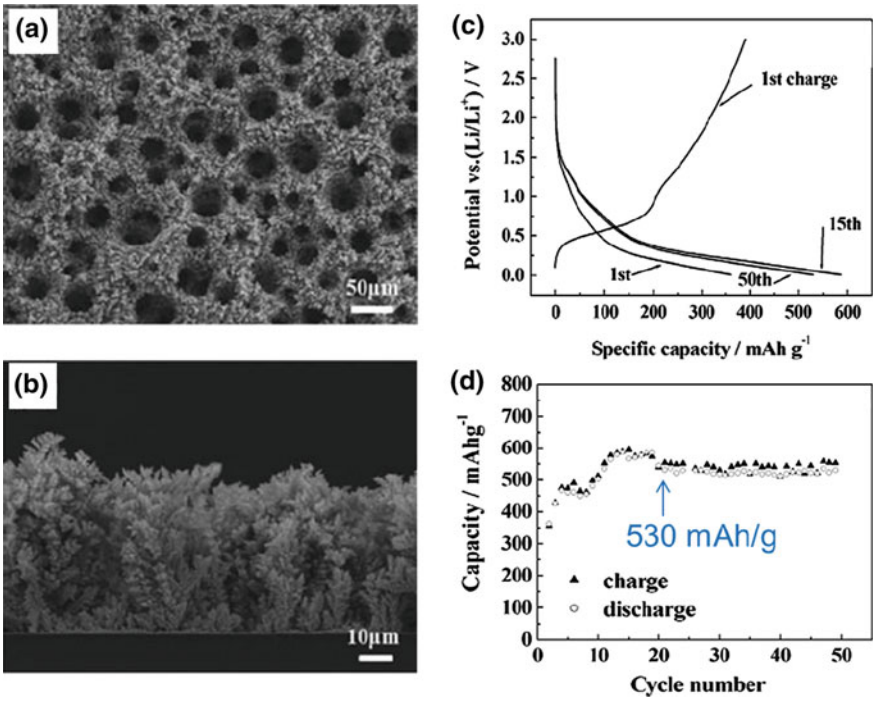

Fig. 5.4 FESEM images of porous $Ni_{50}Sn_{50}$ from **a** top-surface view, and **b** cross-sectional view. **c** First charge route and discharge profiles of $Ni_{50}Sn_{50}$ at 1 C rate; **d** Related cycle performance (Adapted from Ref. [14].)

nanoporous structure and the inclusion of TiO_2, which mitigate the volume change during the insertion/desertion of Li-ions of the Sn nanocrystals.

Micrometer-sized Al–Si particles with nanoporous structure are synthesized via a facile selective etching process from Al–Si alloys [12]. Thin Al_2O_3 layers are coated on the Si foam surface, forming Si/Al_2O_3 composite. The fabricated process is illustrated in Fig. 5.5a and the Al_2O_3 layer coating is realized via selective oxidation of Al by a wet thermal oxidation process. Figure 5.5b shows the EDS mapping of the etched Al–Si alloy, where Al_2O_3 particles of 500–600 nm diameter are found to locate in the core of the Si/Al_2O_3 foam. After a thermal oxidation process, the original foam-like structure is maintained while the amount of oxygen is increased substantially, due to the formation of thin Al_2O_3 layer on the Si frame in the outer shell (Fig. 5.5c). Electrochemical performance is examined in a Li-ion battery in the potential range of 0.005–2 V at C/5 as shown in Fig. 5.5d. The nanoporous Si/Al_2O_3 composite electrode exhibits outstanding cycle performance up to 150 cycles. In comparison, Al–Si electrode shows fast capacity fading and poor coulombic efficiency. The capacity retention is also dependent on the thermal

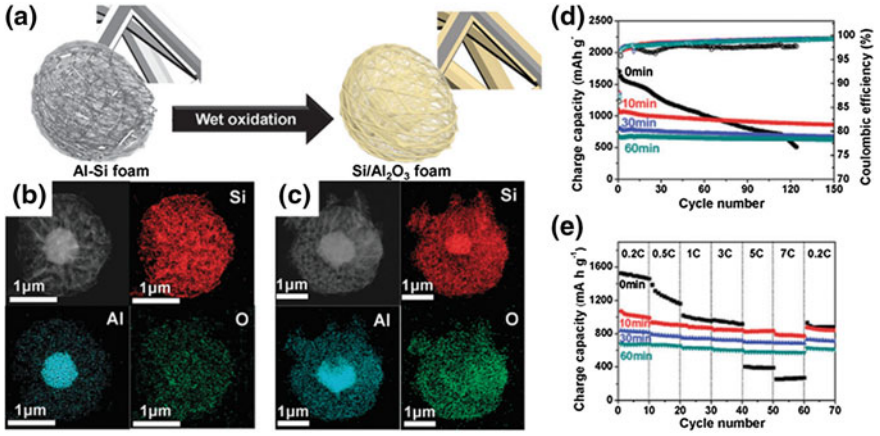

Fig. 5.5 **a** Schematic illustration showing the thermal oxidation process of chemically etched Al–Si particles. HAADF-STEM and the corresponding EDS mapping images of **b** etched Al–Si powder and **c** thermally oxidized (10 min) Al–Si powder. Electrochemical performances of etched Al–Si and thermally oxidized (10, 30, and 60 min) Si/Al_2O_3 electrodes. **d** Cycling performances at the C/5 rate for four Si-based electrodes. **e** Rate capabilities of four Si-based electrodes obtained in the range of C/5–10 C (the lithiation rate was fixed at C/5) (Reproduced from Ref. [12]. Copyright 2015, The Royal Society of Chemistry.)

oxidation time. The 10-min-oxidized composite electrode shows excellent long-term cycling stability. The rate capabilities are also tested with varying discharge rates from C/5 to 10 C. The Si/Al_2O_3 composite electrode shows improved rate performance even at the 5 C rate. The Si/Al_2O_3 foam with a thin Al_2O_3 layer has a sponge-like structure in the shell region, therefore the rate capability of this electrode is not affected too much by the thermal oxidation time. In addition, the Al_2O_3 protecting layers prohibit side reaction of the nanosized Si frame work and allow fast transport of Li-ions. The porous structure can also accommodate the volume expansion of Si during the repeated cycles.

Nanoporous Ge has been synthesized by chemical dealloying $Al_{71.6}Ge_{28.4}$ to work as anode of LIBs [13]. Figure 5.6a shows the SEM images of dealloying Al–Ge for 10 h. The etching process removes almost all of the Al in the matrix and the resulting powder materials are obtained. The interconnected structure of the crystals and the opening between the crystals have been confirmed as shown in Fig. 5.6b. The electrochemical performance as anode in LIBs is examined in coin cells. The voltage profiles at certain cycles are shown in Fig. 5.6c in the voltage range of 0.05–0.9 V at a current density of 160 mA/g. Good capacity retention has been observed even up to 150 cycles for nanoporous Ge, which is evidently better than that of normal Ge powder as shown in Fig. 5.6d. In addition, nanoporous Ge also shows enhanced rate performance. This excellent cycle and rate performance were again attributed to the unique nanoporous structure.

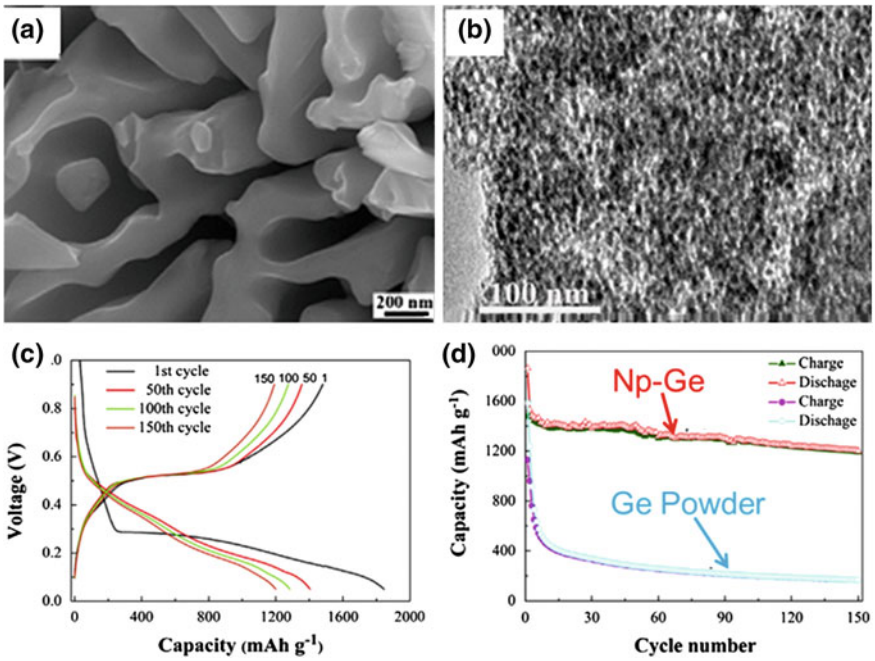

Fig. 5.6 **a** SEM image of the Al–Ge sample after etching in 10 h later, **b** TEM image of nanoporous Ge, Electrochemical characterizations for the np-Ge and Ge particles as negative electrodes for lithium-ion batteries. **c** Galvanostatic discharge (Li insertion, voltage decreases)/charge (Li extraction, voltage increases) curves of np-Ge electrodes. **d** Comparative cycling performance showing the discharge/charge capacities of the np-Ge and Ge particles (Adapted from Nano Energy Ref. [13].)

5.4.2 *Metal/Alloys Deposited on Nanoporous Metal Scaffolds*

Nanoporous metal materials may also function as unique substrates to anchor electrochemically active species to further enhance their energy storage properties. Acting as 3D substrates, they can readily accommodate the volume expansion and facilitate the electron/charge transfer during discharge/charge process. One of the first examples in this category is NPG supported Sn-based nanocomposites that work as high-performance anodes for LIBs [7].

The synthetic scheme and SEM images of 3D NPG and Sn composites electrode materials are shown in Fig. 5.7a–d. The porous substrate is prepared by chemical dealloying and followed by electroless plating of Sn nanocrystallines. The corresponding SEM images demonstrate the 3D nanoporous structures before and after deposition of Sn particles. The porous structures have been well kept. The composite electrode can exhibit a high and reversible capacity of 620 mAh g^{-1} after 140 cycles at 0.1 C. Moreover, high-rate performance has been achieved as 260 mAh g^{-1} at 8 C.

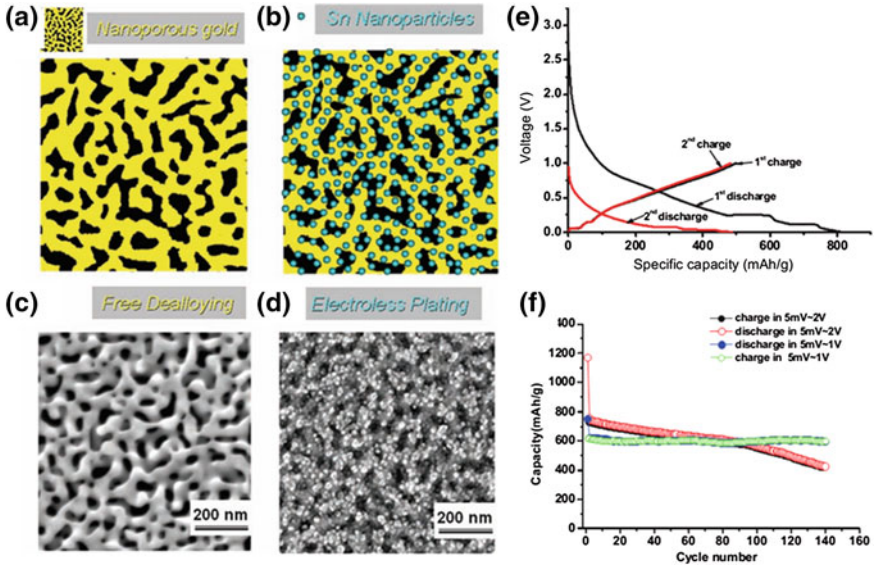

Fig. 5.7 Synthetic scheme of nanoporous Au-supported nanocrystalline tin. The dealloying process in **a** generates a 3D nanoporous Au substrate, the pores of which are traps for the nanocrystalline Sn in **b**. Corresponding SEM images in **c** and **d** reveal the microstructure of the 3D nanoporous Au-supported nanocrystalline Sn thin foil for the stages shown in (**a** and **b**), respectively; **e**Voltage profiles of a pure 3D Au substrate electrode during the first two cycles at a cycling rate of 0.1 C; **f** capacity–cycle number curves of Au-supported 3D nanoporous Sn electrodes at a cycling rate of 0.1 C (Reproduced from Ref. [7]. Copyright 2011, Wiley-VCH.)

This porous structure can accommodate the large volume variations during cycling and promote the mass transfer, preserve the good conductivity of gold framework, and simultaneously improve capacity retention and rate performance.

NPG has also been adopted as a scaffold to support Ge as anodes for LIBs [14]. The deposition of Ge was realized by a thermal evaporation technique. The TEM images of the fabricated Ge/NPG composites are shown in Fig. 5.8. There is a uniform pore size distribution and a bicontinuous 3D architecture of the prepared film composite. The thickness of Ge film is estimated to be about 20 nm (Fig. 5.8b). The thin layer of Ge consists of nanoscale Ge particles dispersed in an amorphous Ge matrix. This special structure provides highly conductive pathways for electrons, short ion diffusion length, and fast mass transport channel. This Ge/NPG has also been tested as an anode in LIBs and exhibits an excellent rate performance. Even at a rate of 60 C, it still delivers a capacity of 360 mAh/g. Here nanoporous Au substrate not only promotes the ionic and electronic conductivity, but also acts as a volume buffer cushion.

The high price of gold undoubtedly restricts its practical applications. Lower cost nanoporous copper has then been developed as the substrate for Sn deposition, using an electroless plating method [15]. After Sn particle deposition, no obvious morphology change is observed and a thin layer of tin appears on the surface as shown in Fig. 5.9a. Two sets of lattice fringes with different lattice spacing can be

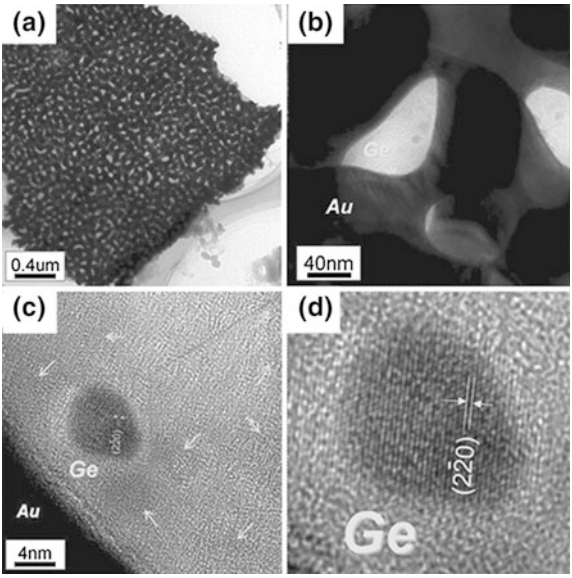

Fig. 5.8 **a** TEM micrographs of the as-prepared 3D nanoporous Au film; **b** Representative TEM micrograph of nanoporous Au/Ge composite deposition for 3 h; **c** High-resolution TEM image of Au/Ge interface, indicating that the nanoscaled Ge particles dispersed in an amorphous Ge matrix. **d** Corresponding HRTEM image from the *marked region* showing that the nanoscaled Ge particles (~7 nm) structure (Reproduced from Ref. [14]. Copyright 2013, Wiley-VCH.)

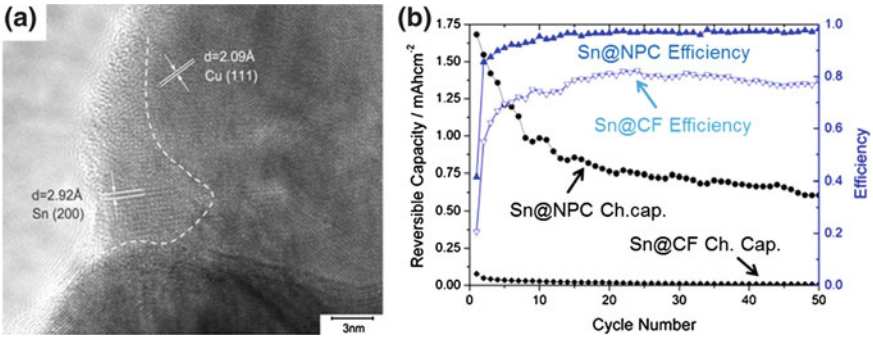

Fig. 5.9 **a** TEM image of Sn@nanoporous copper, **b** Cycle performances of Sn@nanoporous copper and Sn@CF electrodes (Adapted from Ref. [15].)

distinguished, i.e., 2.09 and 2.92 Å, corresponding to that of fcc Cu (111) and tetragonal β-Sn (200). It also indicates that metal tin has been thoroughly and evenly deposited into the entire 3D surfaces of nanoporous copper. Both higher capacity and better coulombic efficiency are achieved for the Sn@nanoporous copper composites than the control sample of Sn@copper foil. The charge capacity is 1.68 mA/cm^2 in the first cycle, which is higher than the reported nanoarchitectured electrode. The coulombic efficiency remains nearly 100 % up to 50 cycles.

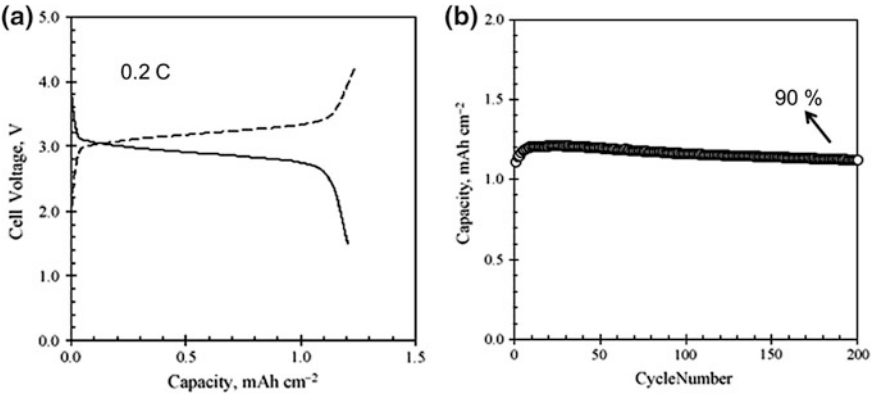

Fig. 5.10 Charge/discharge curves (**a**) and cycle performance (**b**) of the full $LiFePO_4$/Cu–Sn cell using the aqueous slurry at the 20th cycle. The 3D substrates were applied for both the positive and negative electrodes. Current density: 0.2 C rate, potential range 1.5–4.2 V, temperature 30 °C (Adapted from Ref. [16].)

This good performance is associated with the special structural merits of NPMs which facilitate the Li-ion transports and electronic conductivity, and can accommodate large volume expansion during discharge/charge process.

The 3D foam-type substrate is also investigated in full cells both for Sn-based negative electrodes and $LiFePO_4$ positive electrode to improve the cycle performance. In a typical synthesis procedure, nickel is plated on foamed polyurethane followed by heat treatment to remove the inner polyurethane. In positive electrode, a high tolerance nickel–chromium (Ni–Cr) substrate is adopted. And the electrodes are fabricated by loading the aqueous slurries (including active materials Cu–Sn alloy powder or $LiFePO_4$, conductive agents and binders) into the 3D substrates followed by roll-press. A careful drying process at the temperature over 150 °C under vacuum is required to remove the water. The charge/discharge curves of the prepared full cell are shown in Fig. 5.10a at the current density of 0.2 C rate. It exhibits an excellent cycle performance and maintains more than 90 % capacity of the maximum value even at the 200th cycle. The utilization of 3D current collector makes the aqueous slurry practicable. It is noteworthy that the 3D substrate has high flexibilities in structure, such as thickness, porosity, and pore size. By optimizing the structure of the 3D substrate and the annealing conditions, further improvement in the LIBs using alloy-based negative electrodes will be expected.

5.4.3 Metal Oxides Deposited on Nanoporous Metal Scaffolds

Metal oxide (including those of SnO_2, Sb_2O_3, MnO_x, FeO_x, NiO_x, Co_2O_3, etc.) based anode materials have received significant attentions due to their high

theoretical capacity and low work potential versus Li/Li^+ [17]. The Li storage mechanism is based on the conversion reactions as $MO + Li \leftrightarrow M + Li_2O$, which is also characterized by large volume expansions and subsequent pulverization and cracking of electrodes during Li insertion and extraction [1]. This is also one of the most important obstacles for the practical applications of these kinds of materials. Similar to those of metal-based NPM composite electrodes, decoration of metal oxides onto NPMs can provide multifunctional scaffolds which not only decrease the electrical resistances, but also offer rigid skeletons with moderate space for the fast ion diffusion and volume expansion [1]. The MO/NPM composites are mainly fabricated by plating, chemical bath deposition, and hydrothermal techniques.

Tin oxide and manganese oxide have been deposited on nanoporous copper by plating techniques [18]. Before the active materials deposition, the nanoporous copper substrate is first fabricated by depositing an 800 nm thick $Cu_{30}Mn_{70}$ (at.%) alloy film onto a flat Cu foil by direct current magnetron sputtering and a subsequent chemical dealloying in acidic aqueous solution to produce a nanoporous layer. The representation top-view SEM image of the SnO_2/nanoporous copper electrode is shown in Fig. 5.11a, which demonstrates uniform distribution of SnO_2

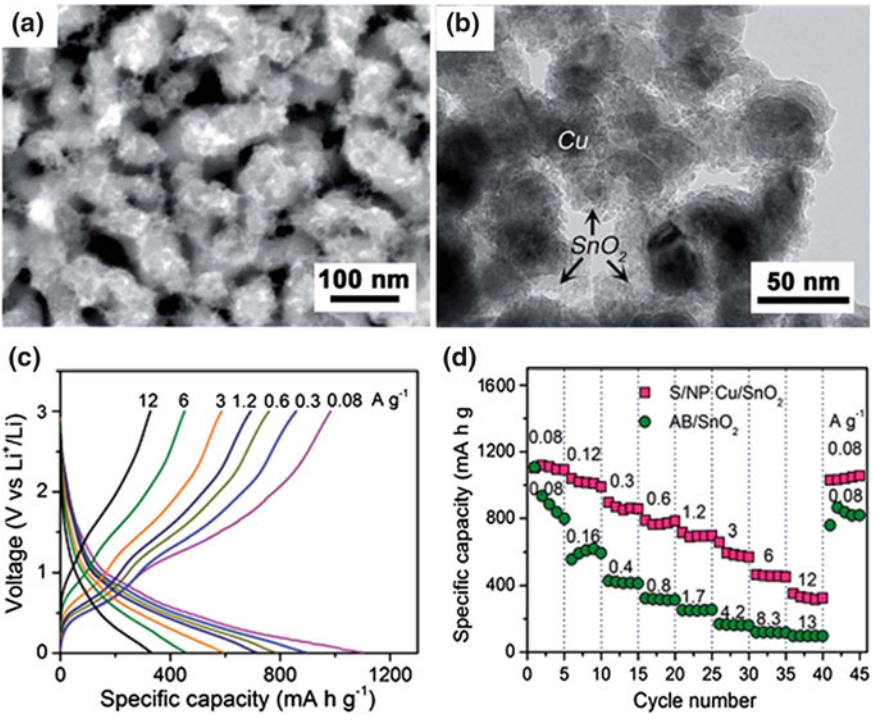

Fig. 5.11 **a** Top-view SEM images of S/NP Cu/SnO_2 electrodes; **b** Typical low-magnification TEM micrograph for NP Cu skeleton supported SnO_2 nanoparticles; **c** Voltage profiles of the S/NP Cu/SnO_2 electrode at various current densities; **d** Rate capability of the S/NP Cu/SnO_2 electrode (Reproduced from Ref. [18]. Copyright 2014, The Royal Society of Chemistry.)

particles over the entire nanoporous layer with well retention of a porous structure. The hybrid nanoporous structure is further verified by TEM (Fig. 5.11b), where the contrast difference between Cu framework and SnO_2 particles can be identified clearly. To examine the electrochemical performance of the SnO_2/nanoporous copper, the synthesized composites are processed into coin cells and subjected to electrochemical tests. The voltage profiles in the range of 0.005–3 V at various current densities are presented in Fig. 5.11c. A specific capacity of 331 mAh/g is obtained even at a discharge/charge current density of 12 A/g. After long cycles rate test, the specific capacity reverts to 1056 mAh/g at 0.08 A/g, about 96 % of initial charge capacity (Fig. 5.11d).

MnO_2/nanoporous copper composites can be fabricated by the similar method as expressed in Fig. 5.12a–d. MnO_2 nanocrystals are plated onto nanoporous copper foils by a modified electroless plating technique in the aqueous mixture of 5 mM $KMnO_4$ and 10 mM KOH for 30 min under the gas reagent of hydrazine (N_2H_4) [19]. The composite electrode shows exceptional mechanical flexibility and stability while minimizing the primary resistances in the entire hybrid electrodes for the enhanced charge storage. The first discharge/charge steps deliver specific capacities of 1324 and 1179 mAh/g, respectively, and a well reversibility of conversion reaction of MnO_2 can also be obtained in the following cycle. This hybrid bulk electrodes store/deliver high energy at ultrahigh rates with excellent stability by a dual mechanism of pseudocapacitive and Li insertion/extraction processes.

Three-dimensional porous Ni/NiO and Cu/Cu_2O electrodes can be fabricated via a facile H_2 gas bubble dynamic template route as illustrated in Fig. 5.13 [20].

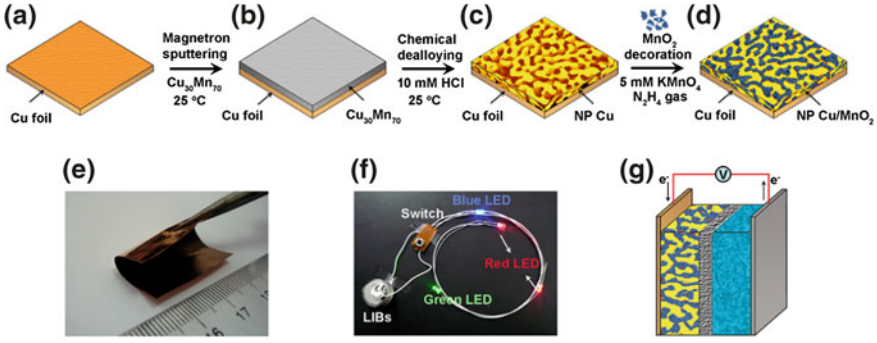

Fig. 5.12 Hybrid bulk electrodes with 3D nanoporosity for Li-ion batteries. Scheme showing the fabrication of seamlessly integrated S/NP Cu/MnO_2 bulk electrode, **a** Cleaned copper foil substrate. **b** $Cu_{30}Mn_{70}$ alloy film deposited on the copper foil by magnetron sputtering. **c** Nanoporous Cu layer on the copper foil produced by chemically dealloying $Cu_{30}Mn_{70}$ in diluted HCl solution. **d** Nanocrystalline MnO_2 directly grown onto S/NP Cu skeleton using electroless plating. **e** Photograph of a flexible S/NP Cu/MnO_2 hybrid bulk electrode being bend. **f** Four batteries assembled with S/NP Cu/MnO_2 bulk electrodes power blue, red and green LEDs. **g** Schematic battery constructed with S/NP Cu/MnO_2 and lithium foil as electrodes, 1 M $LiPF_6$ in EC/EMC/DMC as electrolyte, and porous polymer as separator (Reproduced from Ref. [19]. Copyright 2013, Nature Publishing Group.)

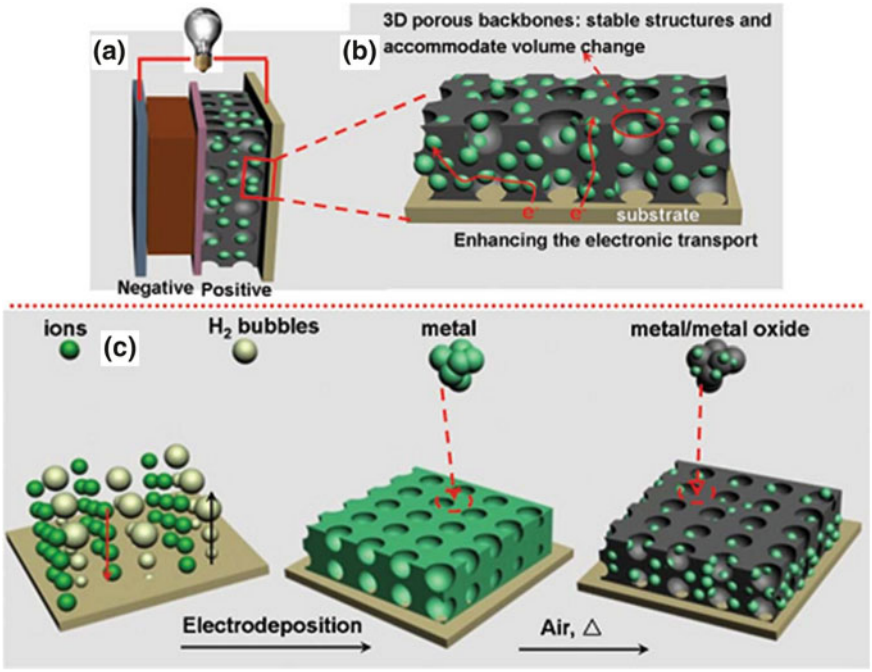

Fig. 5.13 **a** A schematic of LIBs, including the 3D PMNI metal/metal oxide electrode. **b** A structural illustration of a 3D PMNI metal/metal oxide electrode. **c** The 3D PMNI metal/metal oxide electrode is fabricated via an H_2 gas bubble dynamic template route (Reproduced from Ref. [20]. Copyright 2013, The Royal Society of Chemistry.)

The 3D porous metal is grown on the conductive substrate by drastic cathodic deposition. The H_2 gas bubbles are used as dynamic pore-forming templates which are essential to the formation of 3D porous metal. Metal grows between the H_2 gas bubbles and forms a 3D metallic network structure directly connected to the substrate. Afterwards, the 3D porous metal is partially thermally oxidized at low temperature in air, eventually forming interconnected metal/metal oxide. The metal in the interconnected metal/metal oxide structures functions as a 3D conductive scaffold which is beneficial for enhancing the Li storage properties of metal oxide active materials.

The SEM images of Ni/NiO are shown in Fig. 5.14a, b [20], where Ni/NiO composites are found to inherit the intact porous foam and dendrites structure of 3D porous Ni, and their grain size is around 240–350 nm. At 1 C rate, the initial discharge and charge capacities are 1066.3 and 659.3 mAh/g, respectively. It delivers an increasing reversible capacity due to the sufficient contacts between the electrode and electrolyte and the increased SEI film, and remains 766.7 mAh/g after 100 cycles as shown in Fig. 5.14c. Furthermore, the Ni/NiO composite electrode also exhibits high-rate Li storage properties. Varying the discharge/charge rates from 0.5–20 C, the reversible capacities are found to decrease slowly with the

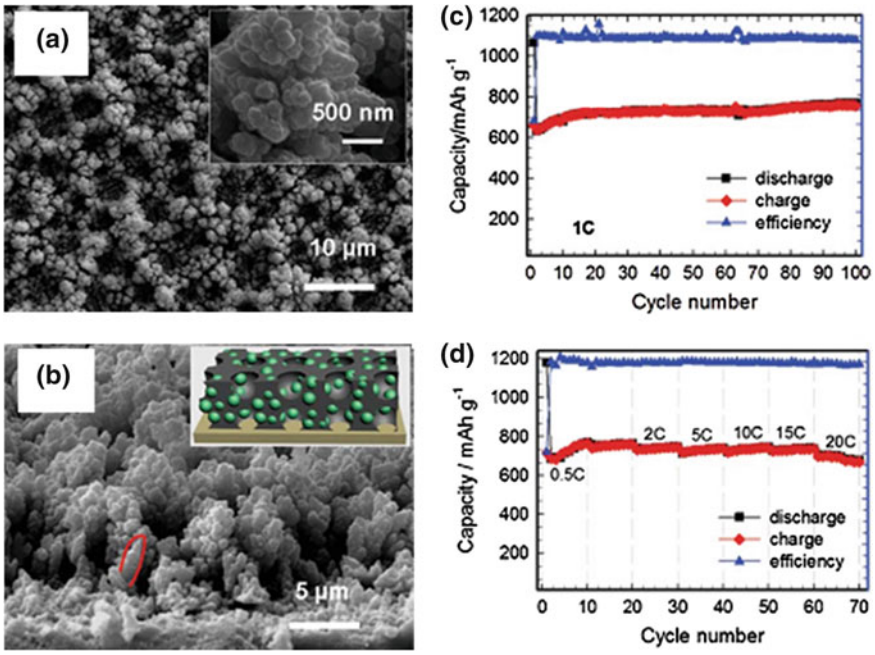

Fig. 5.14 **a** SEM image of 3D porous Ni obtained by cathodic deposition and **b** 3D PMNI Ni/NiO after partially thermally oxidizing the 3D porous Ni in air. **c** Cycle stability and coloumbic efficiency of 3D PMNI Ni/NiO. **d** Rate performance (Reproduced from Ref. [20]. Copyright 2013, The Royal Society of Chemistry.)

increased rates. High capacities of 762.7, 743.7, 735.1, and 675.9 mAh/g can be obtained at 0.5, 10, 15, and 20 C rates as shown in Fig. 5.14d, respectively.

The results of Cu/Cu_2O composites electrode are illustrated in Fig. 5.15 [20]. It is noted that Cu/Cu_2O with a height of 18–20 μm is directly grown on the substrate, inheriting the porous foam and micro-dendrite structure of 3D porous Cu scaffold. Examined as an anode for LIBs, it shows high-rate Li storage properties (Fig. 5.15d). The initial discharge and charge capacities are 560.7 and 370.5 mAh/g, respectively. The reversible capacity slowly decreases as the increasing of the discharge/charge rates, and high-rate capacity of 381.8, 327.4, 321.3, and 312.8 mAh/g can be obtained at 0.5, 10, 15, and 20 C rates, respectively. The capacity performance is the highest to date in comparison to other reported Cu_2O anodes. The superior performance both in Ni/NiO and Cu/Cu_2O is originated from the 3D interconnected metal/metal oxide design with a stable 3D scaffold, highly conductive pathway, and shorter ion diffusion length.

Cu_2O/nanoporous Cu composite has been prepared by etching $Cu_{50}Al_{50}$ alloy precursors and subsequent in situ thermal oxidation [21]. The high-resolution TEM image of Cu_2O/Cu composite is shown in Fig. 5.16a. It indicates that Cu_2O is formed on the nanoporous copper foam surface. Working as an anode for LIBs, its

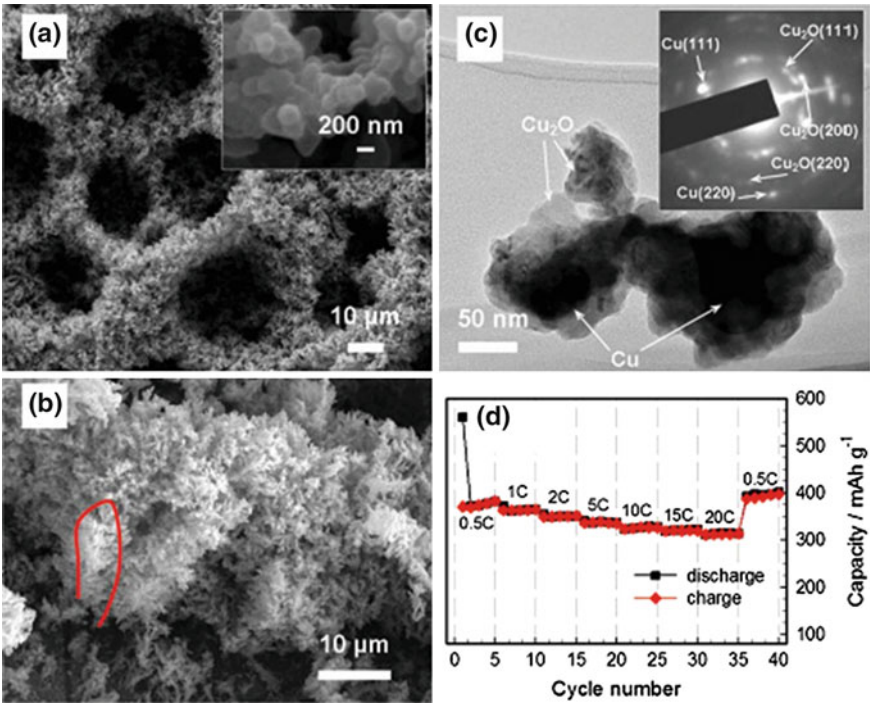

Fig. 5.15 SEM (**a**, **b**) and TEM (**c**) images and rate cyclability (**d**) of 3D PMNI Cu/Cu_2O after partially thermally oxidizing the 3D porous Cu in air. Herein, 1 C is regarded as 375 mAh/g, in light of the theoretical capacity of Cu_2O (375 mAh/g). The *inset* of **c** shows the corresponding ED pattern of 3D PMNI Cu/Cu_2O (Reproduced from Ref. [20]. Copyright 2013, The Royal Society of Chemistry.)

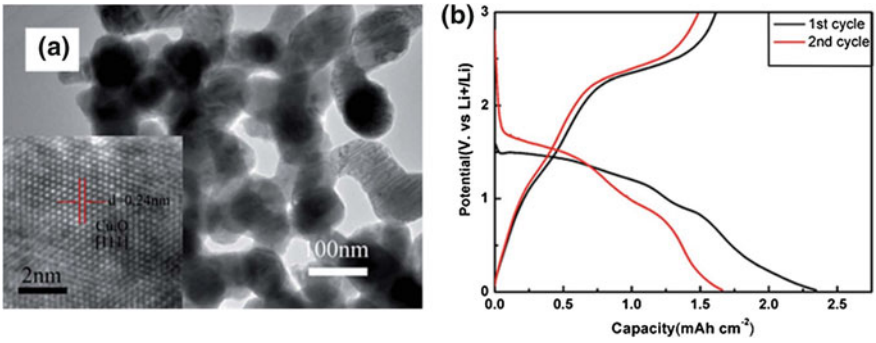

Fig. 5.16 **a** TEM micrographs of 3D NPCu@Cu_2O, **b** Electrochemical performance of the 3D NPCu@Cu_2O electrodes, charge and discharge curves in the voltage range of 0.02–3 V at a current density of 0.175 mA/cm^2 (Reproduced from Ref. [21]. Copyright 2013, The Royal Society of Chemistry.)

first and second discharge/charge cycles are shown in Fig. 5.16b. An abrupt drop in potential down to about 1.4 V is observed, followed by a long plateau between 1.4 and 0.8 V, which can be explained as a decomposition process of Cu_2O to Cu and Li_2O. It also shows a very stable cycle performance. This excellent battery performance is originated from the 3D nanoporous architecture, which provides efficient and rapid pathways for ion and electron transport as well as short solid-state diffusion lengths.

NiO nanorod-anchored Ni foam electrode is fabricated by anodization followed by annealing treatment [22]. The SAED pattern shown in Fig. 5.17a demonstrates the formation of fcc NiO (JCPDS 65-2901). The HRTEM images in Fig. 5.17b illustrates the NiO nanorod-anchored Ni foam electrode. The rod-like structures are composed of nanocrystals of 10–15 nm in size. The average pore size distributions calculated based on the BET data is in a range of 2–10 nm (Fig. 5.17c). Electrochemical performance is conducted to evaluate the performance of NiO/Ni foam composite electrode.

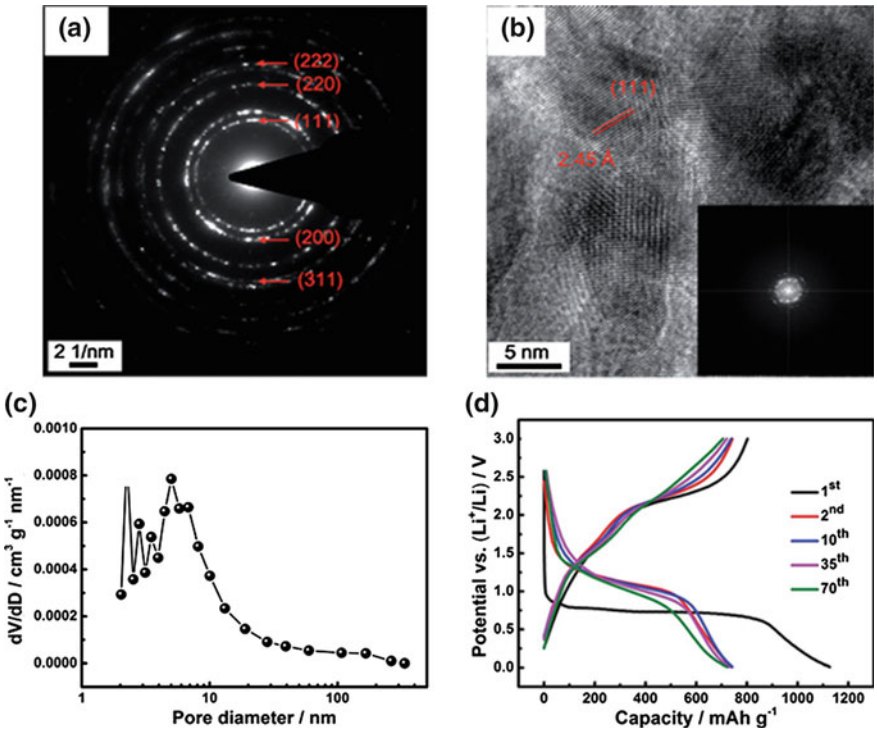

Fig. 5.17 **a** SAED pattern and **b** HRTEM image of the NiO nanorod-anchored Ni foam electrode. *Inset* of **b** shows the FFT pattern corresponding to the HRTEM image. **c** Pore size distribution of the NiO nanorod-anchored Ni foam electrode (based on the total mass of the electrodes). **d** Galvanostatic charge–discharge curves of the NiO nanorod-anchored Ni foam at different cycles in a potential range of 0.01–3 V (vs. Li^+/Li) at a current density of 1 A/g (Reproduced from Ref. [22]. Copyright 2014. The Royal Society of Chemistry)

Figure 5.17d depicts the voltage profiles for the selected cycles at 1 A/g. The potential decreases rapidly during the first discharge, followed by an extended plateau around 0.73 V (vs. Li/Li^+), corresponding to the reduction of NiO and the formation of an SEI layer. From the second cycle, the electrode maintains high reversibility. No obvious capacity and voltage fading can be observed even up to 70 cycles. The ultrastable electrochemical performance is associated with that the special morphology can maintain structural integrity by accommodating partially the strain induced by the volume change during the fast discharge/charge process. Additionally, the Ni framework can also enhance the electrical conductivity.

The 3D porous Ni/NiO nanoflake composite film has been constructed by a cathodic electrodeposition method [1]. NiO is first deposited on the 3D porous nano-Ni film to form a composite film via a chemical bath deposition method, which is followed by annealing at 350 °C for 1.5 h in argon to form 3D porous structure. The SEM images of NiO nanoflake formed on the nickel foam are shown in Fig. 5.18a and b. The highly porous features can be observed clearly. The discharge/charge profiles shown in Fig. 5.18c demonstrate that the nanoporous-Ni/NiO nanoflake composite film exhibits an improved round-trip efficiency with higher discharge and lower charge plateaus than the NiO film. It also presents much better cycle performance as shown in Fig. 5.18d. After 50 cycles at 1.5 A/g, the specific

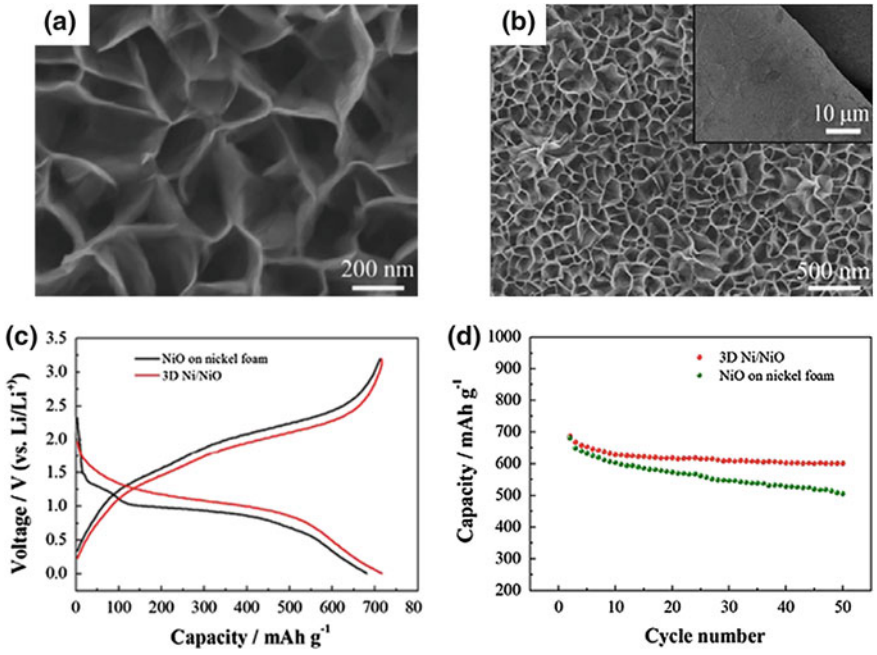

Fig. 5.18 SEM images of NiO nanoflake film on Ni foam (**a**, **b**); charge/discharge curves of both NiO films at the second cycle, cycle performance at 1.5 A/g (Reproduced from Ref. [23]. Copyright 2013, Elsevier.)

capacity of the 3D nano-Ni/NiO nanoflake composite film is 601 mAh/g, much higher than the NiO film on Ni foam (505 mAh/g), which demonstrates the high specific capacity and remarkable rate capability of the 3D porous nano-Ni/NiO nanoflake composite film for high-performance LIBs.

Unique mesoporous metal oxide nanosheets covered by a carbon layer can be fabricated by directly growing $Ni_xCo_{1-x}O$ nanosheets on a nickel foam substrates through a hydrothermal method, followed by an atomic layer deposition of amorphous carbon [24]. The fabrication process is illustrated in Fig. 5.19a, b. Ternary oxides are initially designed to increase both the conductivity and capacity. With the aim to further improving the structural stability of the porous oxides, the metal oxide surfaces are further coated with carbon flakes to provide connections between the skeletons. The morphology of the fabricated $Ni_xCo_{1-x}O$ nanonets embedded with large carbon flakes are characterized by SEM and TEM as shown in Fig. 5.19c, d. The carbon flakes are generated from the glucose composite layer and uniformly coated on the $Ni_xCo_{1-x}O$ skeleton. As a result, the porous nanonets not only have better utilization of the open space of the porous skeleton with larger surface areas but also have better electric conductivity and mechanical flexibility. The cycle and rate performance are shown in Fig. 5.19e, f. The $Ni_xCo_{1-x}O$@C can maintain a stable capacity of 1093.5 mAh/g after 50 cycles, whereas the capacity of $Ni_xCo_{1-x}O$ is only 536.0 mAh/g at a current density of 400 mA/g. The carbon flake modified electrode can also consistently retain higher capacities than the pure $Ni_xCo_{1-x}O$ electrode as varying the current density from 400 to 2400 mA/g. The improved cycling stability and rate performance can be attributed to the surface

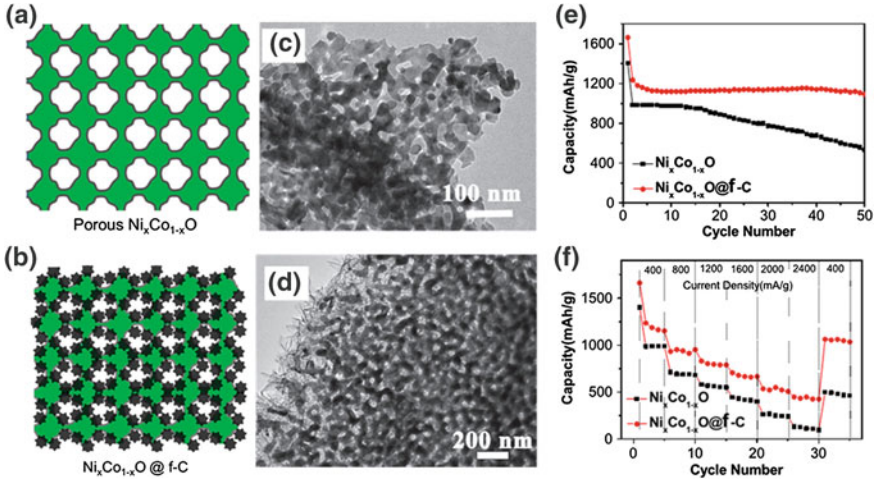

Fig. 5.19 Schematics of the nanostructure, **a** as-grown $Ni_xCo_{1-x}O$ porous sheets; **b** $Ni_xCo_{1-x}O$@carbon composite sheets after growth of carbon nanoflakes via ALD alumina assisted carbonization. TEM images of $Ni_xCo_{1-x}O$ (**c**) and $Ni_xCo_{1-x}O$@carbon composite sheets (**d**); Cycle (**e**) and Rate performance (**f**) (Reproduced from Ref. [24]. Copyright 2013, IOP Science.)

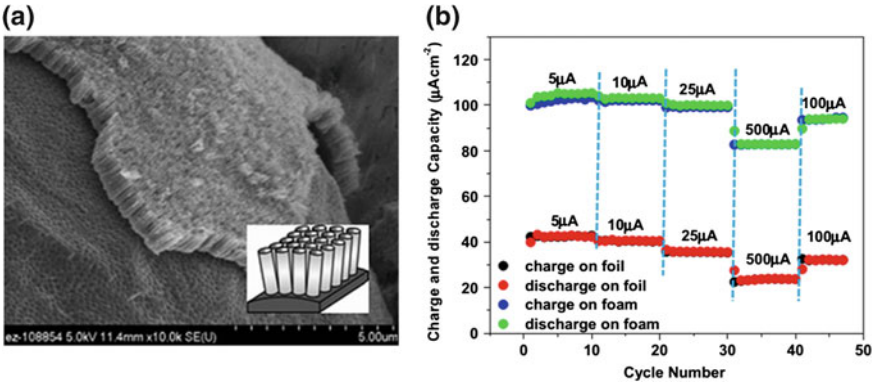

Fig. 5.20 **a** SEM images of prepared TiO_2 NTAs on the Ti foam at the cross-sectional view, the *inserted picture* is the schematics of the TiO_2 NTAs grown on the surface of Ti foam; **b** Rate performance of TiO_2 NTAs on Ti foil and foam in the voltage range of 0.9–2.5 V versus Na/Na^+ (Adapted from Ref. [25].)

carbon layer that can effectively buffer the mechanical stress, maintain kinetics with facile charge transport and provide a linkage between individual $Ni_xCo_{1-x}O$ nanocrystallites.

Self-organized amorphous TiO_2 nanotube arrays can be fabricated on the Ti foam through an electrochemical anodization technique and used as anodes both for lithium-ion battery and sodium-ion battery [25]. The SEM image in Fig. 5.20a shows that the average length of the nanotubes is around 1.5 μm and the diameters of the nanotubes vary from 80 to 150 nm. When examined as anode in LIBs, high capacities of 103 $\mu Ah/cm^2$ at 10 $\mu A/cm^2$ and 83 $\mu Ah/cm^2$ at 500 $\mu A/cm^2$ can be obtained, which are two to three times higher than those on nonporous substrate. The rate performance in Na battery is shown in Fig. 5.20b. Under low current rate of 5 $\mu A/cm^2$, the charge capacities are close to 43 $\mu Ah/cm^2$ for Ti foil and 105 $\mu Ah/cm^2$ for Ti foam after 10 cycles. By increasing the charge–discharge rate, the charge capacity of the Ti foil-based electrode reduces to 32 $\mu Ah/cm^2$ at 100 $\mu A/cm^2$. In comparison, the performance reaches up to 94 $\mu Ah/cm^2$ for the Ti foam-based electrode. The superior performance from the Ti foam-based substrate is associated with the porous structure which provides not only good electrical contact between the active materials and the current collector, but also more surface area for Li or Na storage.

5.4.4 *Metal Sulfides Deposited on Nanoporous Metal Scaffolds*

Transition metal oxide anodes, which are usually based on a conversion reaction mechanism, can be extended to sulfides and lead to impressive capacity improvements

[26]. These kinds of materials lead to a reversible conversion process that can be summarized by the generalized half-reaction equation: $M_xS_y + ne^- + nLi^+ \leftrightarrow xM + Li_nS_y$, where M is a transition metal such as Ni, Co, Fe, etc. Among various candidates, Ni_3S_2 and NiS incorporated in NPM framework, have been intensively studied as electrode for LIBs.

Porous NiS/Ni nanostructure electrode can be fabricated by a novel dry thermal sulfuration approach [26]. Thiourea is chosen as the sulfur source and Ni foam as the substrate, both placed in a Teflon-lined autoclave. The contents on the surface of Ni foam surface are confirmed to be NiS by XRD characterization. The as-prepared NiS/Ni electrode exhibits homogeneous morphology as shown in Fig. 5.21a, b. The holes on the surface of electrode build up the 3D fine porous architecture of the NiS electrode. As an anode in LIBs, Fig. 5.21c shows the cycle performance and the initial three cycles of discharge/charge profiles for this material. The discharge plateaus move from 1.5 to about 1.4 V in the second cycle compared with the initial cycle. The initial discharge capacity is about 978 mAh/g, much higher than the theoretical value (590 mAh/g) of NiS, mainly due to the formation of solid

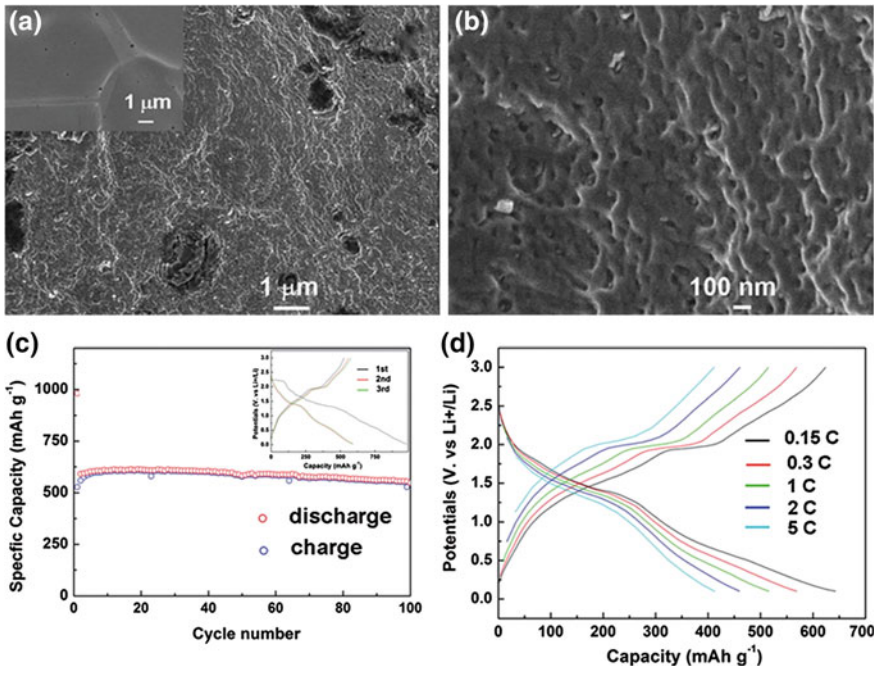

Fig. 5.21 SEM images of the NiS/Ni electrode with low (**a**) and high (**b**) magnifications. The *inset* of **a** is a SEM image of Ni foam. The electrochemical performance and rate capability of the NiS/Ni electrode. **c** Capacity retention of the galvanostatic test run at a rate of 0.15 C; the inset shows the galvanostatic charge–discharge voltage profiles for the initial three cycles. **d** Representative charge and discharge voltage profiles at various C rates (Reproduced from Ref. [26]. Copyright 2012, The Royal Society of Chemistry.)

electrolyte interface. It shows good cycling stability even up to 100 cycles. More interestingly, it demonstrates that superior rate performance and a high capacity of 394 mAh/g can be achieved even at a rate as high as 5 C, which is much better than the traditional anode materials without nanoporous structures. The enhanced electrochemical performance is ascribed to the nanoporous structure which promotes the effective electrode/electrolyte contact and strain accommodation.

Porous Ni_3S_2 electrode has also been deposited on Ni foam [27] substrates using a hydrothermal technique. The morphology of Ni_3S_2/Ni foam electrode is shown in Fig. 5.22a, b, featuring a large number of holes and interspaces among those rod-like and flocky-like Ni_3S_2. Those nanorods are composed of nanoflakes with a mean size about 100 nm, among which a large number of interspaces exist. The voltage profiles in the initial five cycles and the cycle performance are displayed in Fig. 5.22c, d. A high initial discharge capacity of 535 mAh/g with a plateau near 1.35 V suggests a classical conversion reaction process. Upon subsequent charges, the voltage increases rapidly to reach a well-defined plateau appearing near 1.93 V, corresponding to the oxidation process of Ni/Li_2S mixture into Ni_3S_2. The 2nd to 5th discharge and charge curves show little capacity attenuations and steady voltage plateaus near 1.44 and 1.93 V, respectively. At the end of 80th cycle, the charge capacity is 398 mAh/g, which is 92.8 % of the 2nd cycle. The morphology of the cycled electrode is also illustrated in Fig. 5.22b. There are many holes in the cycled

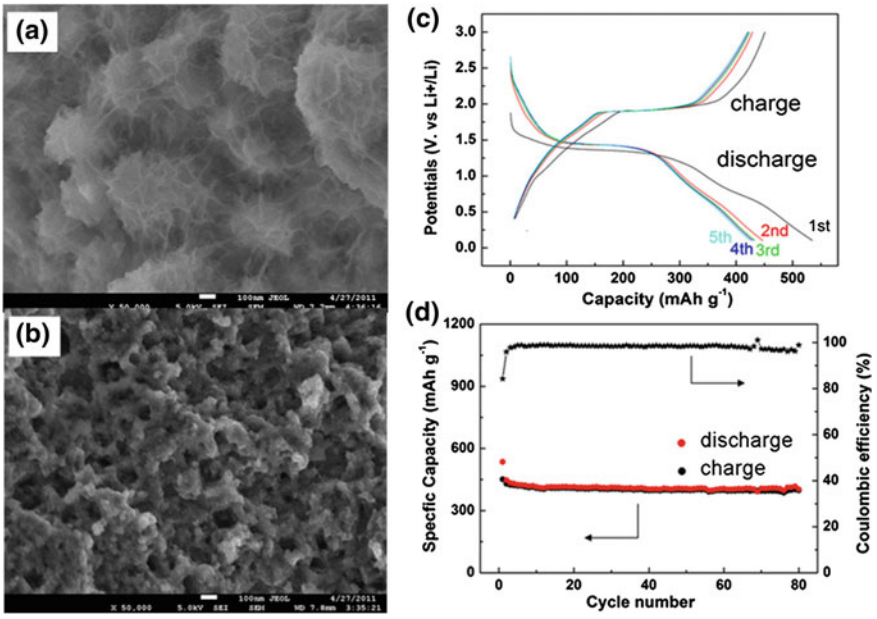

Fig. 5.22 SEM images of the as-synthesized Ni_3S_2/Ni electrode (**a**) and cycled electrode (**b**), first 5 charge and discharge curves (**c**) and cycle performance and coulombic efficiency (**d**) of Ni_3S_2/Ni nanostructured electrode at a current density of 0.1 mA cm^{-2}. (Adapted from Ref. [27].)

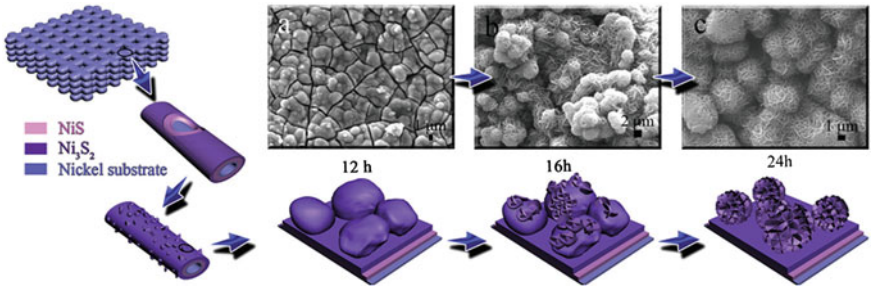

Fig. 5.23 The morphology evolution of Ni_3S_2 flower-like spheres which are grown in situ on nickel foam at 160 °C in the mixed solvents of 5 mL EDA and 11 mL EG with different reaction times (Reproduced from Ref. [28]. Copyright 2013, The Royal Society of Chemistry.)

electrode, and the mean size of those holes is about 80 nm. A large number of nanoparticles interweave with each other. The formation of porous architecture facilitates the electrochemical reactions between electrolyte and electrode, resulting in high capacity and excellent cycle performance.

Series of nickel sulfide nanocrystallines have been fabricated on Ni foam using a solvothermal method [28]. The structure and morphology of each compound can be controlled by adjusting the polarity of the mixed solvents. The flower-like Ni_3S_2 spheres are obtained in the mixed solvent of 5 mL anhydrous ethylenediamine and 11 mL ethylene glycol at 160 °C for different reaction time. As shown in Fig. 5.23, a thin layer of NiS covers on the substrate initially, and gradually transforms into the Ni_3S_2 phase. At the same time, a few small protuberances or cone structured Ni_3S_2 appear in the covering layer. As the reaction goes on, some thick flake structure starts to grow on the sphere-like protuberances. Finally, the Ni_3S_2 flower-like spheres composed of a nanoslice structure are obtained after 24 h. As an anode for LIBs, it shows a smooth discharge voltage plateau in the range of 1.1–1.2 V with a discharge capacity of 353.1 mAh/g. This performance can be further improved by optimizing the morphology of the electrode composites.

5.4.5 *Insertion Materials Deposited on Nanoporous Metal Scaffolds*

The spinel $Li_4Ti_5O_{12}$ is a well-known insertion anode with nearly zero-strain during the discharge/charge process [8]. Accompanied by the structure studies, electrode materials at nanoscale with exposed highly reactive crystal planes can deliver superior electrochemical performance. 3D nanoporous Cu has been adopted to construct a bicontinuous $Cu/Li_4Ti_5O_{12}$ composite electrode with highly exposed (111) facets [8]. The preparation of the composite electrode is finished under moderate conditions by co-precipitation, followed by sintering in mixed gas of H_2/

Ar at 600 °C for 1.5 h. Compared with the commonly constructed $Li_4Ti_5O_{12}$ electrode (Fig. 5.24), the Cu/$Li_4Ti_5O_{12}$ composite electrode can realize the supercapacitor-like rate performance due to the following reasons. On one hand, the nanoporous copper scaffold provides greater electroconductivity than typical current collector and electrode structure. On the other hand, it is possible to obtain $Li_4Ti_5O_{12}$ with their active planes highly exposed, which provides high lithium-ion conductivity in this unique Cu/$Li_4Ti_5O_{12}$ bicontinuous structure.

The Cu/$Li_4Ti_5O_{12}$ composite electrode is fabricated into coin cells to investigate its battery performance [8]. The selected cycles of voltage profiles at 1st, 50th, 100th, 600th, and 1200th cycles are shown in Fig. 5.25a. There are negligible changes during the 1200 cycles both in the capacity and discharge/charge plateau. The 3D nanoporous architectures are indeed beneficial for the improvement of cycle stability. In addition, the Cu/$Li_4Ti_5O_{12}$ composite electrode also displays high-rate cycling performance, maintaining ultrastable capacity at 1 C for over 2000 cycles (Fig. 5.25b). The high reversible capacity of 172 mAh/g is obtained at a rate

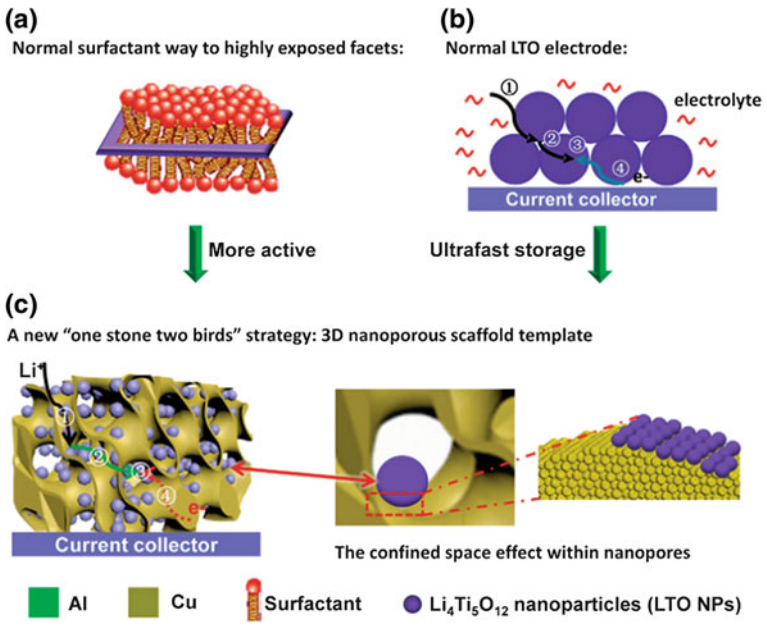

Fig. 5.24 Comparison of two traditionally used methods and the new strategy of a Cu/LTO scaffold: **a** Illustration of the normal surfactant method to obtain nanomaterials with highly exposed planes. **b** Schematic representation of a commonly used electrode consisting of LTO particles, an electrolyte and a current collector. **c** Schematic illustration for the fabrication of a bicontinuous Cu/LTO electrode via a three-dimensional nanoporous Cu scaffold template route, where LTO NPs can be encapsulated into the Cu nanopores (Reproduced from Ref. [8].)

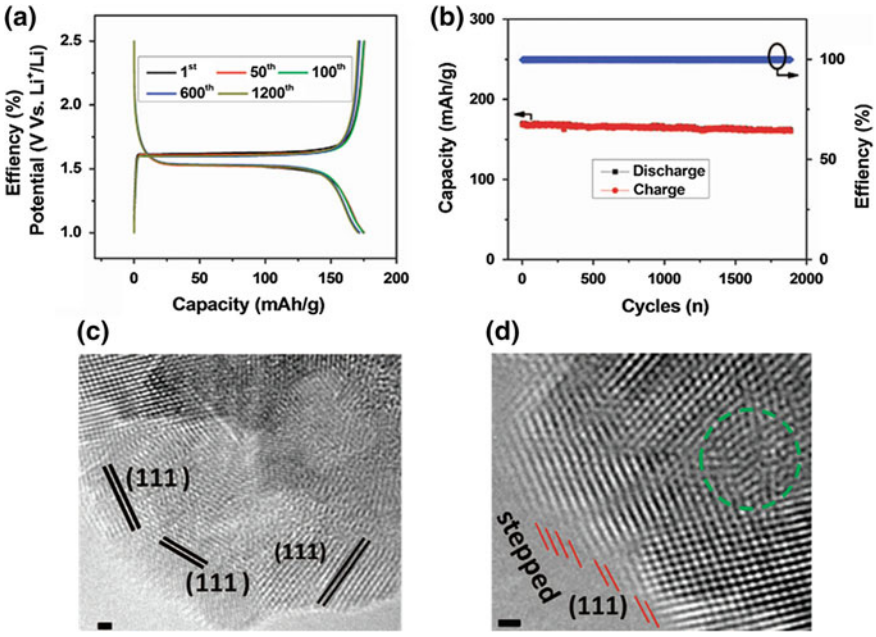

Fig. 5.25 Electrochemical characterization of Cu/LTO scaffold: **a** The galvanostatic discharge/charge voltage profiles of Cu/LTO at 0.5 C in the 1st, 50th, 100th, 600th, and 1200th cycles. **b** The cycling performance and corresponding Coulombic efficiency of Cu/LTO at 1 C. The capacities were estimated based on their total mass of electrode materials. The detailed morphologies of the Cu/LTO edge: **c** HRTEM image taken of the edge area of Cu/LTO. **d** HRTEM image of a piece of the exposed LTO (111) planes showing a stepped surface. The *green circle* denotes a defect on the surface (Reproduced from Ref. [8]. Copyright 2015, Nature Publishing Group.)

of 0.5 C which is comparable to the theoretical value (175 mAh/g). The excellent rate performance is believed to be associated with the structure features of the electrode composites.

The detailed morphologies of Cu/$Li_4Ti_5O_{12}$ edge have been carefully studied by HRTEM as shown in Fig. 5.25c, d. On the edge of Cu/$Li_4Ti_5O_{12}$ particles, there are large number of exposed high energy (111) facets resulting from the space confining effect of the nanosized pores. The $Li_4Ti_5O_{12}$ surfaces are terminated by a high density of atomic steps and kinks together with many zig–zag interfaces. Generally, the high density of atomic steps is believed to be one of the important origins of the high catalytic or electrochemical activities of small nanomaterials. Similarly, this feature of the Cu/$Li_4Ti_5O_{12}$ composite electrode may facilitate the enhancement of the electrochemical performance.

5.5 Nanoporous Metal Materials as Electrode for Li-Air Batteries

Li-air battery is an emerging energy storage device with huge theoretic specific energy and energy density (5.21 kWh/kg), which is based on a reversible redox reaction between Li metal and air (O_2). The fundamental cathodic reaction is shown in the following equation: $2Li^+ + 2e^- + O_2 \leftrightarrow Li_2O_2$ ($E_0 = 2.96$ V vs. Li/Li^+) [29]. The cathode reaction is based on the formation/decomposition of Li_2O_2 during discharge/charge processes. However, despite the great advantages in its electrochemical performance, several challenges remain unsolved before the practical applications, with the most critical issues including low round-trip efficiency and poor cycle stability, which are associated with the problems resulting from cathode performance fading. During the past few years, great efforts have been devoted to investigating new cathode materials for Li-air battery and there are many encouraging results. Among the reported results, carbon nanotubes, graphene nanosheets and carbon/metal oxide or metal composites are popular choices [30]. However, the carbon-based electrode can react with the discharge products Li_2O_2 to form Li_2CO_3 which should be further decomposed at a much higher potential and lead to a much lower round-trip efficiency. Moreover, the carbon-based materials usually show catalytic effects toward the decomposition of organic electrolytes. Therefore, tremendous efforts have been devoted to search for carbon-free materials as cathodes. NPMs emerge as one of the promising candidates due to the following advantages. Compared with carbon, 3D NPMs have natural chemical affinity for oxides and can dramatically enhance the conductivity of insulating oxides. The high catalytic efficiency, conductivity, and excellent electrochemical/mechanical stability promise the reversible formation/decomposition of Li_2O_2. The interconnected porous structures provide enough space for the storage of discharge products such as Li_2O_2. In this context, NPG and core–shell metal oxides/NPG have been investigated as cathodes in Li-air batteries.

NPG electrode, prepared by dealloying white gold leaf, has been adopted as the cathode in Li-air battery using 0.1 M $LiClO_4$-DMSO electrolyte [29]. An ultrastable cycle performance has been retained even after 100 cycles. The variation of the discharge/charge plateaus is also negligible. Although the capacity may look relatively modest with a capacity 300 mAh/g, it must be noted that this value is normalized to the mass of gold, which is equivalent to about 3000 mAh/g of carbon. The reversible formation/decomposition of Li_2O_2 on NPG surface has been further confirmed by the Raman spectra and DEMS analysis. The purity of the discharge products Li_2O_2 is higher than 99 % even on the 100th cycle and nearly all of the discharge products can be decomposed upon charging. NPG electrode also shows particular catalytic effects at promoting the decomposition of Li_2O_2, with all of the Li_2O_2 being decomposed below 4 V and nearly 50 % decomposed below 3.3 V, which demonstrates superior Li_2O_2 decomposition kinetics. It is about 10 times faster than on carbon electrodes. The superior performance can be attributed to the good catalytic activity of gold and nanoporous structure features.

NPG has also been investigated as skeleton to support other insulator oxide electrocatalysts such as RuO_2, MnO_2, and Co_3O_4 as advance cathodes in Li-air batteries [31]. The hybrid catalysts show a synergy effect of highly conductive NPG scaffold and catalytically active metal oxides. The metal oxide/NPG hybrid are usually fabricated by an electrochemical plating method. Heat treatment is necessary for the formation of metal oxides. The microstructure of the as-annealed RuO_2/NPG composite cathode is characterized by TEM as shown in Fig. 5.26. The hybrid composite displays an open nanoporous structure and RuO_2 coating layer appears in relatively dark contrast compared to gold ligaments as displayed in Fig. 5.26a. The zoom-in image displays that the RuO_2 uniformly coats on the surface of gold ligaments, forming a 3D core–shell nanostructure (Fig. 5.26b). High-resolution STEM images reveal that the oxide coating bonds well with the gold substrate, and the oxide layer is comprised of 3–5 nm crystallites (Fig. 5.26c). STEM-EDS

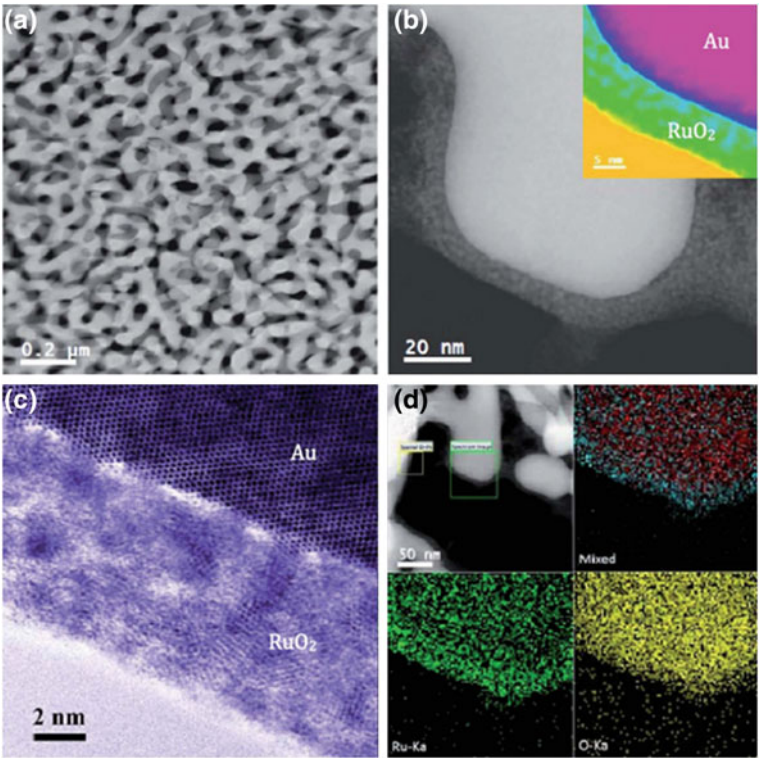

Fig. 5.26 Microstructure of the as-annealed RuO_2–NPG composite cathode. **a** Bright-field TEM image showing the open porous composite. **b** HAADF-STEM image displaying a 3D core–shell nanostructure with the oxide shell thickness of ~10 nm. The *inset* is the temperature gradient color image to highlight the core–shell structure. **c** HRTEM image revealing the nanocrystalline RuO_2 and well-bonded interface. **d** EDS mappings of the RuO_2–NPG composite (Reproduced from [31]. Copyright 2015, The Royal Society of Chemistry.)

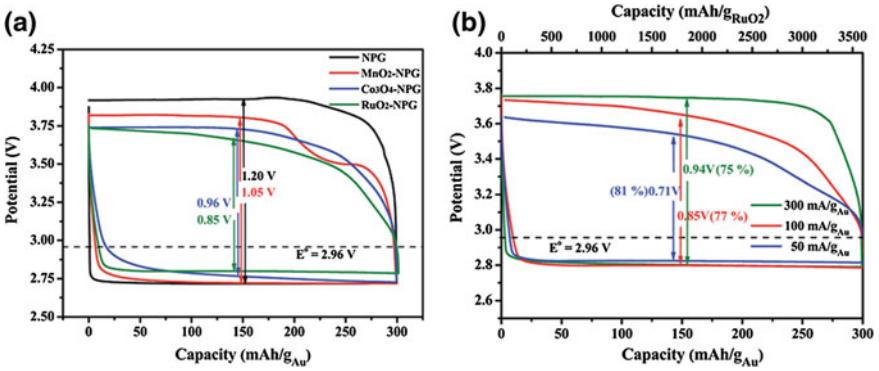

Fig. 5.27 **a** The galvanostatic discharge/charge curves of the Li–O_2 batteries with RuO_2–NPG, Co_3O_4–NPG, MnO_2–NPG and pure NPG cathodes at the current density of 100 mA/gAu. Rate dependence (**b**) of RuO_2–NPG based batteries (Reproduced from Ref. [31]. Copyright 2015, The Royal Society of Chemistry.)

mappings (Fig. 5.26d) further confirm that Ru and O atoms uniformly distribute in the coating layer. Similar microstructures of MnO_2 and Co_3O_4 coated composite electrode have also been obtained.

These metal oxide/NPG composites are then processed as cathodes of Li-O_2 batteries [31]. The voltage profiles of bare NPG and electrodes deposited with different metal oxides are shown in Fig. 5.27a. Three metal oxides/NPG composites electrodes all demonstrate considerably lower average charge potential (about 3.6–3.8 V) than that of pure NPG (about 3.9 V), demonstrating that metal oxides can effectively enhance the decomposition kinetics of Li_2O_2. On the other hand, the metal oxide cathodes exhibit an average discharge potential close to 2.8 V, which is also slightly higher than pure NPG, revealing the efficient formation of discharge products. Interestingly, the charge and discharge overpotentials of the cathodes show the evident dependence on the type of metal oxides. The RuO_2/NPG electrode shows the lowest charge potential and is fairly consistent with the reported results.

5.6 Synthesis of Nanoporous Metals Based on Delithiation Mechanism

In LIBs, Li-ions shuttle between anode and cathode during discharge/charge processes. In a half battery with a Li metal counter electrode, the desertion of Li-ions from the electrode during charging has been experimentally found to result in the formation of nanoporous structures. This phenomenon has been explored to be a versatile template-free method for the synthesis of not only transition metals but also metal oxides with large surface area and pronounced nanoporosity.

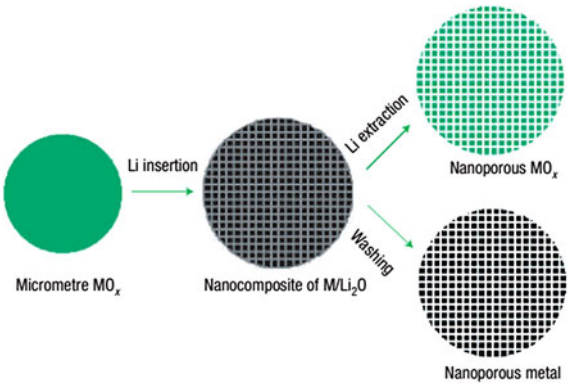

Fig. 5.28 General scheme for the template-free electrochemical lithiation/delithiation synthesis of nanoporous structures (Reproduced from [32]. Copyright 2006, Nature Publishing Group.)

The overall synthetic procedure is shown in Fig. 5.28 [32]. The metal oxides with grain sizes typically at the micrometer scale are used as electrode and fabricated into Li batteries. Upon discharging, Li-ions insert into electrode materials to form nanocomposites. It should be noted that both NPMs and metal oxides can be generated from the nanocomposites according to different treatments. For example, metal oxides with nanoporous structures can be obtained by desertion of Li-ions during the electrochemical process. Meanwhile, NPMs can be observed after dissolving the Li_2O component. The obtained Pt nanograins are found to possess sufficient porosity with most pores locating in the range of 2–20 nm. Nanoporous RuO_2 has also been fabricated from sub-micrometer RuO_2 by an electrochemical lithiation/delithiation process. The obtained nanoporous RuO_2 show a microstructure of disordered aggregation of nanoparticles around 2–8 nm, with an overall porosity about 58 %.

Bicontinuous nanoporous Sn by dealloying Li from Li–Sn alloys have also been constructed in Li-ion battery [33]. The morphology can be remarkably affected by alloy composition, particle size, and dealloying rate. The nanoporosity formation is illustrated in Fig. 5.29 during a potentiostatic dealloying process. Thus-obtained Sn particles show a roughened sinusoidal-like surface structure, containing 30 at.% Li. By increasing the Li content to 50 at.%, a bicontinuous microstructure starts to appear. This porous structure can further evolve into a morphology very similar to that of NPG when Li concentration is larger than 75 at.% as shown in Fig. 5.29g. The Li segregation process from this system can be ascribed to two different mechanisms, i.e., percolation dissolution and solid-state diffusion. Any solid elements that can form alloys with Li or other guest ion elements over a sufficient composition range can be transformed into nanoporous structure by this method.

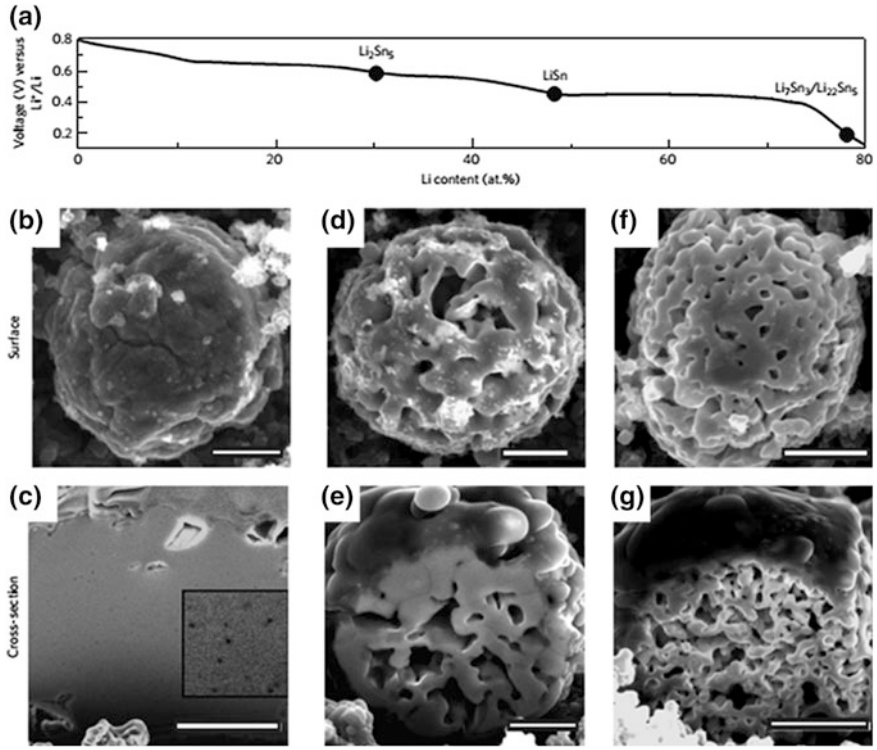

Fig. 5.29 Potentiostatic dealloying (1 V vs. Li^+/Li) results of Sn particle morphologies as a function of Li composition obtained by a single alloying/dealloying cycle in 1 M $LiPF_6$ in ethylene carbonate/diethylcarbonate, 1:1 v/v at room temperature. **a** Voltage versus Li content for alloying Li into Sn particles at a fixed current of −49.7 mA/g Sn. The voltages define the composition of the particles. **b**–**g** The *first row* of SEM images corresponds to particle surfaces and the *second row* to focused ion beam milled cross sections of the particles. **b**, **c** $Li_{0.30}Sn_{0.70}$; the surface is roughened with void nodules and the particle interior contains 10-nm-diameter voids (**c**), *inset*, size of image, 200 nm) that may have formed through a Kirkendall process. These voids are absent in virgin Sn particles. **d**, **e** $Li_{0.48}Sn_{0.52}$; collapsed bicontinuous morphology yielding a hollow core–shell-like structure. **f**, **g** $Li_{0.77}Sn_{0.23}$; bicontinuous morphology with a ligament size of 50–100 nm. *Scale bars* 500 nm (Reproduced from Ref. [33]. Copyright 2013, Nature Publishing Group.)

5.7 Summary and Outlook

NPM-based electrode materials have gained great success both in Li-ion batteries and Li-air batteries. Besides the straightforward fabrication of active nanoporous electrodes using dealloying, NPMs with three-dimensional bicontinuous structures have also been widely used as scaffolds to support active materials which ranges from metals, alloys, metal oxides, sulfides to insertion electrode materials. The improved electrochemical performances are mainly originated from the following

three aspects: (1) 3D bicontinuous architectures provide high surface areas readily accessible by carrier charges and electrolyte; (2) porous structure at nanometer scale allows the reducing of the Li-ion diffusion length between the electrolyte and the electrode, and also the diffusion pathway inner the active materials; (3) the residual space in the electrode composite can accommodate large volume expansion during discharging–charging processes.

Although significant progresses have been achieved, NPM-based electrodes are still in their early stages of research and development. There is still a long way to go before their ultimate applications, and substantial technical challenges remain which include at least the following critical points:

1. Reducing the usage of NPM scaffolds. Because metals generally have large mass density, active materials decorated on NPM scaffolds typically account for less than 20 wt% in the resulted nanocomposites, far less than the percentage of active materials in the present commercialized electrodes. Researches should therefore focus on exploring high porosity lightweight electrode structures, especially those with hierarchical porous structures in both nanometer and micron scales, in order to improve the ratio of active materials in the entire electrodes.
2. Investigating non-noble metals with nanoporous structures for composite electrodes. It is widely recognized that the utilization of noble metals such as Au and Pt in LIBs or LABs is impractical and will undoubtedly increase the total cost. It is thus highly urgent to develop non-noble metals with nanoporous structures for LIBs or other energy storage devices. Normally, the transition metals can be easily oxidized by the oxygen in ambient air during the heat treating process. Great care and new technologies should be taken and developed to deal with these advanced materials.
3. Fabrication of electrode composites with high exposure of desired crystal facets by taking full advantages of the space effects of the porous structure. As discussed above, the insertion/desertion rates of Li and other guest ions are highly dependent on the crystallographic planes. The $Li_4Ti_5O_{12}$/nanoporous Cu composite electrodes show ultrahigh rate and cycle performance as compared with normal nanostructured $Li_4Ti_5O_{12}$ materials. Theoretical calculations also prove that the superior performance is associated with the exposure of {111} facets. New fabrication techniques should therefore be explored to functionalize 3D NPM scaffolds in this way based on the understanding of interfacial structures between active materials and the substrate metals.

References

1. Bruce PG, Scrosati B, Tarascon JM (2008) Nanomaterials for rechargeable lithium batteries. Angew Chem Int Ed 47(16):2930–2946
2. Thackeray MM, Wolverton C, Isaacs ED (2012) Electrical energy storage for transportation—approaching the limits of, and going beyond, lithium-ion batteries. Energy Environ Sci 5 (7):7854

3. Goodenough JB (2014) Electrochemical energy storage in a sustainable modern society. Energy Environ Sci 7(1):14–18
4. Choi NS, Chen Z, Freunberger SA, Ji X, Sun YK, Amine K et al (2012) Challenges facing lithium batteries and electrical double-layer capacitors. Angew Chem Int Ed 51(40): 9994–10024
5. Park M, Zhang X, Chung M, Less GB, Sastry AM (2010) A review of conduction phenomena in Li-ion batteries. J Power Sour 195(24):7904–7929
6. Jeong G, Kim Y-U, Kim H, Kim Y-J, Sohn H-J (2011) Prospective materials and applications for Li secondary batteries. Energy Environ Sci 4(6):1986
7. Yu Y, Gu L, Lang X, Zhu C, Fujita T, Chen M et al (2011) Li storage in 3D nanoporous Au-supported nanocrystalline tin. Adv Mater 23(21):2443–2447
8. Wang X, Liu D, Weng Q, Liu J, Liang Q, Zhang C (2015) Cu/$Li_4Ti_5O_{12}$ scaffolds as superior anodes for lithium-ion batteries. NPG Asia Mater 7(4):e171
9. Park CM, Jeon KJ (2011) Porous structured SnSb/C nanocomposites for Li-ion battery anodes. Chem Commun 47(7):2122–2124
10. Zhang J, Wang Z, Hong Y, Li S, Jin X, Chen GZ (2014) Electrochemical fabrication of porous Sn/SnSb negative electrodes from mixed SnO_2–Sb_2O_3. Electrochem Commun 38:36–39
11. Kure-Chu SZ, Satoh A, Miura S, Mizuhashi M, Yashiro H (2015) Nanoporous Sn–SnO_2–TiO_2 composite films electrodeposited on cu sheets as anode materials for lithium-ion batteries. J Electrochem Soc 162(7):D305–D311
12. Hwang G, Park H, Bok T, Choi S, Lee S, Hwang I et al (2015) A high-performance nanoporous Si/Al_2O_3 foam lithium-ion battery anode fabricated by selective chemical etching of the Al–Si alloy and subsequent thermal oxidation. Chem Commun 51(21):4429–4432
13. Liu S, Feng J, Bian X, Qian Y, Liu J, Xu H (2015) Nanoporous germanium as high-capacity lithium-ion battery anode. Nano Energy 13:651–657
14. Yu Y, Yan C, Gu L, Lang X, Tang K, Zhang L et al (2013) Three-dimensional (3D) Bicontinuous Au/Amorphous-Ge thin films as fast and high-capacity anodes for Lithium-ion bateries. Adv. Energy Mater 3:281–285
15. Zhang S, Xing Y, Jiang T, Du Z, Li F, He L et al (2011) A three-dimensional tin-coated nanoporous copper for lithium-ion battery anodes. J Power Sour 196(16):6915–6919
16. Yao M, Okuno K, Iwaki T, Awazu T, Sakai T (2010) Long cycle-life $LiFePO_4$/Cu–Sn lithium ion battery using foam-type three-dimensional current collector. J Power Sour 195(7): 2077–2081
17. Reddy MV, Rao GVS, Chowdari BVR (2013) Metal oxides and oxysalts as anode materials for Li ion batteries. Chem Rev 113(7):5364–5457
18. Hou C, Shi X-M, Zhao C-X, Lang X-Y, Zhao L-L, Wen Z et al (2014) SnO_2 nanoparticles embedded in 3D nanoporous/solid copper current collectors for high-performance reversible lithium storage. J Mater Chem A 2(37):15519
19. Hou C, Lang X, Han G, Li Y, Zhao L, Wen Z et al. (2013) Integrated solid/nanoporous copper/oxide hybrid bulk electrodes for high-performance Lithium-ion batteries. Sci Reports 3:2878
20. Chen X, Sun K, Zhang E, Zhang N (2013) 3D porous micro/nanostructured interconnected metal/metal oxide electrodes for high-rate lithium storage. RSC Adv 3(2):432–437
21. Liu DQ, Yang ZB, Wang P, Li F, Wang DS, He DY (2013) Preparation of 3D nanoporous copper-supported cuprous oxide for high-performance lithium ion battery anodes. Nanoscale 5 (5):1917–1921
22. Yang W, Cheng G, Dong C, Bai Q, Chen X, Peng Z et al (2014) NiO nanorod array anchored Ni foam as a binder-free anode for high-rate lithium ion batteries. J Mater Chem A 2 (47):20022–20029
23. Yan X, Tong X, Wang J, Gong C, Zhang M, Liang L (2013) Construction of three-dimensional porous nano-Ni/NiO nanoflake composite film for electrochemical energy storage. Mater Letters 106:250–253

24. Guan C, Wang Y, Zacharias M, Wang J, Fan HJ (2015) Atomic-layer-deposition alumina induced carbon on porous $Ni_xCo_{1-x}O$ nanonets for enhanced pseudocapacitive and Li-ion storage performance. Nanotechnology 26(1):014001
25. Bi Z, Paranthaman MP, Menchhofer PA, Dehoff RR, Bridges CA, Chi M et al (2013) Self-organized amorphous TiO_2 nanotube arrays on porous Ti foam for rechargeable lithium and sodium ion batteries. J Power Sour 222:461–466
26. Ni SB, Yang XL, Li T (2012) Fabrication of a porous NiS/Ni nanostructured electrode via a dry thermal sulfuration method and its application in a lithium ion battery. J Mater Chem 22(6):2395–2397
27. Ni SB, Yang XL, Li T (2012) Fabrication of porous Ni_3S_2/Ni nanostructured electrode and its application in lithium ion battery. Mater Chem Phys 132(2–3):1103–1107
28. Mi L, Ding Q, Chen W, Zhao L, Hou H, Liu C et al. (2013) 3D porous nano/micro nickel sulfides with hierarchical structure: controlled synthesis, structure characterization and electrochemical properties. Dalton Trans 42:5724–5730
29. Peng Z, Freunberger SA, Chen Y, Bruce PG (2012) A reversible and higher-rate Li-O_2 battery. Science 337(6094):563–566
30. Luntz AC, McCloskey BD (2014) Nonaqueous Li-air batteries: a status report. Chem Rev 114:11721–11750
31. Chen LY, Guo XW, Han JH, Liu P, Xu XD, Hirata A et al (2015) Nanoporous metal/oxide hybrid materials for rechargeable lithium–oxygen batteries. J Mater Chem A 3(7):3620–3626
32. Hu YS, Guo YG, Sigle W, Hore S, Balaya P, Maier J (2006) Electrochemical lithiation synthesis of nanoporous materials with superior catalytic and capacitive activity. Nat Mater 5(9):713–717
33. Chen Q, Sieradzki K (2013) Spontaneous evolution of bicontinuous nanostructures in dealloyed Li-based systems. Nat Mater 12(12):1102–1106

Chapter 6
Conclusions and Prospects

Abstract In this chapter, summary and conclusions are drawn from previously-mentioned aspects including dealloying-driven nanoporous metals, microstructural regulation of nanoporous metals, and their applications in energy conversion/storage fields. We also briefly introduce the potential applications of nanoporous metals in other energy-related fields like water splitting. Finally, prospects are put forward considering the formation mechanism, microstructural design/modulation and applications of dealloying-driven nanoporous metals.

Keywords Nanoporous metals · Dealloying · Energy conversion/storage · Water splitting

Environment deterioration and global warming are becoming hot topics of discussion all over the world since the past few decades, because we are excessively dependent on fossil fuels in the current energy consumption system, which account for approximately 68 % of the electrical energy produced. To cope with the ever-increasing energy demand and decreasing of fossil energy reserves as well as global environmental issues, it is highly urgent to develop and utilize renewable energy resources. Among them, electrochemical energy production is under serious consideration as an alternative energy/power source, as long as this energy consumption is designed to be more sustainable and more environmentally friendly. Systems for electrochemical energy conversion and storage include fuel cells, supercapacitors (or electrochemical capacitors, ECs), and batteries. Although the energy conversion (fuel cells) and storage (ECs and batteries) mechanisms are different, there are "electrochemical similarities" of these three systems, as schematically presented in Fig. 6.1 [1]. The common features of these three systems are that the energy-providing processes take place at the phase boundary of the electrode/electrolyte interface and that electron and ion transport are separated. For electrochemical energy systems, electrode materials and electrode assemblies play a dominant role in the operation (energy/power densities, efficiency, and service life) of these systems.

Nanoporous metals (NPMs) have been receiving more and more attention in the past 15 years, due to their unique structures and associated properties. As novel

Y. Ding and Z. Zhang, *Nanoporous Metals for Advanced Energy Technologies*, DOI 10.1007/978-3-319-29749-1_6

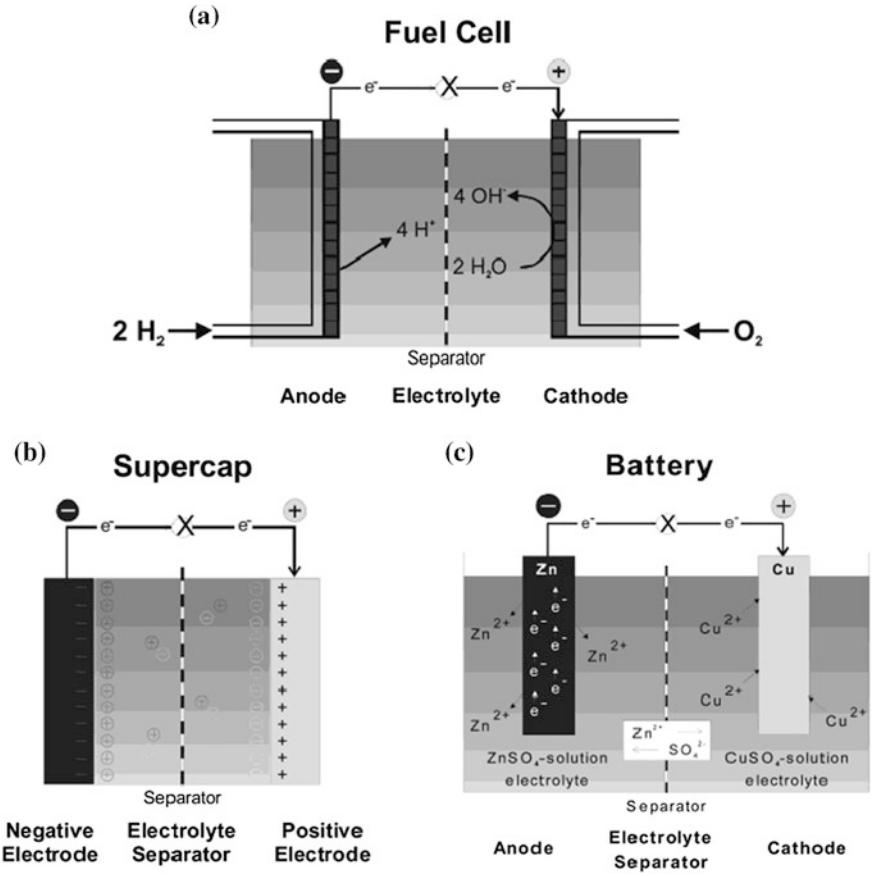

Fig. 6.1 Representation of **a** a fuel cell showing the continuous supply of reactants (hydrogen at the anode and oxygen at the cathode) and redox reactions in the cell, **b** a supercapacitor (electrochemical capacitor), illustrating the energy storage in the electric double layers at the electrode–electrolyte interfaces and **c** a battery (Daniell cell) showing the key features of battery operation and the requirements on electron and ion conduction. (Reproduced from Ref. [1]. Copyright 2004, American Chemical Society)

functional materials, NPMs have a three-dimensional porous structure at the nanoscale. More importantly, NPMs show great potentials in applications including catalytic, sensing, actuation, and especially, energy-related fields like fuel cells, supercapacitors, lithium ion batteries (LIBs), and so forth.

In this book, we mainly discuss NPMs and their applications for advanced energy technologies (fuel cells, supercapacitors, LIBs). Conclusions are drawn from the following.

6.1 Introduction to Nanoporous Metals

In this chapter, we give a brief introduction to NPMs. First, we show the definition of NPMs, the difference between NPMs and normal metal foams, the kind of NPMs and the fabrication methods of NPMs. NPMs are such a kind of metallic materials with interconnected backbones (ligaments) and pores (channels) on the nanoscale (ranging from several nanometers to hundreds of nanometers). And we should know that "nanoporous" is different from "mesoporous." The latter (2–50 nm) is defined by the International Union of Pure and Applied Chemistry (IUPAC). Moreover, the length scale of nanopores in NPMs is several orders of magnitude smaller than that (above tens of microns) of pores in normal metal foams. Moreover, the pore distribution in NPMs could be ordered, or random, or the combination of the former two.

Second, the microstructural characteristics of NPMs are summarized. Nanoporous gold (NPG) is the prototype of NPMs, and actually many pure elements (transition metals, elements from IIIA to VA groups and even semiconductor elements) and alloys could be fabricated into a nanoporous structure. Both bulk (up to centimeters) and nanosized (zero-dimensional (0D), 1D, and 2D) NPMs have been reported. Metallic ligaments and nanopore channels in dealloying-driven NPMs are topologically and morphologically equivalent, which means that they are inverses of each other in three-dimensional space. The microstructure of NPMs may be homogeneous, and NPMs with multiscale or multilevel porous structures can also be prepared including multimodal pore size distribution or hierarchically porous nanostructures, ordered random nanoporous architectures, nanoporous periodic arrays, nanoporous metallic composites, and hollow metallic nanostructures. In addition, the crystalline orientation and lattice defects of NPMs depend upon the microstructure of the precursor alloys and the dealloying process.

Third, the properties and potential applications of NPMs are outlined. NPMs combine the properties of both metals and nanostructured materials, and show the structure-related electrical, magnetic, mechanical, optical, catalytic, and electrocatalytic properties. Owing to their unique microstructures and related properties, NPMs are quite promising in applications like sensors, actuators, fuel cells, LIBs, supercapacitors, metal–air batteries, water splitting, synthesis of chemicals, hydrogen storage, automobile exhaust treatment, drug loading and release, bonding materials, and so forth. In this book, we mainly focus upon their applications for advanced energy technologies such as fuel cells, supercapacitors, and LIBs.

6.2 Formation and Microstructural Regulation of Nanoporous Metals

At present, dealloying is the most important method to fabricate NPMs. In this chapter, we mainly discuss the dealloying-driven formation of NPMs, the methods to characterize the microstructures of NPMs, as well as the strategies adopted to the microstructural regulation of NPMs.

Dealloying has a long history and is a common corrosion process, during which the less noble element(s) is selectively etched away and the more noble element(s) diffuses/reorganizes into a nanoporous structure. Dealloying was called as "depletion gilding" at the time of pre-Columbian Central America and the early Middle Ages in European and Near Eastern, and was used to decorate the surfaces of crafts. In 1920s, Raney® metals were invented and fabricated by dealloying of Al-based precursors. In the most time of last century, much attention was paid to dealloying mainly from the viewpoint of corrosion/protection. At the beginning of the new century, dealloying got renewed attention as a powerful strategy to produce functionalized NPMs.

To understand the dealloying mechanisms is crucial to the design/fabrication of NPMs. During dealloying, complex physical and chemical/electrochemical reactions occur at the alloy/solution interface. In situ/ex situ experiments and computer simulations could be performed to unveil the formation mechanism of NPMs during dealloying. Several mechanisms have been proposed to rationalize the dealloying-driven formation of nanoporous structures, including dissolution/redeposition, dissolution/surface diffusion, volume diffusion, etc. The main concerns are correlated with the selective dissolution of the less noble element(s) and surface diffusion of the more noble element(s), simultaneously considering the critical potential and the parting limit. In addition, the influence of anions (like halide ions) and the phase constitution should also be taken into consideration.

Many techniques can be used to characterize the microstructures (also compositions and morphologies) of NPMs, including X-ray diffraction, scanning electron microscopy, transmission electron microscopy, high-resolution transmission electron microscopy, scanning transmission electron microscopy, scanning tunneling microscopy, energy dispersive X-ray analysis, small angle neutron scattering, and so forth. The combination of scanning transmission electron microscopy with energy dispersive X-ray analysis/electron energy loss spectrometry can well reveal the morphologies and compositional distribution at the nanoscale and even atomic resolution. Three-dimensional tomographic reconstruction is popular to reveal the interior microstructures of NPMs. In addition, the methods to evaluate the characteristic length scale and the specific surface area of NPMs are also summarized.

In the last section, we discuss the strategies to regulate the microstructures/compositions/morphologies of NPMs from three aspects: design of precursors for dealloying, control over the dealloying parameters and post-dealloying treatment, and further modification of NPMs to strengthen their functional applications. As for the design of precursors for dealloying, people should consider the composition (elements), phase constitution, crystallinity, and microalloying of the precursors. Processing parameters are also important for the microstructural regulation of NPMs. The microstructures of NPMs can be regulated by controlling over the dealloying parameters, including chemical/electrochemical dealloying, the dealloying solution, temperature, the applied potential, the dealloying step (two-step or multistep), the effect of atmosphere, and dealloying in nonaqueous media. The post-dealloying treatment like annealing can also be used to regulate the microstructures of NPMs, especially their characteristic length scale. In addition, to

enhance the functions of NPMs for different applications, some strategies could be adopted to further modify the microstructures of NPMs.

6.3 Nanoporous Metals for Fuel Cell Applications

In order to function in real fuel cells, nanoparticulate catalysts have to undergo further processing by adsorbing onto high surface area conducting substrates such as carbon black to facilitate the catalyst dispersion and fuel diffusion. Due to the physical adsorption on the carbon support, the catalyst nanoparticles tend to aggregate to form larger nanoparticles or even lose contact to the support under the operation conditions. Moreover, the large contact resistance between carbon particles, which originates from the incorporation of poorly conductive polymer electrolyte such as Nafion® when preparing the membrane electrode assembly (MEA), leads to the increase of internal resistance in catalytic layer and decrease of overall cell performance.

In comparison, dealloyed NPMs represent a new class of high surface area *structured* nanoelectrodes, as characterized by their clean and readily accessible surfaces, highly conductive open framework structure for free transport of medium molecules and electrons, and tunable surface chemistry which is particularly desirable for electrocatalysis. Being support free and particle free, NPMs completely eliminate the support corrosion problem and particle aggregation/sintering problem, therefore providing a mechanically rigid scaffold for grafting catalytically active species.

Preliminary investigations have revealed some encouraging results not commonly seen from traditional nanoparticle electrocatalysts, such as ultralow Pt loading hydrogen fuel cells and direct formic acid fuel cells. However, this has to be related to the relatively simple and fast oxidation kinetic of hydrogen on Pt and recently clarified formic acid electrooxidation mechanism. This is why the progress in exploring similarly active NPG-based nanoelectrodes for direct methanol, ethanol and/or glucose fuel cells is comparatively slow. Except for NPG-based electrocatalysts, the implementation of NPMs and alloys for actual fuel cells has not been realized. The main difficulty would be the development of cost-effective methods to produce high quality, multicomponent alloy thin films. The nanoporous alloys so far screened are mostly made from melt spun alloy foils which have a thickness of tens of microns or above, and thus are not compatible to any MEA fabrication techniques.

Despite the advantages and disadvantages mentioned above, the overall advancement in fuel cells is still in its infancy. As a relatively new class of materials, the majority of their structural properties and applications remain unexploited, and their applicability in useful technologies such as fuel cells is mainly practiced in a traditional engineering manner, rather than based on a rational system level. In-depth researches, especially those with comprehensive knowledges, skills and resources will lead to more ground-breaking discoveries, and dealloyed NPMs will certainly have a bright future in advanced energy technologies including fuel cells.

6.4 Nanoporous Metals for Supercapacitor Applications

NPMs-based composite electrodes have been widely investigated in supercapacitors and gained great success. With unique three-dimensional bicontinuous structures, NPMs can serve as both supports of active materials and current collectors. Benefited from good electron conductivity and electrolyte penetrability, high energy density and power density can be obtained in NPMs-based supercapacitors. However, before NPMs are feasible for actual applications, critical technological challenges should be overcome and are summarized as follows:

(1) Reducing the cost and weight of the nanoporous metal frameworks. Most of the reports so far are based on nanoporous noble metals or late transition metal elements. Their high cost undoubtedly poses unfavorable economic concerns while their heavy weight limits their practical applications from a system viewpoint. It is thus highly urgent to develop nanoporous non-noble, light weight metals that are still mechanically robust and electrochemical stable for further functionalization for supercapacitor applications.
(2) Improving the porosity of the structure to allow higher mass loading of active materials. Highly porous nanostructures, especially those with narrow ligaments and large open channels can incorporate more active materials without sacrificing their specific surface area. Besides, multimodal structures [2] may provide additional benefits of facilitating mass transfer and improving mechanical rigidity at no cost of surface area decrease. Technological improvement in these areas allows anchoring of more active materials and thus improves the specific capacity of the whole device.
(3) Increasing the operation voltage window. A wide voltage window to 1.8 V has been observed in aqueous electrolyte [3]. This encourages us to further optimize the components and surface oxidation properties of nanoelectrodes, for example, by accommodation of the electrochemical properties of metal substrates, surface active species, and the electrolytes within the whole framework, to realize a much enhanced supercapacitor performance.
(4) Optimizing the active electrode components for asymmetric supercapacitors. The asymmetric supercapacitors usually exhibit large working voltage window due to the different operation voltage range of the respective active materials. By careful design and preparation of composite electrodes with large potential difference, the resulted asymmetric supercapacitors would hold better electrochemical performance.

Finally, special technologies such as wearable electronic devices require particular development of challenging technologies, such as flexible, all solid state, transparent, and durable power devices. As a unique high power density power source, supercapacitors may also find new solutions and applications in these next-generation technologies.

6.5 Nanoporous Metals for Li Battery Applications

NPMs-based electrode materials have gained great success in both Li-ion batteries and Li–air batteries. Besides the straightforward fabrication of active nanoporous electrodes using dealloying, NPMs with three-dimensional bicontinuous structures have also been widely used as scaffolds to support active materials including metals, alloys, metal oxides, and sulfides. The improved electrochemical performances mainly originate from the following three aspects: (i) 3D bicontinuous architectures provide high surface areas readily accessible by carrier charges and electrolyte; (ii) porous structure at the nanometer scale allows the decrease of the Li-ion diffusion length between the electrolyte and the electrode, and also the diffusion pathway inner the active materials; (iii) the residual space in the electrode composite can accommodate large volume expansion during discharging–charging processes.

Although significant progresses have been achieved, NPMs-based electrodes are still in their early stages of research and development. There is still a long way to go before their ultimate applications, and substantial technical challenges remain which include at least the following critical points:

(1) Reducing the usage of NPM scaffolds. Because metals generally have large mass density, active materials decorated on NPM scaffolds typically account for less than 20 wt% in the resulted nanocomposites, far less than the percentage of active materials in the present commercialized electrodes. Researches should therefore focus on exploring highly porous light weight electrode structures, especially those with hierarchically porous structures in both nanometer and micron scales, in order to improve the ratio of active materials in the entire electrodes.

(2) Investigating non-noble metals with nanoporous structures for composite electrodes. It is widely recognized that the utilization of noble metals such as Au and Pt in LIBs or LABs is impractical and will undoubtedly increase the total cost. It is thus highly urgent to develop non-noble metals with nanoporous structures for LIBs. Normally, transition metals can be easily oxidized by oxygen in ambient air during the heat treating process. Great care should be taken and new technologies should be developed to deal with these advanced materials.

(3) Fabrication of electrode composites with high exposure of desired crystal facets by taking full advantages of the space effects of the porous structure. As discussed above, the insertion/desertion rates of Li and other guest ions are highly dependent on the crystallographic planes. The $Li_4Ti_5O_{12}$/nanoporous Cu composite electrodes show ultrahigh rate and cycle performance as compared with normal nanostructured $Li_4Ti_5O_{12}$ materials. Theoretical calculations also prove that the superior performance is associated with the exposure of (111) facets. New fabrication techniques should therefore be explored to functionalize 3D NPM scaffolds in this way, based on the understanding of interfacial structures between active materials and the substrate metals.

6.6 Nanoporous Metals for Other Energy-Related Technologies

As described above, NPMs show great potentials in energy conversion and storage systems including fuel cells, supercapacitors, and LIBs. In addition, these novel functional metallic materials are promising as electrodes for other energy-related applications such as water splitting.

It is known that hydrogen generation through electrolysis of water (water splitting) offers an attractive avenue to store energy from renewable sources such as the sunlight. At the same time, hydrogen as a promising clean chemical fuel is an ideal energy carrier for sustainable energy applications. An efficient electrocatalyst for the hydrogen evolution reaction (HER) is required to afford high current at low overpotential. Pt-based catalysts show high catalytic performance, but suffer from high costs and the scarcity of Pt on earth [4]. The oxygen evolution reaction (OER), as one of the most significant processes in water splitting, has also stimulated extensive studies in recent years. The OER process usually suffers from multiple steps of proton-coupled electron transfer, leading to very sluggish kinetic reactions. The most efficient electrocatalysts for OER are precious metal oxides (Ru or Ir oxides), and both the high cost and scarcity of these noble metals severely limit their practical applications [5]. Thus, successful electrolysis of water will require electrocatalysts that are highly active, cost-effective and durable. While some nanoscale catalysts satisfy these requirements, scaling up the synthesis of these nanostructured catalysts remains a challenge. And more options for robust catalysts that work at varying pHs for large-scale storage of renewable energy are still needed [6].

Most recently, Detsi et al. [6] reported mesoporous $Ni_{60}Fe_{30}Mn_{10}$-alloy based metal/metal oxide composite thick films as highly active and robust oxygen-evolution catalysts. They have used selective alloy corrosion to synthesize the robust and ultrafine mesoporous NiFeMn-based metal/metal oxide oxygen-evolving catalyst with ligament and pore sizes in the range of 10 nm and a BET surface area of 43 $m^2\ g^{-1}$, Fig. 6.2a. It is known that most unsupported, nonprecious metals oxygen-evolution catalysts require at least $\sim$350 mV overpotential to oxidize water with a current density of 10 mA cm^{-2} in 1 M alkaline solution. In contrast, the mesoporous NiFeMn-based nanocomposite catalyst exhibits a catalytic activity toward water oxidation of 500 mA cm^{-2} in 1 M KOH at 360 mV overpotential and is stable for over 11 days. In 0.5 M KOH, the overpotential is only 200 mV to achieve the oxygen oxidation current density of 10 mA cm^{-2}, Fig. 6.2b. They attributed the exceptional OER performance to three factors. First, the small size of the ligaments and pores in the mesoporous catalyst results in the high BET surface area and therefore a high density of oxygen-evolution catalytic sites per unit mass. Second, the open porosity facilitates effective mass transfer at the catalyst/electrolyte interface. Third and finally, the high bulk electrical conductivity of the mesoporous catalyst allows for effective current flow through the electrocatalyst, making it possible to use thick films with a high density of active sites and $\sim 3 \times 10^4$ cm^2 of catalytic area per cm^2 of electrode area. Therefore, they have

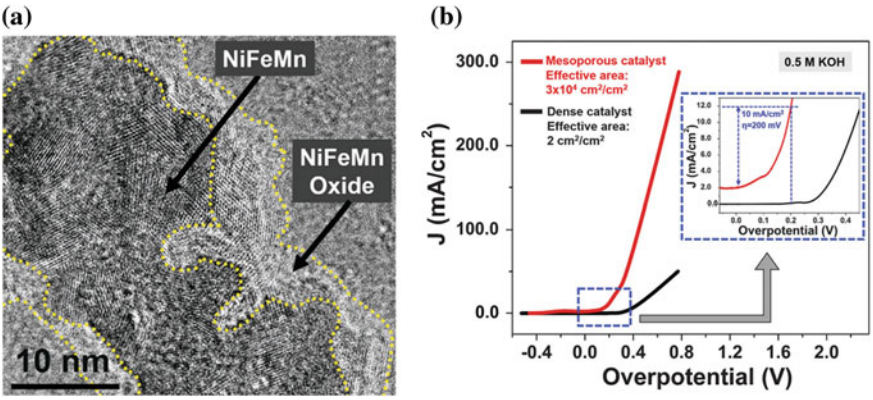

Fig. 6.2 **a** HRTEM image of a ligament in the NiFeMn-based catalyst. The ligament is covered with an oxide layer a few nm thick, demarcated by the *dashed yellow* like. Both the metal ligament and the oxide coating show lattice fringes typical of a crystalline material. Crystallinity in both components arises from electron beam induced crystallization. **b** Catalytic activities in 0.5 M KOH. Linear sweep voltammograms obtained from our mesoporous $Ni_{60}Fe_{30}Mn_{10}$ metal/metal oxide catalyst (*red*) and a dense $Ni_{60}Fe_{30}Mn_{10}$ catalyst counterpart (*black*) at a sweep rate of 1 mV s^{-1} in 0.5 M KOH. The mesoporous catalyst achieves 10 mA cm^{-2} at only 200 mV *Inset*, whereas the dense catalyst counterpart does not achieve 10 mA cm^{-2} until 430 mV (sweep rate of 1 mV s^{-1}; 0.5 M KOH). (Reproduced from Ref. [6]. Copyright 2016, The Royal Society of Chemistry)

argued that their robust catalyst could be very attractive for alkaline electrolyzers, potentially as part of high-performance solar water splitting systems, where they could be coupled to a hydrogen evolution photocathode and photovoltaics cells to generate overall water splitting at low overpotential using sunlight.

Cai et al. [7] reported three-dimensional (3D) nanoporous nickel films and foams for HER catalysts. The fabrication process involved the heat treatment of the electrodeposited zinc layer on nickel substrate and the subsequent electrochemical dealloying. The mutual diffusion of Ni and Zn during the heat treatment resulted in the formation of the Ni_2Zn_{11} alloy surface film. The 3D nanoporous nickel films with open pores and interconnected ligaments were obtained by the electrochemical dealloying of relatively active zinc from the alloy surface film, Fig. 6.3a–c. As the electrodeposited zinc amount increased, the thickness, pore diameter, and pore density of the nanoporous nickel films became larger. The thickest nanoporous nickel film presented a thickness of 8 mm and an average pore diameter of 700 nm. The as-prepared 3D nanoporous nickel films/foams exhibited much higher electrocatalytic activity for HER than smooth nickel foil and nonporous Ni foams (Fig. 6.3d). And their electrocatalytic activities for HER increased with increase in the porosity and thickness. They have argued that the enhanced electrocatalytic activity and excellent electrochemical stability for HER of nanoporous nickel films/foams can be ascribed to their unique nanostructured characteristics.

NPMs and their composites have recently demonstrated the potentials for catalyzing water splitting, but the progress is quite limited. Regardless of HER or

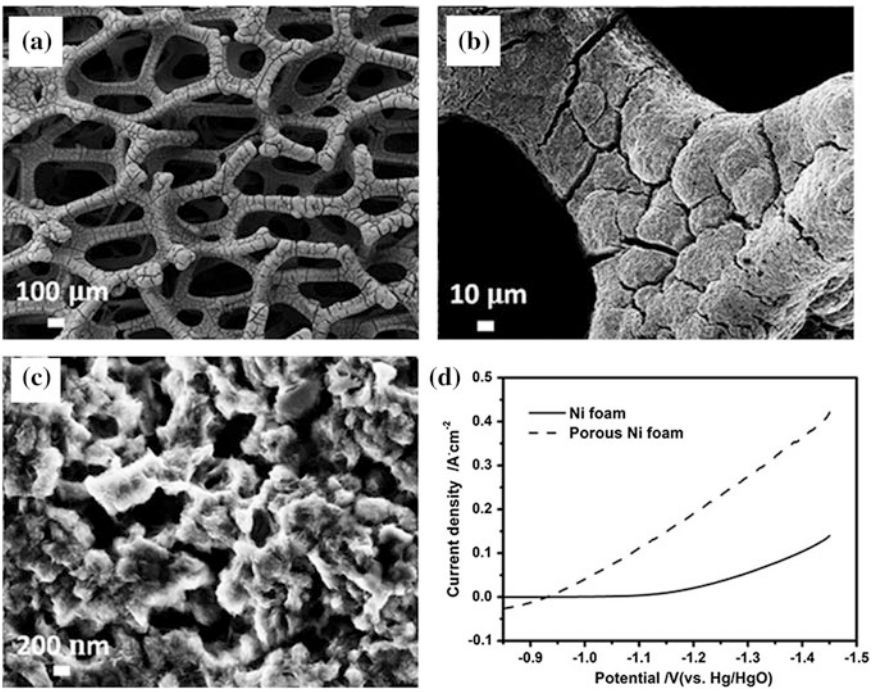

Fig. 6.3 **a–c** SEM images of porous Ni foam obtained by the as-constructed dealloying procedure. **d** Cathodic current-potential curves in 1 M KOH solution at 30 °C of Ni foam and porous Ni foam obtained by the as-constructed dealloying procedure. (Reproduced from Ref. [7]. Copyright 2013, Elsevier)

OER, highly active, cost-effective, and durable catalysts are required for practical applications in water splitting. Combining theoretical calculations and computer simulations, one should design and modulate the microstructures/compositions/morphologies of NPMs and their composites for high-performance catalysis of water splitting.

6.7 Prospects

Dealloying could be dated back to the early Middle Ages, but it got renewed attention at the beginning of this century. In the past 15 years, dealloying-driven NPMs have been receiving ever-growing interests. Due to their unique three-dimensional bicontinuous ligament–channel structure and associated mechanical/physical/chemical properties, NPMs and related materials have shown great potentials in applications such as catalysis, sensing, actuation, and especially energy conversion/storage systems like fuel cells, supercapacitors, lithium batteries,

and so on. Although obvious progress has been made, there still exist challenges with respect to NPMs and their fabrication/microstructures/properties/applications.

To understand the formation mechanisms of NPMs during dealloying is the prerequisite for the design and microstructural regulation of NPMs. People have known more about the formation of NPG during dealloying of the prototype Ag–Au precursor. But the dealloying of multicomponent multiphase precursors is quite complicated and still unclear. Great efforts should be done to reveal the underlying mechanisms during dealloying of such precursors, through the combination of in situ/ex situ experimental techniques with computer simulations. Moreover, the effects of the compositions, phase constitution, crystallinity of the precursors should be taken into consideration. As for nanosized precursors like nanoparticles, the compositions and sizes may play a dominant role during the dealloying process as well as the nanoporosity evolution.

Microstructural regulation is another important issue to explore the properties and applications of NPMs. The design of the precursors is the first step, and one should consider both the parting limit and the dealloying critical potential (for electrochemical dealloying), as well as the microstructures (phase constitution, grain size, etc.) and the sizes (bulk forms, microsized or nanosized) of the precursors. The microstructures of NPMs can also be tuned by controlling over the dealloying parameters, such as the applied potential, the dealloying solution, temperature, the dealloying duration, atmosphere, etc. Post-dealloying treatment like annealing can be adopted to modulate the characteristic length scale of NPMs or to fabricate nanoporous metal composites (for example, metal/metal oxides). To further enhance the functions of NPMs, some strategies (UPD, displacement reaction, electrochemical or electroless deposition, electropolymerization, hydrothermal synthesis, sol–gel, etc.) can be utilized to decorate functional active nanostructured layers (Pt/Pd for electrocatalysis, transition metal oxides/conducting polymers for supercapacitors, Sn/Si/Ge for LIBs, etc.) onto the ligament surfaces.

One the one hand, some progress has been achieved in dealloying-driven NPMs for advanced energy technologies. On the other hand, the applications of NPMs in energy conversion/storage systems are still in infancy, especially considering their practical applications. For applications in fuel cells, one should design/fabricate NPMs-based electrodes based upon a rational system level, taking both the electrocatalysts and the MEAs/whole cell into consideration. To uncover the reaction mechanisms using in situ spectral measurement technique (Raman, infrared, etc.) and density functional theory (DFT) calculations is quite beneficial for the design of electrocatalysts. Both the electrochemical evaluation of electrocatalysts and the performance assess of the whole cell are required for design/fabrication of high-performance electrocatalysts with high intrinsic catalytic activities at the anode/cathode, good poisoning tolerance, low materials cost and superior stability. For actual applications of NPMs in supercapacitors, critical technological challenges should be overcome, including cost/weight and porosity of NPMs, as well as the performance (specific capacitance, operation voltage window, energy/power densities) of the devices. It is highly urgent to develop nanoporous non-noble, light weight metals, which are still mechanically robust and electrochemically stable for

further functionalization for supercapacitor applications. Highly porous nanostructures, especially those with narrow ligaments and large open channels can incorporate more active materials without sacrificing their specific surface areas. For applications in LIBs and LABs, NPMs mainly provide the electrode substrate for constructing active materials and the current collector. Thus, at the prerequisite of good electrical conductivity, high specific surface area, and good stability, the usage of NPMs should be decreased in the entire electrodes. Based upon earth-abundant metals, highly porous light weight electrode materials should be explored.

In a word, as a relatively new class of materials, the majority of their structural properties/applications remain unexploited. More ground-breaking discoveries could be anticipated, provided that in-depth investigations with advanced techniques/calculations/simulations are performed on NPMs. Definitely, dealloying-driven NPMs will have a promising future in advanced energy technologies.

References

1. Winter M, Brodd RJ (2004) What are batteries, fuel cells, and supercapacitors? Chem Rev 104 (10):4245–4270
2. Ding Y, Erlebacher J (2003) Nanoporous metals with controlled multimodal pore size distribution. J Am Chem Soc 125(26):7772–7773
3. Kang J, Hirata A, Qiu HJ, Chen L, Ge X, Fujita T et al (2014) Self-grown Oxy-hydroxide@ nanoporous metal electrode for high-performance supercapacitors. Adv Mater 26(2):269–272
4. Jiang P, Liu Q, Liang Y, Tian J, Asiri AM, Sun X (2014) A cost-effective 3D hydrogen evolution cathode with high catalytic activity: FeP nanowire array as the active phase. Angew Chem Int Ed 53(47):12855–12859
5. Chen P, Xu K, Fang Z, Tong Y, Wu J, Lu X et al (2015) Metallic Co4 N porous nanowire arrays activated by surface oxidation as electrocatalysts for the oxygen evolution reaction. Angew Chem 127(49):14923–14927
6. Detsi E, Cook JB, Lesel BK, Turner CL, Liang Y-L, Robbennolt S et al (2016) Mesoporous $Ni_{60}Fe_{30}Mn_{10}$-alloy based metal/metal oxide composite thick films as highly active and robust oxygen evolution catalysts. Energy Environ Sci 9:540–549
7. Cai J, Xu J, Wang J, Zhang L, Zhou H, Zhong Y et al (2013) Fabrication of three-dimensional nanoporous nickel films with tunable nanoporosity and their excellent electrocatalytic activities for hydrogen evolution reaction. Int J Hydrogen Energy 38(2):934–941

Index

Y. Ding and Z. Zhang, *Nanoporous Metals for Advanced Energy Technologies*, DOI 10.1007/978-3-319-29749-1